

AD-A273 060



2

**TET SUMMER 1992
ENVIRONMENTAL MEASUREMENTS**

Final Report



Science Applications International Corporation
An Employee-Owned Company

DTIC
ELECTE
NOV 17 1993
A

*Original contains color
plates: All DTIC reproduct-
ions will be in black and
white*

This document has been approved
for public release and sale; its
distribution is unlimited

93-26694



24248

93

11

3

001

2

**TET SUMMER 1992
ENVIRONMENTAL MEASUREMENTS**

Final Report

Contract Number:

N00014-92-C-0174

DTIC
ELECTE
NOV 17 1993
A

Prepared For

Office of Naval Research
Code 452N
800 North Quincy Street
Arlington, Virginia 22217

*Original contains color
plates: All DTIC reproductions
will be in black and
white*

This document has been approved
for public release and sale; its
distribution is unlimited.

Prepared By



SCIENCE APPLICATIONS INTERNATIONAL CORPORATION

13400B Northup Way Suite 36
Bellevue, Washington 98005
(206)747-7152

November 1, 1993

Preceding Pages Blank In DOCUMENT

TET SUMMER 1992 ENVIRONMENTAL MEASUREMENTS

Final Report

Authors:

John T. Gunn
Richard K. Dewey
David Rubenstein
Clay Wilson

DTIC QUALITY INSPECTED 5

Accession For	
NTIS GRA&I	<input checked="" type="checkbox"/>
DTIC TAB	<input type="checkbox"/>
Unannounced	<input type="checkbox"/>
Justification	
By	
Distribution/	
Availability Codes	
Dist	Avail and/or Special
A-1	

TABLE OF CONTENTS

LIST OF FIGURES	5
LIST OF TABLES	8
LIST OF APPENDICES	9
EXECUTIVE SUMMARY	10
1. INTRODUCTION	1-1
1.1. Background	1-2
1.2. Goals and Objectives	1-3
1.3. Organization of Report	1-3
2. INSTRUMENTATION	2-1
2.1. Current Meters	2-1
2.2. Temperature Recorders	2-3
2.3. Acoustic Doppler Current Profiler	2-3
2.4. Conductivity Temperature and Depth Profiler	2-6
3. OBSERVATIONS	3-1
3.1. Field Operations	3-1
3.2. Data Processing	3-1
3.2.1. Current Meter Data Processing	3-5
3.2.2. MicroTemp Data Processing	3-5
3.2.3. ADCP Data Processing	3-6
3.2.4. CTD Data Processing	3-7
3.3. Moored Current Measurements	3-8
3.4. Moored Temperature Measurements	3-8
3.5. Current Profiles	3-12
3.6. CTD profiles	3-19
4. DISCUSSION	4-1
4.1. Stratification	4-2
4.1.1. Transects	4-3

4.1.2. Time Series	4-3
4.2. Internal Waves	4-15
4.2.1. SIW Structure	4-17
4.2.2. Soliton Internal Wave Occurrence	4-19
4.3. Fronts	4-23
4.4. Bottom Boundary Layer	4-30
4.4.1. Turbulence	4-34
4.4.2. Secondary Boundary Layer Flow	4-45
4.5. Electric Field Modeling	4-50
5. CONCLUSIONS AND RECOMMENDATIONS	5-1
REFERENCES	6-1

LIST OF FIGURES

Figure 2-1	SACM Acoustic Paths	2-2
Figure 2-2	ADCP Drift Configuration	2-5
Figure 3-1	Location of ADCP Drift Tracks	3-2
Figure 3-2	Data Collection Time Line for Time Series; Shaded Areas Represent Good Data Return	3-3
Figure 3-3	Instrument Deployment Timeline	3-4
Figure 3-4	Perspective View of Mooring Locations	3-9
Figure 3-5	Vertical Arrangement of Mooring Instrumentation	3-10
Figure 3-6	MicroTemp Mooring 1 Temperature Data	3-13
Figure 3-7	MicroTemp Mooring 2 Temperature Data	3-14
Figure 3-8	Mooring 1 Temperature Isotherms	3-15
Figure 3-9	ADCP Track, Drift 1, Day 265	3-17
Figure 3-10	Alongshore, Across-shore and Vertical Current Time Series, ADCP Drift 1 and 2, Day 265	3-18
Figure 3-11	CTD Station Locations	3-20
Figure 4-1	Vertical Structure of Temperature in Cross Shelf Transect	4-4
Figure 4-2	Vertical Structure of Salinity in Cross Shelf Transect	4-5
Figure 4-3	Vertical Structure of B-V Frequency in Cross Shelf Transect	4-6
Figure 4-4	CTD Time Series, Temperature	4-8
Figure 4-5	Comparison at CTD Time Series Profiles (Left) and Thermistor String on Mooring 1 (Right).	4-9
Figure 4-6	CTD Time Series, Salinity	4-10
Figure 4-7	CTD Time Series Brunt-Väisälä Frequency	4-11
Figure 4-8	Two-Day Time Series of Temperature Isotherms and of Alongshore (E/W) and Across-Shore (N/S) Current Velocity at 15 m, Mooring 1, Day 268 to 270	4-12
Figure 4-9	Two-Day Time Series of Temperature Isotherms and of Alongshore (E/W) and Across-Shore (N/S) Current Velocity at 15 m, Mooring 1, Day 274 to 276	4-13
Figure 4-10	An Internal Soliton in a Two-Layer Fluid of Finite Depth When $h_1 < h_2$ (from Osborne and Burch, 1980.	4-16
Figure 4-11	Time Series of N/S (Solid) and E/W (Dashed) Current Velocity at 15 m and 145 m and of Temperature Isotherms, Mooring 1.	4-18
Figure 4-12	Map of ADCP Drift (Top) Along with Vertical Current from ADCP,	

	Horizontal Current at 15 m from Mooring 1 and ADCP Current at 15 m.	4-20
Figure 4-13	Four-Day Time Series of Alongshore (E/W) and Across-Shore (N/S) Current Velocity at 15 m, Mooring 1.	4-22
Figure 4-14	Mean Current Velocity for SIWS and SIW Propagation Velocity	4-24
Figure 4-15	Time Series of Current Velocity at 15, 30 and 60 m, Mooring 1, Julian Day 268.8 to 269.0: (a) Across-Shore (N/S) Current Velocity and (b) Alongshore (E/W) Current Velocity	4-25
Figure 4-16	Time Series of Temperature Isotherms and currents at 15 m depth, Mooring 1, Julian Day 268 to 270	4-27
Figure 4-17	Time Series of Temperature Isotherms and Currents at 15 m Depth, Mooring 1, Julian Day 274 to 276	4-28
Figure 4-18	Time Series of Current Velocity at 15, 60 and 145 m, Mooring 1, Julian Day 275.6 to 275.8: (a) Across-Shore (N/S) Current Velocity and (b) Alongshore (E/W) Current Velocity.	4-29
Figure 4-19	Time Series of Alongshore (E/W) Current Velocity at 10 m, 5 m and 1 m Above the Bottom, Mooring 4, Julian Day 265 to 278.	4-31
Figure 4-20	Time Series of Cross-Shore (N/S) Current Velocity at 10 m, 5 m and 1 m Above the Bottom, Mooring 4, Julian Day 265 to 278.	4-33
Figure 4-21	Time Series of Alongshore (E/W) and Cross-Shore (N/S) Current Velocity at 1 m above the Bottom, Mooring 4, Julian Day 272 to 276.	4-36
Figure 4-22	Variance-preserving spectra at 10 and 1 m above bottom on mooring4. Spectra are for total current (U+V) between 0.33 and 0.5 cpm.	4-37
Figure 4-23	Time Series Estimated Vertical Velocity Shear Between 0 and 1 m Above the Bottom and Between 1 and 5 m Above the Bottom, Mooring 4, Julian Day 272 to 276.	4-39
Figure 4-24a	Regression Coefficient and Slope and Intercept of Log Fit of Velocity Using Three Depths (0, 1 and 5 m)	4-41
Figure 4-24b	Regression Coefficient and Slope and Intercept of Log Fit of Velocity Using Two Depths (0 and 5 m)	4-42
Figure 4-25	Drag Coefficient Versus Reynolds Number (a) Estimated from 10 Minutes and 5 Minutes ITA (1991 Data) and (b) Theoretical Predictions	4-44
Figure 4-26	Comparison Between Two Methods of Estimates u.. the "law of the wall" and from the ITA	4-46
Figure 4-27	Plots of U (E/W Velocity) Versus V (N/S velocity) for Three Depths (1,5 and 20 m) on Mooring 4	4-47
Figure 4-28	Conductivity Profiles from Four CTD Casts, Along with a Smooth-Fitting	

	Function Given by Equation (3)	4-52
Figure 4-29	Eastward Component of Velocity at 15 m (Thin Solid) and 145 m (Thin Dash-Dot) Depths. Thick Solid Curve Shows Conductivity-Weighted, Depth-Averaged Velocity. Note That the Depth-Averaged Record is Much Smoother.	4-53
Figure 4-30	Eastward Component of Velocity at Depths 15, 30, 60 and 145 m. The Thick Solid Curve Shows $\langle u \rangle^*$, the Conductivity-Weighted, Depth-Averaged Current.	4-54
Figure 4-31	Temperature in °C From Four Depths, 15, 30, 50 and 145 m.	4-55
Figure 4-32	Spectral Density of Eastward Velocity Component. Thin Curve Shows Spectrum of Current at 15 m, Thick Curve Shows Spectrum of Conductivity-Weighted, Depth-Averaged Current.	4-56
Figure 4-33	Coherence Amplitude Between Three Pairs of Depths; a) 15 & 30 m; b) 30 & 60 m; and c) 60 & 145 m. Dashed Horizontal Line shows 95% Confidence Level	4-58
Figure 4-34	Spectral Density of Components of Electric Field at Ocean Bottom. Upper Panel Shows North and East Components; Bottom Panel Shows Vertical Components.	4-59
Figure 4-35	Profiles of Density From Five CTD Casts, in Sigma-Theta Units.	4-62
Figure 4-36	Top: Horizontal Electric Field Averaging Kernel Ω_1 , as a Function of Range in Units of Bottom Depth.	4-63
Figure 4-37	Spectral Density of Horizontal Components of Electric Field, After Applying the Transfer Function Shown in Figure 4-36	4-64

LIST OF TABLES

Table 2-1	Specifications for Mooring Instrumentation	2-3
Table 2-2	Specifications for the Measurement of Current Relative to the ADCP	2-4
Table 2-3	Sensor Specifications for the SeaCat CTD	2-6
Table 3-1	Mooring Deployment Summary	3-11
Table 3-2	ADCP Drift Times	3-16
Table 3-3	Hydrographic Data Collected	3-19
Table 4-1	Parameters of Observed Soliton-like Internal Waves	4-21

LIST OF APPENDICES

- Appendix A Current Velocity, Time Series, Moorings 1-4
- Appendix B Time Series of Temperature Isotherms and Current Velocity at
15 m, Mooring 1
- Appendix C ADCP Drift Tracks
- Appendix D Alongshore, Across-Shore and Vertical Current Time Series from ADCP Drifts
- Appendix E CTD Station Locations
- Appendix F CTD Transects: Temperature, Salinity, Density, and B-V Frequency
- Appendix G CTD Station Time Series: Temperature, Salinity, Density, and B-V Frequency

EXECUTIVE SUMMARY

Physical oceanographic environmental data were collected during the 14-day Technology Evaluation Testbed (TET) experiment conducted in late September and early October, 1992. The TET experiment is part of the Port Area Surveillance (PAS) program, which is investigating a variety of acoustic and non-acoustic sensors to detect surface and subsurface vessels at and around the entrance to ports. The purpose of the TET experiments is to evaluate sensor performance and assess noise reduction techniques in a realistic ocean environment.

The goals of the oceanographic measurements made during the 1992 experiment were (1) to provide environmental data to support the performance evaluation of the TET sensor systems deployed during the experiment and (2) to extend the base of knowledge of physical oceanographic phenomena in the local area beyond the measurements of the previous years. Sea water is an electrolyte and the motion of sea water produces electric and magnetic fields that may degrade the performance of electric and magnetic sensors. In particular, two hydrographic phenomena--the bottom boundary layer turbulence and internal waves-- were identified in previous TET oceanographic studies as specific phenomena for study during for the 1992 experiment. These phenomena were examined by studying the bottom boundary layer, characterizing the strength and persistence of fronts, characterizing the frequency of occurrence of internal waves, and estimating the electromagnetic field induced by natural hydrographic phenomena.

During the 1992 TET experiment, four moorings instrumented with current meters and temperature recorders were deployed for 14 days at the TET site near Neah Bay, Wa. They collected time series of current and temperature data at fixed locations and depths. Three moorings were arranged in an "L"-shaped configuration and contained instruments in the upper 60 m and the bottom 10 m of the water column to measure the speed and direction of internal waves. A single mooring deployed several instruments in the bottom 10 m of the water column to measure the current and temperature in the bottom boundary layer.

In addition, vertical profiles of currents and of temperature and salinity were collected during multiple surveys over the duration of the 1992 TET experiment using, respectively, an Acoustic

Doppler Current Profiler (ADCP) and a conductivity, temperature, and depth (CTD) profiler.

Of the moored instruments, the 15 temperature recorders provided a data return of 94% while the 11 current meters provided a return of 66%. ADCP surveys were conducted on 5 days and approximately 25 hours of data were obtained on 20 ADCP drifts. CTD surveys were conducted on 5 days and included 28 cross shelf transects and 53 time series surveys for a total of 81 casts and a data return of 84%.

Processed data and preliminary data products were provided to program participants for evaluation of sensor performance. In addition, various data products generated from the data sets are included in this Final Report. For each current meter, a time series of the alongshore (E/W) and across-shore (N/S) current velocities was generated. For mooring 1, with 50% of the temperature recorders concentrated in the upper 50 m, a times series showing the progression of the temperature isotherms was generated to portray the evolution of the vertical temperature structure with time. For each ADCP survey, a plot of the alongshore, across-shore, and vertical current velocity time series was generated. For the CTD surveys, transects and time series' of the temperature, salinity, density, and B-V frequency were presented for the cross shelf transect and time series surveys, respectively.

The passage of fronts, as evidenced by a rapid change in the velocity or temperature structure of the water column, is a common occurrence in the study area. There were three or four strong frontal passages over the course of the experiment. The presence of fronts may have implications in the operation of acoustic sensors that rely on the knowledge of the speed of sound distribution.

The bottom boundary layer was investigated with a mooring instrumented with current meters and temperature recorders at about 1 m, 5 m, and 10 m above the bottom. A rectified secondary flow was observed in the near bottom boundary layer producing offshore flow during both flood and ebb tides. Increased turbulent activity in the near bottom boundary layer was also evident when flow above this layer reached approximately 50 cm/s. The achievement of this threshold varied with the tidal cycle. The periodic variations of increased turbulent activity have been shown by other investigators to adversely affect performance of some TET sensors presumably

because of the electric and magnetic "noise" generated by the near bottom turbulence.

Internal waves are of interest because of their potential to generate electro-magnetic signals. Understanding the structure and occurrence of soliton-like internal waves may provide the ability to improve signal to noise and false alarm rates in TET sensor systems. In 1992 soliton-like internal waves were strongly associated with the peak flood tide. Median values of the propagation speed and wave length from 13 distinct internal waves were 56 cm/s and 514 m respectively. Propagation directions were evenly distributed between both alongshore directions.

To summarize, the 1992 environmental measurements have provided a unique data set with detailed information regarding the occurrence of soliton-like internal wave, bottom boundary layer phenomena including turbulent activity and frontal activity for the TET site. Significant physical phenomena occurring during the experiment have been identified and quantified. This data set should be a valuable resource to be used in the evaluation of the performance of TET sensor systems.

1. INTRODUCTION

This report describes the physical oceanographic measurements of the ocean environment collected during the 1992 Technology Evaluation Testbed (TET) experiment. The TET is part of the Port Area Surveillance (PAS) program, which is investigating a variety of acoustic and non-acoustic sensors to detect surface and subsurface vessels at and around the entrance to ports. The purpose of the TET experiments is to evaluate sensor performance and assess noise reduction techniques in a realistic environment. Oceanographic environmental measurements were made to investigate various oceanographic phenomena which are potential sources of noise.

The 1992 TET experiment was conducted from 20 September to 3 October in the Strait of Juan de Fuca, offshore of Neah Bay, Washington. Non-acoustic data were collected using bottom-mounted arrays of magnetometers and long baseline electric field sensors, both of which had previously been deployed at the TET site. These sensors were used to collect background noise throughout the experiment and to collect target data during calibrated source runs. All the dates and times are in Universal Coordinated Time (UTC). The local time in the study area (PDT) was seven hours earlier than UTC.

In support of the non-acoustic measurements, standard oceanographic instruments were used to make environmental measurements. There were three types of measurements: moored current and temperature instrumentation; drifting current measurements with a downward-looking Acoustic Doppler Current Profiler (ADCP); and vertical profiles of conductivity, temperature and depth (CTD) with a CTD profiler. The CTD data also allows calculation of the vertical salinity and density structure.

The measurements discussed here have focused on the study of strong internal waves and the bottom boundary layer (BBL): two types of hydrographic phenomena which are potential sources of magnetic and electric field noise.

1.1. Background

As part of the TET program, oceanographic environmental data has been collected near Neah Bay, Washington during various periods over the last three years: September 1989, August/September 1990, and August/September 1991.

During September 1989 (Gunn and Rubenstein, 1989), a single subsurface mooring was deployed to monitor the temperature and current structure at the test site in order to evaluate the need for further detailed measurements. Significant internal wave activity was observed in both the vertical temperature structure and in the near bottom velocities. Strong peak tidal flows (> 60 cm/s) in the near bottom currents (~ 1 m above the bottom) were also observed. These measurements were confirmed by more detailed surveys in 1990 with multiple moorings of thermistor strings and current meters deployed for two periods (in August and September) (Gunn and Rubenstein 1991).

In August and September 1991 (see Gunn et al 1992), after the deployment of some TET sensor systems (short baseline electric field and acoustic sensor systems) a more extensive study of oceanographic phenomena was conducted with the goal of parameterizing the amplitude, phase speed and propagation direction of the internal waves. The internal waves observed during this deployment propagated with speeds of approximately 60 cm/s superimposed on a tidal flow which reached speeds in excess of 150 cm/s. Amplitudes of the internal waves ranged from 10 to 35 m with a typical wave length of approximately 300 m. Soliton-like internal waves were found to be common with wave lengths between 300 and 600 m and amplitudes of 11-23 m. Propagation directions were all in the southeast quadrant. BBL measurements showed depth limited internal waves present just above the bottom and turbulence to be a regular occurrence at times of peak tidal flows.

Based on the results of previous years work and recommendations from the analysis of those studies the goals and objectives of the present study were defined.

1.2. Goals and Objectives

The goals of the oceanographic measurements conducted during the 1992 TET experiment were (1) to provide environmental data to support the evaluation of the performance of the TET sensor systems deployed during the experiment and (2) to extend the base of knowledge of physical oceanographic phenomena in the local area beyond the measurements of the previous years. Specific objectives for the 1992 study included the following:

- *bottom boundary layer*: sample the bottom boundary layer, preferably over a spring and neap tidal cycle.
- *fronts*: characterize the strength and persistence of fronts.
- *internal waves*: characterize the frequency of occurrence of soliton-like internal waves, including their propagation speed, direction, and wave length.
- *induced electric and magnetic fields*: estimate the induced electric and magnetic fields due to natural hydrographic phenomena.
- *stratification*: characterize the stratification as it relates to internal waves.

1.3. Organization of Report

This remainder of this report is divided into four major sections. Section 2 is a discussion of the instrumentation used, while Section 3 is a presentation of the observations and a discussion of the field operations. Section 4 is a detailed discussion of the phenomena of interest and Section 5 presents conclusions and recommendations. Complete data products are presented in Appendices A-G.

2. INSTRUMENTATION

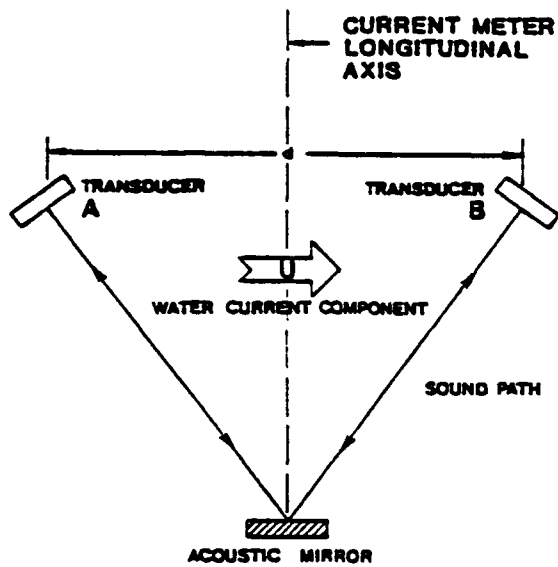
A variety of oceanographic instruments were used to make measurements during the 1992 TET experiment and included current meters, temperature recorders, a current profiler and a conductivity and temperature profiler. The current meters and temperature recorders were deployed in an array of moorings to provide a continuous time series of the temperatures and currents at fixed depths. Profiling instruments were used in surveys to provide information on the vertical structure of the water column over short time intervals. These oceanographic instruments are described below.

2.1. Current Meters

Commercial current meters were chosen for this study in order to provide proven, reliable technology and to facilitate logistical support. Because of the number of instruments needed, two types of current meters were used in this program: the EG&G Smart Acoustic Current Meter (SACM) and the InterOcean S4 electromagnetic current meter (S4). Both are vector averaging instruments that measure the current velocity along two orthogonal paths but with different measurement techniques.

The SACM computes two current velocity components by measuring the Doppler shift along two acoustic paths as a 1600 kHz acoustic signal is bounced off an acoustic mirror located below and between two pairs of orthogonal transducers (Figure 2-1). The velocity along each path is converted to north/south and east/west (magnetic) components by comparison with an internal compass. Specifications for the SACM are shown in Table 2-1. Communication with the SACM was performed for instrument set-up and data retrieval using a PC and EG&G-supplied OEM interface (SAIL current loop).

The S4 computes current velocity components by sensing the induced electric field as seawater (an electrolyte) flows past electrodes in the side of this spherical current meter while present in the magnetic field of the earth. These components are also converted to magnetic north/south



Sensor Geometry

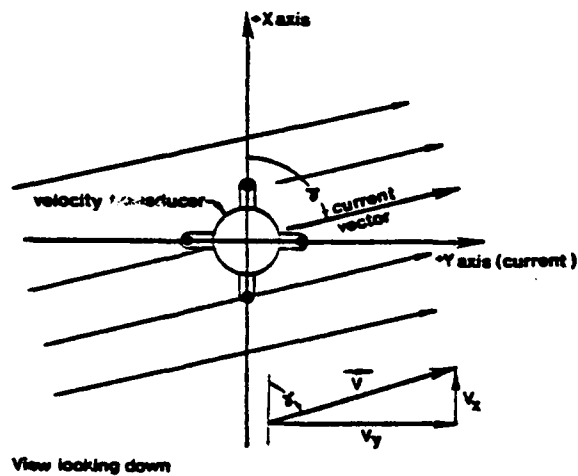


Figure 2-1 SACM Acoustic Paths

Table 2-1 Specifications for Mooring Instrumentation

INSTRUMENT	SACM	S4	MICROTEMP
Velocity Range	0 - 360 cm/s	0 - 350 cm/s	N/A
Velocity Resolution	0.1 cm/s	0.2 cm/s	N/A
Velocity Accuracy	± 1 cm/s or 3%	± 1 cm/s or 2%	N/A
Direction Range	360 Degrees	360 Degrees	N/A
Direction Resolution	N/A	0.5 Degrees	N/A
Direction Accuracy	± 5 Degrees	± 2 Degrees	N/A
Direction Tilt Limit	± 25 Degrees	± 25 Degrees	N/A
Temperature Range	N/A	N/A	0.0 - 40°C
Temperature Resolution	N/A	N/A	$\pm 0.01^\circ\text{C}$
Temperature Accuracy	N/A	N/A	$\pm 0.1^\circ\text{C}$
Thermistor Response Time	N/A	N/A	3 - 5 secs

and east/west components using an internal compass. See Table 2-1 for specifications for the S4. Communication with the S4 for instrument set-up and data retrieval was accomplished using a PC and OEM interface (RS232).

2.2. Temperature Recorders

The temperature recorders used were Coastal Leasing MicroTemps, which are self-contained instruments that store the data in internal random access memory (RAM). The temperature sensor used is a YSI thermistor with a response time of 3-5 seconds. Direct communications between the MicroTemp and a computer (PC) are via a RS232 cable and vendor supplied software. Specifications for the MicroTemp are listed in Table 2-1.

2.3. Acoustic Doppler Current Profiler

A self-contained RD Instruments Acoustic Doppler Current Profiler (ADCP) mounted on a spar buoy was used to collect current profiles in the upper 60 m of the water column. The ADCP measures currents in discrete bins throughout a depth range of the water column by calculating

the Doppler shift of acoustic pings of a precise frequency as they are reflected back toward the instrument by particulates in the water. The ADCP measures water velocity along each of four beams and computes two horizontal components and a vertical component of velocity.

The ADCP used had a remote transducer head with a 600kHz downward-looking array of four orthogonal transducers, each angled at 30° from the vertical. The ADCP electronics were attached via cable and kept on the boat. The spar buoy was deployed from the stern of the survey boat and allowed to drift through the study area, driven by the tidal flow and wind (Figure 2-2). The ADCP was deployed at sites intended to allow the buoy to drift past the current meter moorings. As the buoy drifted away from the study area it was retrieved and redeployed at a new up-current location so that it would drift past the mooring array repeatedly. Drifting past the current meter array allowed comparison of the two data sets. Ship motion was measured by a differential Global Positioning System (GPS) receiver with the master unit located at the operations base in Neah Bay.

The ADCP was programmed to ensemble average 114 pings every 30 seconds and store the average in memory. The vertical profiles were segmented into 30 vertical bins, each 2 m deep, for a total vertical range of 60 m. The data was collected relative to magnetic north with a reduction of the system noise in velocity to a standard deviation of 1.2 cm/s. Specifications for the ADCP velocity data are summarized in Table 2-2.

Table 2-2 Specifications for the Measurement of Current Relative to the ADCP

Velocity Range (horizontal)	$\pm 0.01 - 9.5$ m/s
Velocity Resolution	0.25 cm/s
Velocity Accuracy	0.5% of measured velocity ± 0.5 cm/s
Maximum Profiling Range	70 m

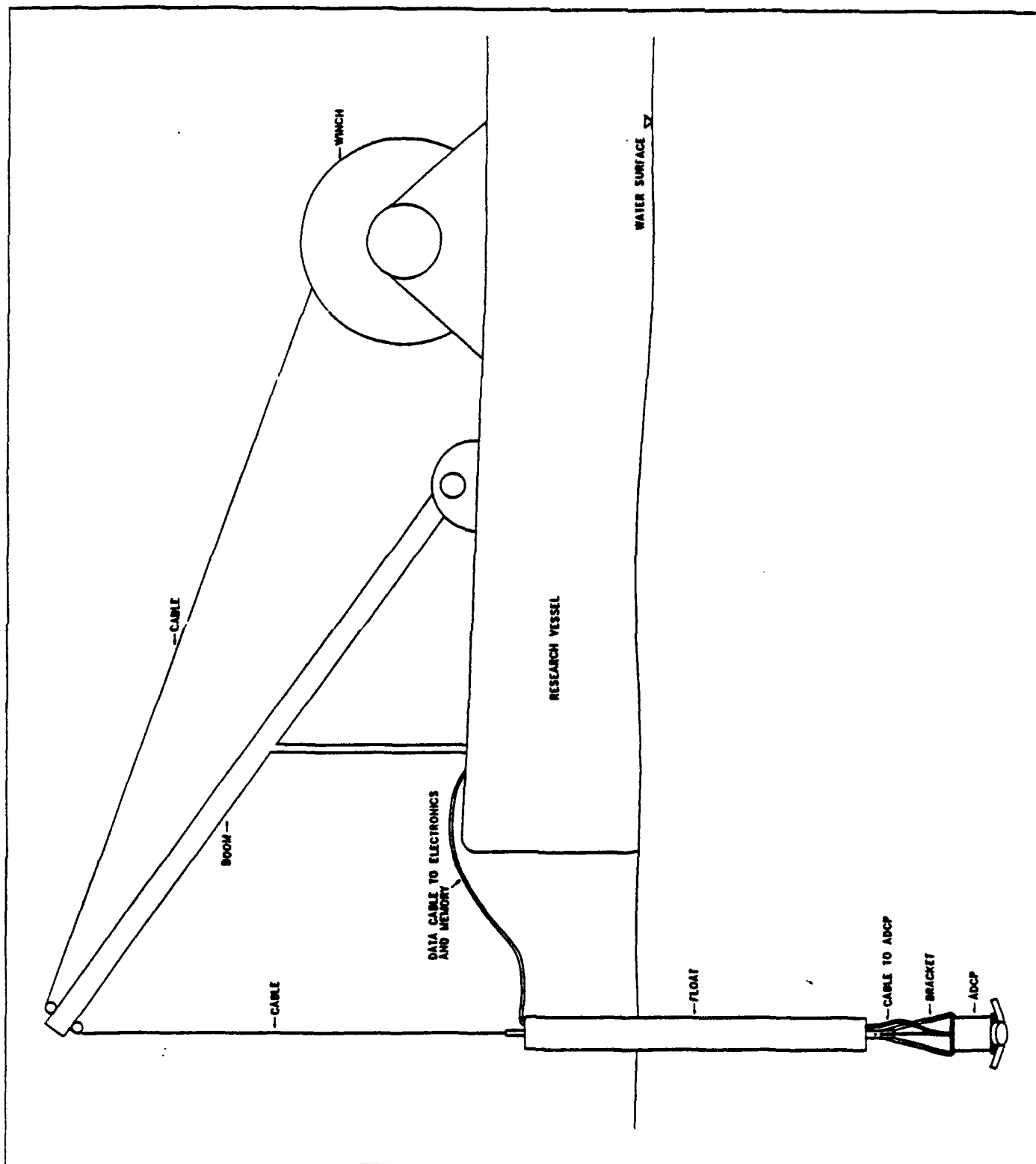


Figure 2-2 ADCP Drift Configuration

2.4. Conductivity Temperature and Depth Profiler

The vertical structure of the temperature and conductivity was measured using a SeaBird SeaCat SBE19 Profiler with a pumped conductivity cell. This self-contained instrument uses the SeaBird temperature and conductivity sensors and a Sensor-Metrics strain gauge pressure sensor. Data collection is controlled by an external magnetic on/off switch which, when triggered, records the cast number, date, and time with the associated temperature, conductivity, and pressure data. Data are collected at a rate of 2 data scans per second, recorded internally in random access memory (RAM). Direct communications and data retrieval between the CTD and a PC are via a RS232 cable and vendor supplied software. The specifications for the CTD profiler are summarized in Table 2-3.

Table 2-3 Sensor Specifications for the SeaCat CTD

Sensor	Range	Resolution	Accuracy
CTD Temperature (°C)	-5 to 35	0.001	0.01
CTD Conductivity (S/m)	0 to 6.5	0.0001	0.001
CTD Pressure (psi)	0 to 300	0.15	1.5

3. OBSERVATIONS

This section describes the oceanographic observations made during the 1992 TET experiment. First, the field operations are reviewed, followed by a description of the data processing approach for each of the data sets. Then, the observations are presented for moored current measurements, moored temperature measurements, current profiles, and CTD profiles.

3.1. Field Operations

The 1992 environmental measurement for the TET took place in the Strait of Juan de Fuca, approximately 3 kilometers northeast of Neah Bay, Washington, from 20 September to 3 October 1992. The instrumented moorings were deployed the first day and retrieved the last. Four moorings instrumented with current meters and temperature recorders were deployed on the first day of the experiment and were recovered on the last day. During the experiment, profile data were collected during surveys on five days at various locations using the CTD profiler and on five other days along various drift tracks using the ADCP. The location of the moorings, the CTD stations, and the envelope of the ADCP drift tracks are shown in Figure 3-1 and timeline of the mooring and survey periods are displayed in Figures 3-2 and 3-3. After the initial data processing, the data return for the various types of oceanographic instruments was determined, as summarized in Figure 3-2. Overall, the ADCP provided the best data return (100%), followed by the temperature recorders (94%), the CTD profiler (84%) and finally, the current meters (66%).

3.2. Data Processing

Data from the internal recording instruments were recovered in ASCII characters as either uncalibrated integer counts or scientific units, depending on the instrument. The data were converted into scientific units, if necessary, and then checked for proper calibration and time base. Any unusable portions of the data, such as pre- and post-deployment periods, were removed. Data were then analyzed and displayed using MATLAB, a commercial time series analysis software package.

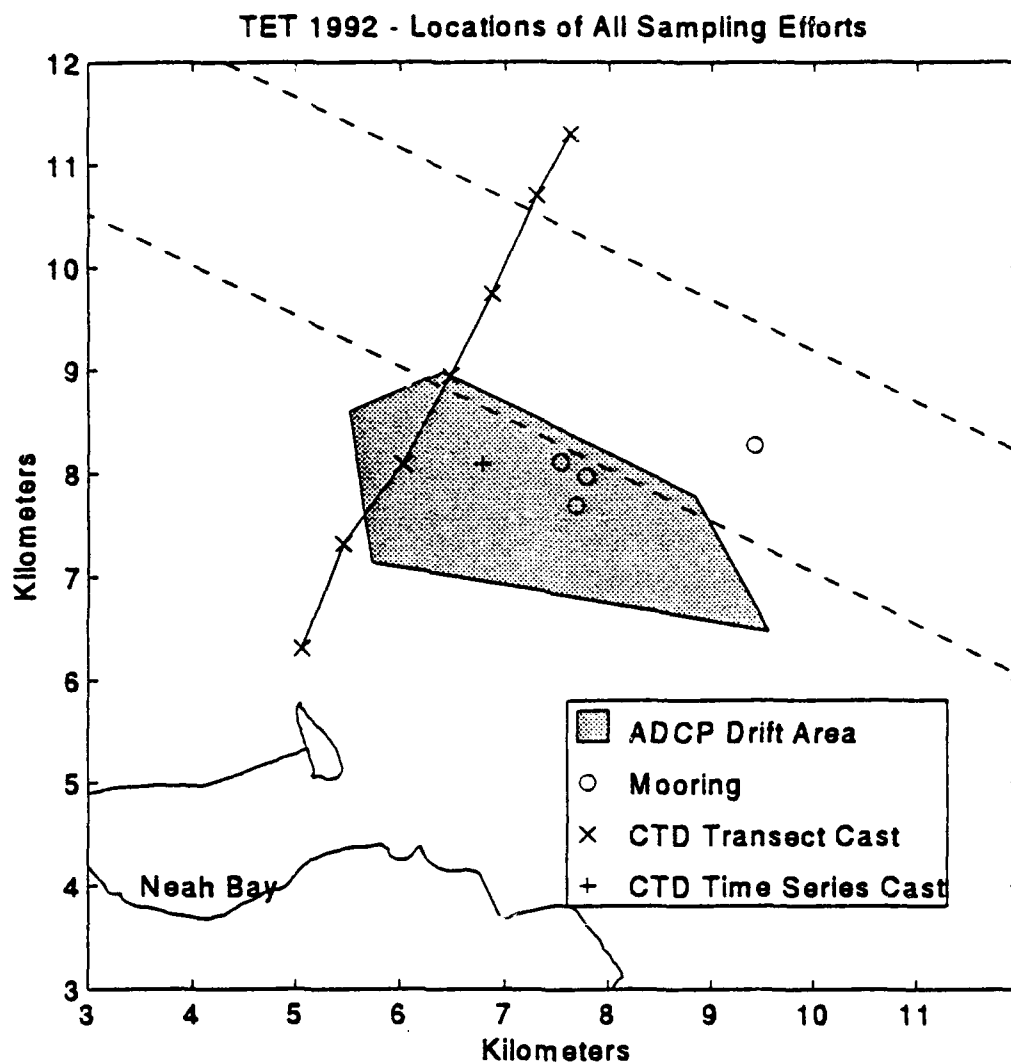
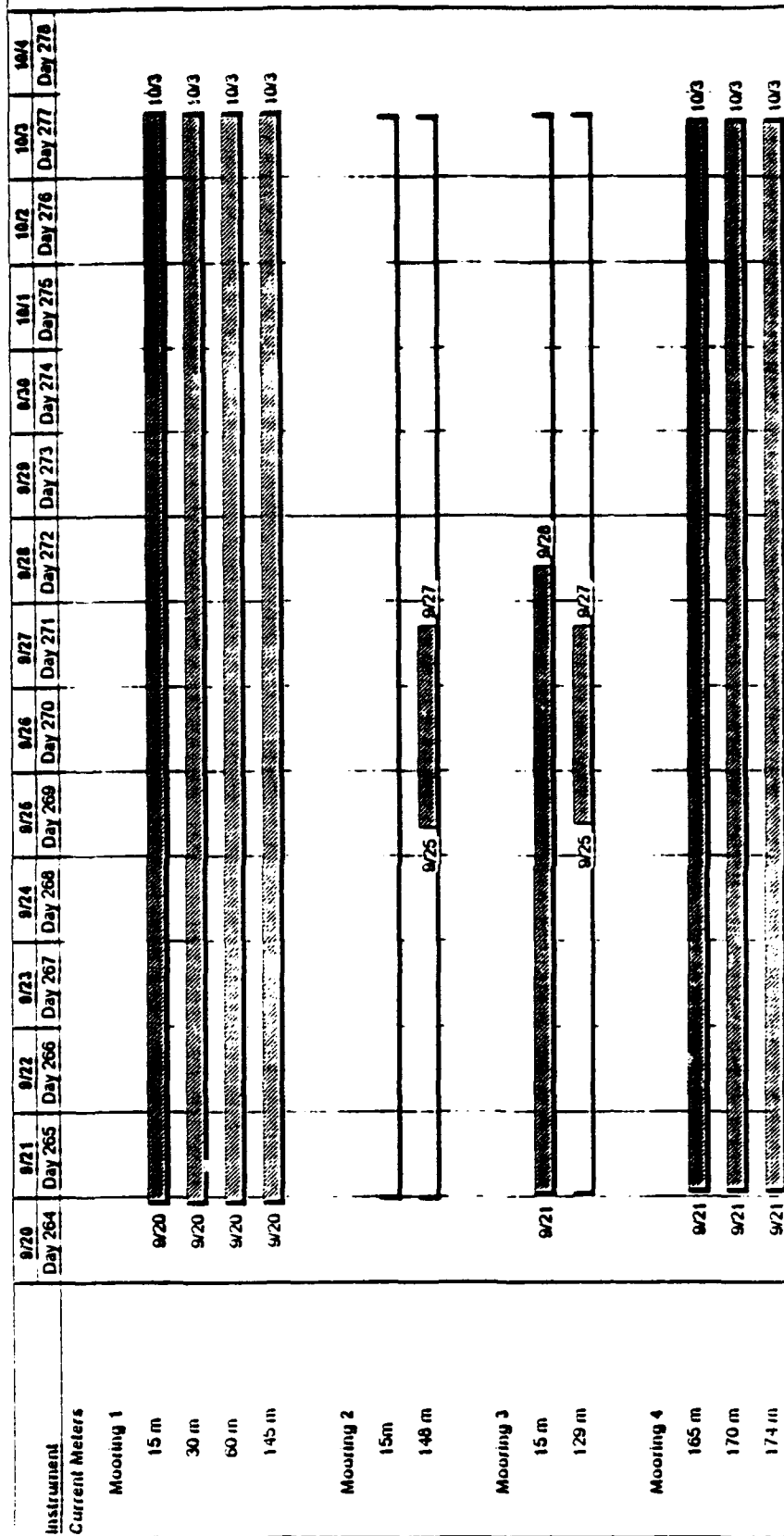


Figure 3-1 Location of ADCP Drift Tracks

Current Meter Data (UTC) TET Experiment, Summer 1993



Usable Data
Instrument Deployed

Project: Current Meter Data (UTC)
Date: 9/27/93

TET#18 MPP

8 55 am 9/27/93

Figure 3-2 Data Collection Time Line for Time Series; Shaded Areas Represent Good Data Return

Instrument Time Line TET Experiment, Summer 1993

Instrument	9/20 Day 264	9/21 Day 265	9/22 Day 266	9/23 Day 267	9/24 Day 268	9/25 Day 269	9/26 Day 270	9/27 Day 271	9/28 Day 272	9/29 Day 273	9/30 Day 274	10/1 Day 275	10/2 Day 276	10/3 Day 277	10/4 Day 278
Mooring 1															
Mooring 2															
Mooring 3															
Mooring 4															
ADCP Surveys															
Drifts															
CTD Surveys															
Time series surveys															
Transects surveys															

Instrument Deployed

Project Instrument Time Line
Date 9/28/93

TET#3 MPP

10 10 am 9/28/93

Figure 3-3 Instrument Deployment Timeline

3.2.1. Current Meter Data Processing

The current meter data was recovered from the individual instruments in ASCII format using either a terminal emulation program (KERMIT) or software supplied by the manufacturer (SACM). The data were converted into scientific units after conversion into a MATLAB format. The time bases for the individual records were checked by comparing deployment events (in and out of water changes) to the logged times recorded during the field work. Pre and post deployment periods of unusable data were removed as well as any periods of poor quality data. The quality of the data was evaluated by comparison of the data with adjacent instruments or with data values typical for the study area.

A subset of the current meters (5) required more complex consideration of the data quality due to problems that prevented deployment and/or recovery periods from the instrument memory.

Some data were lost due to instrument problems, ships hitting the moorings and other problems of an unresolved nature. The upper current meter on mooring 3 was hit by a cable from a tug and barge which terminated the data collection. The upper current meter on mooring 2 failed to record usable data shortly after being deployed. The other current meters showed data gaps beginning from initially after deployed, however they then started to collect data in September within a few hours of each other. All but one failed at approximately the same time 4 days later. A reasonable explanation for the coincidental failure and performance of these instruments has not been determined. Tests by the manufacturer have failed to show any susceptibility for failure due to external stimulus. All but the 60 m microtemp on mooring 1 performed well.

3.2.2. MicroTemp Data Processing

MicroTemp data was transferred to a PC via manufacturer supplied software¹. After downloading into a personal computer (PC), the data were converted into an ASCII format. For this

¹WIZARD v5.00Rb

deployment the MicroTemps were set to collect data at 7.5 second intervals. The data were averaged to 1-minute samples before being loaded into MATLAB. It was plotted, calibrated, truncated to in-water time only, and re-plotted. Prior to the deployment, an in-house calibration had been performed on the MicroTemps to insure accuracy. The instruments were submerged in a tank and comparisons between the MicroTemp recorded temperature and coincident data collected in the tank with a SeaBird SeaCat profiler resulted in 6 point calibration between 6.0 °C and 18.5 °C. These values provided the calibration coefficients for the data.

The lack of data from the upper current meter on Mooring 2 required a slight modification of the procedure for calculating the wave propagation speed and wave length from last year's report (Gunn, et. al., 1992). In that previous report the current meter data was used for calculating the passage of the soliton internal wave (SIW) past each mooring. Since this year's data did not have upper level current data at all moorings the temperature time series from each mooring was used to indicate the arrival of a particular SIW at a mooring. This time difference, with the known distance between moorings, was used to calculate a net velocity between moorings. The current data was then low pass filtered with a cutoff frequency of 1 hour to estimate the mean velocity of the tidal flow. When the mean velocity was subtracted from the net velocity, the difference was the propagation velocity of the SIW.

3.2.3. ADCP Data Processing

The ADCP data were downloaded from the instrument after each day's survey using RD Instruments software². These files were converted to ASCII and input to MATLAB for correction for ship drift and display. The GPS data which was collected at 1 second intervals was low-pass filtered and decimated to a 30 second interval to match the sampling parameters of the ADCP. The ship's velocity was then calculated from the latitude and longitude of the GPS data and added to the ADCP relative velocity resulting in the absolute water velocity. The data from the ADCP were retrieved in earth coordinates, meaning the u, v velocities were relative to magnetic north. The data were converted from integer counts in the ASCII files to "cm/s",

²SCADCP version 4.03

the velocity magnitude was adjusted for the local speed of sound in water then the data were converted into a MATLAB data base. The data displays were produced either by mapping the velocities into a range of color values (color map) or by standard time series type plots.

3.2.4. CTD Data Processing

The CTD data is initially processed with manufacturer supplied software³. The Pressure, Temperature, and Conductivity data are calibrated and converted to an ASCII file. The temperature is advanced in time relative to the pressure to account for the slower sensor response time. The upcast is removed from the data file, since the conductivity for this portion of the data is unusable when using the pumped conductivity cell. Only the downcast data are processed through the following steps. A routine, LOOPEDIT, is then run to mark scans where the CTD is moving less than the minimum velocity (0.25 m/s) or travelling upwards due to ship roll. The depth, salinity, and density are computed from the pressure, conductivity, and temperature and the data is averaged into 1 meter bins and plotted. Data spikes are edited out using a text editor by substituting the bad data values with a no data value of -9.99Ex10-29.

After the cleaned data set was plotted and examined, an ASCII data file was extracted, with the header and no data values removed. A header file was created for the survey that lists cast numbers and start times. The data files were then formatted into files compatible with MATLAB for advanced processing and analysis.

Once in MATLAB, the data for each variable (temperature, salinity, sigma-t(density), depth, & pressure), were merged into a uniform matrix so that the data could be contoured. Data for each survey were contoured on a transect across the shelf and in a time series near the moorings for each variable. The Brunt-Väisälä (B-V) or buoyancy frequency was then calculated, merged into a uniform matrix, and contoured.

³ SEASOFT v4.018

3.3. Moored Current Measurements

The currents were measured at four mooring sites from 20 September 1992 through 3 October 1992. Three of the moorings were arranged in an "L-shaped array," with 4 current meters on the central mooring (at 15, 30, 60 meters depth and at 10 m above the bottom (145 m)), and two on each of the outer moorings (at 15 m and 10 m above the bottom). The fourth mooring had three current meters vertically spaced at one, five, and ten meters above the bottom and was located approximately 1 km to the ENE.

A perspective view of the mooring location is shown in Figure 3-4. The vertical arrangement of the instruments on each mooring is shown in Figure 3-5 and listed in Table 3-1. The three moorings south of the inbound shipping lane were arranged in a L-shape, nominally 300 m on a side, to allow measurements directed at studying the propagation of the soliton-like internal waves. The fourth mooring was positioned in the center of the inbound shipping lane between the two TET sensor arrays (not shown) in order to study the BBL and turbulence in the vicinity of these sensor systems.

The instruments were set to store one minute vector averages throughout the two week deployment period. The current measurements were concentrated in the upper portion of the water column (5 current meters at depths less than 60 m) and in the near-bottom portion of the water column (6 current meters within about 10 m of the bottom) in order to resolve the boundary effects of waves and turbulence. The data will be discussed in Section 4 and is presented in its entirety in Appendix A.

3.4. Moored Temperature Measurements

MicroTemp recorders were also deployed on the same moorings as the current meters, although at a greater number of depths, in order to measure the evolution of the vertical temperature structure.

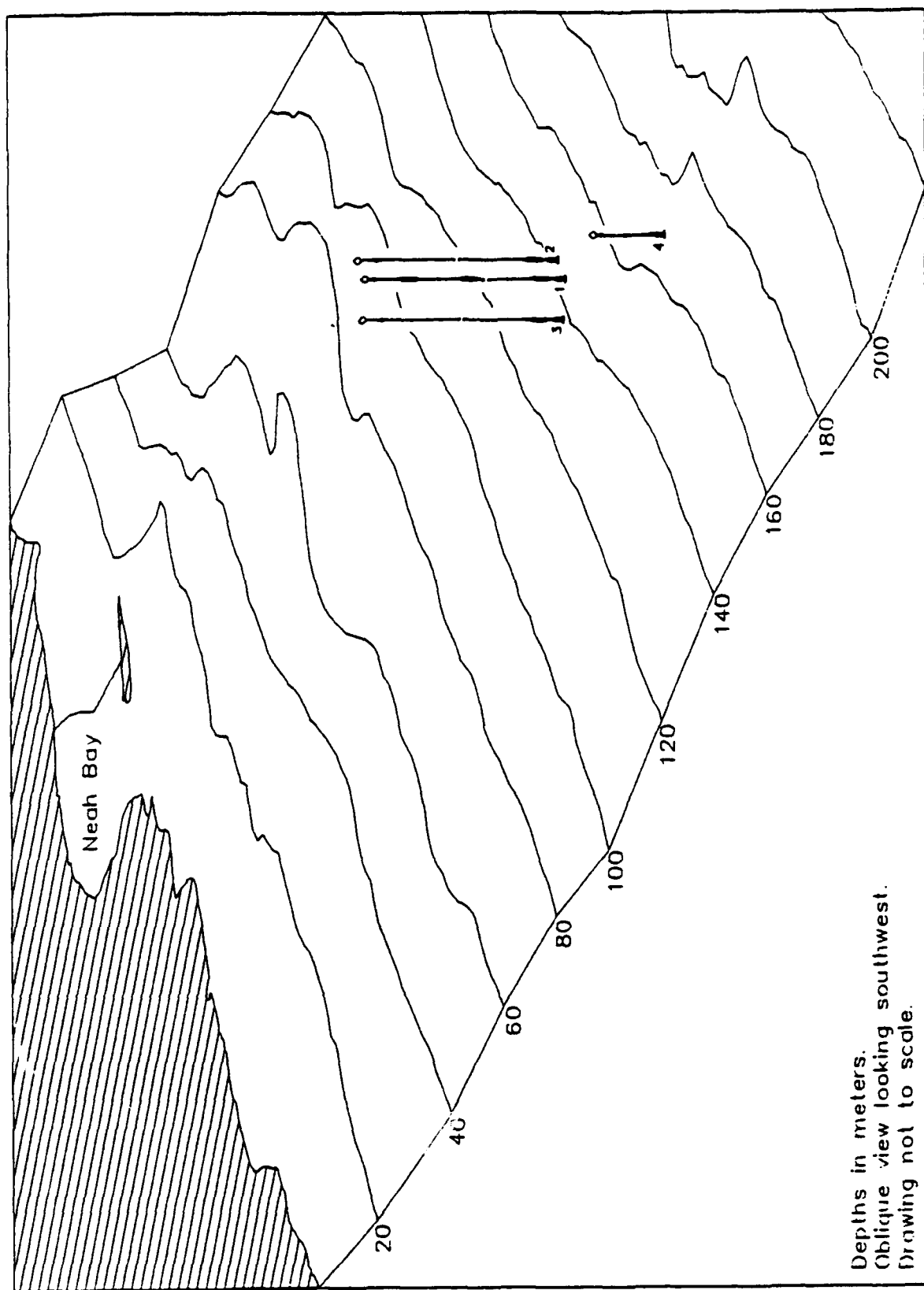


Figure 3-4 Perspective View of Mooring Locations

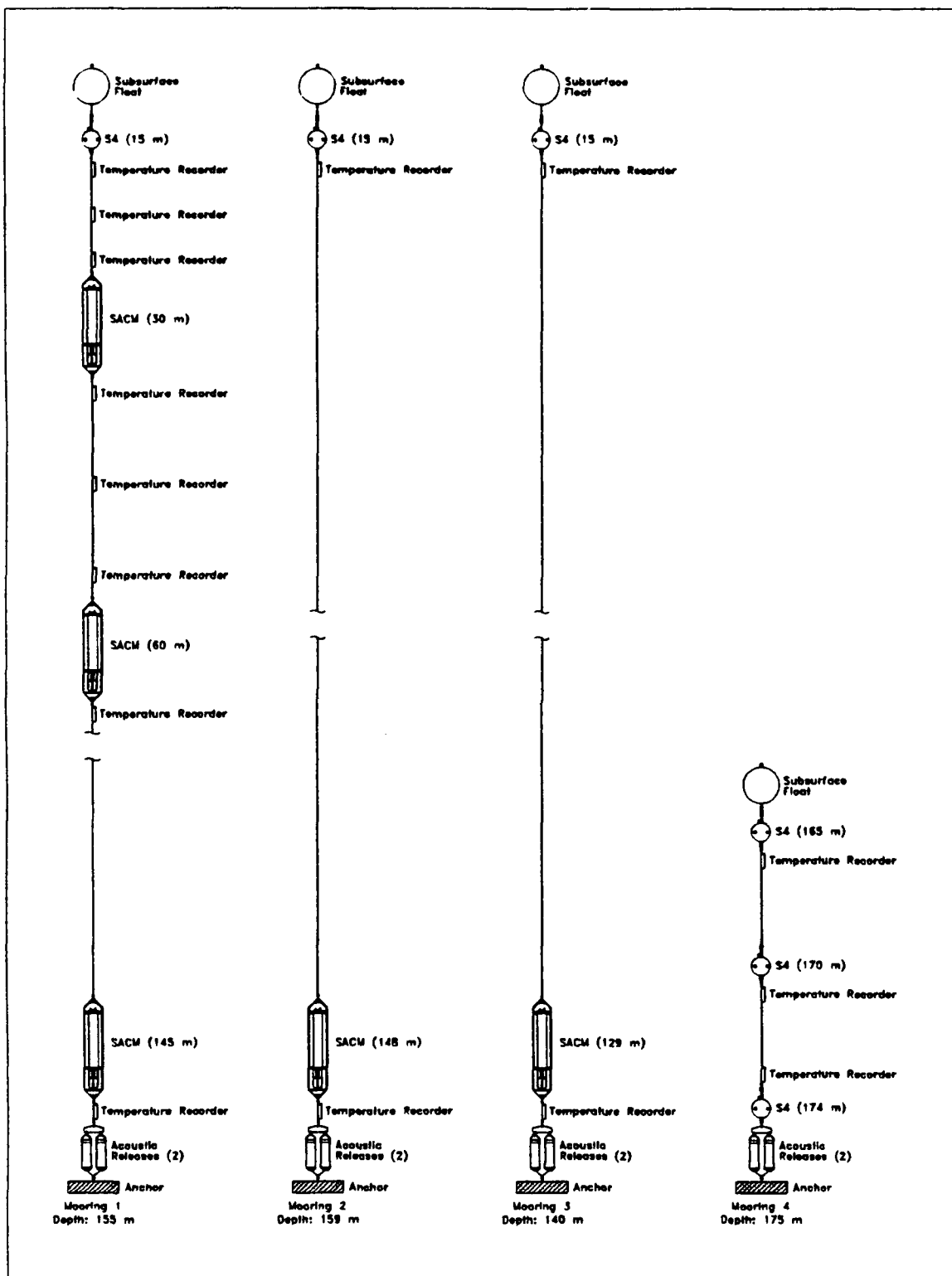


Figure 3-5 Vertical Arrangement of Mooring Instrumentation

Table 3-1 Mooring Deployment Summary

Mooring	Depth (m)	Instr.	Serial #	Sample Rate	Start Date/Time	Latitude N	Longitude W
1	15	S4	0642	60 s	9/20/92 22:26	48°24.3040'	148°33.6822'
	15	MT	10127	7.5 s			
	17.5	MT	10128	7.5 s			
	20	MT	10129	7.5 s			
	30	SACM	1228	60 s			
	30	MT	10130	7.5 s			
	40	MT	10140	7.5 s			
	50	MT	10141	7.5 s			
	60	SACM	5171	60 s			
	60	MT	10142	7.5 s			
	145	SACM	5332	60 s			
	145	MT	10143	7.5 s			
2	15	S4	0760	60 s	9/20/92 23:46	48°24.3762'	148°33.8795'
	15	MT	10144	7.5 s			
	148	SACM	1230	60 s			
	148	MT	10145	7.5 s			
3	15	S4	1670	60 s	9/21/92 00:59	48°24.1523'	148°33.4076'
	15	MT	10146	7.5 s			
	129	SACM	1231	60 s			
	129	MT	10147	7.5 s			
4	165	S4	5047	60	9/21/92 01:44	48°24.4800'	148°32.3489'
	165	MT	10148	7.5 s			
	170	S4	0661	60 s			
	170	MT	10149	7.5 s			
	174	MT	10156	7.5 s			
	174	S4	0655	60 s			
Note: MT = Microtemp Instrument							

Figures 3-6 and 3-7 show time series of the temperatures measured at the different moorings. The amount of temperature variability seen in the time series is greater at the locations near the surface (depths < 50 m) due to the greater vertical temperature gradient present. Vertical motions past the sensors show greater temperature change for a given displacement due to the greater gradient. The time series of temperatures from Mooring 1 were contoured in time and displayed with the currents from 15 m as shown in Figure 3-8. The variability of the temperature structure and its relationship with the tidal flow is evident. The entire deployment is shown in Appendix B.

3.5. Current Profiles

Surveys of current profiles in the vicinity of the moorings were conducted on five days using an ADCP. On each day a number of "drifts" were conducted, where a "drift" consisted of positioning the vessel up-current from the moorings, deploying the ADCP with a spar buoy behind the vessel, and allowing the vessel and ADCP to drift with the current past the moorings. Once the vessel had drifted some distance past the moorings, the ADCP was recovered and a new drift was conducted.

The drifts conducted on each survey day are summarized in Table 3-2. A total of 20 ADCP drifts were conducted on five days, with durations of 0.1 to 2.2 hours, depending on the initial position of the vessel and on the speed and direction of the drift. An example of a typical drift track conducted on September 21 (JD 265) is shown in Figure 3-9. The complete set of drift tracks is shown in Appendix C.

For each survey day, the profile time series of three absolute velocity components (U, V and W) of the vertical profiles were plotted as shown in Figure 3-10. The time series for all survey days are shown in Appendix D. In these time series, rapid changes in the velocity are evident in the horizontal components and, at times, in the vertical velocity. The variation of velocity with depth as the tidal flow changes gives some indication of the strong vertical shear in the upper 60 m occurring during reversals of the tidal flow. There are also abrupt changes in the velocity field

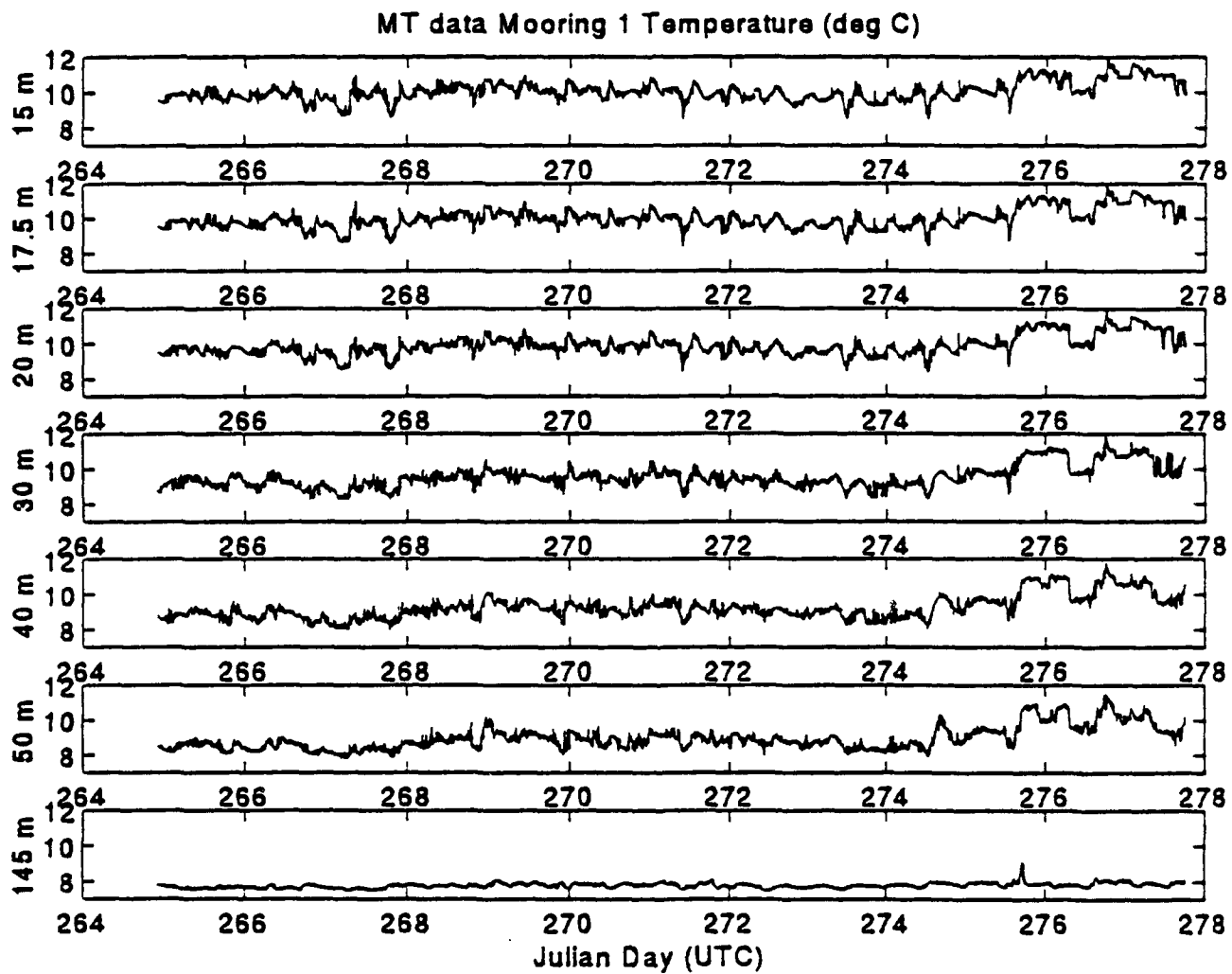


Figure 3-6 MicroTemp Mooring 1 Temperature Data

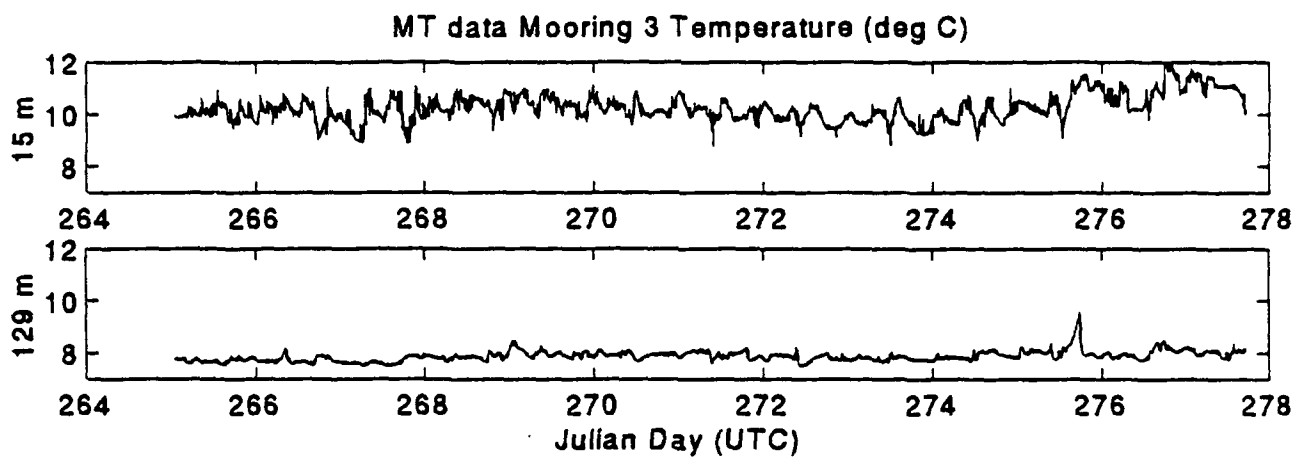
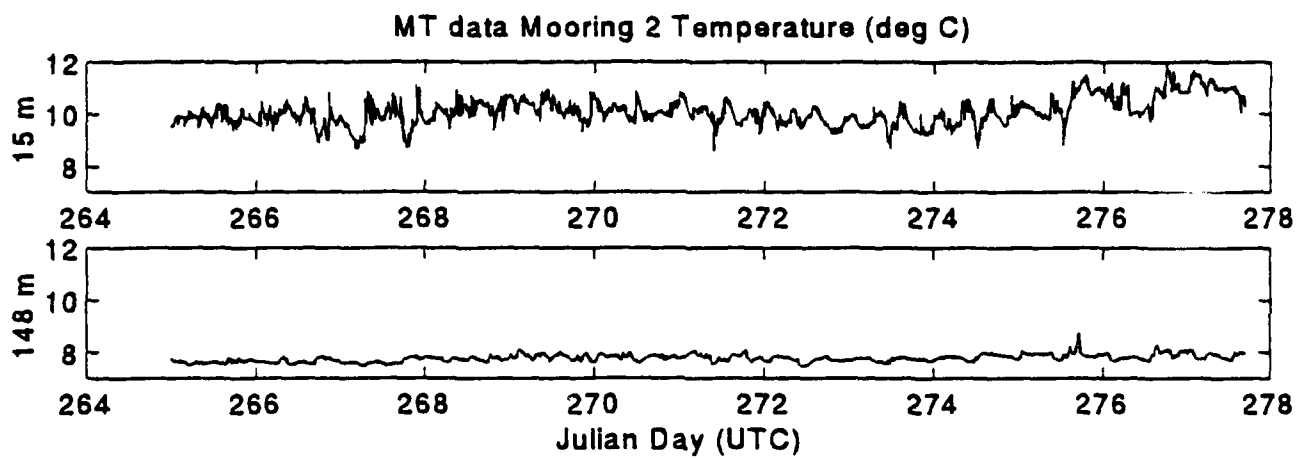


Figure 3-7 MicroTemp Mooring 2 Temperature Data

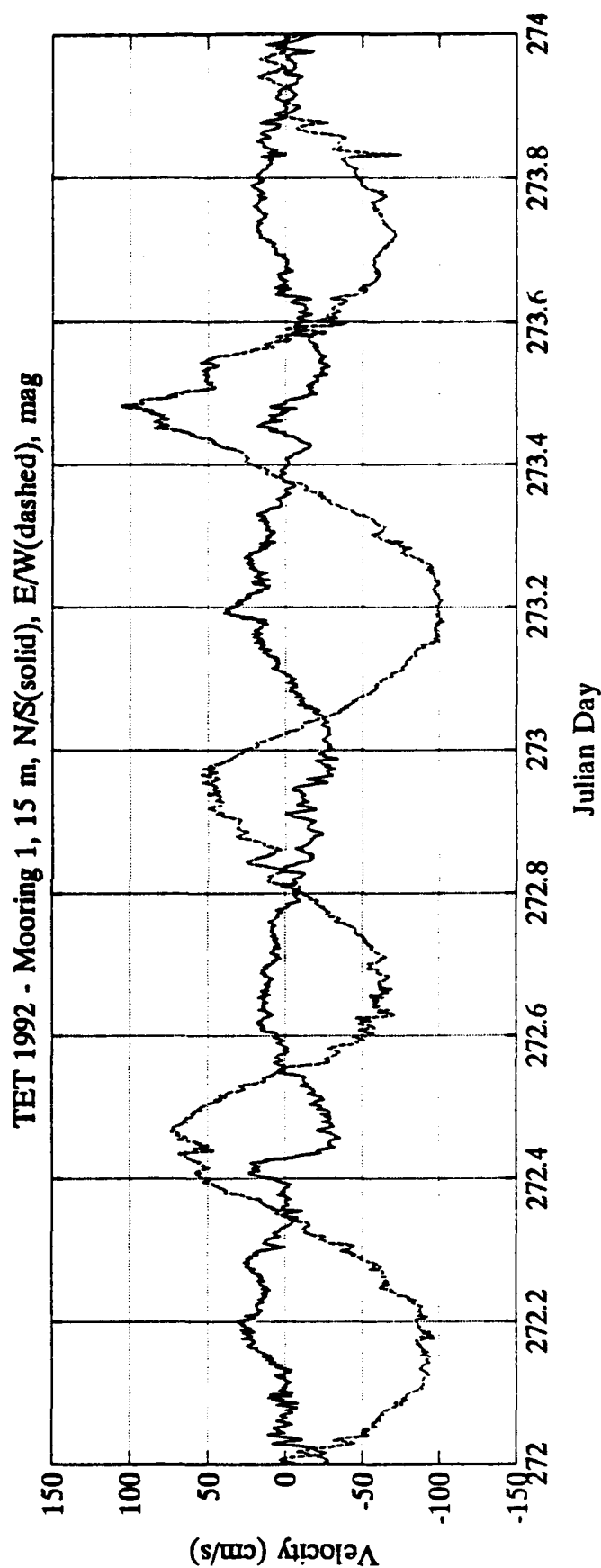
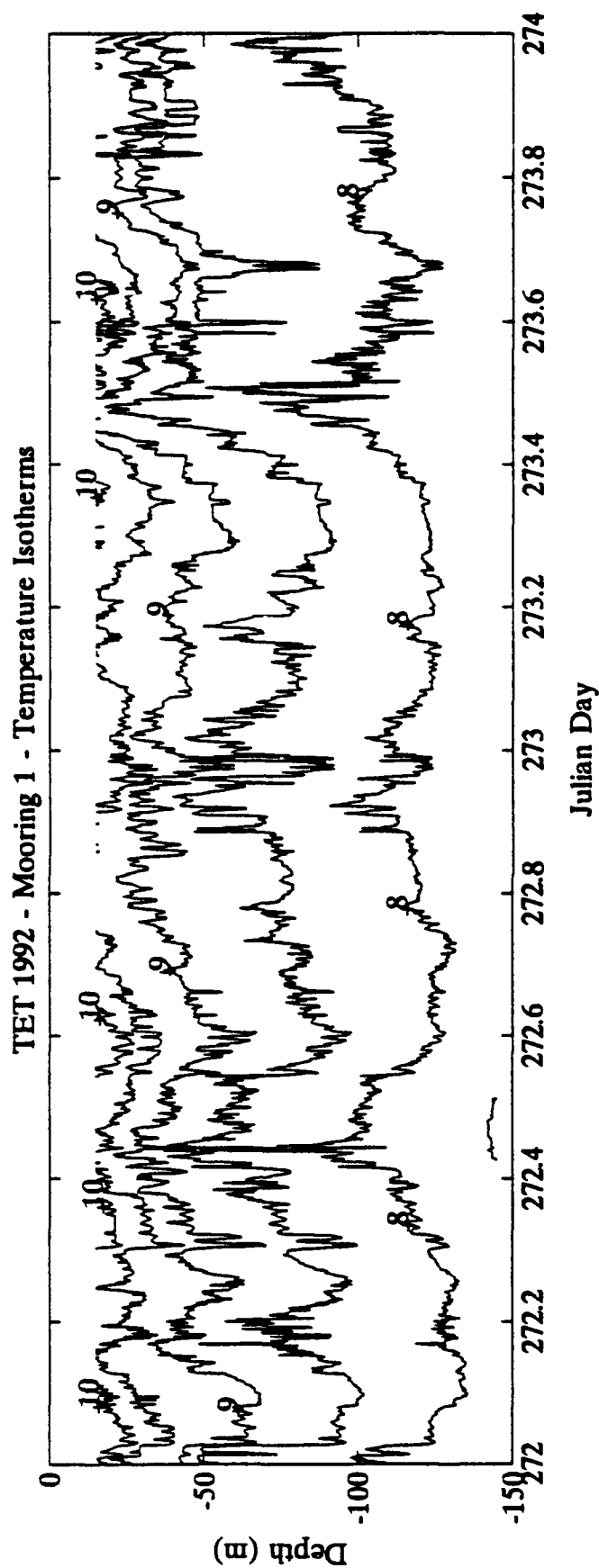


Figure 3-8 Mooring 1 Temperature Isotherms

Table 3-2 ADCP Drift Times

Julian Day	Date	Drift	Start	Stop	Duration
			hh:mm		
265	09/21/92	1	19:56	22:23	02:27
		2	22:48	23:35	00:46
268	09/24/92	1	16:02	18:11	02:09
		2	18:36	19:28	00:51
		3	19:59	20:53	00:53
		4	21:33	22:44	01:10
		5	23:07	23:15	00:07
272	09/28/92	1	17:00	18:16	01:15
		2	18:46	20:03	01:17
		3	23:03	00:04	01:01
273	09/29/92	1	15:33	16:40	01:06
		2	17:36	18:22	00:46
		3	18:54	20:10	01:16
		4	20:37	22:13	01:36
		5	22:37	00:13	01:36
274	09/30/92	1	15:57	17:16	01:19
		2	17:57	18:18	00:20
		3	18:33	18:54	00:20
		4	19:01	21:19	02:18
		5	21:34	00:00	02:26
Total Elapsed Time = 1 day 1 hour 8 minutes = 25:08					

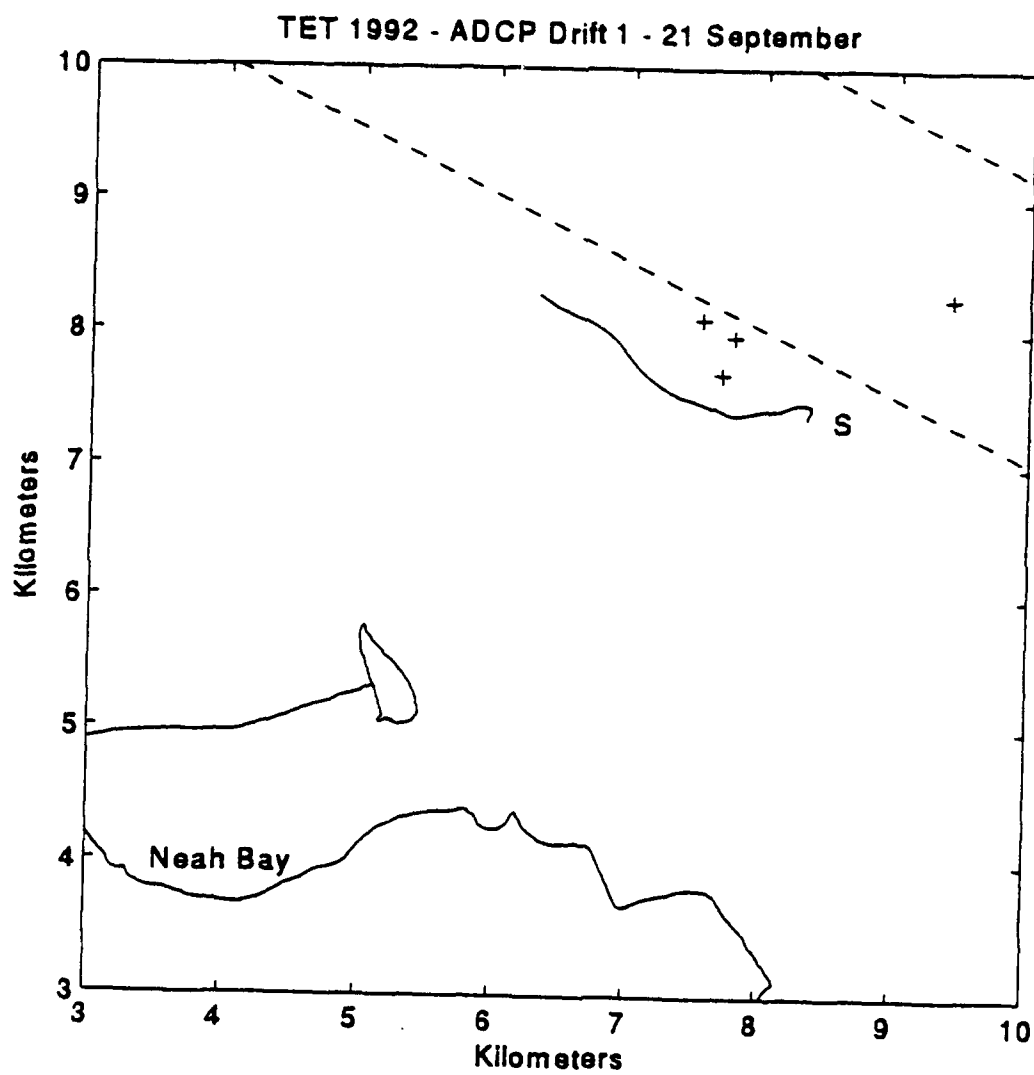


Figure 3-9 ADCP Track, Drift 1, Day 265

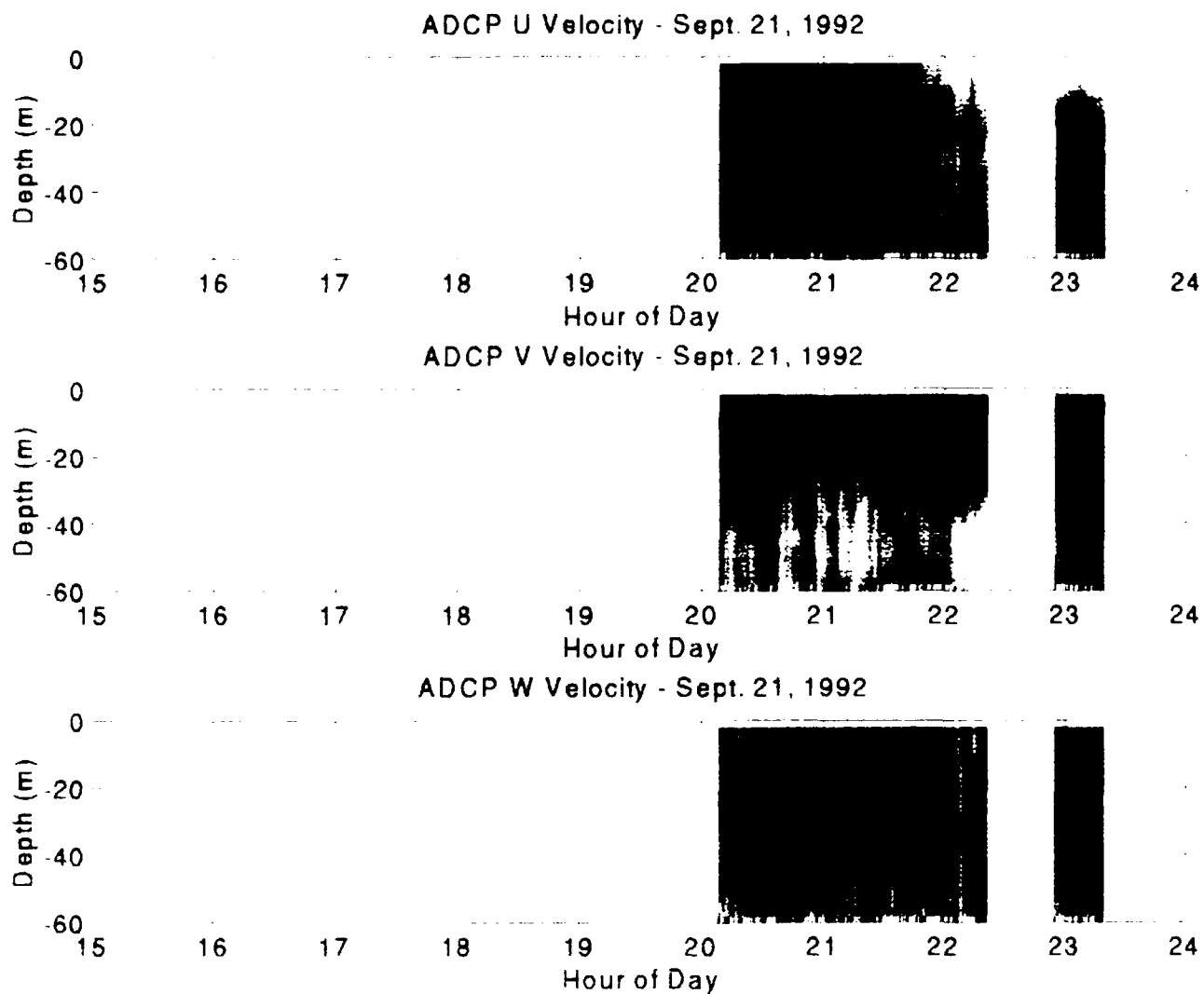


Figure 3-10 Alongshore, Across-shore and Vertical Current Time Series, ADCP Drift 1 and 2, Day 265

as fronts pass under the ADCP and occasional sharp velocity changes indicative of the passage of internal waves. At times a strong vertical coherence of the currents is evident as the velocities pulse throughout the upper 60 m.

3.6. CTD profiles

CTD data were collected during five days of the mooring deployment. Profiles were collected along an across-shelf transect station and at a specific location for a time series of profiles. The across-shelf transect included seven stations starting near Waddah Island and heading northeast across the channel (Figure 3-11). During the time series profiles, between 11 to 18 casts were taken at a single location, designated "TS" in Figure 3-11. Table 3-3 lists the specific type of profiles collected on each day of data collection. A total of 81 CTD casts were taken with 68 casts returning usable data for a data return of 84%. Thirteen casts were unusable due to a malfunction of an electronic component in the CTD.

Table 3-3 Hydrographic Data Collected

CTD Surveys		Transect # casts	Time Series # casts
Survey Day	Julian Day		
09/22/92	266	7	0
09/23/92	267	0	18
09/25/92	269	7	12
10/01/92	275	7	11
10/02/92	276	7	12

The CTD profiles provide specific information on the fine vertical scale structure of temperature and salinity. In the waters off Neah Bay the strong tidal flow quickly advects the water past a given location, confusing temporal and spatial variability. CTD profiles took approximately 5 - 10 minutes and were taken as the ship drifted with the current. Thus the vertical structure

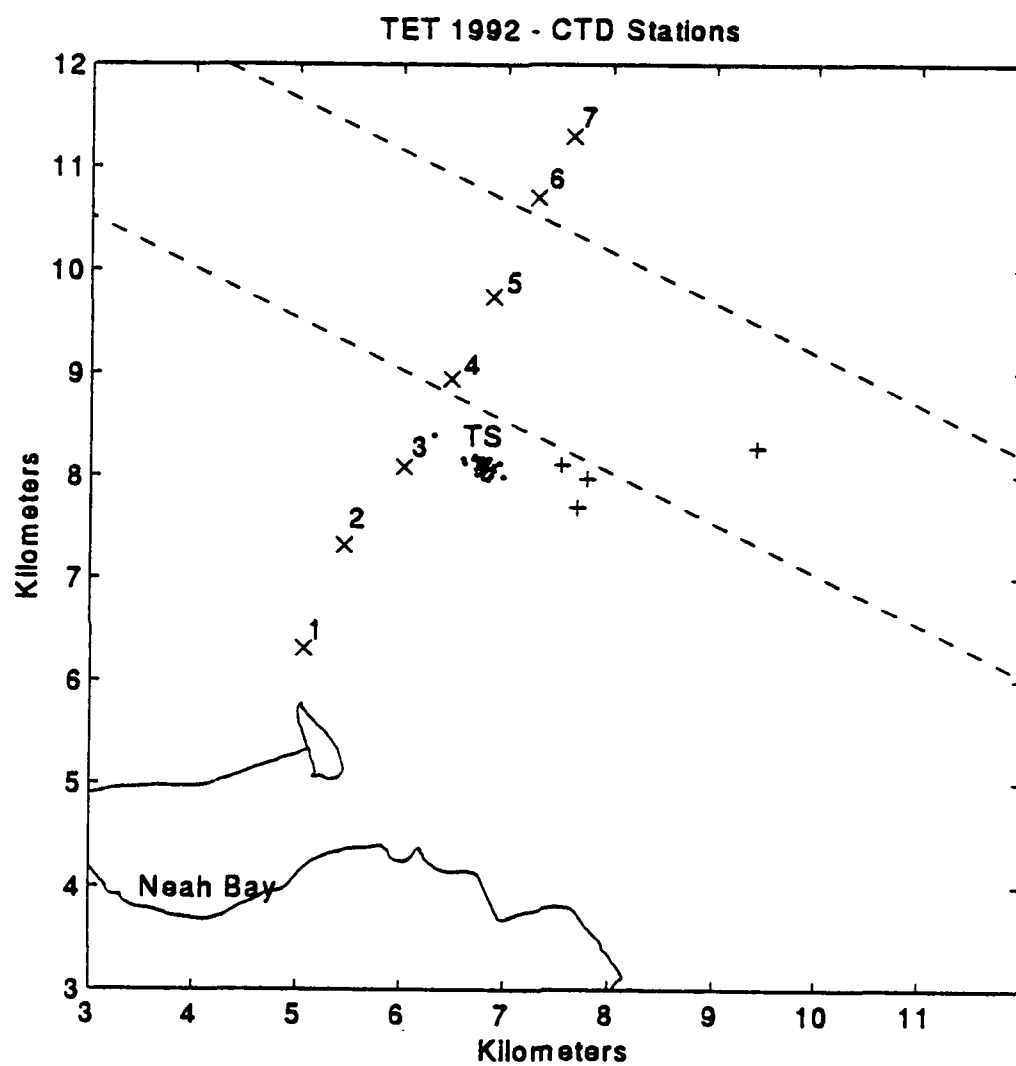


Figure 3-11 CTD Station Locations

revealed represents a close approximation of the instantaneous profile, since the instrument was moving in a similar direction as the water throughout the cast.

The vertical structure can vary quite rapidly in time, from relatively smooth profiles, to ones with step like structures in the thermocline. A long time series of profiles taken over a significant portion of the tidal cycle (12 hours), reveals a changing maximum cast depth that varies with the tide. This is a result of the measurement technique. Since the profiler doesn't have a real-time deck readout, the casts were taken to a predetermined wire-out point. At certain times of the tidal cycle noticeably shallower casts resulted because of stronger drag on the cable which caused significant wire angle with the vertical. The CTD locations, contour plots and transects of time series profiles are shown in Appendix E and G.

4. DISCUSSION

Understanding the response of TET sensors to environmental phenomena requires an examination of what phenomena are capable of effecting TET sensors, specifically what phenomena produce EF and MF signals in the frequency bands of interest with amplitudes that could be measured with present sensor technology. As a precursor to answering this question it is important to know the types of phenomena present at the study site and the range of their variability. Previous years work have shown that phenomena of interest are principally soliton-like internal waves and BBL turbulence. These two phenomena are dynamically distinct and well-enough understood to lend themselves to theoretical treatment to predict their effect on the electric and magnetic fields.

The purpose of the present discussion is to present the observations of these phenomena with sufficient detail to allow evaluation of possible signals measured by the different sensor systems. Other phenomena are discussed in order to clarify the processes taking place, particularly in the BBL, that may effect sensor performance due to unforeseen interaction. It is important to understand the dynamics of the BBL because of its proximity to the sensor systems even if the processes seem unrelated to BBL turbulence per se. For example, the 1991 measurements showed that internal waves were present in the BBL. The presence of these wave so close (2-3 meters) to the sensor systems could result in signals unforeseen by just consideration of SIW's or BBL turbulence.

This discussion will first present the variability observed in the vertical stratification due to its supporting role in the presence of SIW's. Next the structure and occurrence of the internal waves themselves will be discussed with comparisons between the different measurement systems. The variability of the characteristics of the BBL with the tidal flow will be presented as well as the dynamics driving an offshore flow in the boundary layer, a phenomena observed to date only at the site of the 1992 BBL mooring. This suggests that sensor deployment sites should be studied individually for the presence of any localized phenomena. Finally we discuss the induced electric and magnetic fields as estimated by a depth averaged model.

4.1. Stratification

Stratification provides the mechanism for supporting internal waves. Knowledge of the variability in the strength of the stratification, as represented by the buoyancy frequency, provides means for insight into the causes of the variability in the strength and occurrence of the soliton-like internal waves discussed later (Section 4.2). The stratification is a result of the variation of density with depth and is affected by the temperature and salinity of the water. Salinity can be changed by variations in river runoff or the influx of more saline ocean water, which flows in at depth. The flood and ebb of the tide, seasonal and shorter period solar insolation variability as well as fronts and internal waves can affect the vertical distribution of density. The previous year's measurements have suggested that the stratification is weakening this time of year as the solar insolation diminishes with the season. Actual quantification of this would require measurements over a longer period than the present two week survey since the stratification is also affected by shorter period variability such as the diurnal and semi-diurnal tide as well as the fortnightly spring and neap tidal variability. However the trend is consistent with the known seasonal variability of the region.

In examining the stratification we present views of the vertical structure of temperature, salinity and buoyancy frequency. The buoyancy (or Brunt-Väisälä) frequency represents the natural frequency of oscillation for a water parcel displaced vertically and influenced by gravity and the restoring force of buoyancy. The buoyancy (or Brunt-Väisälä) frequency, N , is defined by the equation (Phillips, 1969):

$$N^2 = -\frac{g}{\rho_o} \frac{\partial \bar{\rho}}{\partial z}$$

where ρ = density, z = depth and g is the acceleration of gravity. Since N^2 is negative, it only results in a real frequency (N) when the density is increasing with depth. N represents the highest internal wave frequency supported by the stratification and the distribution of N gives some indication of the location of the interface along which the interfacial internal waves travel.

Two views of the temperature and salinity distribution and buoyancy frequency are presented here. First are five cross shelf transects which delineate the structure as one proceeds off shore.

The second is a time series derived from the profiles which elucidates how the vertical structure evolves in time at a specific location.

4.1.1. Transects

Cross shelf transects of CTD profile data were collected on four different days, three of which were just prior to the CTD time series data discussed in the next section. The transect consisted of 7 stations, extending 5 km offshore into the separation zone between the inbound and outbound shipping lanes (Figure 3-11). The vertical sections of temperature (Figure 4-1) and salinity (Figure 4-2) show that the thermocline and halocline vary in position and time, but are generally in the upper 100 meters. The result of the variability of temperature and salinity on the stratification is shown in Figure 4-3. The maximum in the Brunt-Väisälä (B-V) frequency is generally between 0.2 and 0.3 cycles/min (cpm) and is limited to the upper 25 m in two of the four days. In the other two days it is deeper (40-60 m) and weaker on 1 October, when it remains less than 0.2 cpm. There is no evidence of any persistent cross shelf structure in the stratification. In contrast, the temperature does show a mid-shelf temperature maximum in three of the four days.

4.1.2. Time Series

Time series' of the vertical stratification were measured by two methods: by multiple casts of the CTD profiler and by the thermistor string temperature measurements on Mooring 1. Comparison between the two measurement systems requires some insight into their differences since the CTD sampled the water column at 0.5 hour intervals, but had detailed depth resolution (1 meter), whereas the thermistor string sampled very frequently in time (1 minute), but had coarser depth resolution (generally 5-10 meters in the thermocline). The CTD provides detailed information concerning the vertical structure, but can alias the internal wave activity in time, whereas the thermistor string provides excellent information on the temporal variability but less information on vertical spatial structure at depth (between 50 and 145 m). The mooring sites and the CTD profile locations were also slightly different. Despite these differences both time series agreed qualitatively.

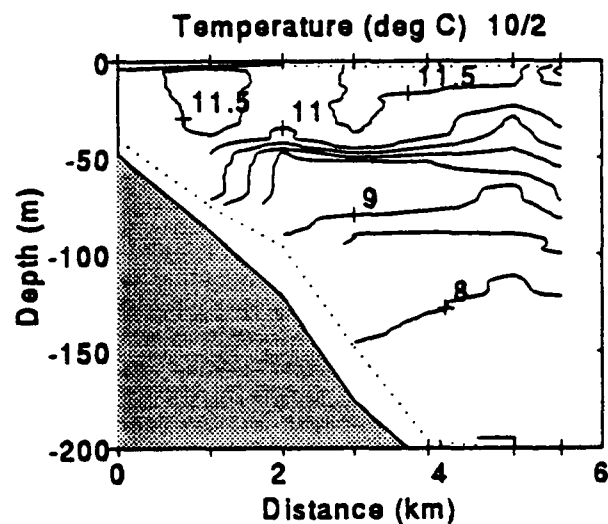
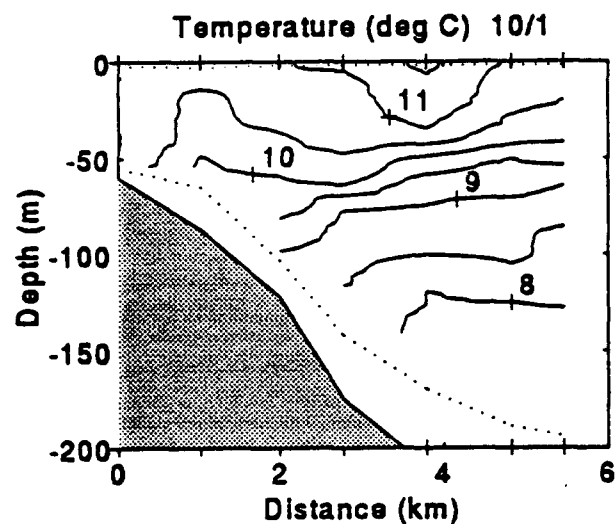
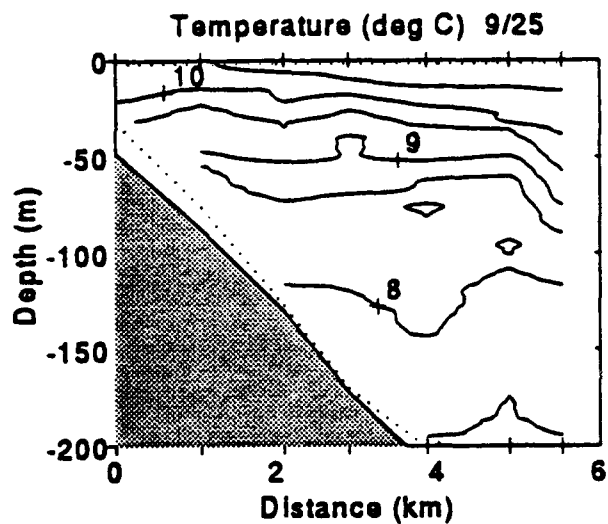
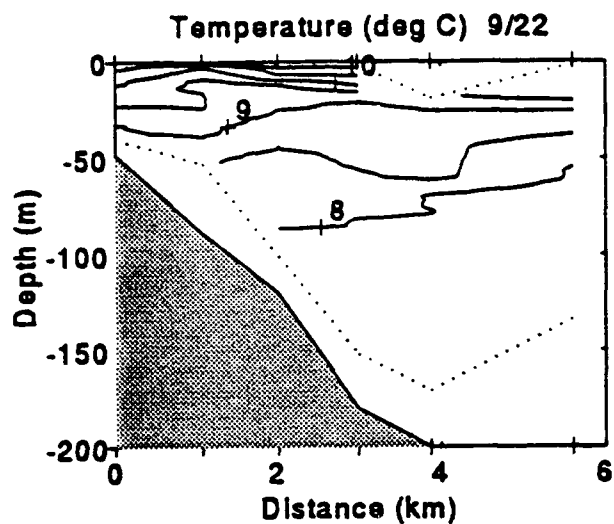


Figure 4-1 Vertical Structure of Temperature in Cross Shelf Transect

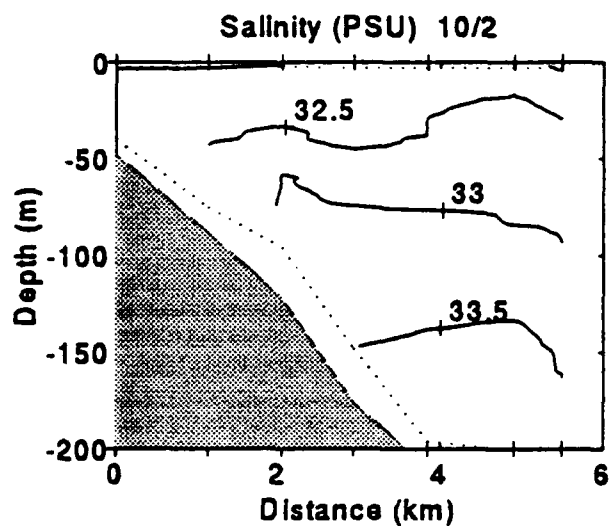
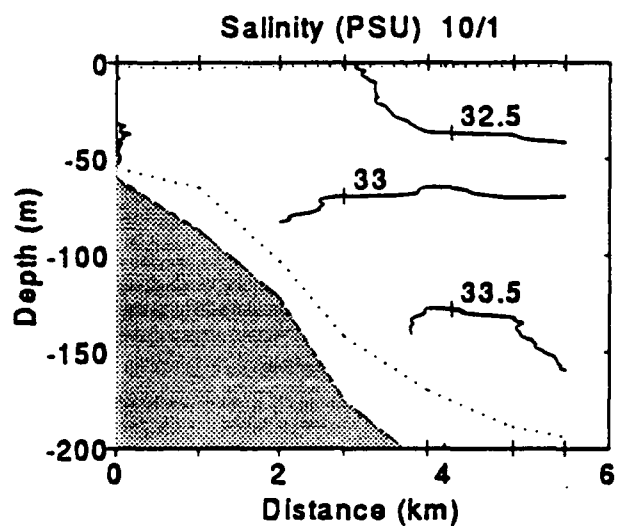
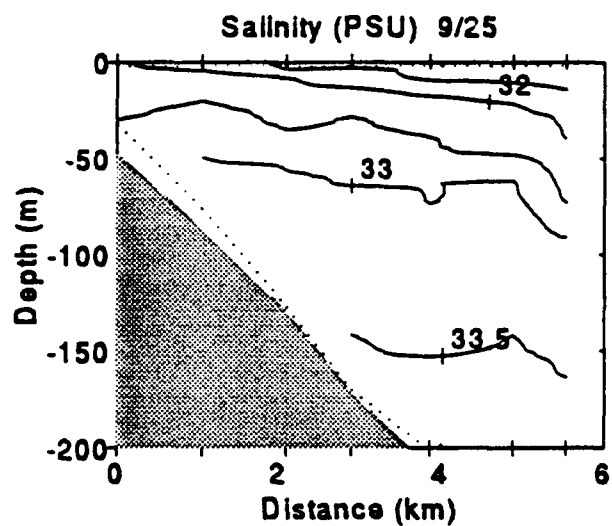
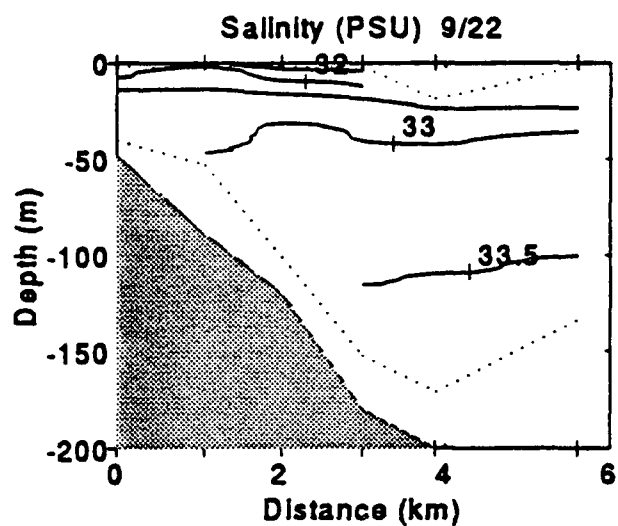


Figure 4-2 Vertical Structure of Salinity in Cross Shelf Transect

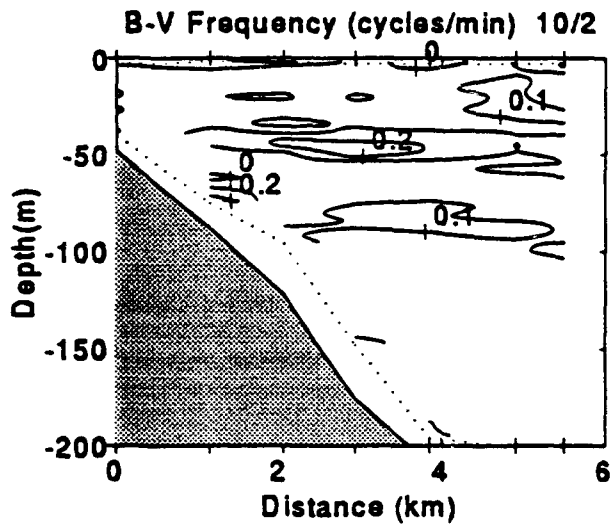
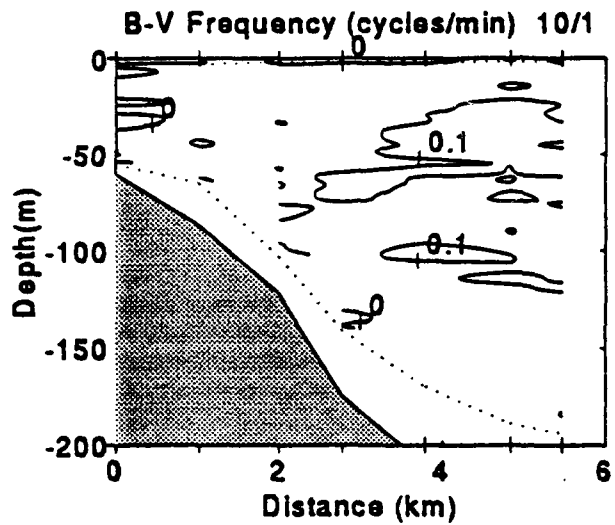
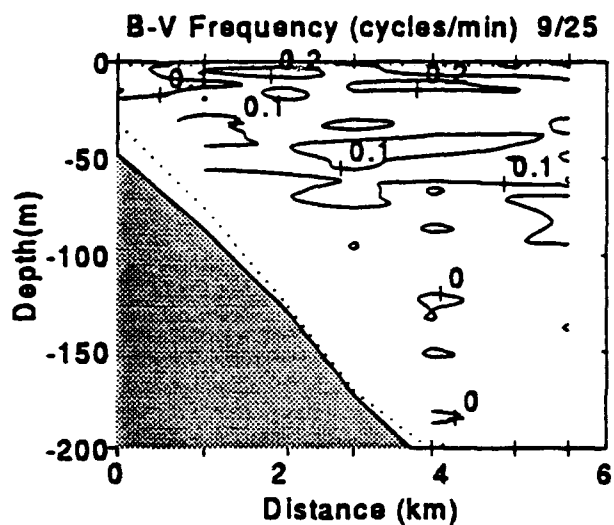
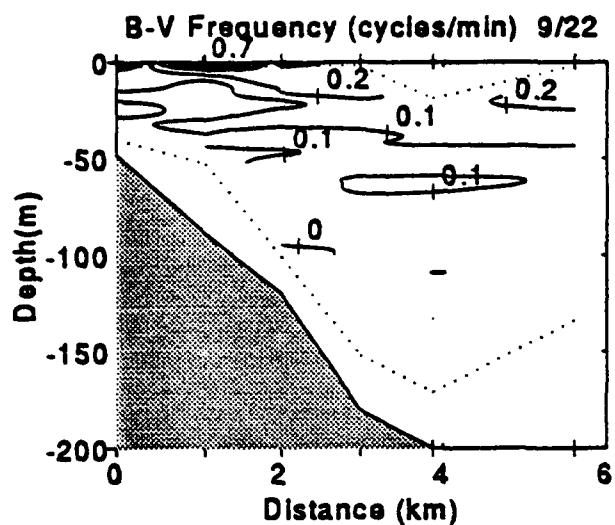


Figure 4-3 Vertical Structure of B-V Frequency in Cross Shelf Transect

The first CTD surveys (Figure 4-4) show a shallow thermocline with some vertical variability and with the thermocline deepening later in the day. The latter two surveys show a deep thermocline at first, shallowing later in the plot. The time series from the mooring shows this variation in the depth of the thermocline to be an effect seen with each tidal cycle (~ 12 hours) rather than a result of longer period variability. A more detailed comparison between the CTD and mooring data for the first survey is shown in Figure 4-5. Although the moored data shows more temporal variability, as would be expected, the general trends are consistent. From this we are able to conclude that the thermistor string on mooring 1 was adequate to resolve general temporal variations of the temperature structure.

The salinity (Figure 4-6) shows a strong halocline in the upper 50 m during the first two surveys. The last two surveys, a week later, the salinity is much lower in the upper 100 m of the water column, consistent with the depressed thermocline. This transition also agrees with the picture presented by the thermistor array which shows a significant change in the water column characteristics after JD 275 (1 Oct).

The associated contours of B-V frequency (Figure 4-7) also show a transition of stratification between early and late. Peak values greater than 0.25 cpm are common in the upper 20-30 m for the first two days, actually reaching values over 0.3 cpm. Deeper values (depths > 50 m) are generally less than 0.1 cpm. For the later part of the survey however the maximum values are much deeper with peaks values (> 0.2 cpm) in the 80-100 m depth range.

The temperature variability, as observed by the thermistor string, is shown in Figures 4-8 and 4-9 for two 2-day periods. (The entire study period is displayed in Appendix B.) The current measured at 15 m is also displayed to provide a cross reference to the velocity field. In Figure 4-8 the temperature stratification is strongest in the upper 50 m with a definite weakening of the stratification associated with the maximum flood tide, as indicated by the peaks in the dashed (E/W) current line. This could be a result of the normal two-layer estuarine distribution being replaced by less stratified oceanic water as the estuarine-type water is pushed inward by the tidal flow. There also appears to be more high frequency variability with the flood tide than at other times. This conclusion is supported by the other portions of the time series.

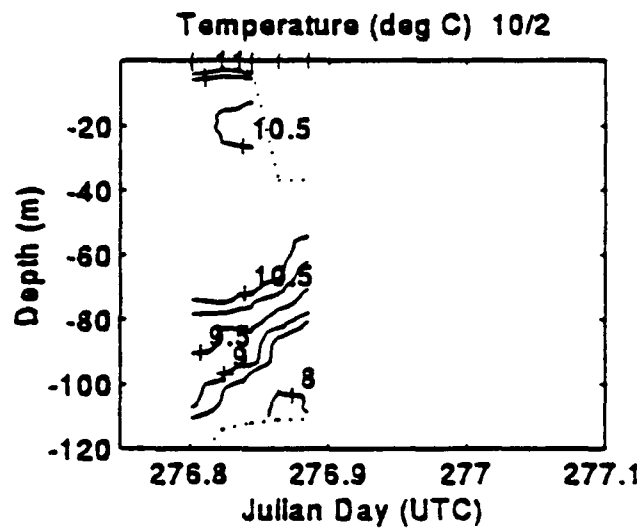
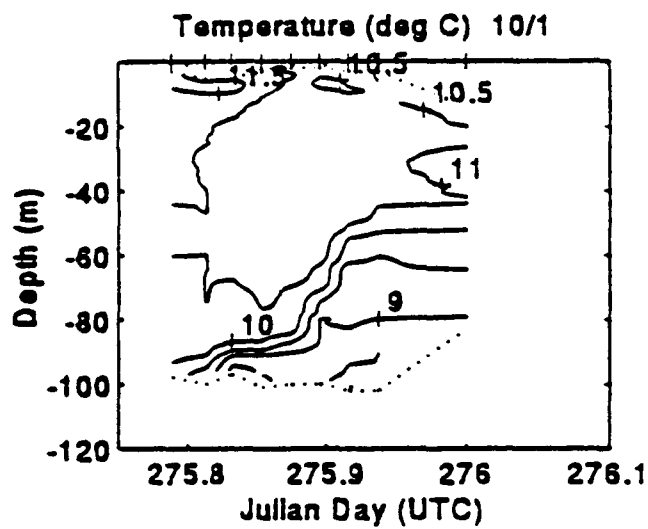
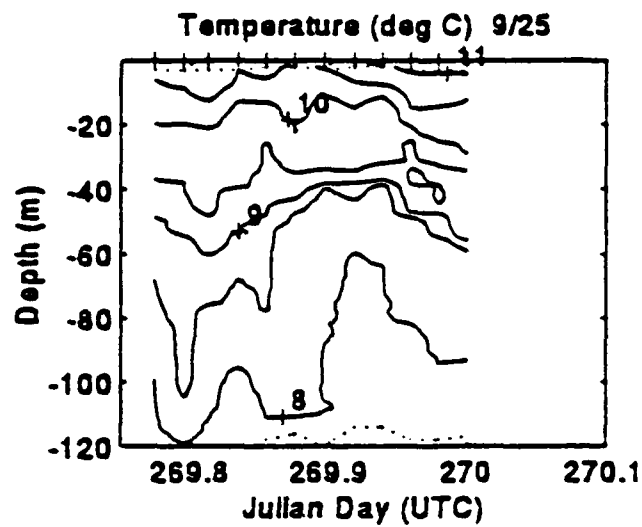
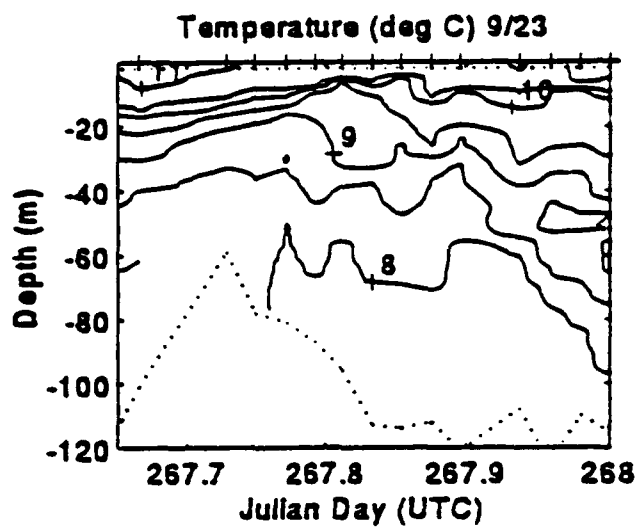


Figure 4-4 CTD Time Series, Temperature

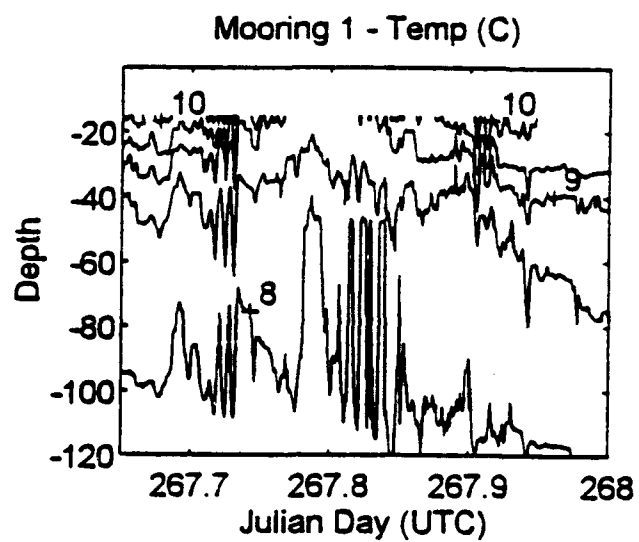
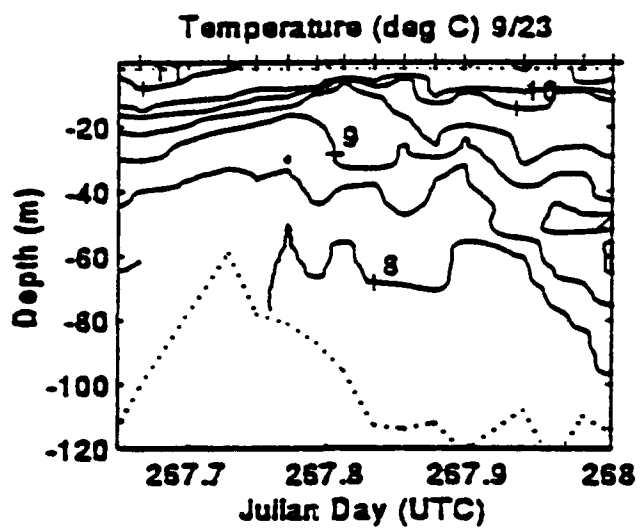


Figure 4-5 Comparison at CTD Time Series Profiles (Left) and Thermistor String on Mooring 1 (Right).

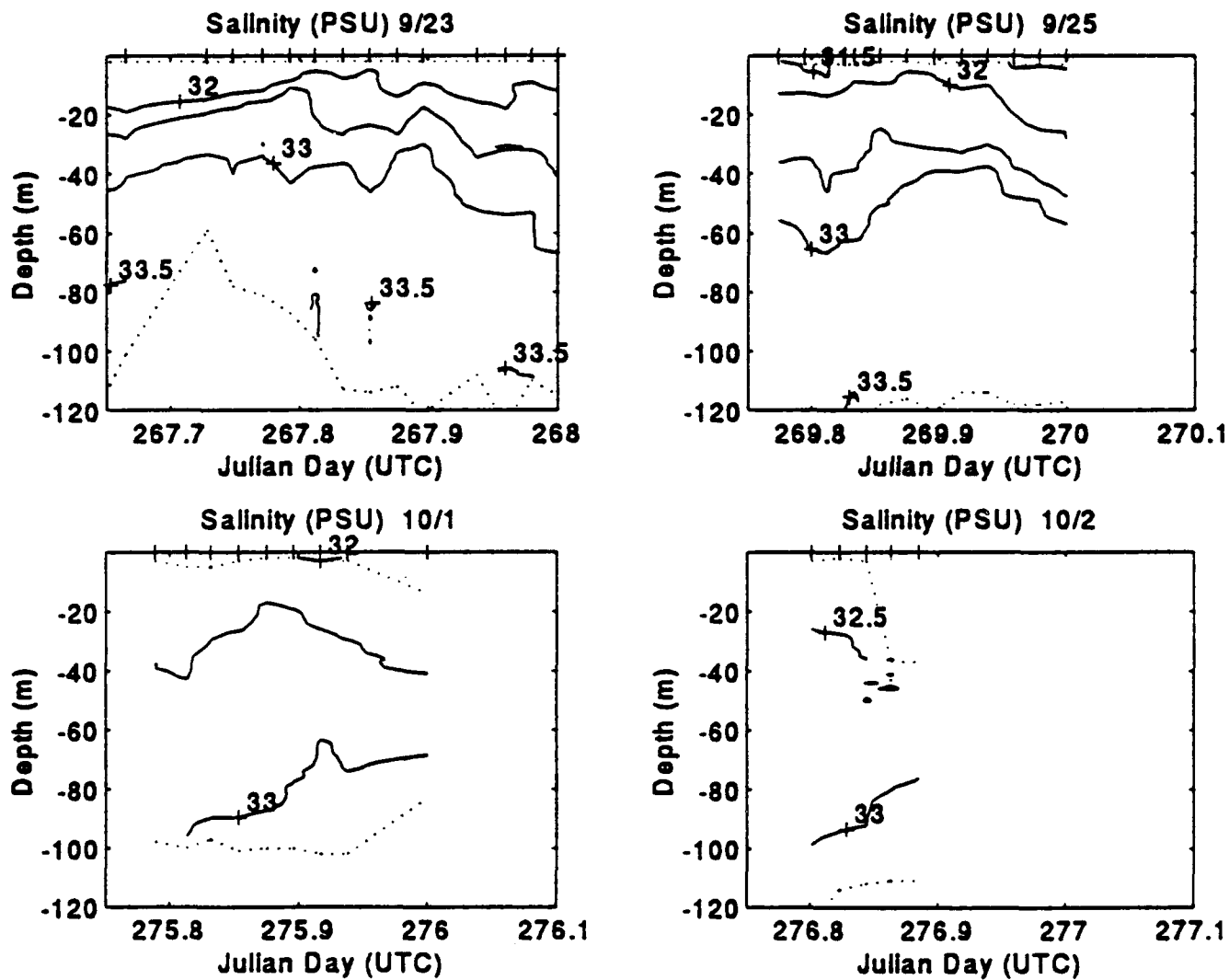


Figure 4-6 CTD Time Series, Salinity

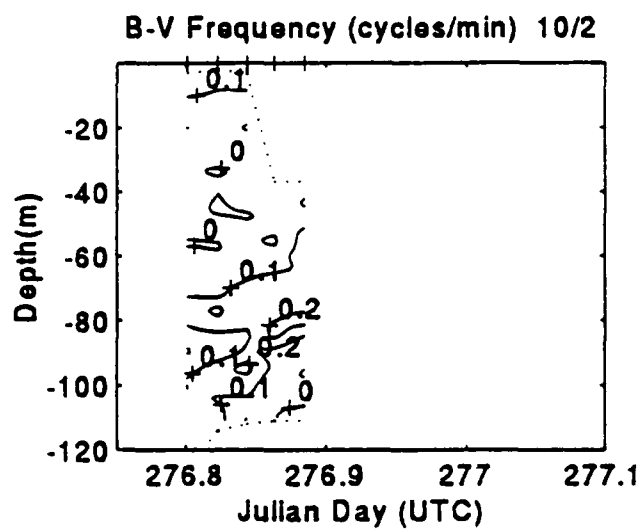
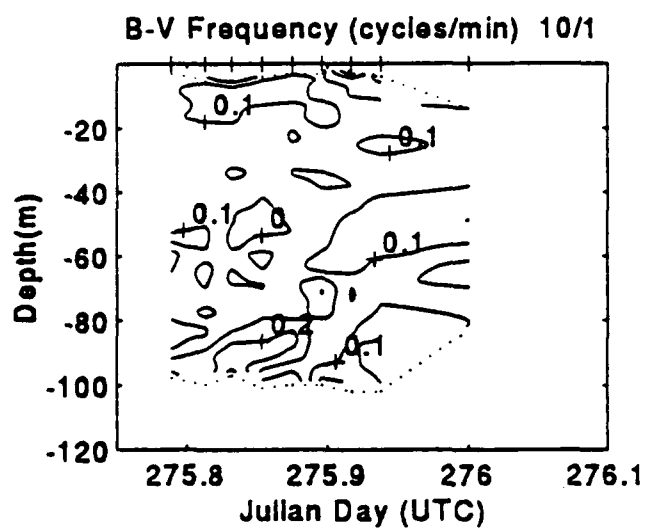
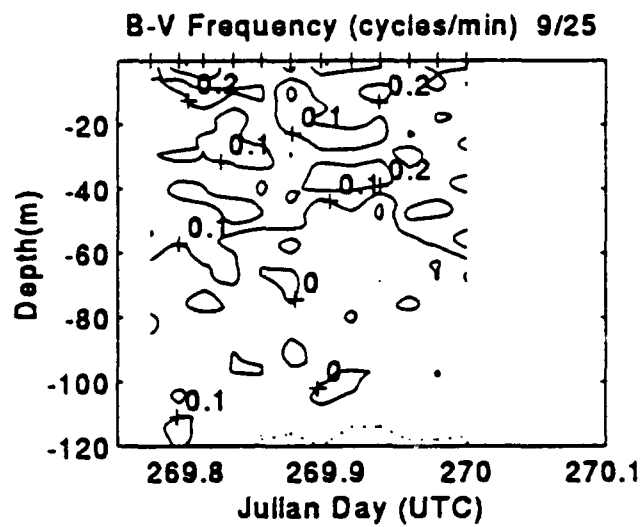
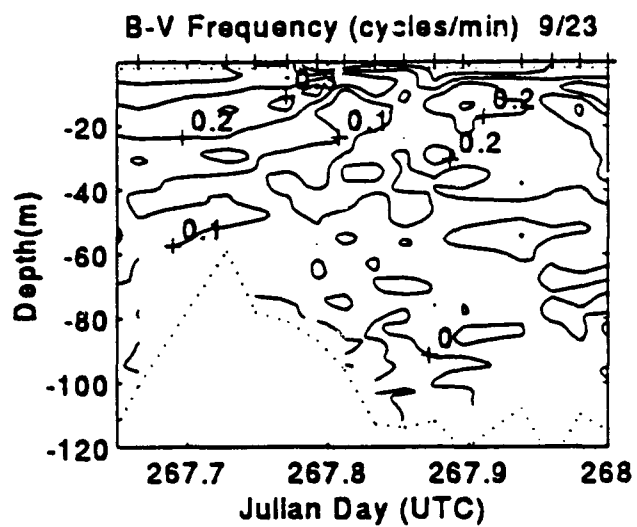
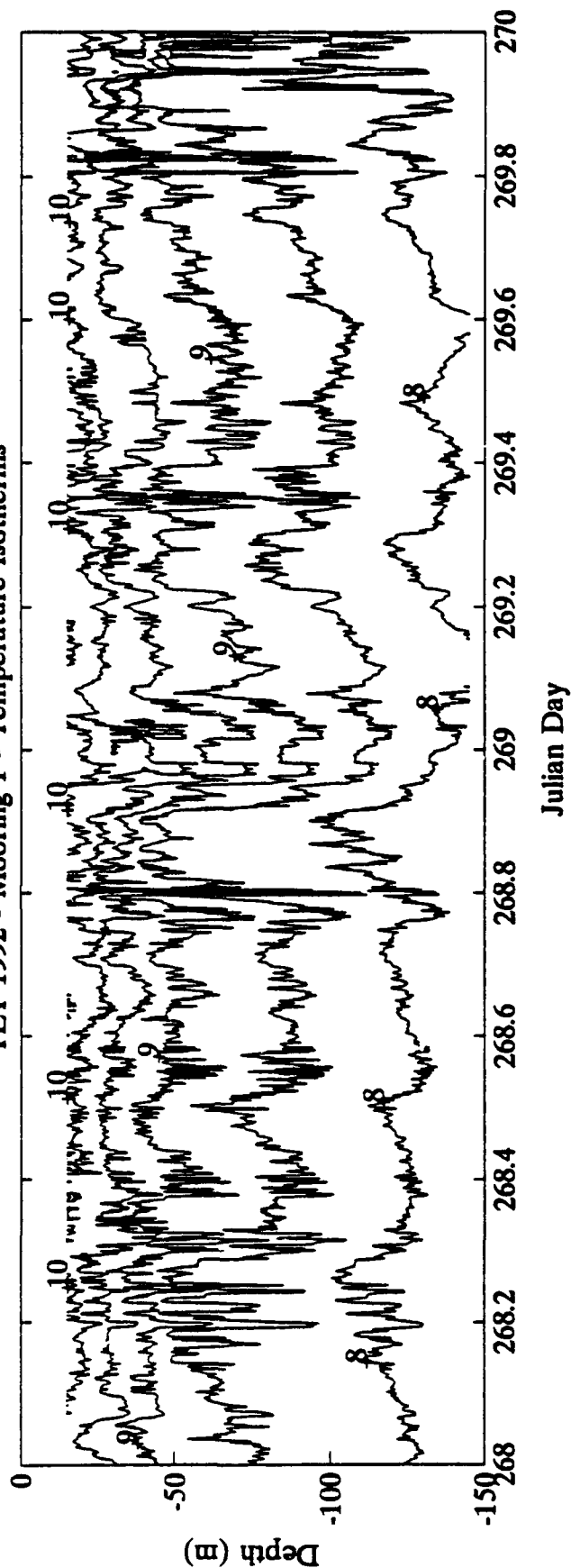


Figure 4-7 CTD Time Series Brunt-Väisälä Frequency

TET 1992 - Mooring 1 - Temperature Isotherms



TET 1992 - Mooring 1, 15 m, N/S(solid), E/W(dashed), mag

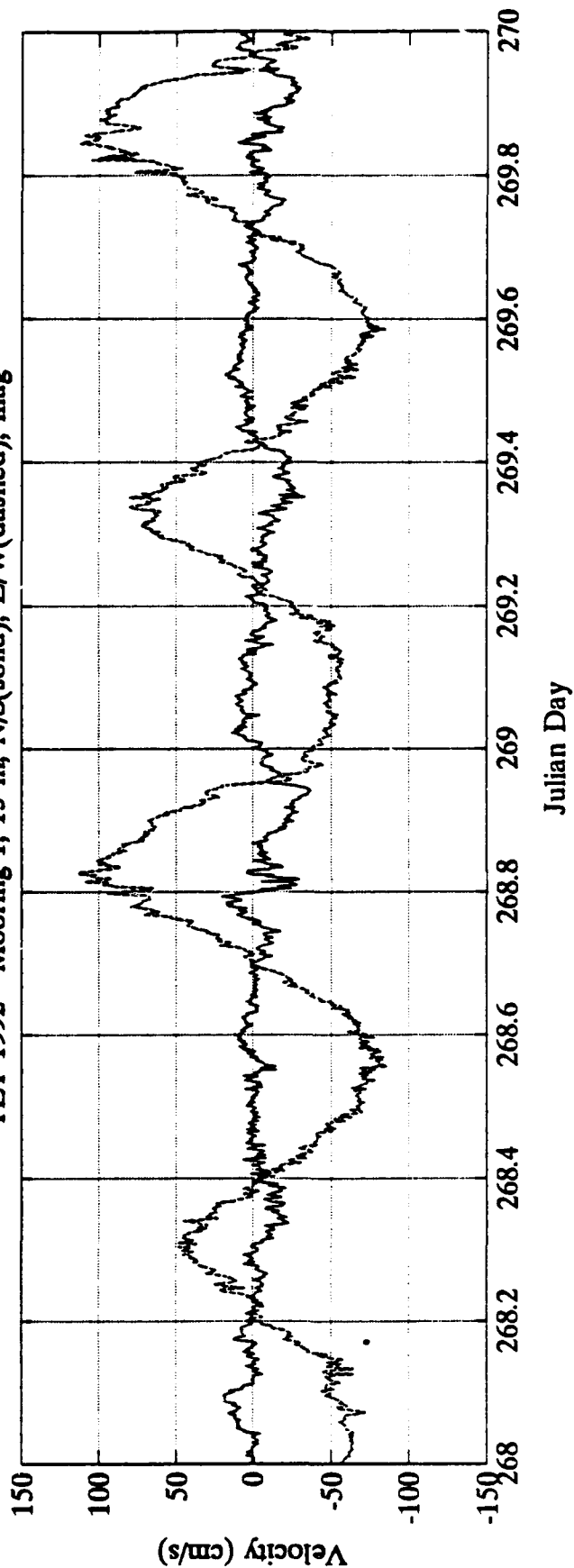


Figure 4-8 Two-Day Time Series of Temperature Isotherms and of Alongshore (E/W) and Across-Shore (N/S) Current Velocity at 15 m, Mooring 1, Day 268 to 270

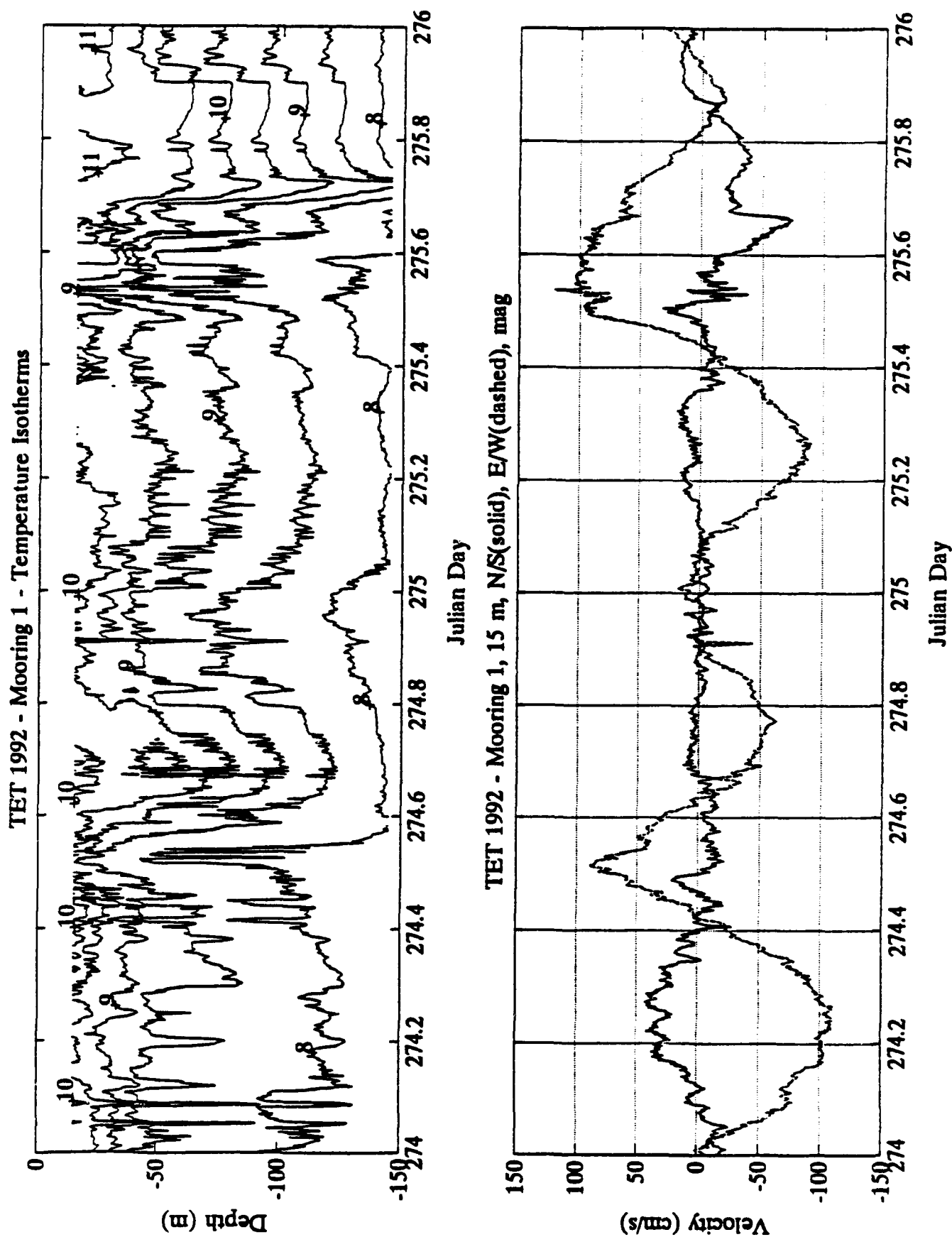


Figure 4-9 Two-Day Time Series of Temperature Isotherms and of Alongshore (E/W) and Across-Shore (N/S) Current Velocity at 15 m, Mooring 1, Day 274 to 276

Figure 4-9 shows a period later in the survey, when the temperature structure changes from this "two-layer" character to a continuously stratified regime. This change is associated with the passage of two fronts (at $t=274.55$ and 275.70). The latter portion of the figure shows a temperature gradient that is fairly constant throughout the 150 m water depth. The second front is marked by a very strong decrease in the N/S velocity with initially a drop and then a rapid increase in the N/S velocity (~ 50 cm/s change). This front was also evident in the currents at 145 m depth.

The stratification in the study region therefore varies on tidal time scales and with longer period variability due to frontal movements or the influx of different water types from the open ocean or estuarine region. The most significant factor as far as the generation of SIW's is concerned appears to be the tidal variability. The influx of different water types could change the stratification enough to preclude the generation of SIW's but the extent to which this happens cannot be addressed during such a short study. The typical distribution for the stratification seems to be characterized by a strongly stratified layer positioned over a deeper weakly stratified layer rather than by two layers separated by a interface as desired for the simple dynamics for theoretical considerations (see Section 4.2). Although peak B-V frequencies in the thermocline were typically between 0.2 to 0.3 cpm suggesting wave periods of 3-5 minutes, the strongest SIW's observed had periods 3-4 times longer. This suggests that the period of the SIW is more dependent on the stratification averaged over longer depth scales which would give values in the 0.05-0.1 cpm range (wave periods of 10-20 minutes).

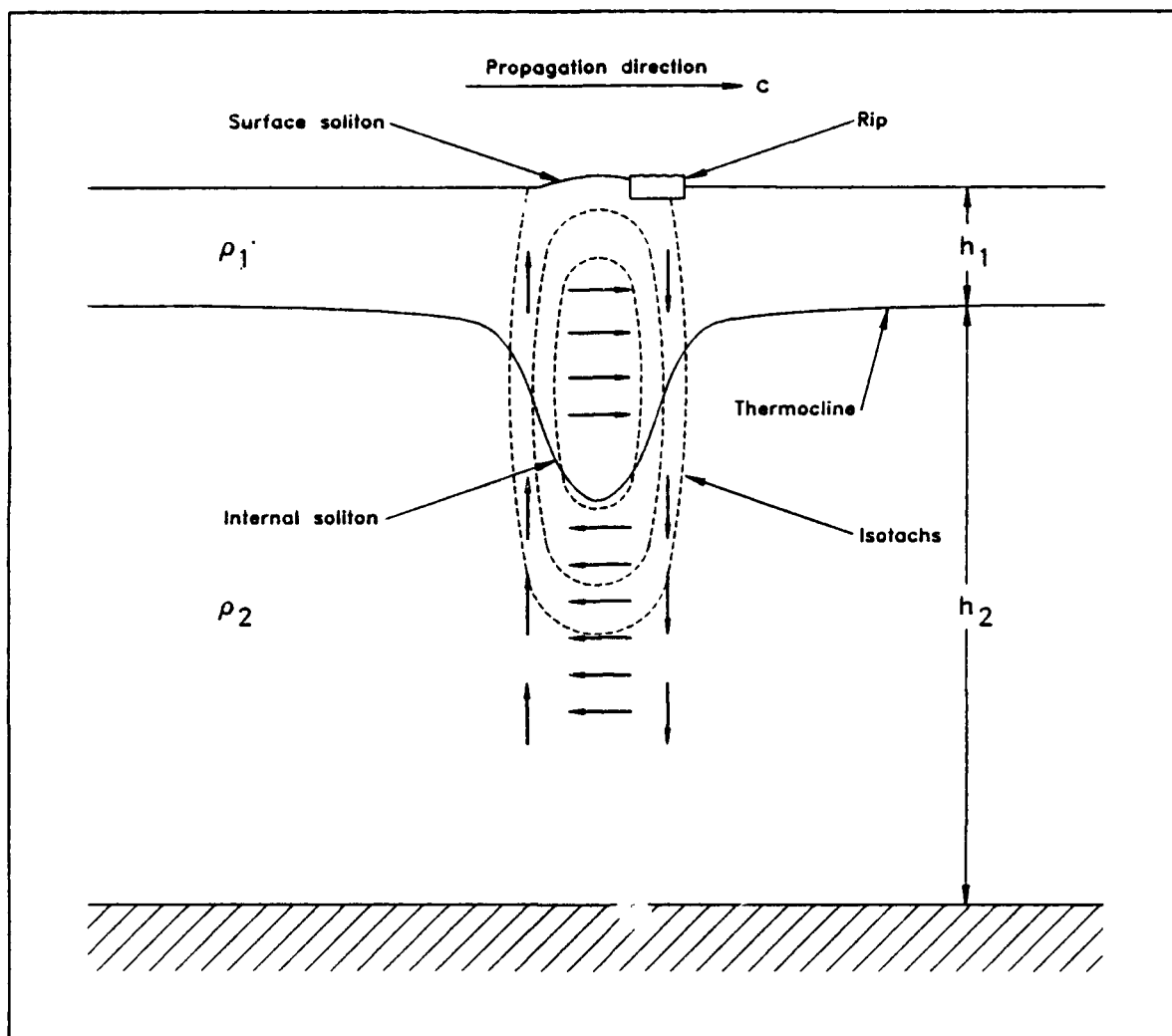
The implications of these observations of stratification on the distribution of SIW's are that the two level structure required for optimal application of the theory varies in its position of the interface. There is significant structure in the upper level which will complicate the internal wave structure. This is commonly the case, however, and is one reason why the isolation of these phenomena and the application of a theoretical picture is so complex.

4.2. Internal Waves

The use of electric and magnetic field sensors in the TET program requires knowledge of the environmentally induced EF and MF fields. This section documents the occurrence of strong soliton-like internal waves in order that the effect of these on the TET sensor systems can be evaluated.

Knowledge of the nature of soliton-like internal waves (SIW's) in the TET region is important because of their potential impact on electric and magnetic field sensors. As sea water, an electrolyte, flows through the earth's magnetic field, it produces electric and magnetic fields and electric currents. Although the resulting fields are complex, understanding the structure and probability of occurrence of SIW's can allow analysis of their possible effects and evaluation of their importance in target detection.

In a two-layer system, interfacial internal waves can propagate along the interface and under the proper conditions can become non-dispersive. These non-dispersive internal waves are designated as Soliton Internal Waves (Apel et al 1985). The 1992 TET experiment did not try to determine the dispersive characteristics of these internal waves, so they will be referred to as soliton-like internal waves (SIW). Following the discussion of Osborne and Burch (1980), these internal solitary waves, or solitons, propagate on the interface with a distinctive signal. Figure 4-10, adapted from Osborne and Burch (1980), shows an idealized picture of an internal soliton. It clearly shows the relationship between the horizontal velocities in upper and lower layers, thermocline depression and vertical velocity structure. This idealized picture matches the structure observed in the Strait of Juan de Fuca, described below, thus providing some justification for this simplification. In this idealized picture the horizontal velocity pulses in the upper and lower layers are directionally opposed with magnitudes inversely proportional to the thicknesses of the respective layers and with little variation of velocity with depth in each layer. The vertical velocity is oppositely directed on either side of the wave and its magnitude may vary with depth.



Dashed lines are lines of constant water particle speed. Arrows indicate the magnitude and direction of the water particles. A small surface soliton of amplitude $\sim (\rho_2 - \rho_1)\eta_0$ accompanies the internal soliton. The appropriate location of surface rips is also shown.

Figure 4-10 An Internal Soliton in a Two-Layer Fluid of Finite Depth When $h_1 < h_2$ (from Osborne and Burch, 1980).

In the Strait of Juan de Fuca these solitons are generated by and transported back and forth by the strong tidal flow. The oscillating tidal currents, the strong velocity shear in the vertical, and the closeness of the study site to the coast all contribute to the complexity of the local situation and significant deviation from the idealized picture. Nevertheless, at times very good agreement with the theoretical picture is seen.

4.2.1. SIW Structure

Following the discussion of Osborne and Burch (1980) there are three regimes where SIW's occur -- very deep, very shallow and intermediate -- defined by the ratio of the water depth to the length scale of the soliton. The SIW's encountered during the TET experiment fall into their very shallow case defined as $h/\lambda \gg 1$, where λ = twice the wave length of the soliton and h = depth of water.

The waters of the Strait of Juan de Fuca have essentially a two layer structure with the interface between the layers typically between 20 and 50 meters depth this time of year. The stratification can be more complex with multiple intermediate interfaces or with vertical gradients evenly distributed throughout the water column (see Sections 3.4 and 4.1.2) but for the purposes of this discussion we will choose the two layer system with the simpler dynamics. The complexity of the actual situation and the presence of an interface between layers with a discrete width produces a less distinct signal of these processes in the measurements.

The time series of current velocity showed many events consistent with SIW's passing the mooring. One particularly well-defined event (JD=274.91) occurred during a relative maximum in the flood tide with a current velocity magnitude near zero and had a strong negative pulse in the east/west current at 15 meters depth, as observed by the current meter and a 30 m depression of the isotherms (Figure 4-11). There was no opposing pulse in the velocity in the deep current meter (145 m. depth) on Mooring 1, only a small "jump".

Another view of this SIW was collected by the ADCP on the fifth drift of the day. The ADCP was a short distance away from the mooring and observed a different part of the wave. The

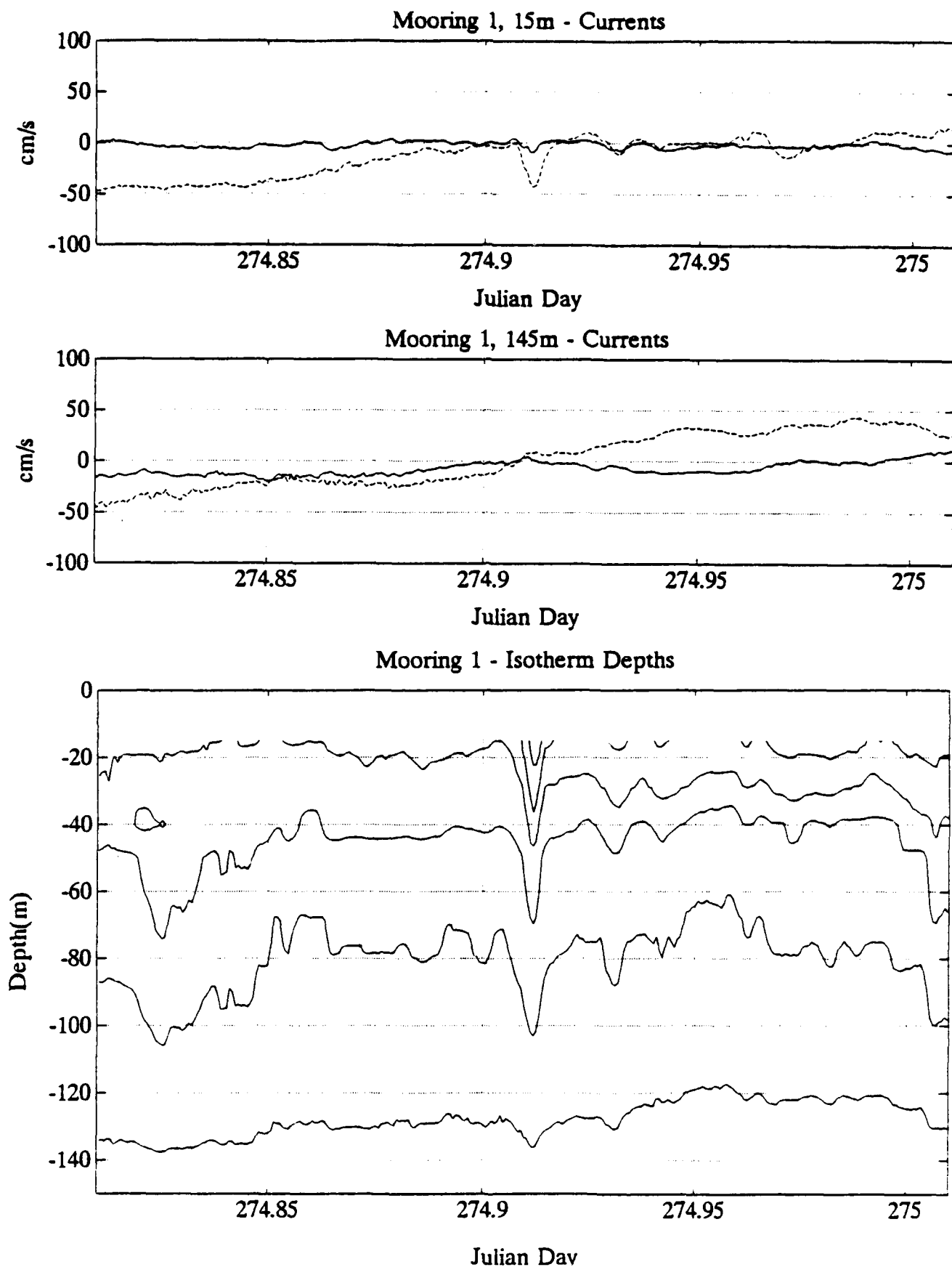


Figure 4-11 Time Series of N/S (Solid) and E/W (Dashed) Current Velocity at 15 m and 145 m and of Temperature Isotherms, Mooring 1.

details of the velocity signal as seen by the ADCP, however show very good agreement with the data observed by the current meter as shown in Figure 4-12, and with the expected theoretical signal. The ADCP observed the horizontal pulse flanked by the downward and upward vertical velocity. The duration of the velocity pulses in the ADCP data are considerably longer than those observed with the current meter. This may be because it is measuring a different section of the wave or it could be a doppler shift due to the fact that the ADCP is drifting under the influence of the wind and surface current.

4.2.2. Soliton Internal Wave Occurrence

The time series of the currents and temperature from the mooring array were used to investigate the occurrence of strong and well defined SIW's. The time series was examined for the characteristic short duration (10-15 minute), solitary pulse in horizontal velocity. When possible these events were examined in both the current and temperature data bases to determine their spatial and temporal extent. Table 4-1 lists thirteen SIW events that were distinct and observed in both the velocity and temperature time series.

Time series of all the current meter data are presented in Appendix A for reference but a representative four day time series from Mooring 1 at 15 m depth is shown in Figure 4-13. Sharp negative pulses of the east/west velocity are seen at several times (273.58, 273.83, 274.91 and 275.58) as well as in the north/south velocity (274.41, 275.58). There are also some rapid frontal transitions in the north/south velocity (272.44, 275.66). Generally, the SIW's were observed just before or just after peak flood tide.

The times series of temperature from Mooring 1 has been contoured into isotherm depths in Figure 4-11 for the SIW event at 274.91. Also shown is the velocity at 15 and 145 m depth from Mooring 1. The isotherms show a vertical displacement of approximately 25 meters throughout the upper 100 m of the water column. This is concurrent with a decrease in the E/W current component of 45 cm/s, a signal indicative of a SIW passing the mooring. This was one of the strongest, most distinct SIW's during the study period, but it was not unique. A similar pulse occurred a day earlier and less distinct but quite recognizable pulses were common.

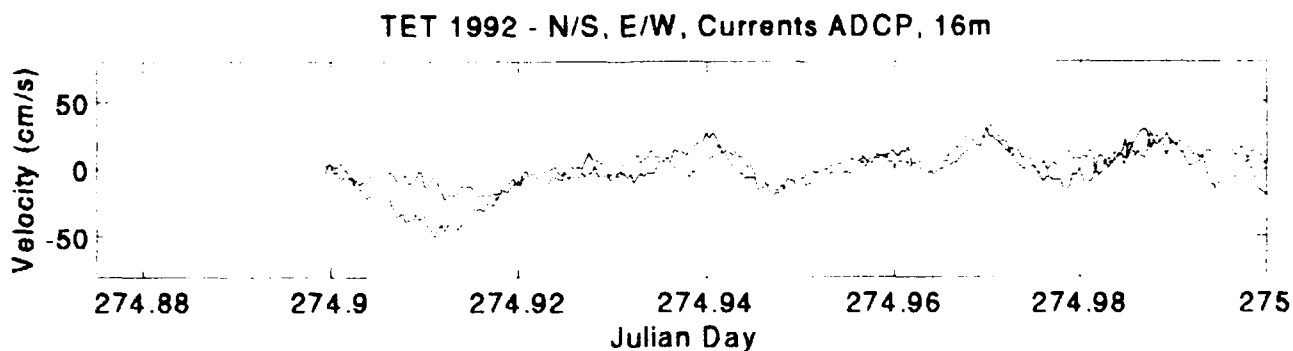
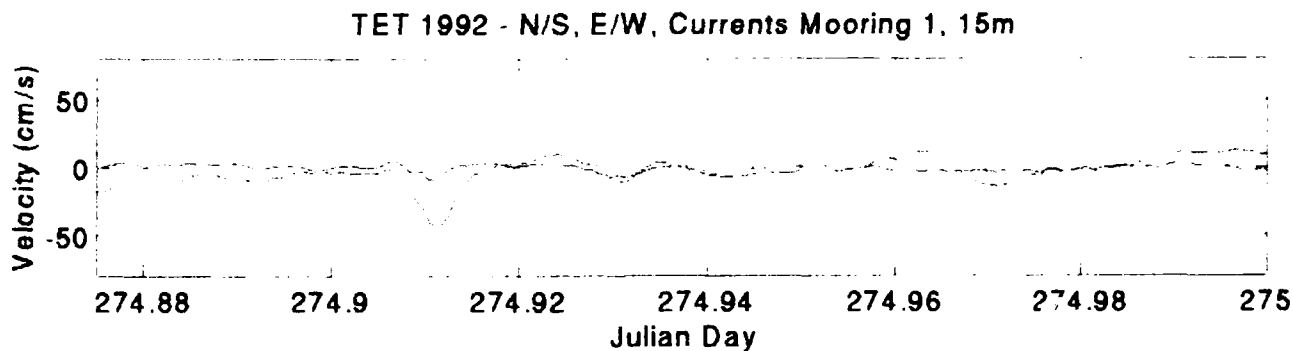
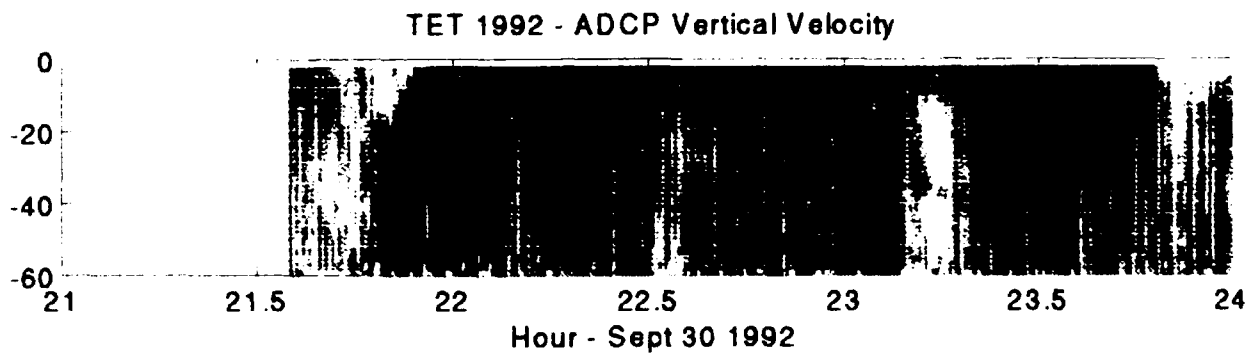
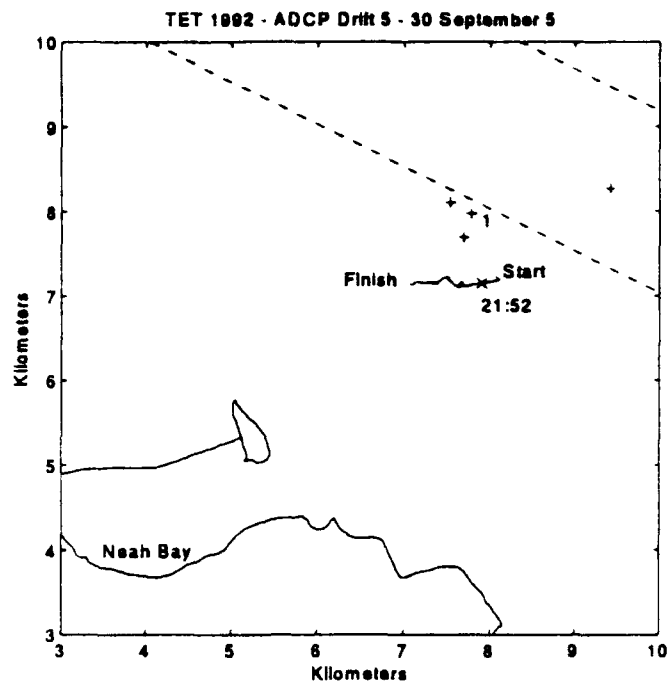


Figure 4-12 Map of ADCP Drift (top) along with Vertical Current from ADCP, Horizontal Current at 15 m from Mooring 1 and ADCP Current at 15 m.

Table 4-1 **Parameters of Observed Soliton-like Internal Waves**

Julian Day	Time UTC	Prop Speed (cm/s)	Prop Direct (mag)	Wave Length (m)	Wave Amplitude (m)
267	21:35	43	168	203	18
268	03:07	100	115	263	11
269	19:12	199	246	885	32
269	19:40	48	100	500	28
269	22:33	51	243	251	50
270	08:52	125	116	1720	44
271	09:21	195	258	762	14
271	21:35	41	149	514	22
273	13:55	56	224	463	25
273	19:55	43	242	856	19
274	09:50	74	123	445	16
274	21:50	63	210	518	25
275	12:43	30	114	736	24

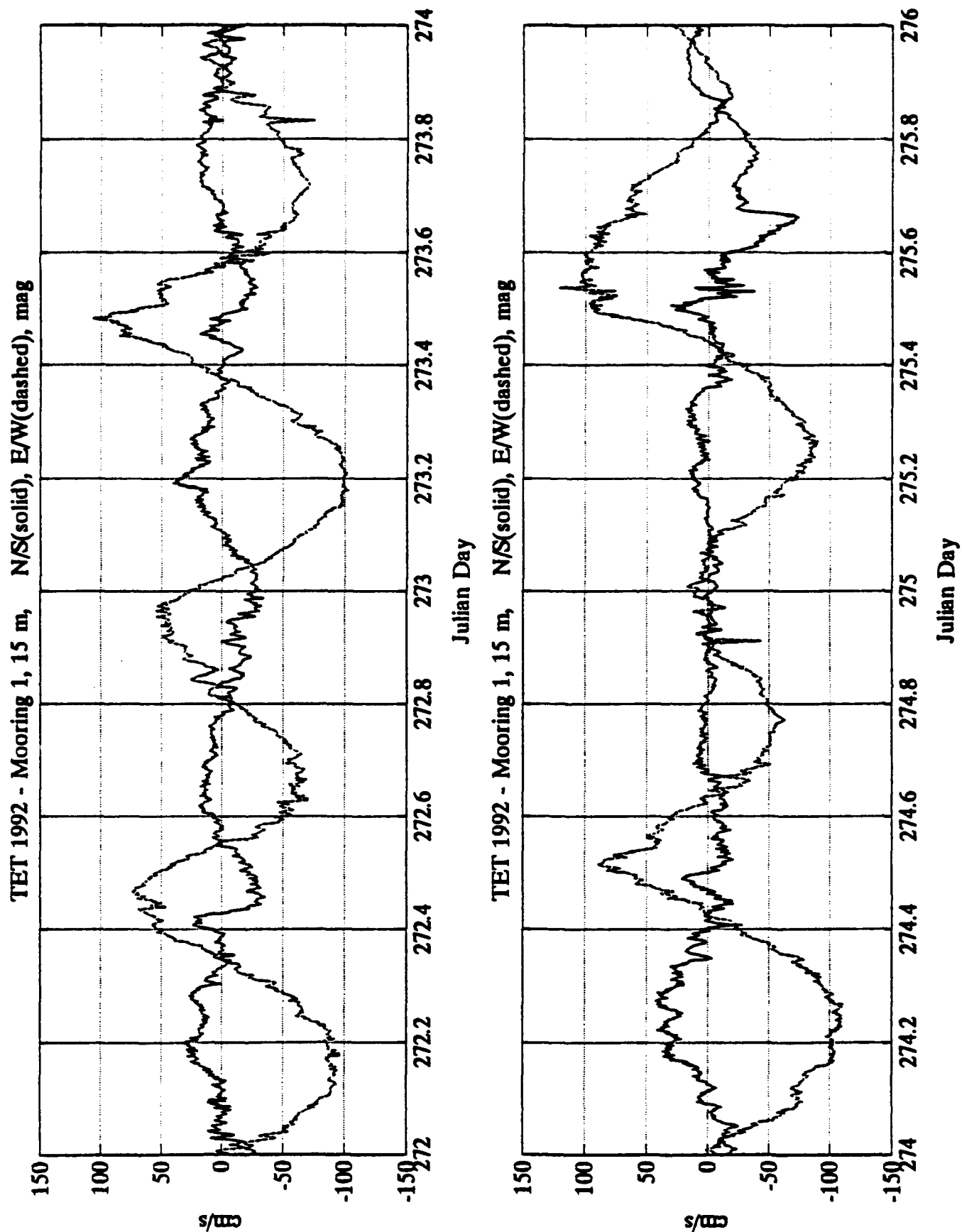


Figure 4-13 Four-Day Time Series of Alongshore (E/W) and Across-Shore (N/S) Current Velocity at 15 m, Mooring 1.

The intensity of the stratification plays a critical role in defining the SIW. Since the stratification seen by the thermistor string varies considerably with the tide (Section 4.1.2) this may be the mechanism that links the SIW to the peak flood tide. There may be other possibilities too, in that the occurrence of SIW's is also associated with the passage of fronts which could provide increased vertical density gradients that promote stronger SIW activity.

The propagation speed of the SIW's can be estimated by subtracting the mean tidal current from the observed velocity of the SIW. The velocity of the SIW (in a vector sense) is estimated by the timing of its passage past the mooring array and the mean tidal current is obtained by low pass filtering the current time series with a cut off frequency of 1 cycle per hour. The propagation speed of the SIW's ranged from 40 to 125 cm/s with a median value of 56 cm/s. The direction was quite evenly distributed between westward and southeastward with some waves traveling directly onshore (Figure 4-14). Most of the SIW's (9 out of 13) occurred on the flood tide with six propagating westward and five travelling southeastward.

Thus SIW's are seen to occur frequently at the TET site with occasional strong and distinct associated velocity signals. They can be propagating in either along-shore direction with a slight on-shore component. Expected propagation speed is 60 cm/s but they can be significantly faster. The SIW's generally (70% of the time) occurred near the peak flood tide.

4.3. Fronts

The passage of fronts, defined here as a rapid change in the velocity or temperature structure of the water column, is a common occurrence in the study area. They can be distinguished from SIW's because fronts typically transit part of the mooring producing a signal that is not a "pulse" as much as a transition to a different current regime. Surface expression of these fronts were quite visible in this and previous year's field operations. The structure of these fronts can be quite abrupt, showing rapid changes in the upper layers both temporally and spatially. An example of this is shown in Figure 4-15, which shows a 4.8 hour window of the alongshore and across-shore current velocity on day 268. The upper plot shows the velocity time series of the

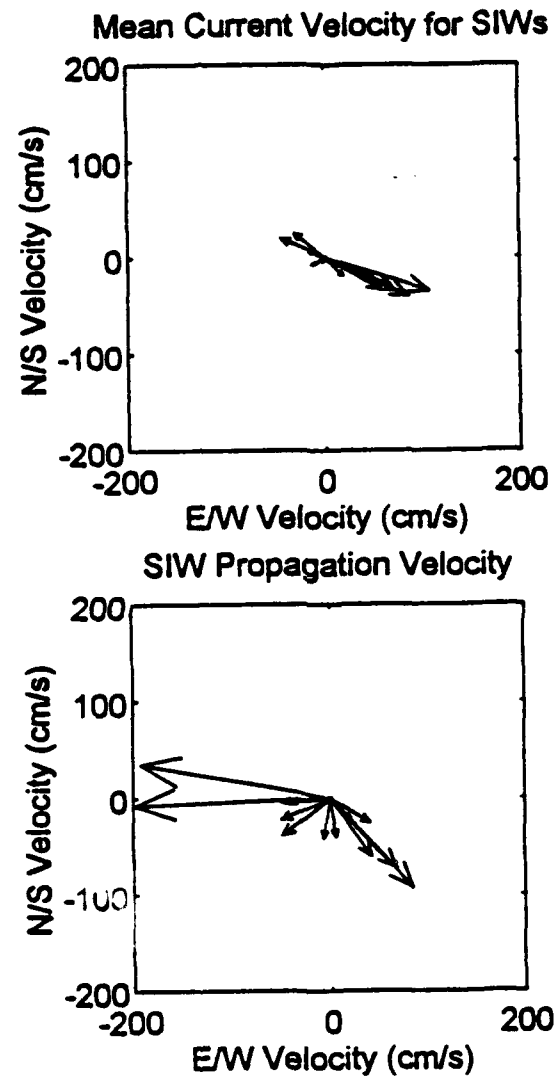


Figure 4-14 Mean Current Velocity for SIWS and SIW Propagation Velocity

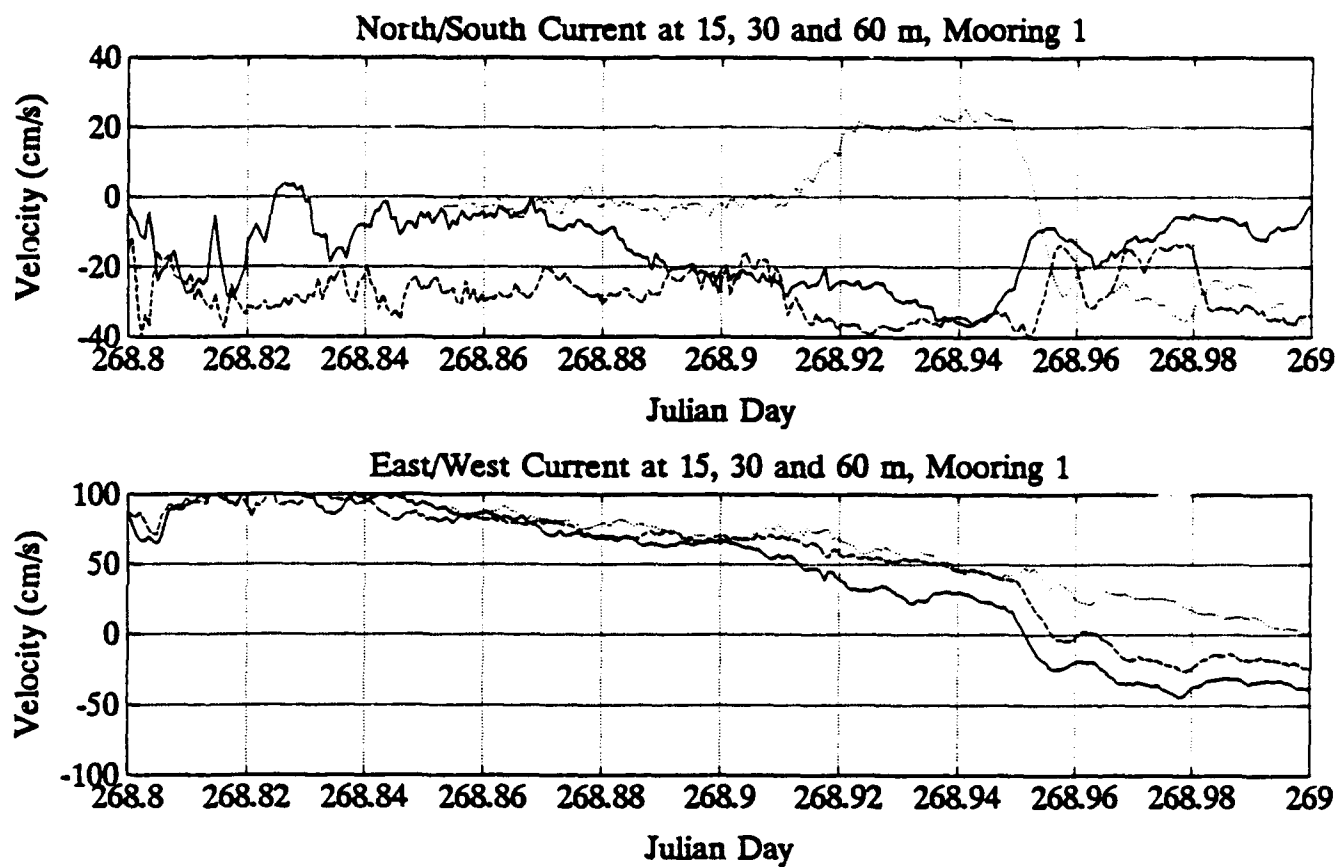


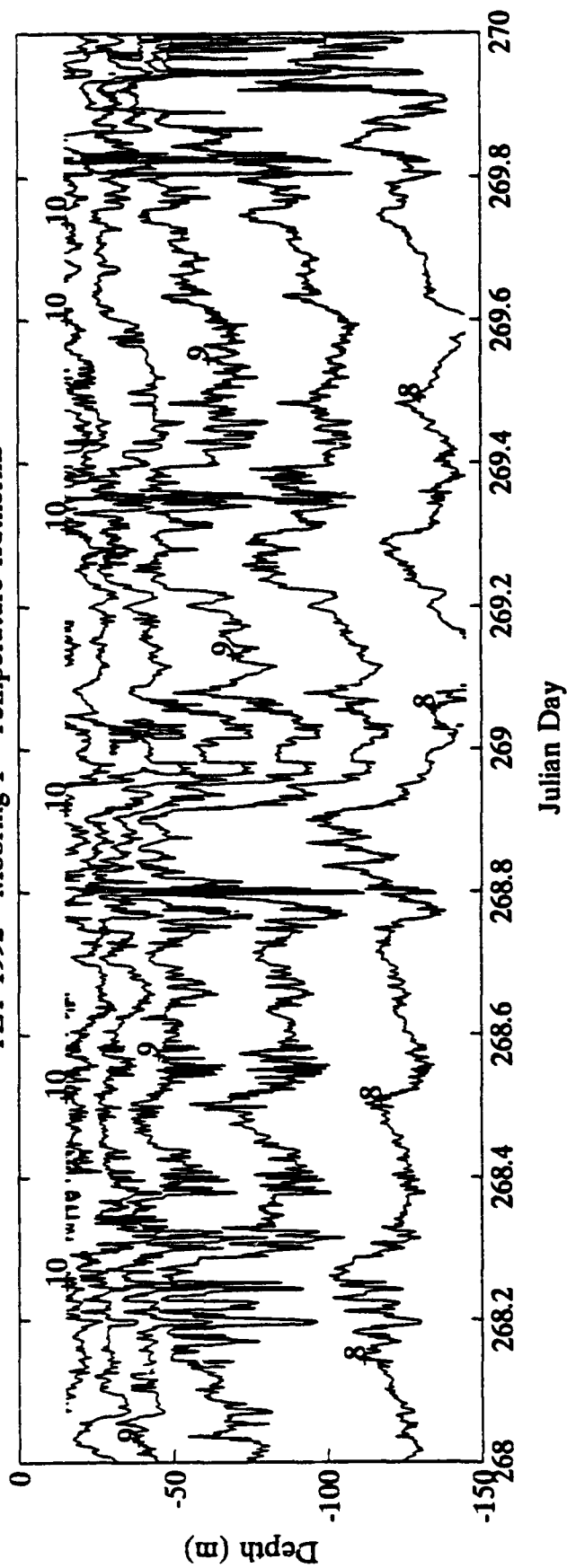
Figure 4-15 Time Series of Current Velocity at 15, 30 and 60 m, Mooring 1, Julian Day 268.8 to 269.0: (a) Across-Shore (N/S) Current Velocity and (b) Alongshore (E/W) Current Velocity

across-shore (N/S) current from the upper meter on Mooring 1. The across-shore currents were weak at 15 and 60 m depth when $t=268.86$, but the 30 m currents were southward at 30 cm/s. The 15 m current then aligns with the 30 m current and the deeper 60 m current increases to 20 cm/s northward resulting in a 55 cm/s shear over the 30 m depth interval. As the front passes the currents at all three depths realign around -20 cm/s. There is only a slight increase in vertical shear in the East/West component as the front passes (lower panel). The rapid decrease in the N/S current at 60 m takes place over a 10 minute period. The passage of this front can also be seen in a larger context in Figure 4-16 where the water column warms up considerably as the front passes. There is a change in depth of the 8.5°C isotherm of approximately 70 meters on either side of the front. This magnitude of change can often be seen associated with the tidal variations and in the temperature and current structures as shown in the figures in the data appendices.

A front marking a transition into a different stratification appeared to have moved past the moorings on day 275 (Figure 4-17). The character of the water column changes at approximately $t=275.7$ as there is a precipitous drop in the isotherms throughout the water column. After the passage of this front the water column is considerably warmer and the stratification is distributed evenly over most of the water column instead of being concentrated near the upper layer. This even distribution persists at least until the end of the study period a day later. The velocity signal associated with this frontal passage is seen in Figure 4-18 (note: no data was available from the 30 m current meter). A sharp change in the N/S current at 15 meters is present but a drop in the deep current (145 m) does not take place until 1.3 hours later and no strong signal is evident at 60 m. This is consistent with the change in the temperature distribution which occurs later at depth also.

The effect of the passage of fronts on magnetic and electric fields is not known but in a region such as the test site where strong fronts are common it is important to note their presence. Since the strength of the velocity changes is similar to the magnitude of SIW's, a similar signal might be produced in those fields with the rapid enough transit of a front.

TET 1992 - Mooring 1 - Temperature Isotherms



TET 1992 - Mooring 1, 15 m, N/S(solid), E/W(dashed), mag

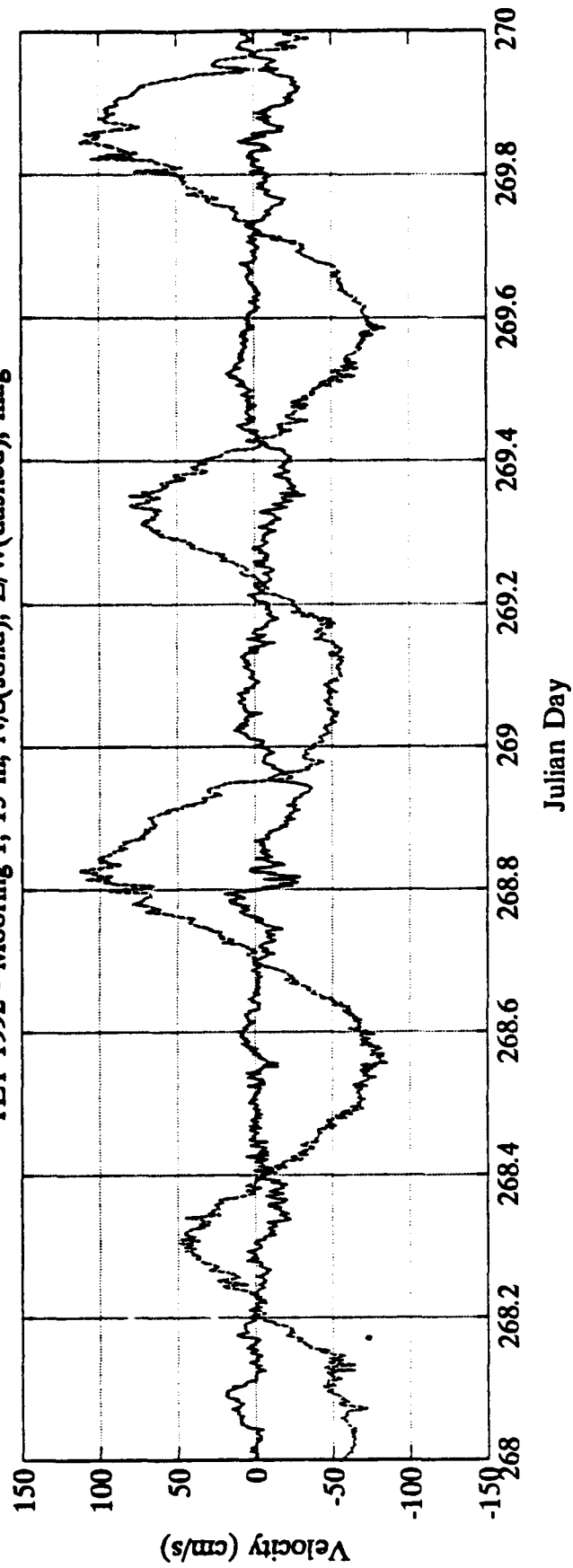
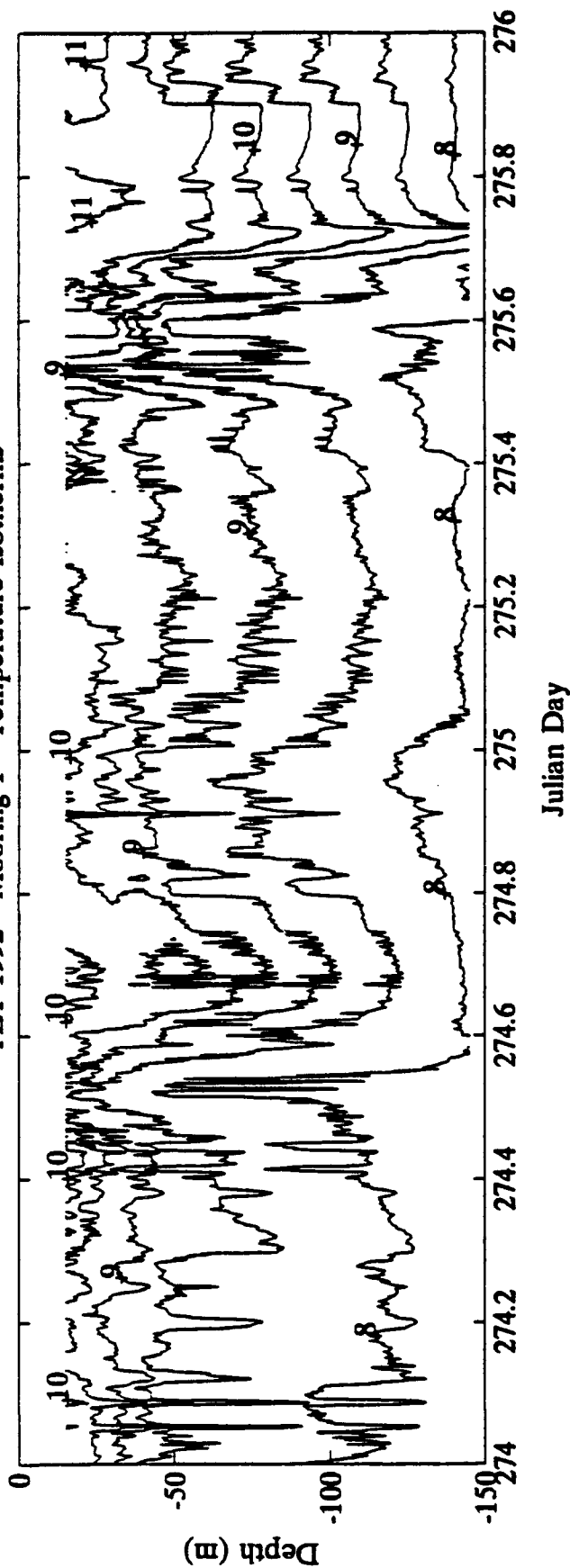


Figure 4-16 Time Series of Temperature Isotherms and currents at 15 m depth, Mooring 1, Julian Day 268 to 270

TET 1992 - Mooring 1 - Temperature Isotherms



TET 1992 - Mooring 1, 15 m, N/S(solid), E/W(dashed), mag

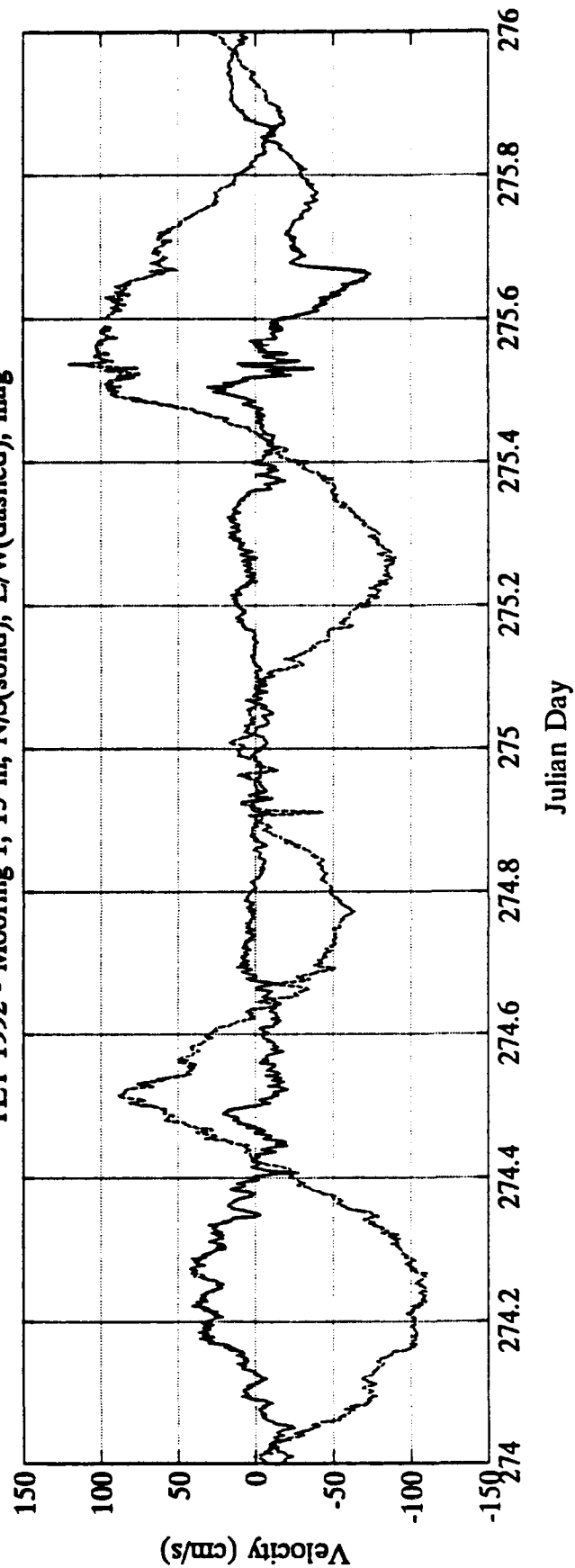


Figure 4-17 Time Series of Temperature Isotherms and Currents at 15 m Depth, Mooring 1, Julian Day 274 to 276

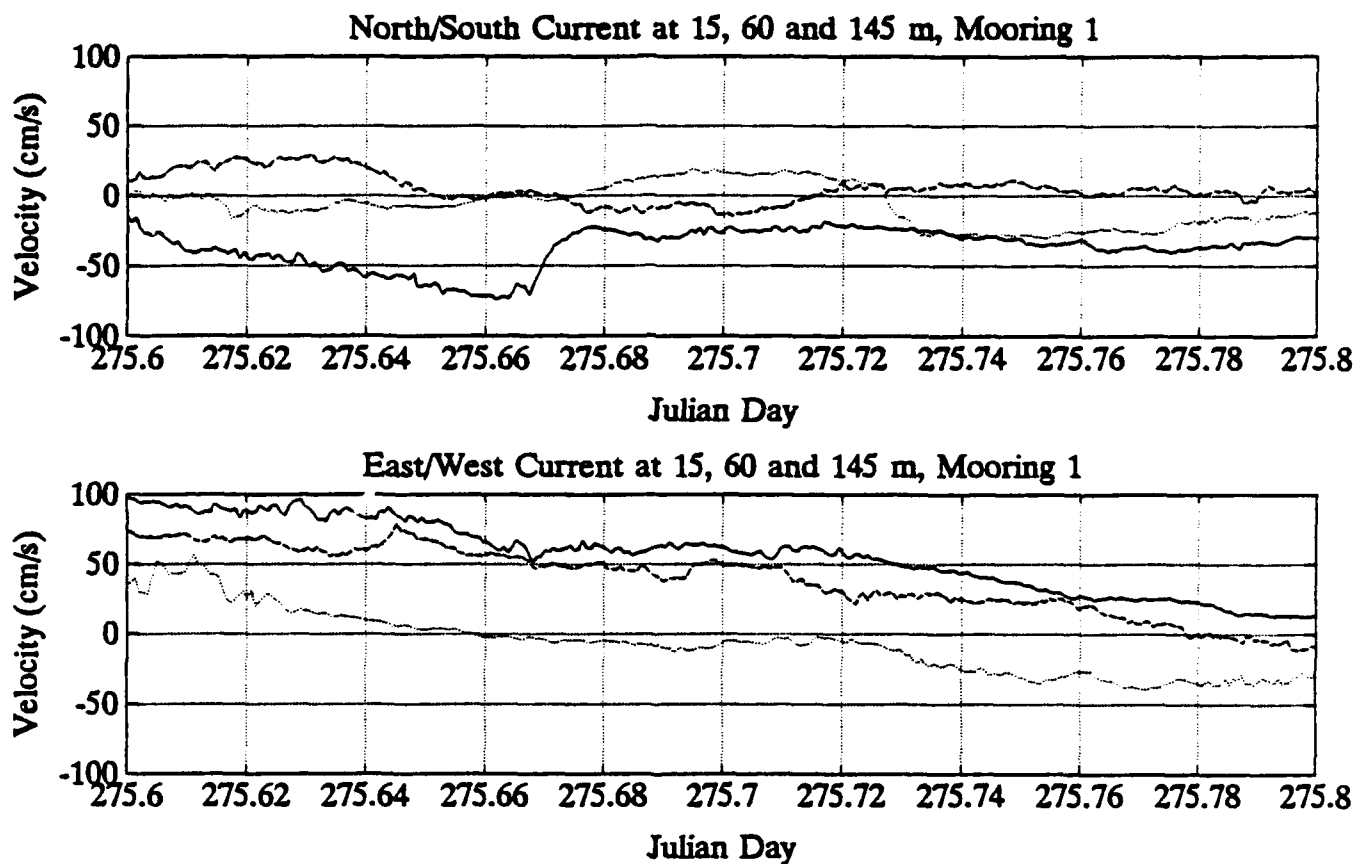


Figure 4-18 Time Series of Current Velocity at 15, 60 and 145 m, Mooring 1, Julian Day 275.6 to 275.8: (a) Across-Shore (N/S) Current Velocity and (b) Alongshore (E/W) Current Velocity.

4.4. Bottom Boundary Layer

The Bottom Boundary Layer (BBL), considering the various TET sensor technologies being mounted on or just above the sea bed, is an important area for study. An analysis of the 1991 TET EF data (Bentson et al, 1992) showed a loss of coherence between separate horizontal components of electric field during periods of strong tidal flow in the near bottom currents. Associated environmental measurements (Gunn et al, 1992) demonstrated a sharp increase in turbulent activity in the BBL during these strong tidal flows. This connection between physical processes in the BBL and sensor performance motivated the present study of site specific BBL processes. In the present study a concerted effort was made to understand observed variability in the BBL, not limited to turbulent activity, since only with such broader understanding can one evaluate the importance of BBL processes to specific sensor performance problems. In pursuit of such understanding we discuss below turbulence, depth limited internal wave signals and secondary flow processes which occur in the BBL as well as estimate the drag coefficient and bottom stress which are important for a full characterization of the BBL so these measurements can be related to other sites.

In 1992 one of the current meter moorings (Mooring 4) was deployed to investigate the structure of the BBL. This mooring was equipped with current meters at heights of 1, 5 and 10 m above the bottom. Data from this mooring were recovered for the period September 21 (Julian day 265) through October 3 (Julian day 277). The current records from this mooring are discussed in this section, with comparisons to similar bottom boundary observations made in 1991 (Gunn et al 1992) and the occurrence of a rectified secondary flow at the semi-diurnal tidal frequency.

Time series of the alongshore current from the current meters at heights of one, five and ten meters are shown in Figure 4-19. These three records clearly show the semi-diurnal tides, with strong coherence between all depths. Maximum current speeds at 10 m above the bottom are on the order of 70 cm/s, while at 1 m above the bottom they rarely exceed 50 cm/s. This is consistent with the TET BBL current observations from 1991 (Gunn et al 1992), and supports the conclusion from Gunn et al 1992 that the current shear associated with the BBL is confined to a very shallow layer (~ 1 m) immediately above the bottom (Gunn et al 1992).

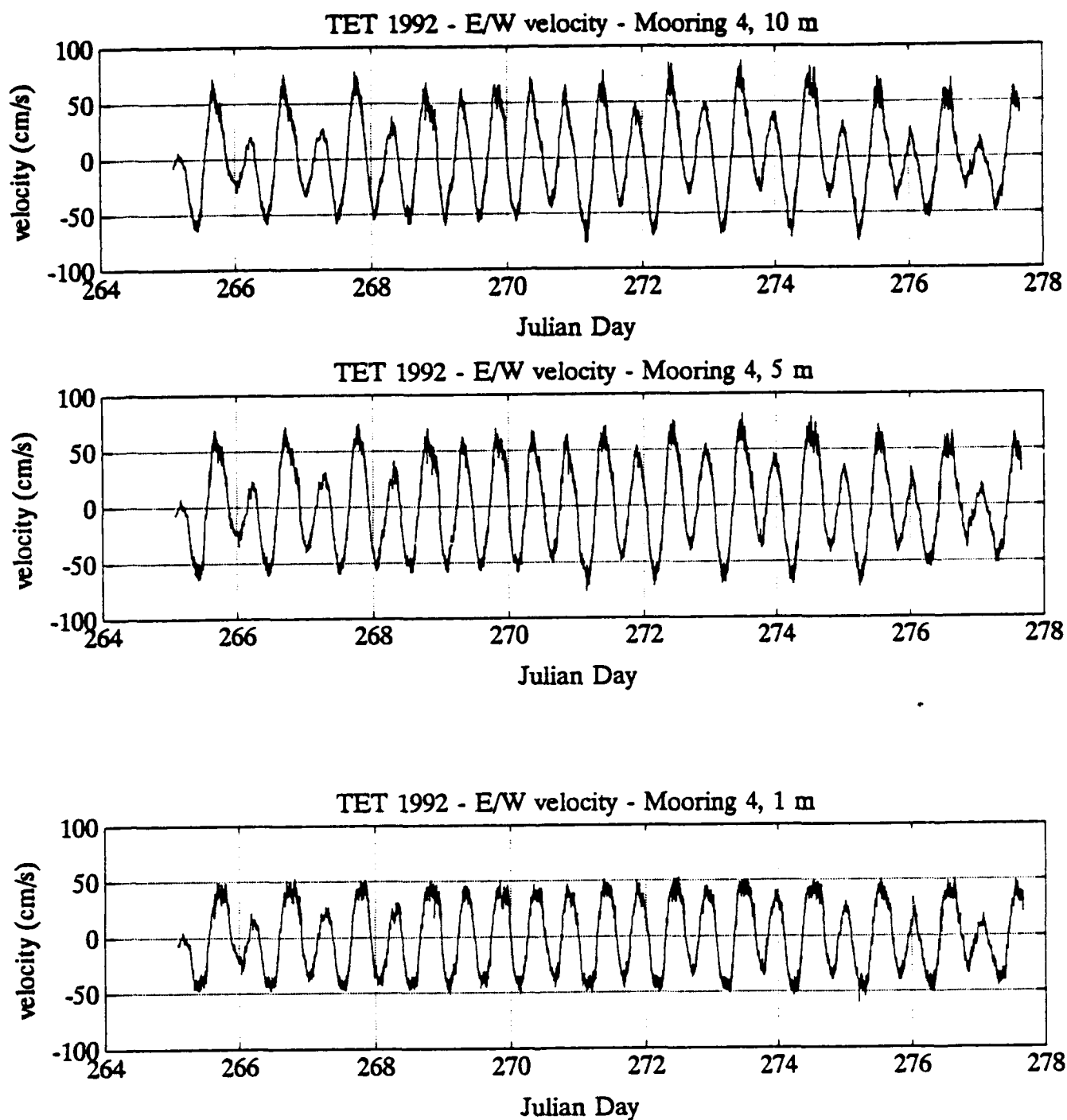


Figure 4-19 Time Series of Alongshore (E/W) Current Velocity at 10 m, 5 m and 1 m Above the Bottom, Mooring 4, Julian Day 265 to 278.

Shown in Figure 4-20 are the cross-shore velocities measured at one, five and ten meters above the bottom. The most striking feature evident in these records is the relatively strong, rectified semi-diurnal currents recorded at a height of 1 m. The data indicate a strong northward (locally offshore) flow at 1 m above the bottom during both ebb and flood tide. No similar northward flow was observed at five or ten meters above the bottom. This phenomenon is believed to be a result of a secondary boundary circulation, and is discussed in detail in Section 4.4.2.

In 1992 the BBL current meters were all set to sample at one-minute intervals. This sample rate is sufficient to provide a qualitative indication of the high frequency variability of the currents in the turbulent boundary layer. Since the time scales associated with BBL turbulence are on the order of 30 s, the present observations can not be used to evaluate the quantitative energy level of the turbulent velocities as estimated in 1991 (Gunn et al 1992). However, the velocity records shown in Figures 4-19 and 4-20 suggest a high signal variance during the periods of maximum ebb and flood. The spatial and temporal variability of this qualitative turbulent signal is discussed in section 4.4.1.

Due to the different sampling strategies employed in 1991 and 1992, the main results of the 1991 BBL analysis will be reviewed. Four current meters located at heights of one, three, four and five meters were deployed for 22 hours in 1991. The high sample rate data from the current meter at four meters above the bottom had significant high frequency ($3.3 \times 10^{-2} \text{ Hz} > f > 1.7 \times 10^{-3} \text{ Hz}$) variance in the currents associated with turbulent fluctuations. This high frequency variance was well correlated ($r=0.82$) with the mean current speed, with an exponential regression of $y=0.234 e^{0.067\bar{u}}$, where y is the high frequency variance (identified as an indicator of turbulent activity (ITA)) and \bar{u} is the low passed current speed at the same height. This result suggests that a quantitative parameter associated with the turbulent kinetic energy in the BBL can be estimated from lower frequency current observations, or even tidal current predictions (if these are available in the BBL).

Also analyzed in the BBL current records from 1991 were strong internal wave signals. Internal wave velocities were measured at heights of three and four meters, with variations on the order

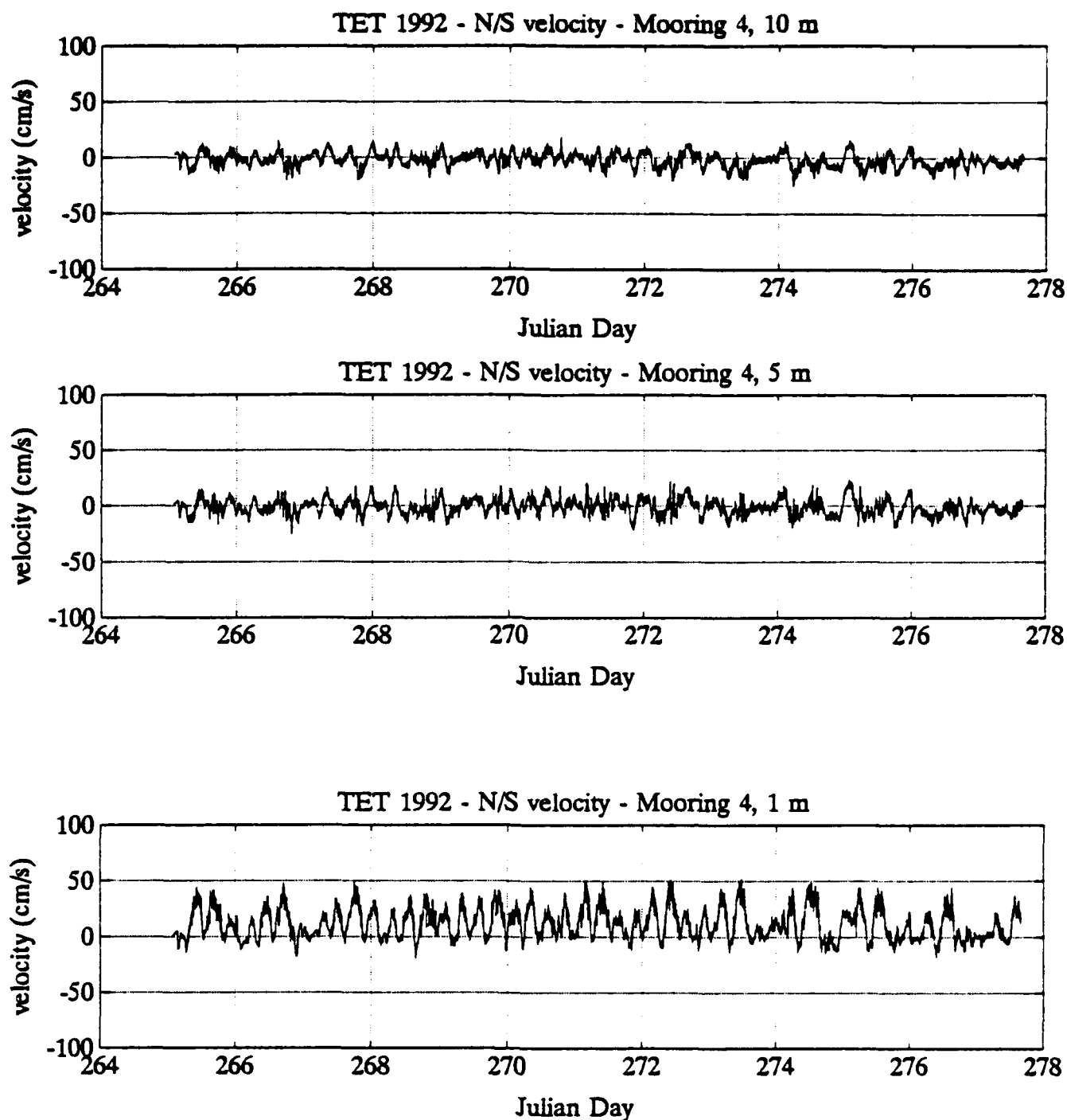


Figure 4-20 Time Series of Cross-Shore (NIS) Current Velocity at 10 m, 5 m and 1 m Above the Bottom, Mooring 4. Julian Day 265 to 278.

of ± 10 cm/s at periods between 15 and 30 minutes. Although only a 22 hour record was collected, the internal wave signatures were present throughout the $1\frac{1}{2}$ tidal cycles. The importance of separating the physics associated with high frequency turbulent velocities and internal wave induced fluctuations was also discussed. The most important distinction is that turbulent kinetic energy must be locally generated and dissipated, while internal waves can propagate, thus extracting energy within a generating region and dissipating or influencing the velocity characteristics at distant locations.

Although the current meter sampling rate in 1992 was slower (1 minute) than the fastest rate of 1991 (15 seconds), there are still strong qualitative indications of turbulent activity revealed in the 1992 BBL current observations. The different nature of the BBL at such closely spaced locations (~ 3 km) supports the need for site specific BBL measurements in future bottom mounted sensor deployments.

4.4.1. Turbulence

Turbulence is the high frequency random motion observed in fluid flows. A simple, yet accurate interpretation of turbulence is that it is a superposition of many eddies of various sizes and energies. Turbulence within the ocean plays two dominant roles with respect to ocean dynamics: 1) the dissipation of kinetic energy, and 2) the mixing and diffusion of quantities associated with the fluid (e.g. heat, salt and momentum). However, turbulence can also interfere with observations not directly related to these processes. In particular, turbulence can contribute to the background electromagnetic noise. Scaling and parameterizing the relative strength and variability both spatial and temporal, of the turbulence within the BBL will assist in the interpretation of other field observations.

Turbulence is generated where flow instabilities arise. Within the BBL, these flow instabilities are primarily associated with regions of strong vertical shear. The flow near the bottom is sheared because frictional and viscous effects result in a gradual decrease in the current speed as the bottom is approached. In a real sense, the stationary bottom acts to slow the near bottom currents. This reduction in speed is characterized by a flux of momentum to the bottom.

Momentum flux (stress) is most efficiently manifested by turbulent exchange. Once the flow becomes unstable and turbulent, turbulent Reynolds stresses work against the mean velocity shear to maintain a vertical momentum flux. Within a boundary layer driven by an oscillatory (tidal) current, the strength of the current shear and consequently the turbulence intensity also fluctuates. However, unlike the tidal currents which may act primarily in two dominant (ebb and flood) directions, the turbulence will contain velocity components in all three (two horizontal and one vertical) directions.

Temporal Variations in the BBL

Currents in the Strait of Juan de Fuca tend to be dominated by tidal variations. The dynamic characteristics of the BBL are driven by the currents above the bottom. Therefore we can expect the temporal variations of the BBL to be dominated by tidal fluctuations in the near bottom currents. Already presented (Figures 4-19 and 4-20) are the along- (U) and cross- (V) shore components of velocity measured within the BBL. Shown in Figure 4-21 are the U and V velocity components from a height of one meter for a four day period. Apparent in both U and V is the increase in small scale "noise" or turbulence during periods of maximum current speeds. To further visualize this temporal variation in the high frequency components of the current measurements, spectra were calculated.

Shown in Figure 4-22 are surface plots of the temporal variation in the high frequency ($0.33 < f < 0.5$ cpm) portion of the total velocity spectra (U+V) from the current meters located at one meter and ten meters heights. The periodic increase in high frequency energy is clearly evident, corresponding to periods of strong near bottom currents. The currents at 1 m height have significantly higher variance (energy) in this frequency band. The timing of the flat portions of the surface are significant. They occur at diurnal intervals (for this time interval) even though the peak tidal currents are principally semi-diurnal. The reason for this is that the strongest turbulence doesn't seem to occur at 1 m height if the tidal flow doesn't exceed approximately 50 cm/s. As seen in Figure 4-19 the ebb tides sometimes don't exceed 50 cm/s on every cycle (for example days 265-268) but during the stronger spring tides they do (days 268-270). The impact of this is that turbulent effects on bottom mounted sensors could depend on the strength

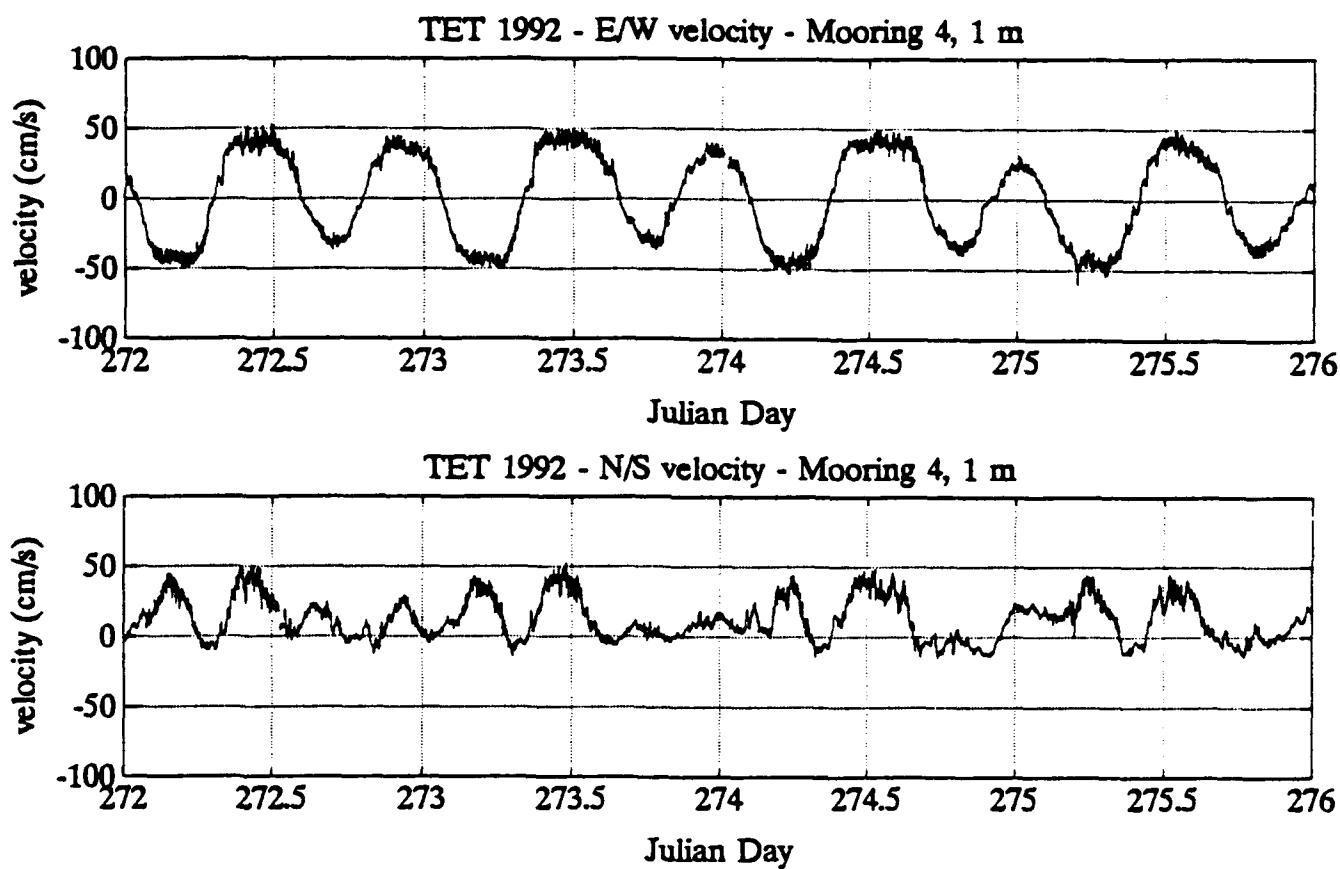


Figure 4-21 Time Series of Alongshore (E/W) and Cross-Shore (N/S) Current Velocity at 1 m above the Bottom, Mooring 4, Julian Day 272 to 276.

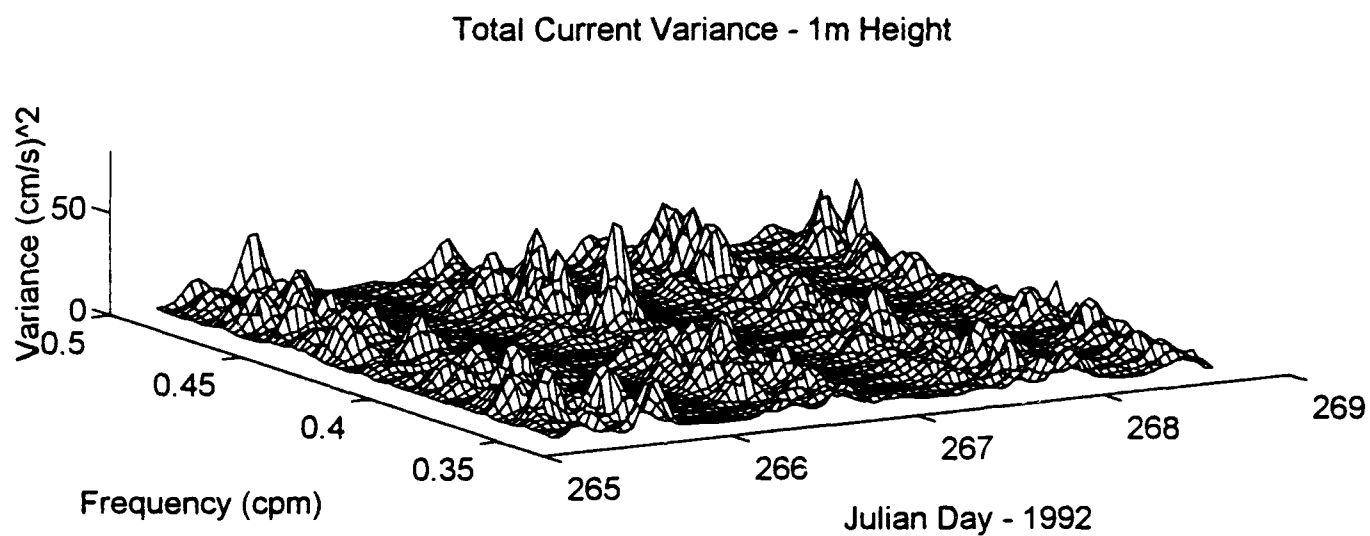
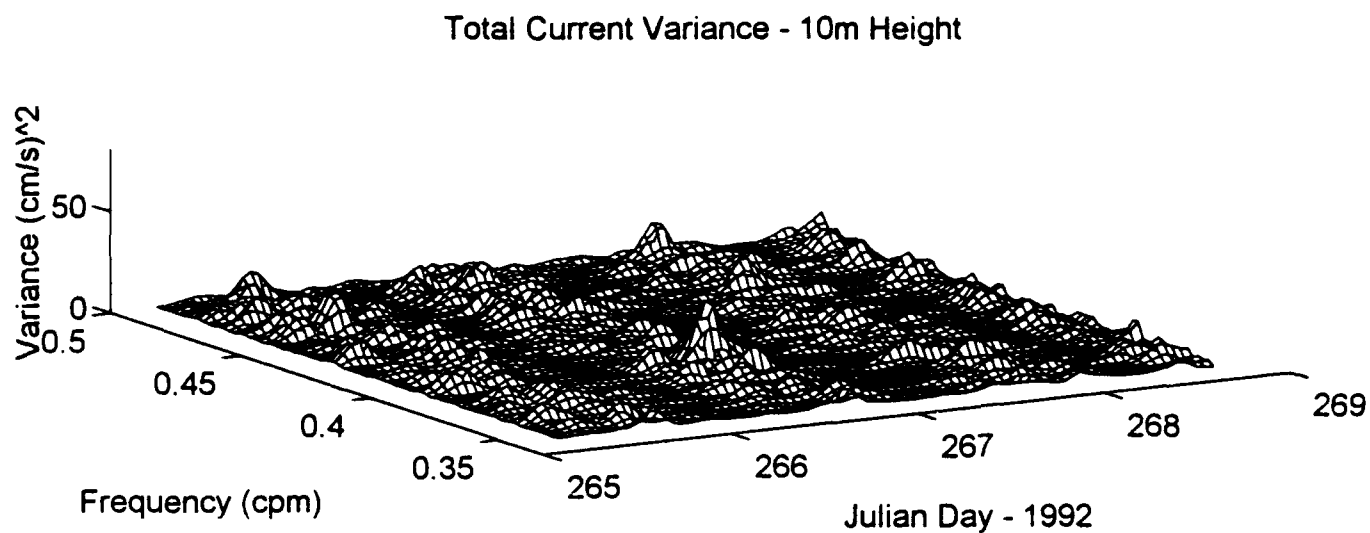


Figure 4-22 Variance-preserving spectra at 10 and 1 m above bottom on mooring4. Spectra are for total current (U+V) between 0.33 and 0.5 cpm.

and extent of this turbulent BBL which is a function of the strength of the tidal flow, shown to have significant variability. Predicting these periods requires knowledge of the lower level currents which have a slightly different phase and magnitude than the well predicted surface currents.

For direct comparison to the analysis conducted in 1991, the variance in the high frequency portion of the spectra was found to be correlated with the mean tidal currents at $r = 0.79$. Due to the lower sampling rate used in 1992, estimates of the "indicator of turbulent activity" (ITA) were not made. This increase in turbulent activity is most prominent when the near-bottom currents (i.e. height = 5 m) reach speeds of 50 cm/s. Below this speed the turbulent layer appears to be confined to a height ≤ 1 m and is significantly less energetic.

Spatial Variations in the BBL

As already discussed, the vertical structure of the BBL depends on the vertical structure of the associated current shear. Shown in Figure 4-23 are the time series for the estimated shear between zero and one meter and between one and five meters. We can therefore safely interpret that the dominant region of turbulence production is nearest the bottom of the BBL. The question of the variability of the height of the BBL can only be fully answered by vertical microstructure profiles (e.g. see Dewey et al 1988) which can provide more detailed vertical measurements. The present study was more focused on the temporal variability of the BBL than in resolving the vertical spatial variability.

The height of the BBL depends both on the energetics of the turbulence generated near the bottom and the strength of the vertical stratification. If the water is neutrally stratified, then the height of the BBL is limited only by the size and energy of the largest turbulent eddies generated. If, on the other hand, there exists stable stratification above the bottom, then the height of the BBL is further limited by the rate at which the turbulent kinetic energy at the top of the BBL can erode the stratification, through buoyancy flux. Three-dimensional turbulence, and indeed any flow with vertical components, must work against both gravity and the restoring pressure forces introduced by stratification. These constraints act to lessen the efficiency of

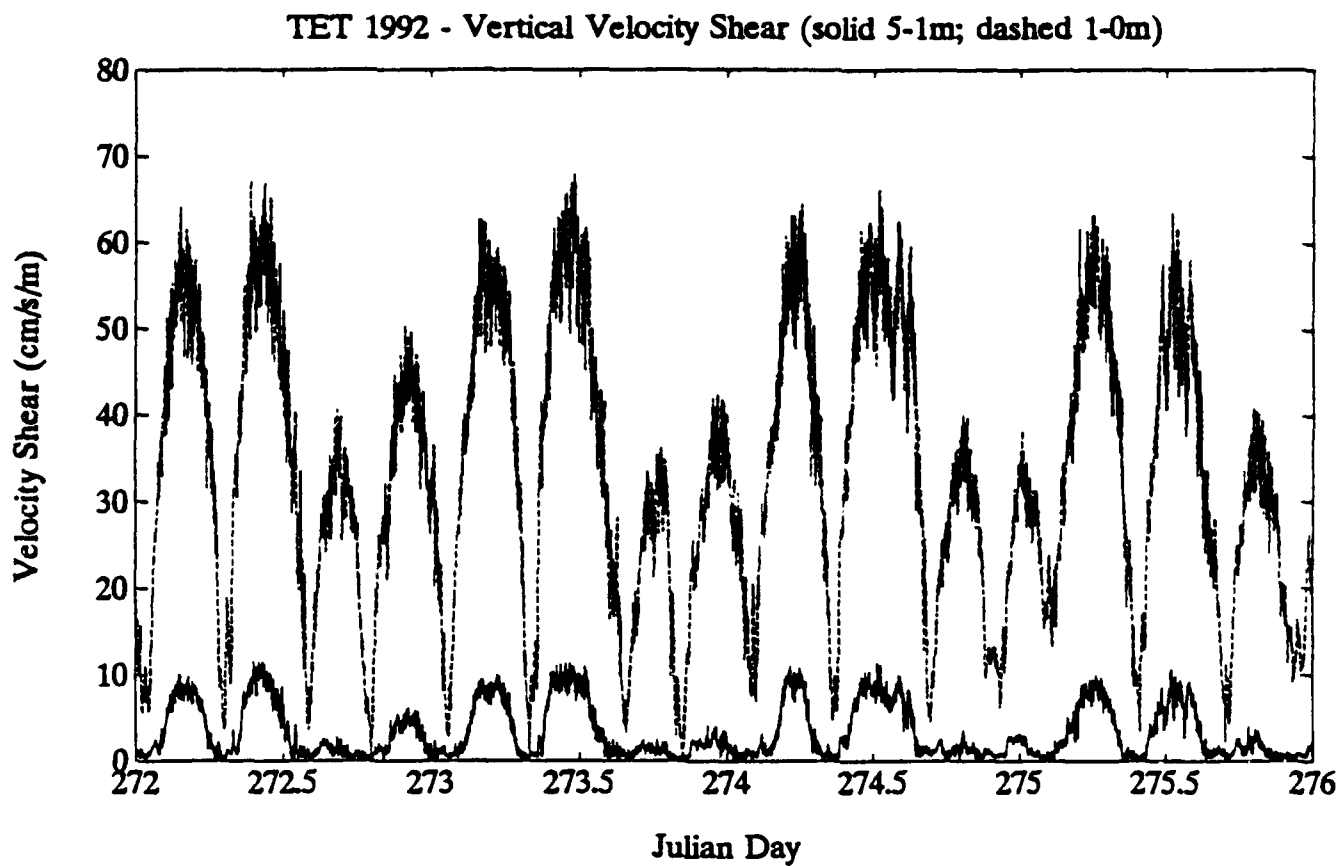


Figure 4-23 Time Series Estimated Vertical Velocity Shear Between 0 and 1 m Above the Bottom and Between 1 and 5 m Above the Bottom, Mooring 4, Julian Day 272 to 276.

turbulent mixing and limit the vertical height of the BBL.

The vertical structure of the currents can be used to estimate the magnitude of the bottom stress, and the effective drag imposed by the bottom on the interior flow. From the current measurements at heights of 1 and 5 m, a logarithmic fit with height allows an estimate of the friction velocity (u_*). Very near the bottom ($z \leq 1$ m) there is a layer where the turbulent Reynolds stress is independent of height and approximately equal to the bottom stress ($T_o = \tau u_*^2$). Within this "constant stress layer", the mean velocity shear is also nearly constant, and can be approximated by

$$\frac{dU}{dz} = \frac{u_*}{\kappa z} \quad (2)$$

where $\kappa = 0.4$ (von Karman's constant) and z is the height above the bottom. Integrating this equation with respect to Z gives the logarithmic friction law (Tennekes and Lumley, 1972).

$$U(z) = \frac{u_*}{\kappa} \ln z + C \quad (3)$$

$$C = \frac{u_*}{\kappa} \ln Z_o$$

where C is the constant of integration and is proportional to the granular roughness of the bottom and z_o is the length scale of the bottom roughness. Fitting the current measurements to this logarithmic function results in a slope proportional to the friction velocity, and therefore the bottom stress. Shown in Figure 4-24 are two plots of the slope and intercept, the first (4-24a) calculated using three heights, 0 (and $v=0$), 1, and 5 m, and the second (4-24b) using two heights, 0 and 5 m. The friction velocities resulting from these two fits are indistinguishable, supporting the conclusion that the velocity and shear structure between 1 and 5 m adds nothing to the estimate of u_* .

Although not unexpected, these results further indicate the limited vertical extent of the shear. Most of the shear associated with the BBL, and therefore that which influences the generation of near bottom turbulence, is confined to a layer of thickness on the order $z \leq 1$ m for the observed current speeds.

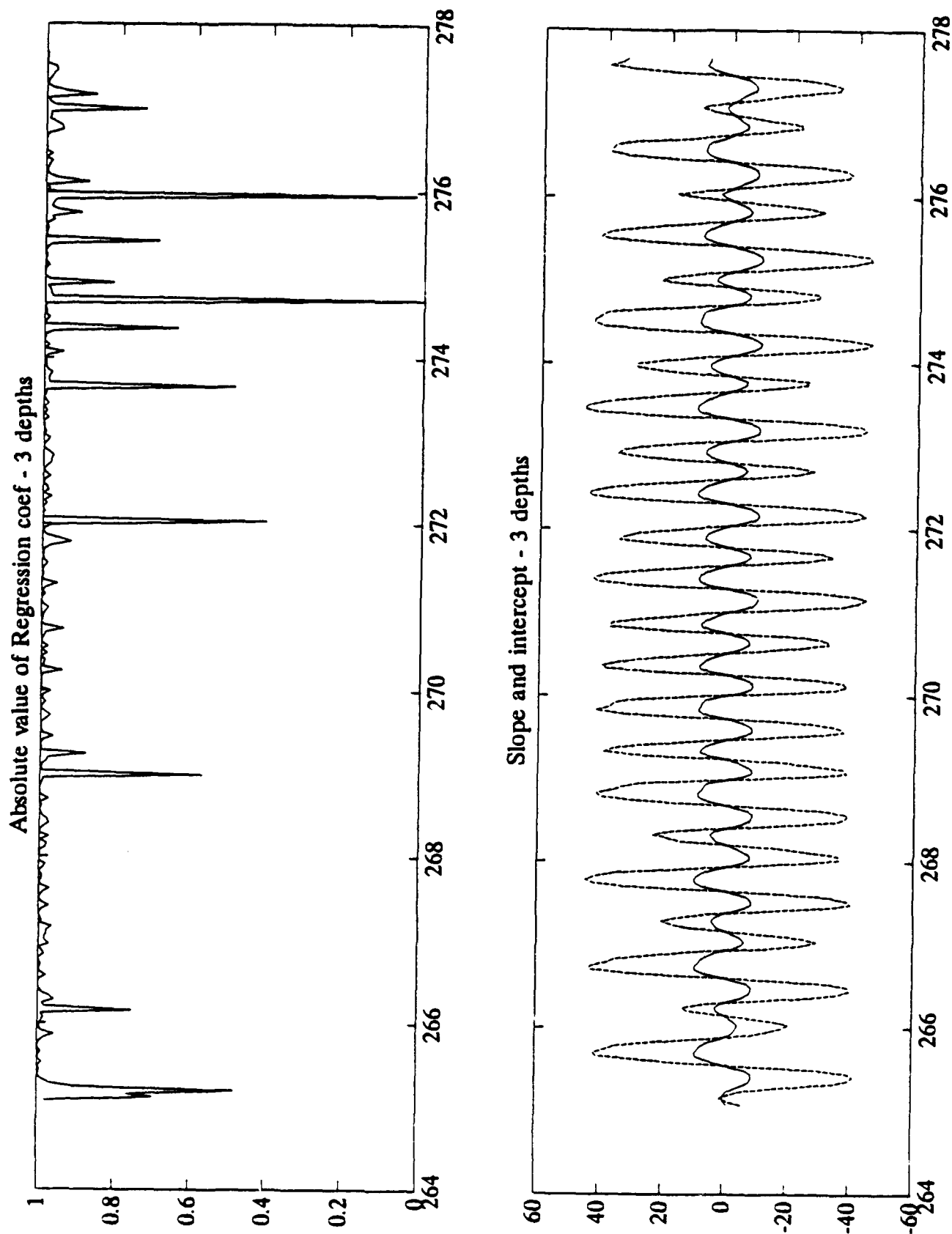


Figure 4-24a Regression Coefficient and Slope and Intercept of Log Fit of Velocity Using Three Depths (0, 1 and 5 m)

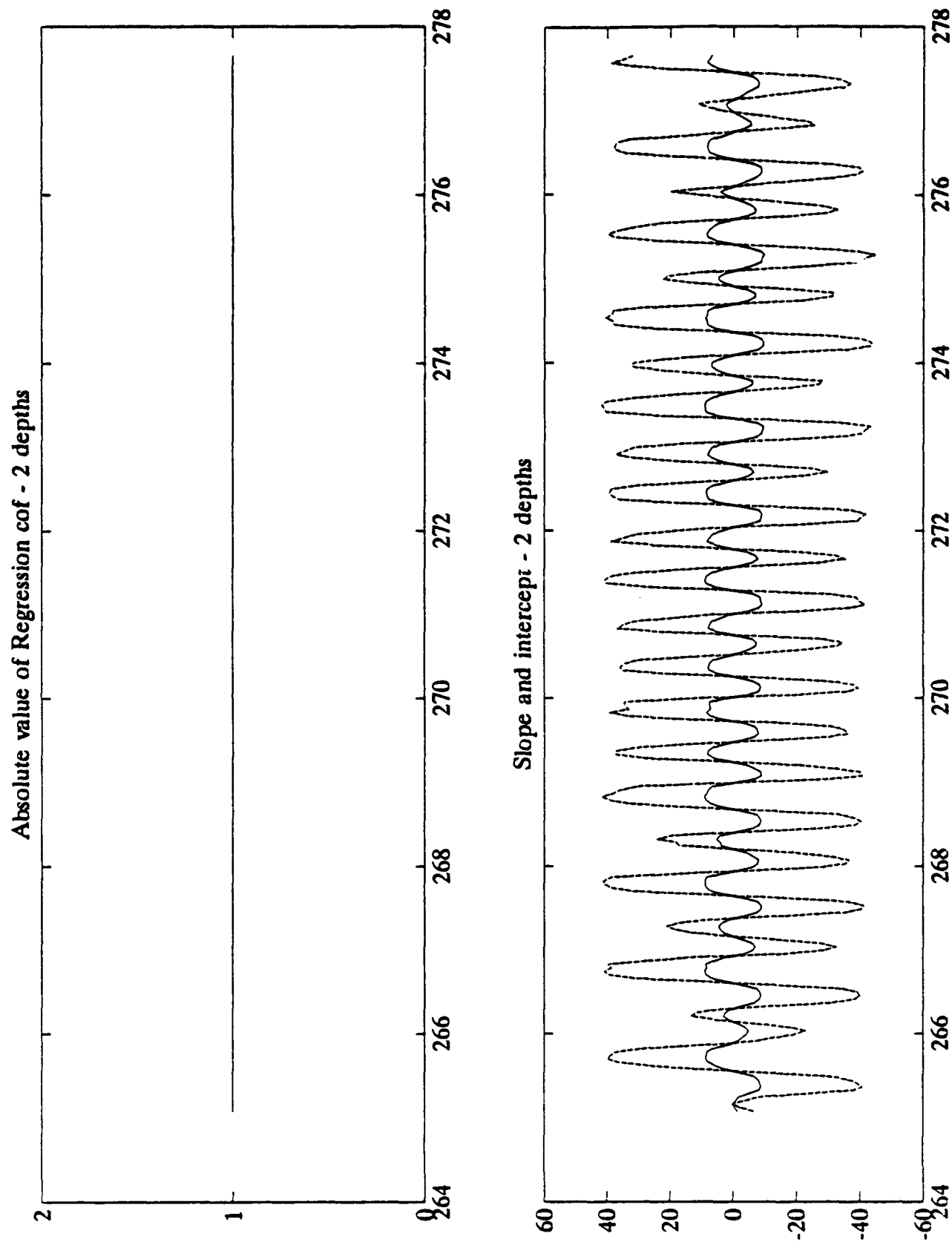


Figure 4-24b Regression Coefficient and Slope and Intercept of Log Fit of Velocity Using Two Depths (0 and 5 m)

From the friction velocity (u_*) estimates, the bottom stress (τ_o) can be calculated ($\tau_o = \rho u_*^2$). The bottom stress is closely related to the drag coefficient, defined by

$$C_D = \frac{u_*^2}{U_1^2} \quad (5)$$

where U_1 is the mean current at a height of 1 m. The drag coefficient provides a means for evaluating the local bottom flow characteristics. High drag regions are more turbulent than low drag regions. In order to estimate the drag coefficient using the above equation (eq. 4), it is necessary to measure the local turbulent field and estimate u_*^2 separately from measuring the mean current at $z=1$ m height. This was accomplished using the 15-second data collected in 1991 (Gunn et al 1992). The variance in the high frequency portion of the velocity spectra was calculated by integrating the spectra above frequencies of 12 cph. This variance was termed the "indicator of turbulent activity" (ITA) and was found to be proportional to the near bottom stress (τ_o). The drag coefficient was then approximated by

$$C_D \approx \frac{ITA}{U_1^2} \quad (6)$$

Shown in Figure 4-25 is a plot of C_D estimated from the ITA integrated above 5 and 10 cph respectively, as well as a number of theoretical predictions (White 1974) for the behavior of C_D as a function of the Reynolds number (UD/ν). The similarity between the fit of C_D calculated using the above equation (eq. 5) and the predicted curves, suggests that the ITA is in fact a reasonable indicator of turbulent-like velocity variance. This is in spite of the fact that the current meters used were not designed to measure small scale turbulent velocities. The curves are most similar at high Reynolds numbers, during periods of peak tidal currents. For high Reynolds numbers, the asymptotic value for the drag coefficient is approximately $C_D \approx 7 \times 10^{-3}$.

Using this value for a drag coefficient, the friction velocity during peak-current periods can be approximated by $u_* \approx 0.08 U_1$. This is in good agreement with the friction velocity calculated using the law of the wall eqn (2). Shown in Figure 4-26 are the two estimates of u_* regressed against each other. The coefficient of fit is $r = 0.99$. For Reynold's numbers on the order of

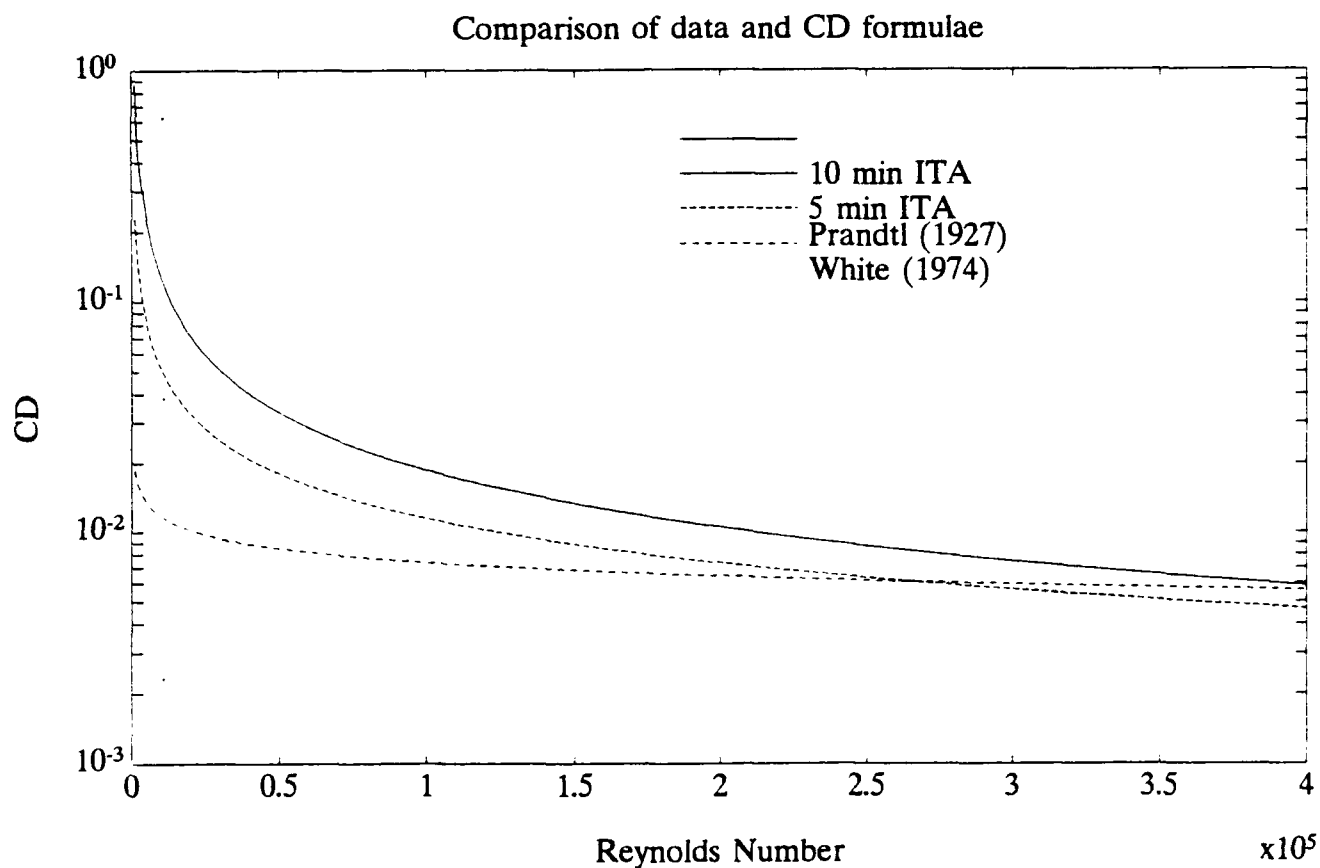
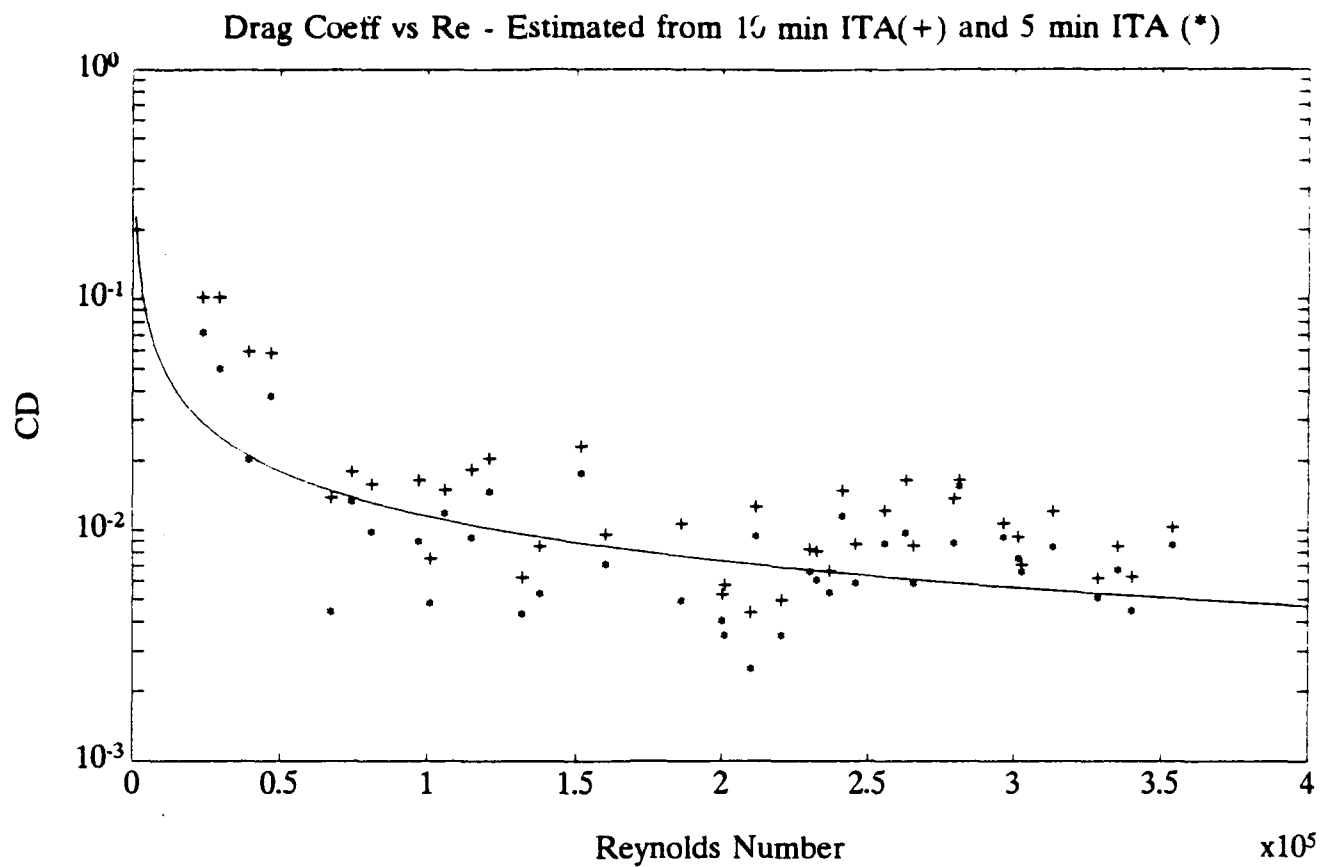


Figure 4-25 Drag Coefficient Versus Reynolds Number (a) Estimated from 10 Minutes and 5 Minutes ITA (1991 Data) and (b) Theoretical Predictions

10^5 , the flow may be transitional between laminar and turbulent. This explains the over-estimated drag coefficient during periods of weak current associated with changing of the tide.

4.4.2. Secondary Boundary Layer Flow

Observations of the near bottom currents in 1991 at the TET site revealed an interesting sequence of depth-limited internal waves (Gunn et al 1992). In 1992, the current observations collected within the BBL reveal an equally interesting phenomena, which we believe indicates the presence of a boundary limited secondary flow. The term secondary flow refers to any small component of the flow that typically flows in a direction opposite to the main flow. Shown in Figure 4-26 are plots of the U-V trace for the currents measured of $z=1, 5$ and 10 m. The strong V (northward) component in the record from $z=1$ m indicates the presence of a secondary flow.

The tidal currents which dominate all the current records for this area are characterized by alternating $\pm U$ velocities (where U in our notation is the alongshore E/W component), for example, the current record from $z=10$ m (Figures 4-19 and 4-20). The cross shore (N/S) velocities are typically weak. However, at $z=1$ m, the currents contained a strong offshore, northward velocity component during each peak along shore current period (Figure 4-27). In other words, during both ebb ($-U$) and flood ($+U$), a strong northward ($+V$) current developed. This northward current was not present at $z = 5$ or 10 m, suggesting a shallow, along bottom secondary flow.

Boundary currents can be rotated from those away from the boundary due to the influence of increased frictional drag. The two most common examples of this include the planetary Ekman transport and pressure induced secondary wall jets. Both of these phenomena are related to the fact that the balance of forces away from the boundary, where friction is weak, drives the flow in a direction quite different from that when friction is introduced (i.e. near the boundary). There are clear indications why we believe the observed currents are not a result of Ekman dynamics, and more likely suggest a local radial flow accompanied by a shallow boundary secondary flow.

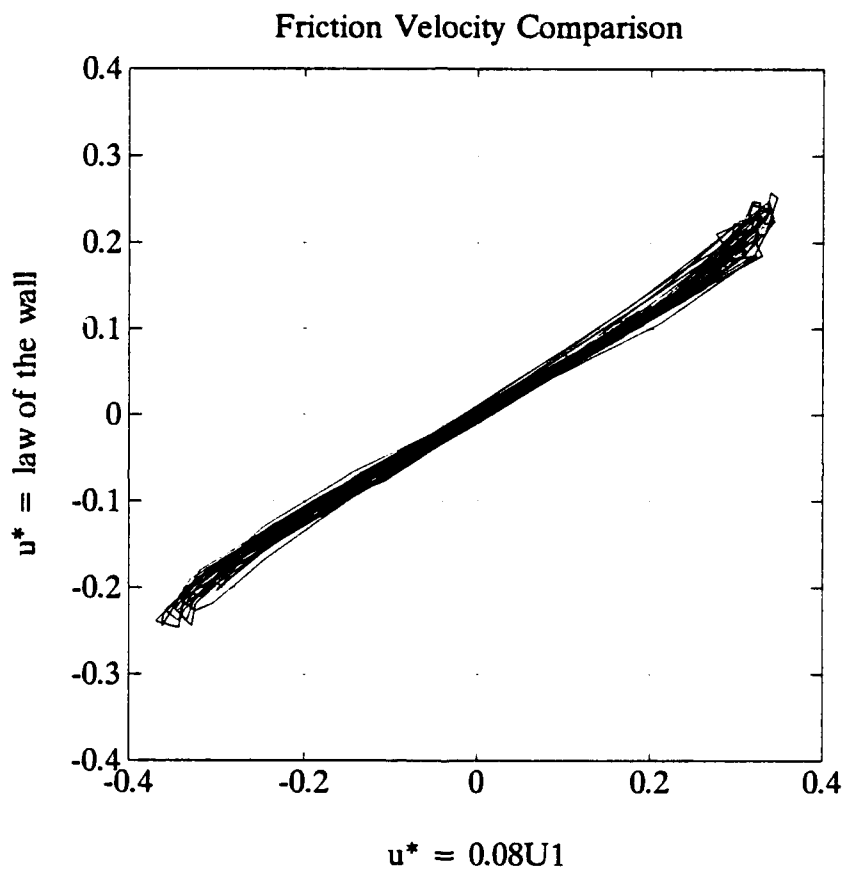


Figure 4-26 Comparison Between Two Methods of Estimates u_* , the "law of the wall" and from the ITA

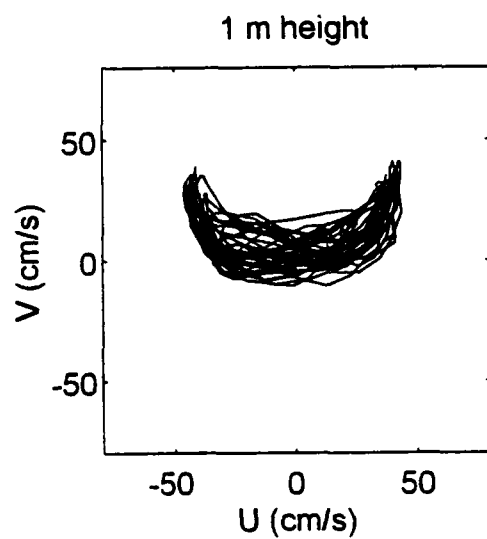
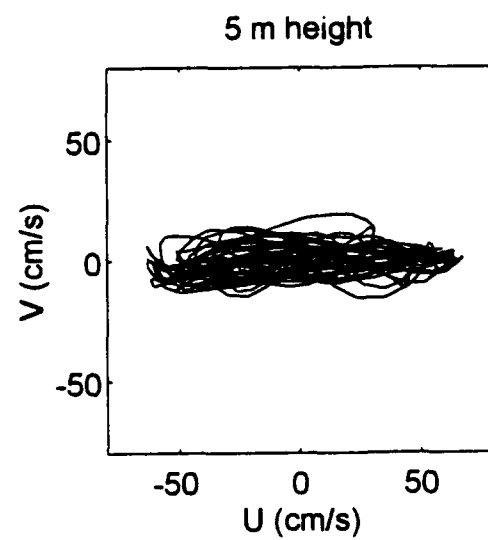
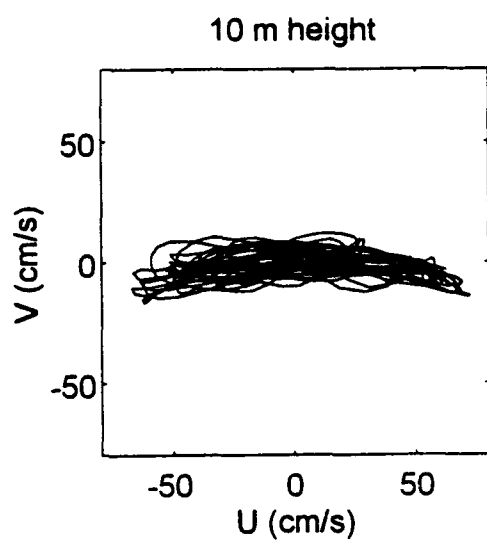


Figure 4-27 Plots of U (E/W Velocity) Versus V (N/S velocity) for Three Depths (1,5 and 20 m) on Mooring 4

Above the BBL, where frictional effects are weak, ocean flows (either tidal or geostrophic) are primarily driven by horizontal pressure gradients. Tidal currents are driven by a large scale tilt in the ocean surface, which oscillates back and forth in response to the gravitational attractions of the moon and sun. The surface tilt resulting from the gravitational forces induces a depth independent (barotropic) pressure gradient, which accelerates the water from the regions of high water to the regions of low water.

Geostrophic currents are driven by a combination of surface slopes (tilt) and inclined isopycnal surfaces (constant density). The 3D structure of the density field, induced by variations in the water temperature and salinity, can result in tilted isopycnal surfaces. These act to induce horizontal pressure gradients from regions of denser water (high pressure) to regions of lower density (lower pressure). On the rotating earth, currents appear to slowly turn towards the right (in the northern hemisphere). [In reality, the earth turns to the left under the ocean.] The apparent force which causes currents to turn is called the Coriolis force. Once the current has turned through approximately 90° , the accelerating pressure gradient becomes oppositely opposed to the Coriolis acceleration. This balance of forces, known as the geostrophic balance, is the primary dynamics for most ocean circulations (i.e. the Gulf Stream, the Kuroshio). Near the ocean bottom, friction begins to become a significant drag force, and the "balance" that exists above the bottom no longer holds. This "imbalance" causes the currents to adjust (accelerate) into a new state of balance, where the direction of flow is rotated from the currents away from the boundary. This rotation is in the sense of alignment with the pressure gradient, and in the northern hemisphere is to the left of the currents above the BBL. This current spiral results in the boundary current which is referred to as the Ekman transport within the planetary layer.

If the boundary layer secondary flow observed at $z=1$ m (Figure 4-27) were, due to Ekman dynamics, then the pattern would be quite different. The pattern traced out in the U-V plane would more closely resemble a hysteresis, (i.e. \sim) with a tilt towards negative V during negative U flow and positive V during positive U flow. The observations reveal positive V during both $\pm U$ conditions. The observations suggest the existence of a pressure gradient in the bottom

layer that is northward during both ebb and flood conditions. This condition is met if the flow above the bottom has some curvature. This case is most easily described in terms of the classic tea leaf experiment.

In an open cylinder, such as a tea cup, a rotating flow will result in a parabolic surface, with low surface elevation in the center region. Within most of the flow in the cylinder, there is a balance between the inward pressure gradient induced by the inward surface slope, and the outward centripetal acceleration induced by the rotation. However, near the bottom, where friction affects the flow, the centripetal acceleration, which has a magnitude of u^2/r , where u is the tangential velocity and r the local radius, is reduced. The pressure gradient is not reduced, and the water particles near the bottom are accelerated towards the center of the circulation. If one performs this experiment with tea leaves, which slowly sink to the BBL, one finds that the leaves pile up in the center. This inward flow occurs under both clockwise and counter-clockwise circulations. If the local flow above the BBL in Juan de Fuca Strait near our BBL mooring is curved, around a radius with a center to the north, then an internal isopycnal may become tilted upwards towards the south during both ebb and flood tide. This tilt will introduce a pressure gradient towards the north. Flow within curved portion of the circulation is maintained by the balance of outward centripetal and inward pressure forces. Near the bottom where U is reduced in magnitude, the centripetal force is less, and the inward (northern) pressure gradient accelerates the flow towards the north (positive V). Since the sense of curvature is similar for both ebb and flood, the bottom current is towards the north during both ebb and flood (Figure 4-27).

Although we have little supporting evidence to support this hypothesis (e.g. strong topographic ridge nearby that might steer the tidal current into a curved circulation), we know of no other dynamics that would consistently generate such a strong, locally confined northward flow within the BBL. The observation of this phenomena, in a similar manner to the locally generated internal wave measurements made in 1991 (Gunn et al 1992), suggest that each deployment location may exhibit unique current dynamic structures which could influence nearby sensor arrays.

4.5. Electric Field Modeling

The performance of non-acoustic sensor systems (magnetic and electric) in coastal oceanographic environments is affected by, among other things, background noise and the motion of seawater in the vicinity of such sensors is a significant contributor to the background noise. The previous subsections have characterized the hydrographic parameters associated with internal waves and the BBL. This subsection uses the environmental data to estimate the induced electric field signals at the TET site.

The complete solution to the problem of predicting the electric field from environmental measurements is a complex problem. This is particularly true for higher frequency motions (super tidal) when certain simplifying assumptions cannot be made. As the water motion becomes more complex, for example when vertical motion becomes important, the full equations are necessary and effects such as self-induction become increasingly significant. The derivation of methods and computational procedures for the complex problem are beyond the scope of this effort. Rather this Section is an attempt to examine a simplified case, discuss the assumptions required and examine the effectiveness of using the present measurements in the simplified case.

We follow the results and notations of Chave et al. (1989), Chave and Luther (1990), and Luther et al (1991). A Cartesian coordinate system is defined as $(x,y,z)=(\rho,z)$, where z is measured positive upward and is zero at the ocean surface. The symbol \hat{z} represents a unit vector pointing upward. The horizontal electric field is given by

$$\mathbf{E}_h(\rho) = C F_z \hat{z} \times \langle \mathbf{v}_h \rangle^* \mathbf{N} , \quad (7)$$

where

$$\langle \mathbf{v}_h \rangle^* = \frac{1}{\langle \sigma \rangle H} \int_{-H}^0 \sigma(z') \mathbf{v}_h(\rho, z') dz' \equiv \langle u \rangle^* \hat{x} + \langle v \rangle^* \hat{y} \quad (8)$$

is the conductivity-weighted vertical average of horizontal velocity. H is the water depth, σ is conductivity (seawater), ρ is a horizontal position vector, and $\langle \sigma \rangle$ is depth-averaged conductivity. The quantity F_z is the vertical component of electromagnetic induction. N is a small error term that depends on the velocity field over a wide area and on random effects.

The quantity C is a scale factor which depends on the structure of electrical conductivity beneath the seafloor. The parameter C varies between 0 and 1 for the two limits of an infinitely conducting and perfectly insulating seafloor, respectively. In the deep ocean, C is predicted to lie between 0.9 and 1.0. Near coastlines, C is expected to vary over a wider range. For example, Spain and Sanford (1987) measured values of C as low as 0.5 in the Florida Straits. In the calculations described here, we take $C=0.9$ as a compromise between deep-water predictions and the possibility of lower values that have been reported in a few shallow-water areas.

Figure 4-28 shows a set of four conductivity profiles provided by four CTD casts from the TET 1992 measurement program. A smooth-fitting function of the form

$$\sigma_s(z) = \sigma_0 [1 + \delta \exp(-z/z_c)] \quad , \quad (9)$$

is overlaid on the conductivity profiles, where $\sigma_0=3.47$ S/m, $\delta=0.13$ S/m, and $z_c=30$ m. The variations of the individual profiles from the smooth function, $\sigma(z)-\sigma_s(z)$, are less than 0.1 S/m, or less than 3% in amplitude. As a result, the conductivity-weighted integral in Equation (7) is almost equal to the barotropic velocity. Baroclinic (depth-dependent) velocities are almost entirely filtered out.

We can see this filtering effect in Figures 4-29 to 4-32. Figure 4-29 shows the eastward component of current u from Mooring 1 from 15 m and 145 m depth. In addition, the conductivity-weighted depth-averaged current component $\langle u \rangle^*$ given by Equation (7) is superimposed. We can easily see that the depth-averaged current is much smoother, and is dominated by the barotropic tide. Short-period motions have been filtered out. Figure 4-30 shows a blow-up of the current time series. The eastward current u is shown from depths 15, 30, 60, and 145 m, along with the depth-averaged component $\langle u \rangle^*$. In particular, note the three sharp spikes in the 15 m record at the approximate time 269.82. These spikes probably correspond to a soliton internal wave packet event, and are also visible in the 15 m temperature record (see Figure 4-31). However, these spikes are almost completely filtered out in the depth-averaging process, as can be seen in Figure 4-30 by comparing the thick and thin solid curves.

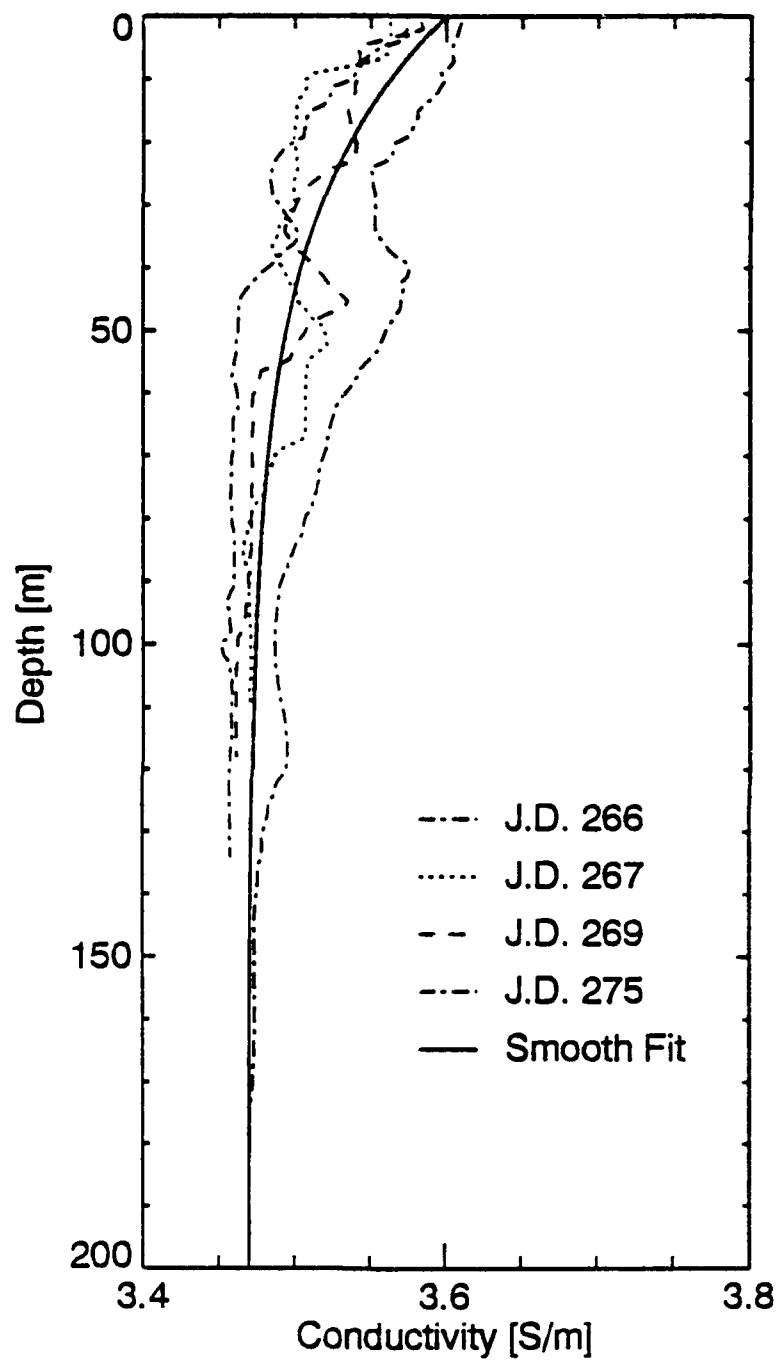


Figure 4-28 Conductivity Profiles from Four CTD Casts, Along with a Smooth-Fitting Function Given by Equation (3)

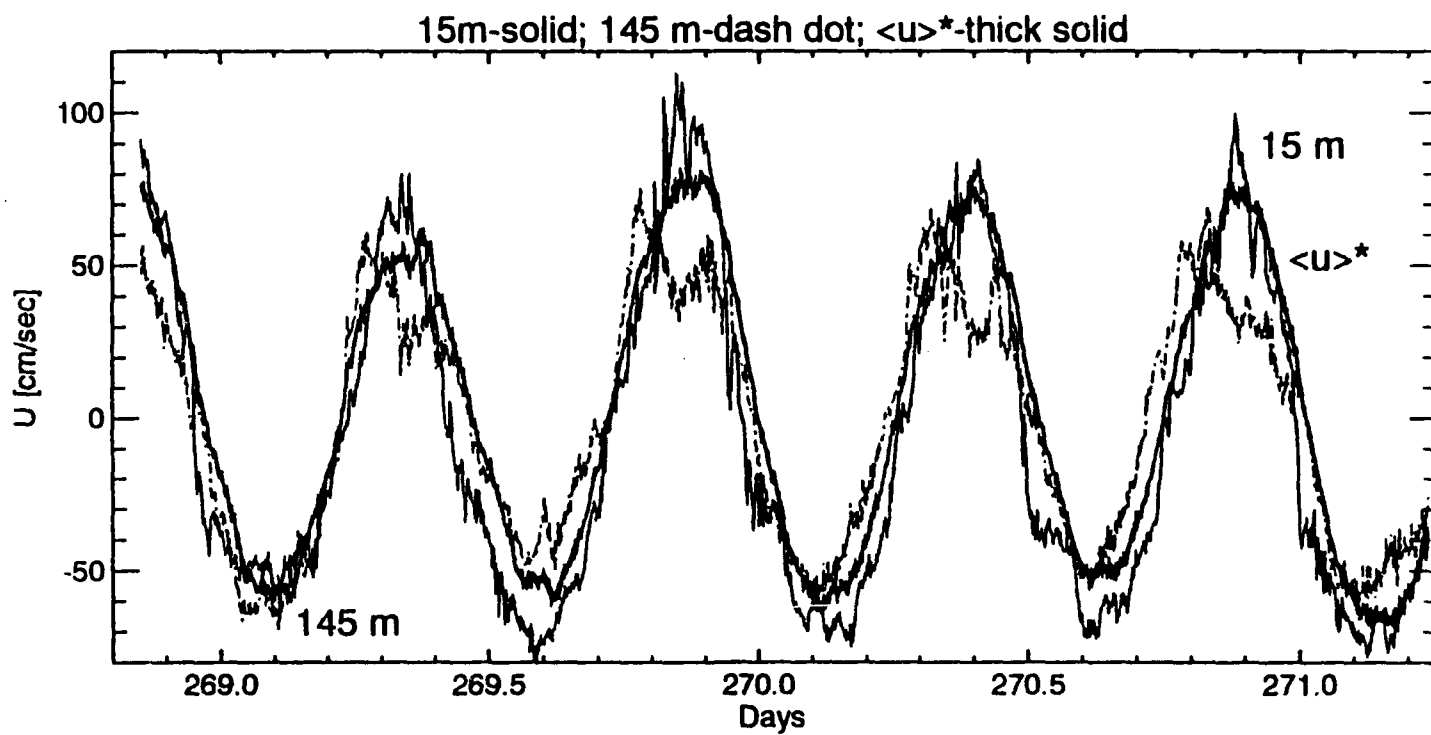


Figure 4-29 Eastward Component of Velocity at 15 m (Thin Solid) and 145 m (Thin Dash-Dot) Depths. Thick Solid Curve Shows Conductivity-Weighted, Depth-Averaged Velocity. Note That the Depth-Averaged Record is Much Smoother.

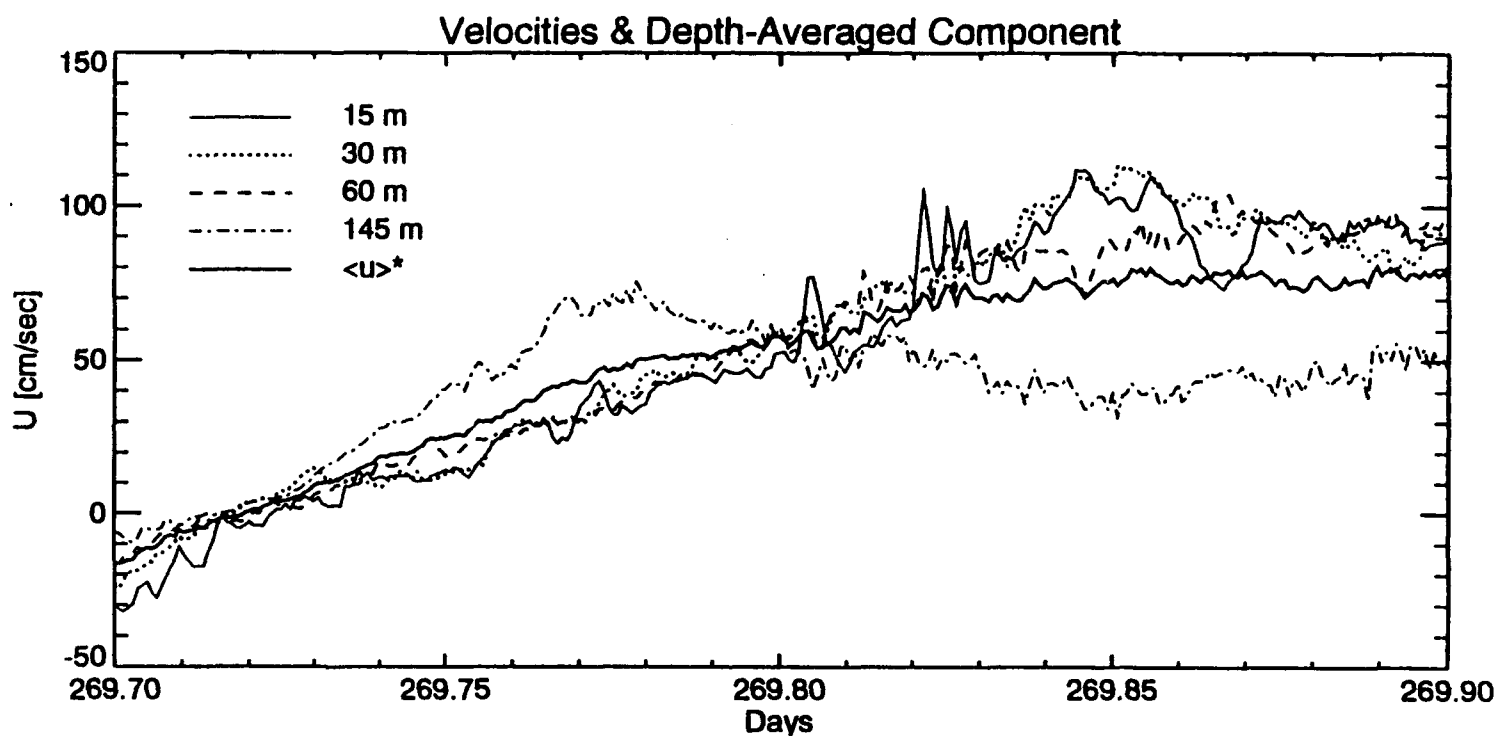


Figure 4-30 Eastward Component of Velocity at Depths 15, 30, 60 and 145 m. The Thick Solid Curve Shows $\langle u \rangle^*$, the Conductivity-Weighted, Depth-Averaged Current.

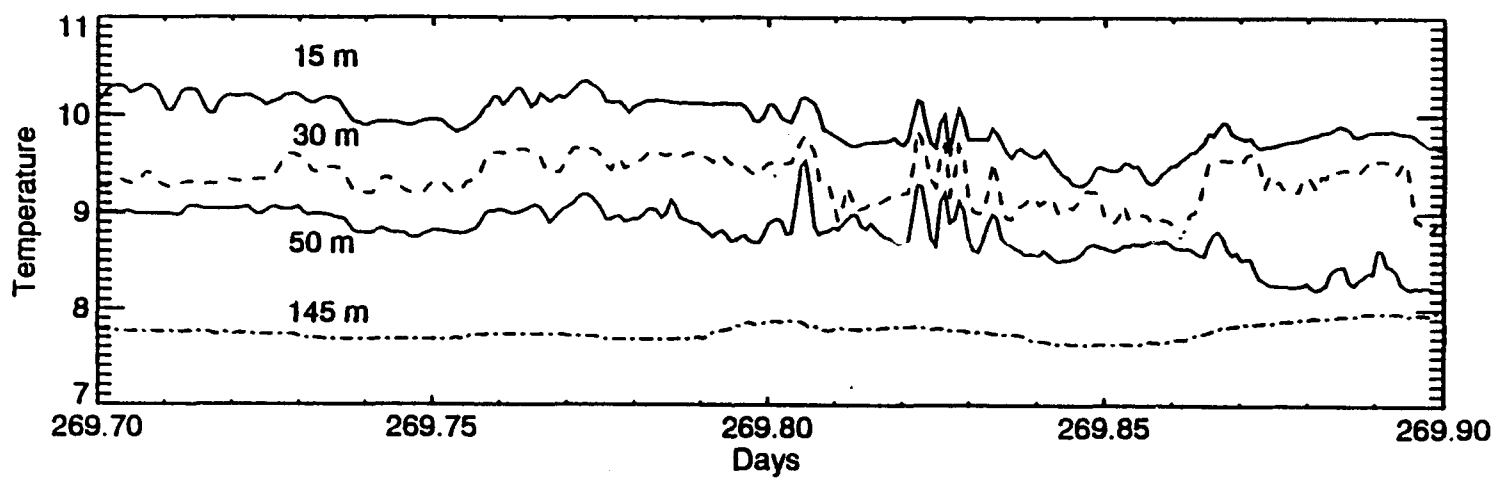


Figure 4-31 Temperature in °C From Four Depths, 15, 30, 50 and 145 m.

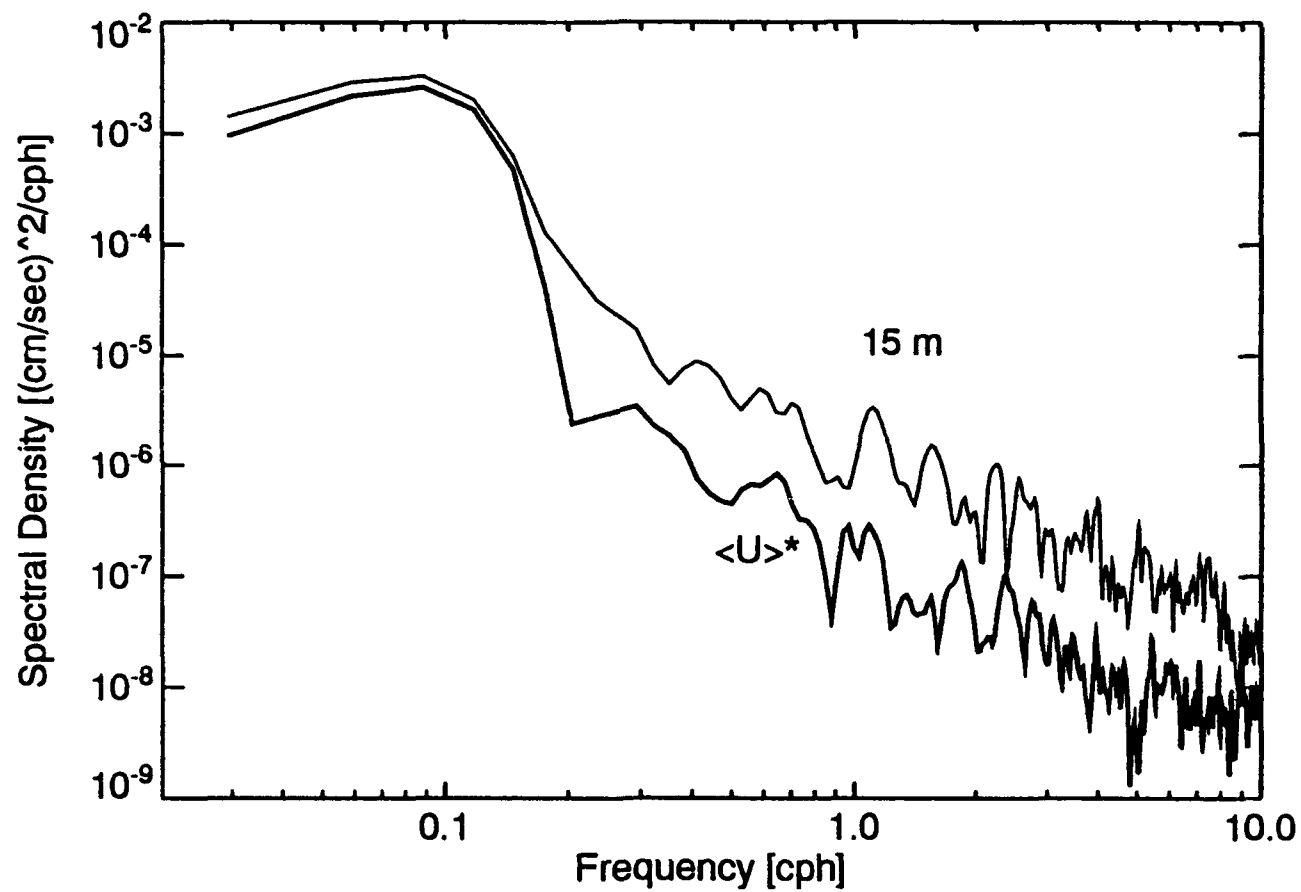


Figure 4-32 Spectral Density of Eastward Velocity Component. Thin Curve Shows Spectrum of Current at 15 m, Thick Curve Shows Spectrum of Conductivity-Weighted, Depth-Averaged Current.

The depth-averaging process smoothes out variance over the entire frequency band, as shown in Figure 4-32. In this figure, the peak at frequency 0.08 cph corresponds to the semi-diurnal tide. In the low-frequency range ($f < 0.1$ cph), the spectra of current at 15 m depth and the depth-averaged current are virtually identical. In the high-frequency range ($f > 0.1$ cph) the spectrum of depth-averaged current is about a factor of 10 weaker than the spectral density at 15 m.

In fact, the factor of 10 reduction in variance due to depth-averaging is probably an underestimate. Four current meters were used to estimate $\langle v_h \rangle^*$ in Equation (7). The vertical resolution of the current meters is aliasing this estimate. To see that this is true, consider Figure 4-33. Coherence amplitude is shown between the u-components of velocity for three pairs of current meters; 15 and 30 m, 30 and 60 m, and 60 and 145 m. The horizontal dashed lines show the 95% confidence levels. Coherence amplitudes which exceeds this level are significant. Significant coherence between vertically-separated current meter records is observed primarily at low frequencies. These low frequencies are dominated by the barotropic tide. The high frequency range ($f > 0.15$ cph, approximately) shows only a few isolated harmonic components with significant coherence. Generally, the internal wave frequency band $f > 1.0$ cph shows little significant coherence. This indicates that our estimate of depth-averaged velocity is aliased due to insufficient vertical resolution. A well-resolved velocity structure should show that the depth-averaged velocity in the internal wave band is close to zero.

The vertical electric field is given by

$$E_z(\rho, z) = -[v_h(\rho, z) \times F_h] \cdot \hat{z} \quad (10)$$

The vertical electric field depends on the horizontal water velocity at the point of measurement; unlike the horizontal electric field, a vertical average is not involved. Note that E_h is depth-independent; its value is the same everywhere in the water column. This result is in contrast to E_z , which is depth-dependent.

Figure 4-34 shows spectra of three components of the electric field. The upper panel shows spectra of the North and East horizontal components from Equations (6,7), while the lower panel shows the spectrum of the vertical component from Equation (9). The power spectra of the

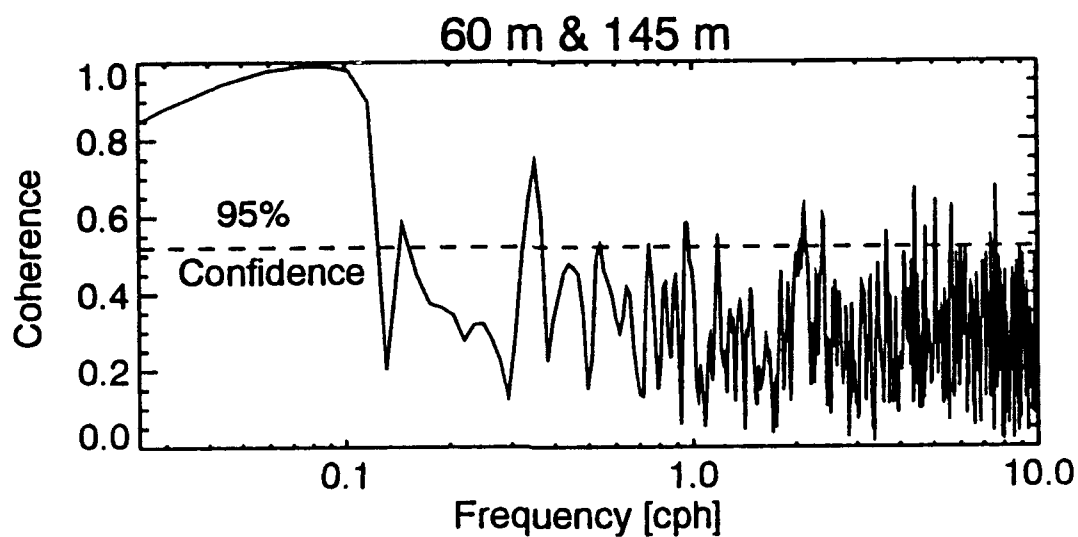
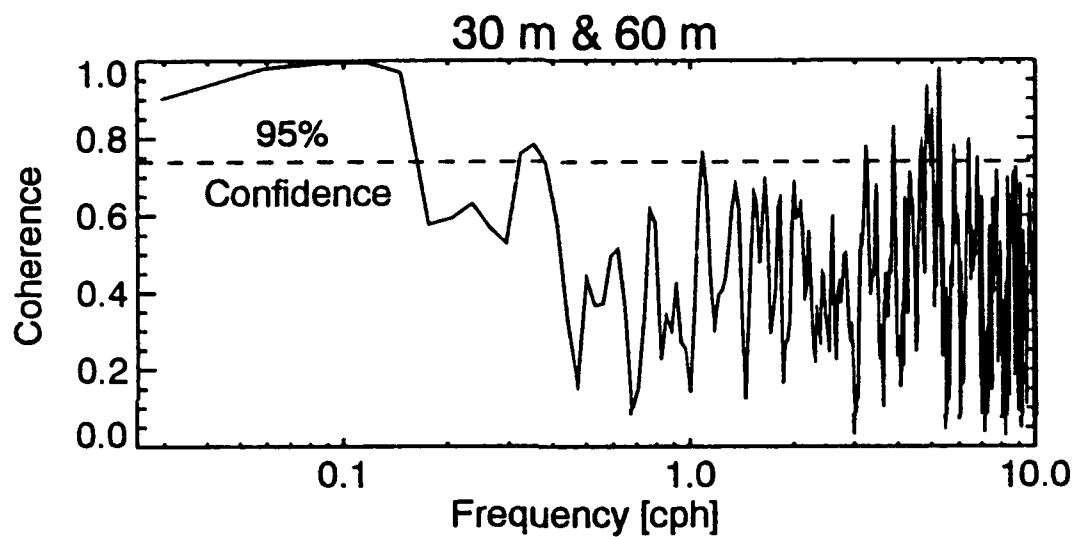
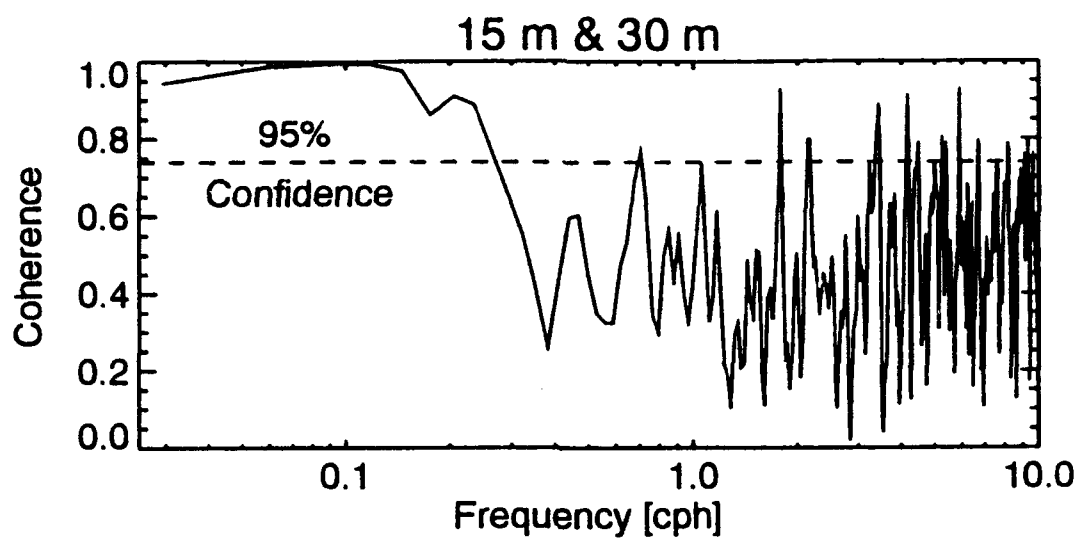


Figure 4-33 Coherence Amplitude Between Three Pairs of Depths; a) 15 & 30 m; b) 30 & 60 m; and c) 60 & 145 m. Dashed Horizontal Line shows 95% Confidence Level

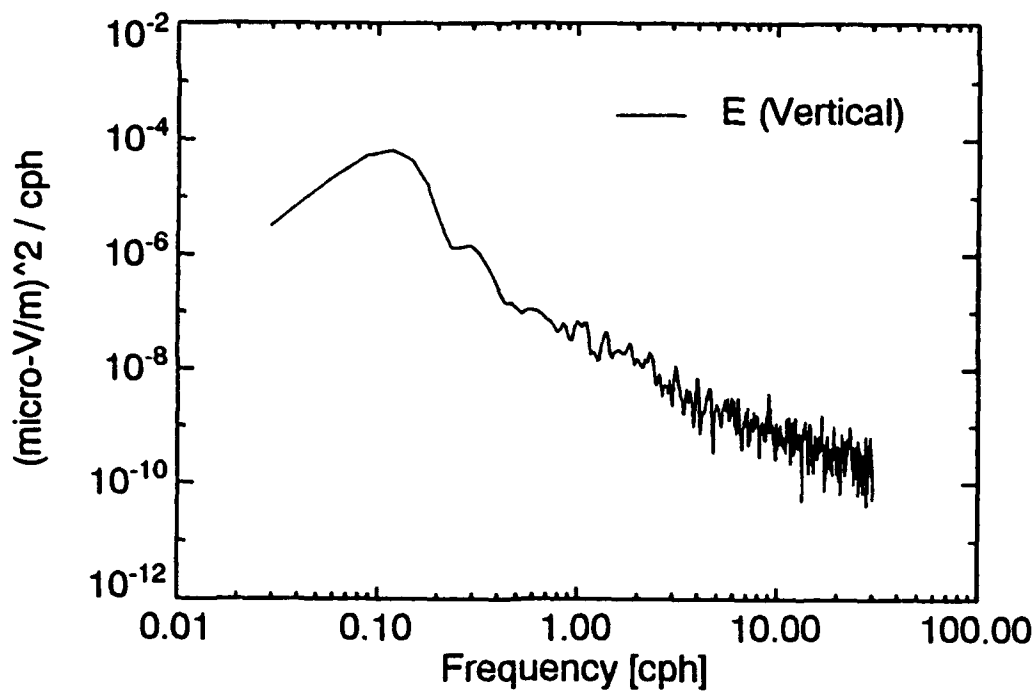
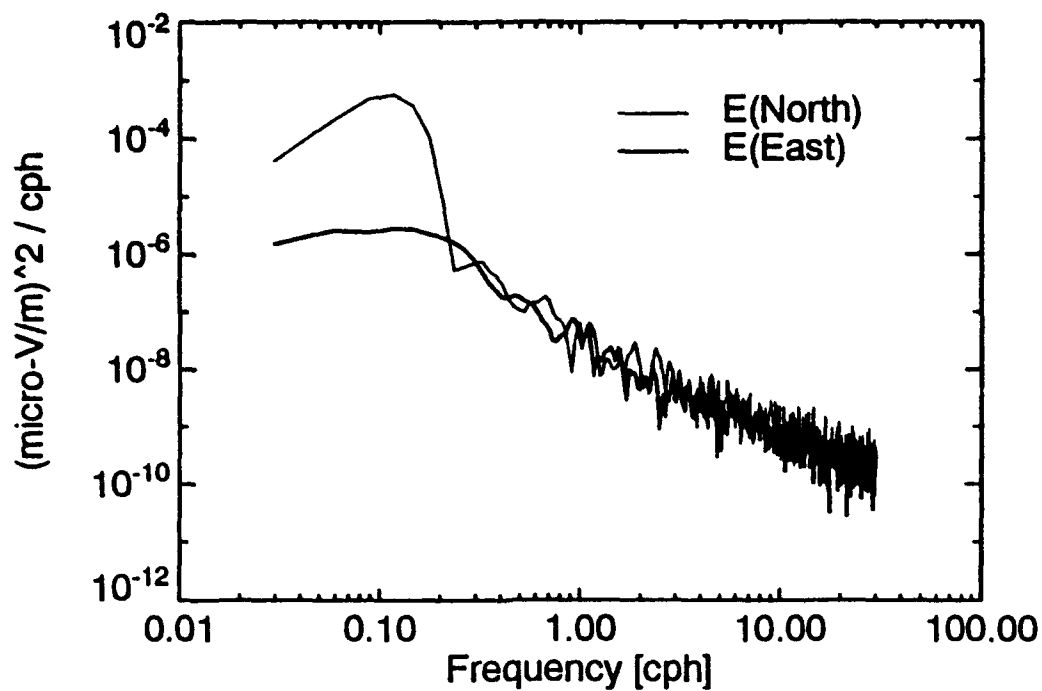


Figure 4-34 Spectral Density of Components of Electric Field at Ocean Bottom. Upper Panel Shows North and East Components; Bottom Panel Shows Vertical Components.

North and East components are comparable in amplitude in the internal wave frequency band ($f > 0.2$ cph). The North component dominates in the low-frequency band ($f < 0.2$ cph) because the barotropic tidal current is dominant in the along-channel (east-west) direction.

In the low-frequency band, the North component of E_h dominates the vertical component E_z because the earth's magnetic component F_z in Equation (6) is about 2.5 times stronger than F_h in Equation (9). In the internal wave band, E_h and E_z are approximately comparable because the stronger magnetic component is approximately counter-balanced by the depth-averaging process.

Equations (6-9) are not exact. They are subject to the following approximations:

- 1) Continental boundaries are distant, and the seafloor is flat with laterally homogeneous conductivity.
- 2) The horizontal length scale of the water motions is assumed to be large compared to the water depth.
- 3) The vertical velocity component is negligible compared to the horizontal components.
- 4) The geomagnetic effect of self-induction is small.
- 5) The geomagnetic field is modeled as an inclined geocentric dipole.

The last three of these assumptions are realistic for the problem at hand, while the first two assumptions are not. The first assumption has to do with the assumption that the seafloor conductivity is negligible. We do not know, *a priori*, whether or not this is the case. Non-negligible seafloor conductivity allows current to leak into the bottom. The problem is swept into the value of the proportionality factor, C . According to Chave et al (1989), direct comparisons between measured ocean currents and horizontal electric fields is a good technique for estimating the value of C . In particular, because barotropic tides are depth-independent, a comparison between the barotropic tides and tidal-frequency fluctuations in E_h would give a direct estimate of C . However these are not available due to limitations in the E-field collection equipment. Because seafloor conductivity does not change in time, once C was estimated at a particular location, Equation (6) could be applied directly to estimate E_h .

The second assumption is certainly correct for barotropic tides, but it is not correct for small-scale internal waves. The assumption is probably of marginal validity for internal soliton packets. Individual waves of a soliton packet have approximately a 150 m wavelength in this environment, approximately equal to the bottom depth. If one were not to make use of Assumption 2, then formally, the factor C in Equation (6) would represent a convolution of a spatial smoothing function with $\langle v_h \rangle^*$. The smoothing function has a width several times the depth of the water column. Its approximate shape is discussed by Chave and Luther (1990), but the importance of its exact shape is downplayed. The net result of applying the smoothing function would be to reduce the amplitude of E_h , as follows.

Consider a prototypical internal wave propagating along the density interface near the surface (e.g., a soliton). Judging from the density profiles in Figure 4-35, the wave's propagation speed would be approximately $c \approx 0.7$ m/sec. We will use this propagation speed to translate from the time domain to the space domain.

Figure 4-36 (upper panel) shows the form of $\Omega_1(k_c \rho)$, the electric field averaging kernel given by Chave and Luther (1990). The parameter k_c is a wavenumber, on the order of the reciprocal of the bottom depth. Its exact value is not stated. If we consider $\Omega_1(k_c \rho)$ to be a filter in the space domain, then its Fourier Transform to the wavenumber domain gives an effective transfer function, as shown in the middle panel of Figure 4-36. We can crudely put this transfer function into the frequency domain through

$$f[\text{cph}] = k_c \rho [\text{cyclesperbottomdepth}] \cdot c \cdot 3600 / H \quad , \quad (11)$$

where $H=150$ m is the bottom depth.

The resulting transfer function is shown in the lower panel in Figure 4-36. Basically the transfer function has a sharp cutoff at about 3 cph. Figure 4-37 shows the result of applying the transfer function to E_h . Variance above the 3 cph cutoff frequency is reduced dramatically. One cannot take this cutoff frequency to be a hard and fast number for several reasons. First, the advective effects of tides may cause it to vary considerably. Second, we have assumed here that all of the internal waves have the same propagation speed, c , and that they propagate as unidirectional plane waves. Third, the value of k_c was not clearly stated.

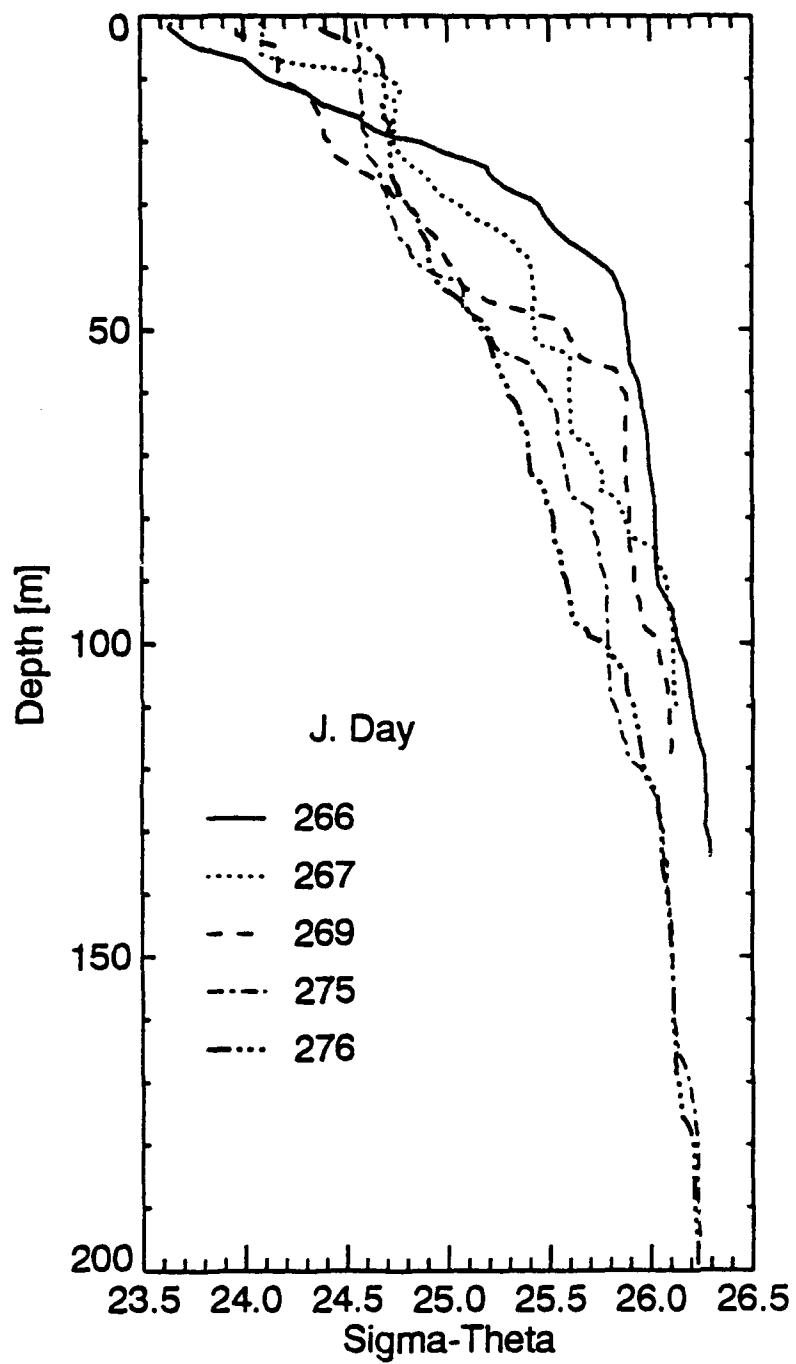


Figure 4-35 Profiles of Density From Five CTD Casts, in Sigma-Theta Units.

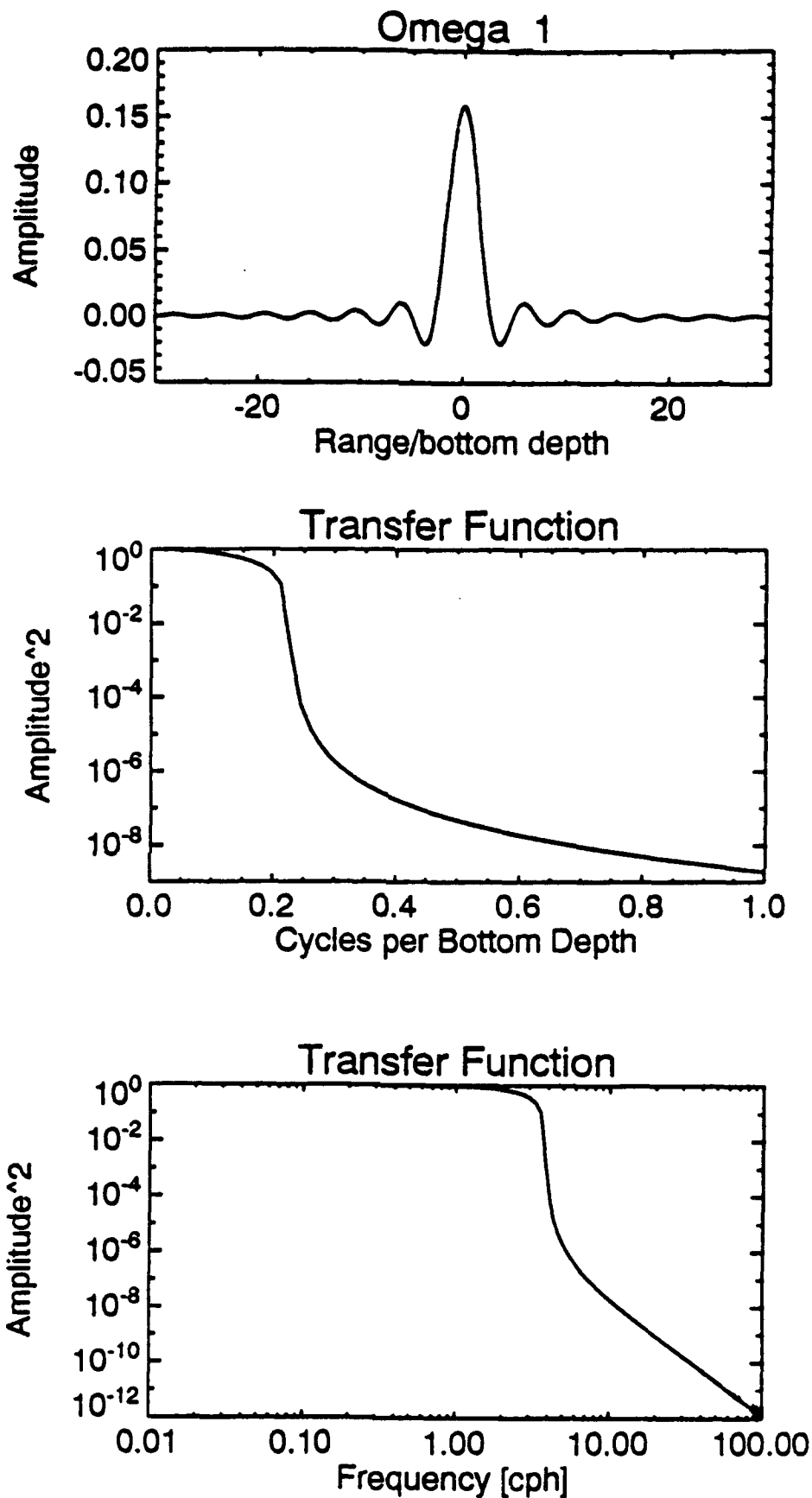


Figure 4-36 Top: Horizontal Electric Field Averaging Kernel Ω_1 , as a Function of Range in Units of Bottom Depth.

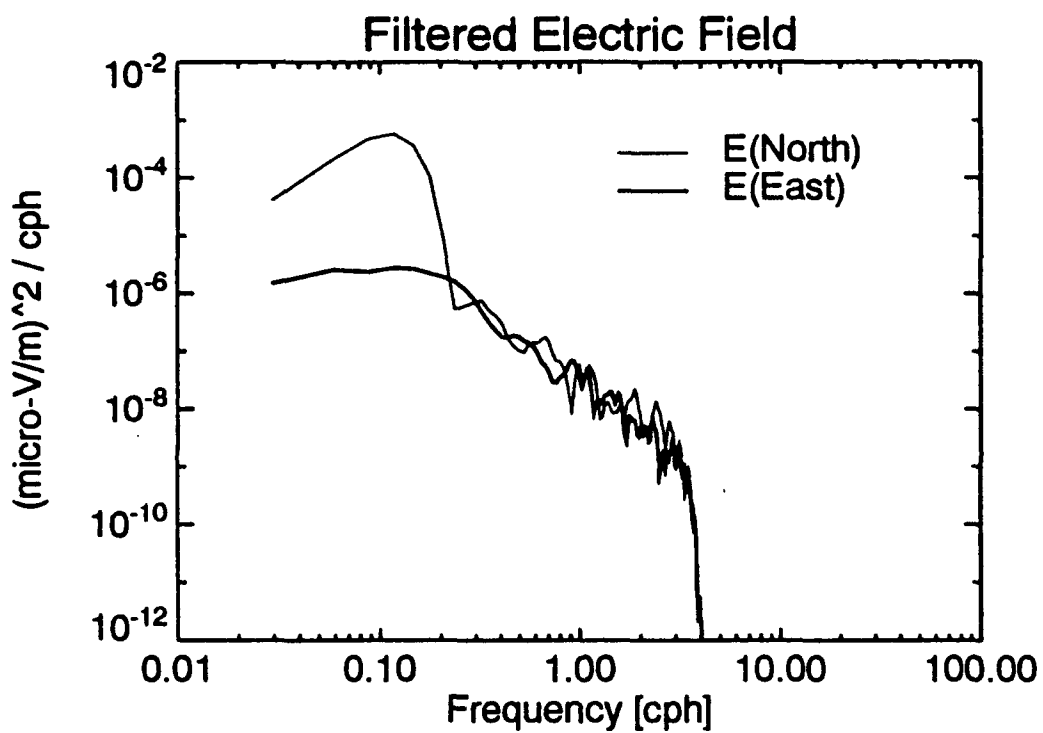


Figure 4-37 Spectral Density of Horizontal Components of Electric Field, After Applying the Transfer Function Shown in Figure 4-36

Thus the assumptions of this simplified theory limit the applicability to addressing the question of the electric field signal of internal waves. Signals that are filtered by the conductivity weighted depth average are significantly reduced. However this model has shown that the vertical current profile is probably undersampled for the higher frequency ranges of motion. This suggests that a full depth ADCP might be a more appropriate instrument to choose for measuring data for an EF model that intends to use a measured velocity structure as input. The model also provides an electric field signal that can be compared to measured values for subtidal frequencies. Comparison of the results of this model with measured electric field from the TET experiment remains a desirable goal.

5. CONCLUSIONS AND RECOMMENDATIONS

This section summarizes the conclusions and recommendations from the 1992 TET environmental measurements. The following conclusions are grouped by subject area.

Field Program

- An ADCP is an effective instrument to monitor internal wave activity. There was good agreement between the ADCP and current meter data and both were useful for identifying internal waves and determining their propagation velocity and phase. A single ADCP could be used to determine speed and direction characteristics of internal waves, as well as providing a detailed description of currents throughout the water column. The ADCP drifts provided useful information but the removal of drift velocity may not be as effective as needed. A continuous time series at a fixed location would be less susceptible to this problem. Differential GPS locations were critical in improving this data set when compared to the 1991 measurements.
- Moorings with instruments deployed over the full depth of the water columns were vulnerable to ship traffic. The use of an upward-looking ADCP for current measurements is recommended to avoid expensive instrument damage in locations where this may be a problem. The temperature recorders were inexpensive enough that duplicative instruments could provide data redundancy with minimal cost impact.
- The current meters suffered a higher failure rate than other instruments but no reason was determined for most of the recording failures. The use of redundant instrumentation may be required in areas of particular importance.
- The current meters were useful in defining periods of increased turbulent activity.

Stratification

- The late summer stratification at the TET site varies with the phase of the tide, intensifying during strong tidal flood currents. This cycle plays a key role in the production of the soliton-like internal waves that occur primarily near peak flood tide.

Fronts

- Strong fronts passed through the mooring array several times over the course of the two week experiment. They presented a strong signal in both the velocity and temperature fields with velocity changes the same order of magnitude as the SIW's but lower on the frequency scale. Fronts may have isolated the inshore mooring from some of the internal wave activity.
- Rapid changes in the water column structure as seen in the passage of these fronts could produce changes in the sound velocity profile. This may be a consideration in optimizing the use of acoustic sensor systems.

Internal Waves

- During the 14 day experiment, 13 clear internal wave signals were identified in the current and temperature time series data.
- Median values for wave length, propagation speed and wave amplitude were 514 m, 56 cm/s and 24 m respectively. Propagation directions were evenly distributed between flood and ebb directions.
- Internal wave structure for the strongest waves, as observed by current meters and the ADCP, was consistent with theory for shallow water solitons.

Bottom Boundary Layer

- Strong vertical shear was present between a height of 1 meter and the bottom with peak velocities at 1 meter of 50 cm/s.
- Indications of strong turbulent activity near the bottom occurred when current at 5 m above the bottom reached or exceeded 50 cm/s. This happened on almost every flood tide, but occasionally this threshold speed was not reached and turbulent activity was noticeably reduced.
- Observations at the BBL mooring were consistent with a rectified return flow, probably a result of a local radial flow. This secondary flow resulted in an offshore component of the current during both flood and ebb tidal cycles.
- Calculations of a drag coefficient for the bottom resulted in a value of 7×10^{-3} for high Reynolds numbers. This compares well with other historical observations for a bottom drag coefficient.

Internal Wave EM Signatures

- A simplified model was applied to the 1992 field data in order to initially evaluate the use of field data to calculate the electric field induced by soliton-like internal waves.
- The assumptions required to simplify the calculations to a reasonable level restricted the value of the results to subtidal frequencies. Complex internal wave signals were small in the depth averaged calculation.

Environmental measurements have been collected at the TET site in late summer from 1989 to 1992. In two of those years various TET sensors were also deployed concurrently. It is evident from these measurements that environmental data has been helpful in the isolation of noise sources in the TET sensor systems. We have the following recommendations for subsequent studies with the TET program.

- Measurements to date in the TET program suggest high variability of environmental phenomena in the near shore area, even over short distances (2-3 km). Individual deployment sites may need to be environmentally characterized to fully understand the range of oceanographic phenomena present.
- The electric field and magnetometer data should be evaluated for possible internal wave induced signals. The 1992 data would be most appropriate for this since both data types were collected concurrently this year.
- Consideration should be given to development of a real time data collection system for the environmental data. This will allow higher data rates than have been used in the past and may improve the evaluation of the TET sensor data in real time. A real-time algorithm for the detection of strong internal waves and strong bottom turbulence would also be useful.
- Further work is required on the SIW/EM signature model to make the transition to super tidal signals. This is a particularly complex problem and should be performed if analysis of electric field and magnetometer data show evidence of internal wave signals.

REFERENCES

- Apel J.R., J.R. Holbrook, A.K. Liu, and J.J.Tsai, (1985), The Sulu Sea Internal Soliton Experiment, Jour. Phys Oceang., Vol 15 (12): 1625-1651.
- Bentson, T., C.Osborn, M.Morey, 1992, TET E-Field Data Analysis Summer 1991 Experiment, Vol 1, Analysis of SIO data, CDRL A043AB, DO2. SAIC Report.
- Chave, A.D. and D.S. Luther, 1990: "Low-frequency, motionally induced electromagnetic fields in the ocean, 1. Theory," JGR, vol. 95, pp. 7185-7200.
- Chave, A.D., J.H. Filloux, D.S. Luther, L.K. Law, and A. White, 1989: "Observations of motional electromagnetic fields during EMSLAB," JGR, vol. 94, pp. 14,153-14,166.
- Dewey, R.K., P.H. LeBlond, and W.R. Crawford, 1988: The turbulent bottom boundary layer and its influence on local dynamics over the continental shelf, Dynamics of Atmosphere and Oceans., vol (12). 143 -172.
- Gunn, J.T. and D. Rubenstein, (1989), TET Predeployment Environmental Measurements. Prepared by SAIC, Bellevue, WA for Naval Ocean Systems Center, Kailua, HI.
- Gunn, J.T. D. Rubenstein, (1991), TET Environmental Measurements - Measurements of Velocity and Temperature in the Strait of Juan de Fuca, Summer 1990. Prepared by SAIC, Bellevue, WA for Naval Ocean Systems Center, Kailua, HI.
- Gunn, J.T., R.K. Dewey and C.W. Wilson, (1992), TET Environmental Survey, August 1991, Data Analysis Report. Prepared by SAIC, Bellevue, WA. for NRaD. CDRL A044, D.O. 28.
- Luther, D.S., J.H. Filloux, and A.D. Chave, 1991: "Low-frequency, motionally induced electromagnetic fields in the ocean 2. Electric field and Eulerian current comparison," JGR, vol. 96, pp. 12,797-12,814.
- Osborne, A.R., and T.L. Burch, (1980), Internal Solitons in the Andaman Sea. Science, Vol. 208(4443), 451-460.

Phillips, O.M. (1969) The dynamics of the Upper Ocean, Cambridge Univ. Press, London, 261p.

Prandtl, L., (1927), Ergeb. AVA Goett., ser III, pp 1-5.

Spain, P. and T. B. Sanford, (1987), Accurately monitoring the Florida Current with motionally induced voltages. Jour. Mar. Res. 45, 843-870.

Tennekes, H., and J.L. Lumley, (1972), A First Course in Turbulence., Cambridge, MA. The MIT Press. 300p.

White, F.W., (1974), Viscous Fluid Flow, New York, McGraw-Hill, 725p.

APPENDIX A

Current Velocity Time Series, Moorings 1-4

Two day alongshore (E/W) and across shore (N/S) current velocity time series plots are shown for each working current meter. Alongshore currents are shown with a dashed line and across shore currents are shown with a solid line. Directions are in magnetic North.

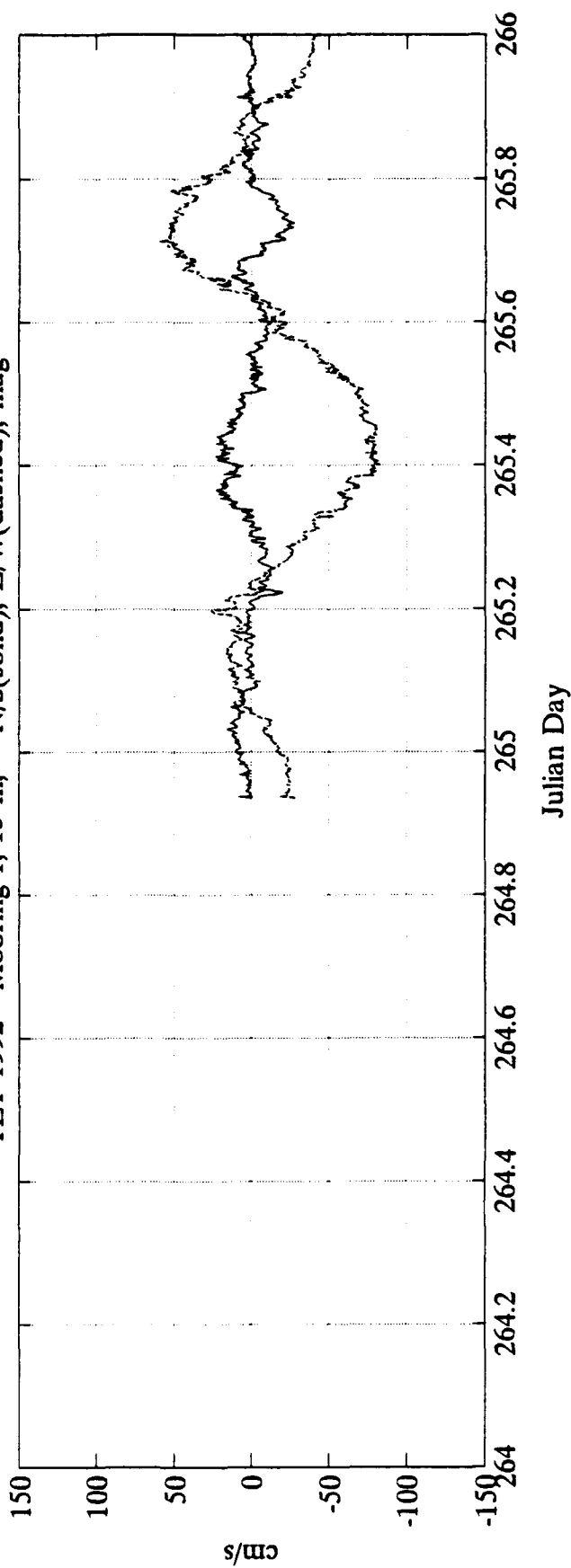
LIST OF FIGURES

APPENDIX A

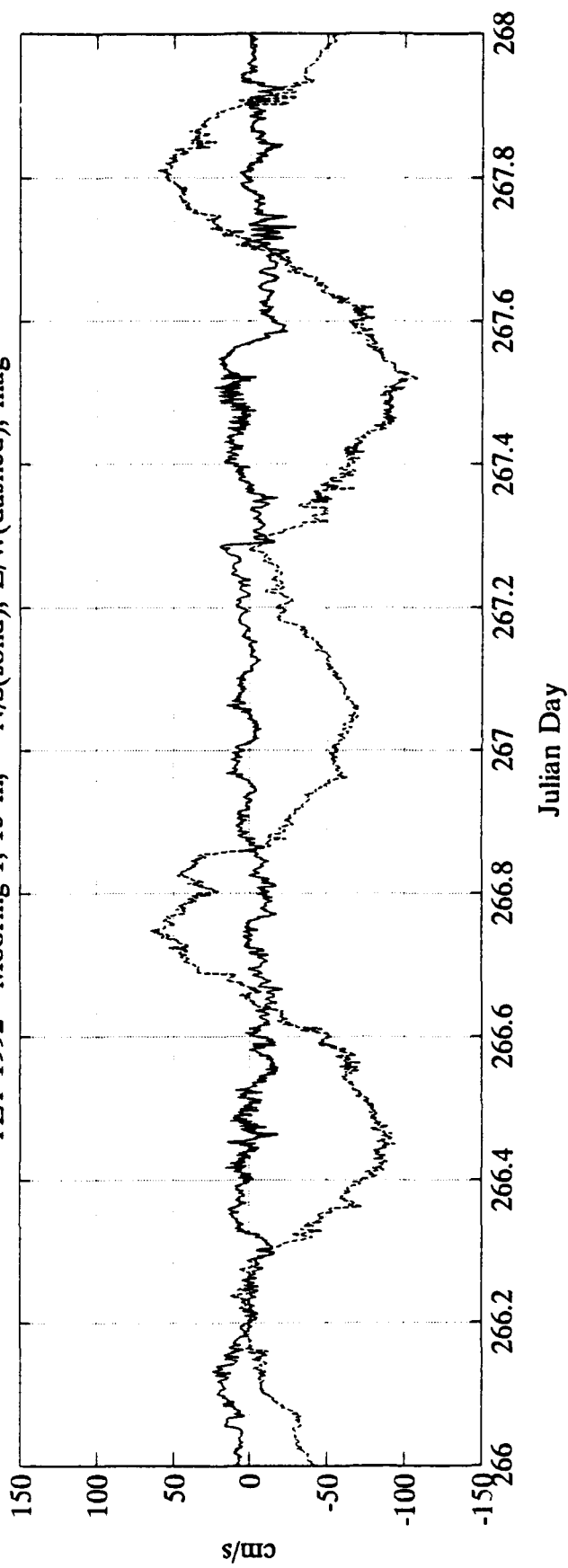
Current Velocity Time Series, Mooring 1, 15 m, JD 264 - 268	A-4
Current Velocity Time Series, Mooring 1, 15 m, JD 268 - 272	A-5
Current Velocity Time Series, Mooring 1, 15 m, JD 272 - 276	A-6
Current Velocity Time Series, Mooring 1, 15 m, JD 276 - 278	A-7
Current Velocity Time Series, Mooring 1, 30 m, JD 268 - 272	A-8
Current Velocity Time Series, Mooring 1, 60 m, JD 268 - 272	A-9
Current Velocity Time Series, Mooring 1, 60 m, JD 272 - 276	A-10
Current Velocity Time Series, Mooring 1, 60 m, JD 276 - 278	A-11
Current Velocity Time Series, Mooring 1, 145 m, JD 264 - 268	A-12
Current Velocity Time Series, Mooring 1, 145 m, JD 268 - 272	A-13
Current Velocity Time Series, Mooring 1, 145 m, JD 272 - 276	A-14
Current Velocity Time Series, Mooring 1, 145 m, JD 276 - 278	A-15
Current Velocity Time Series, Mooring 2, 148 m, JD 268 - 272	A-16
Current Velocity Time Series, Mooring 3, 15 m, JD 264 - 268	A-17
Current Velocity Time Series, Mooring 3, 15 m, JD 268 - 272	A-18
Current Velocity Time Series, Mooring 3, 129 m, JD 268 - 272	A-19
Current Velocity Time Series, Mooring 4, 10 m hgt, JD 264 - 268	A-20
Current Velocity Time Series, Mooring 4, 10 m hgt, JD 268 - 272	A-21
Current Velocity Time Series, Mooring 4, 10 m hgt, JD 272 - 276	A-22
Current Velocity Time Series, Mooring 4, 10 m hgt, JD 276 - 278	A-23

Current Velocity Time Series, Mooring 4, 5 m hgt, JD 264 - 268	A-24
Current Velocity Time Series, Mooring 4, 5 m hgt, JD 268 - 272	A-25
Current Velocity Time Series, Mooring 4, 5 m hgt, JD 272 - 276	A-26
Current Velocity Time Series, Mooring 4, 5 m hgt, JD 276 - 278	A-27
Current Velocity Time Series, Mooring 4, 1 m hgt, JD 264 - 268	A-28
Current Velocity Time Series, Mooring 4, 1 m hgt, JD 268 - 272	A-29
Current Velocity Time Series, Mooring 4, 1 m hgt, JD 272 - 276	A-30
Current Velocity Time Series, Mooring 4, 1 m hgt, JD 276 - 278	A-31

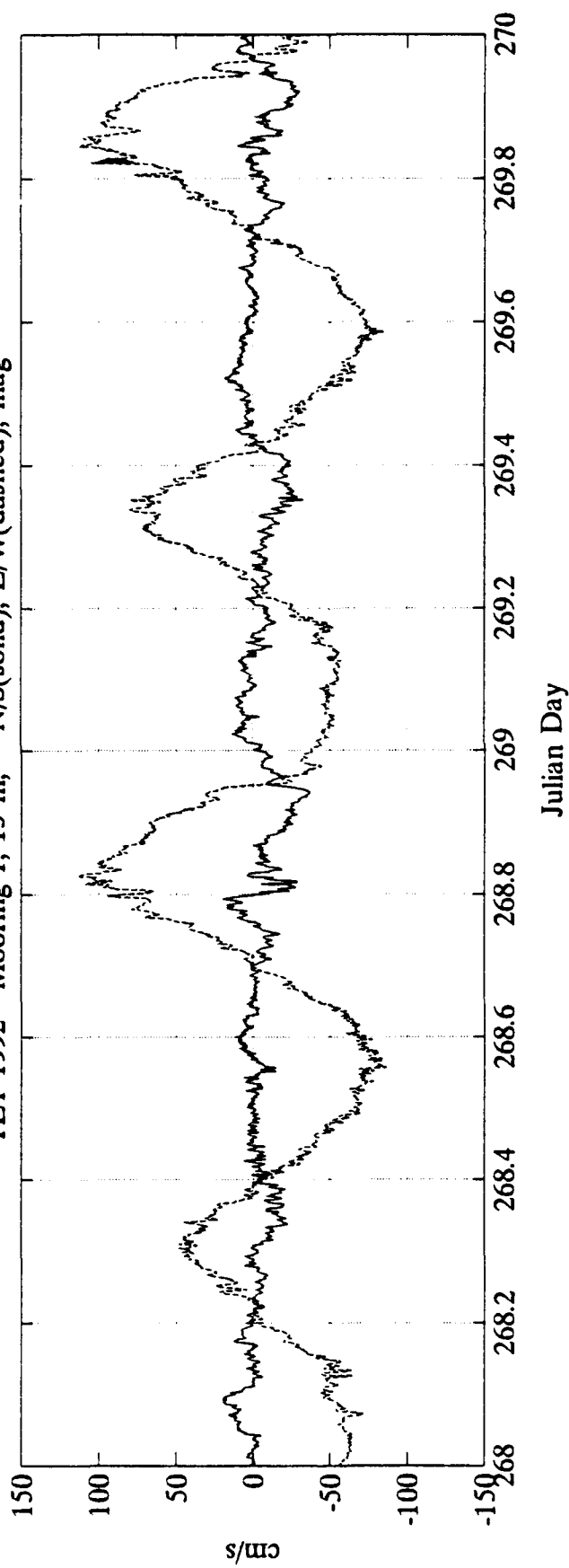
TET 1992 - Mooring 1, 15 m, N/S(solid), E/W(dashed), mag



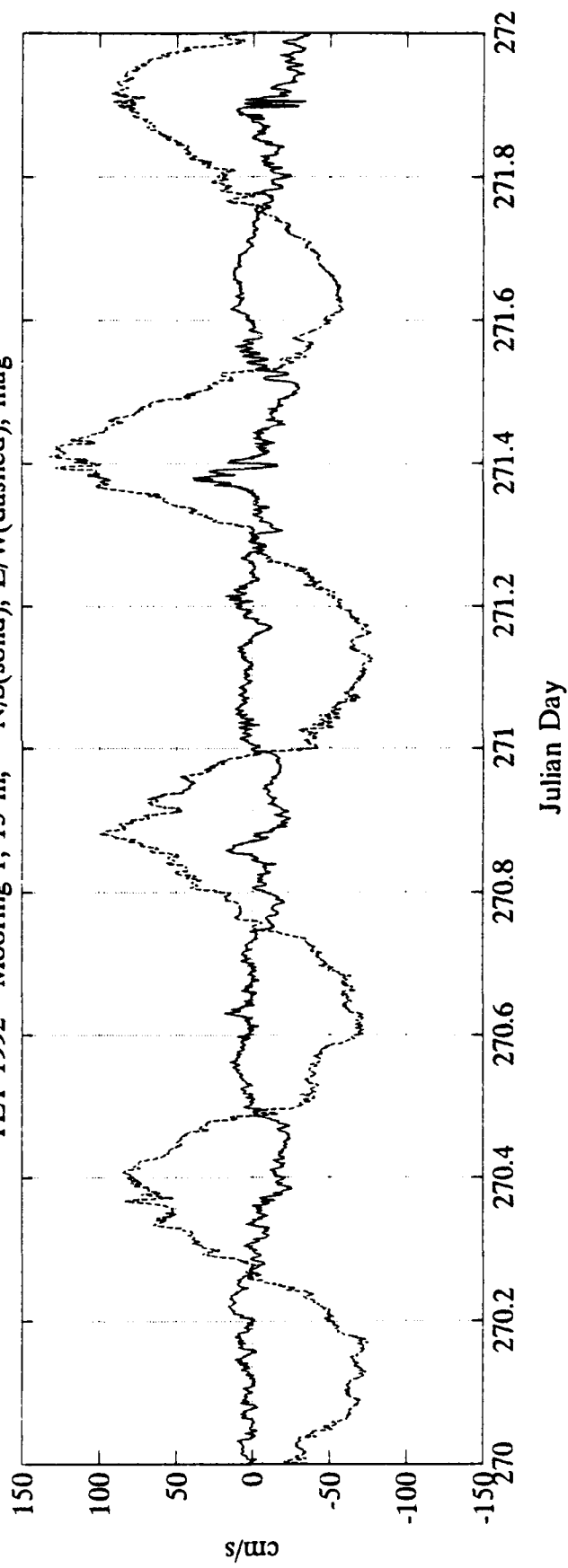
TET 1992 - Mooring 1, 15 m, N/S(solid), E/W(dashed), mag

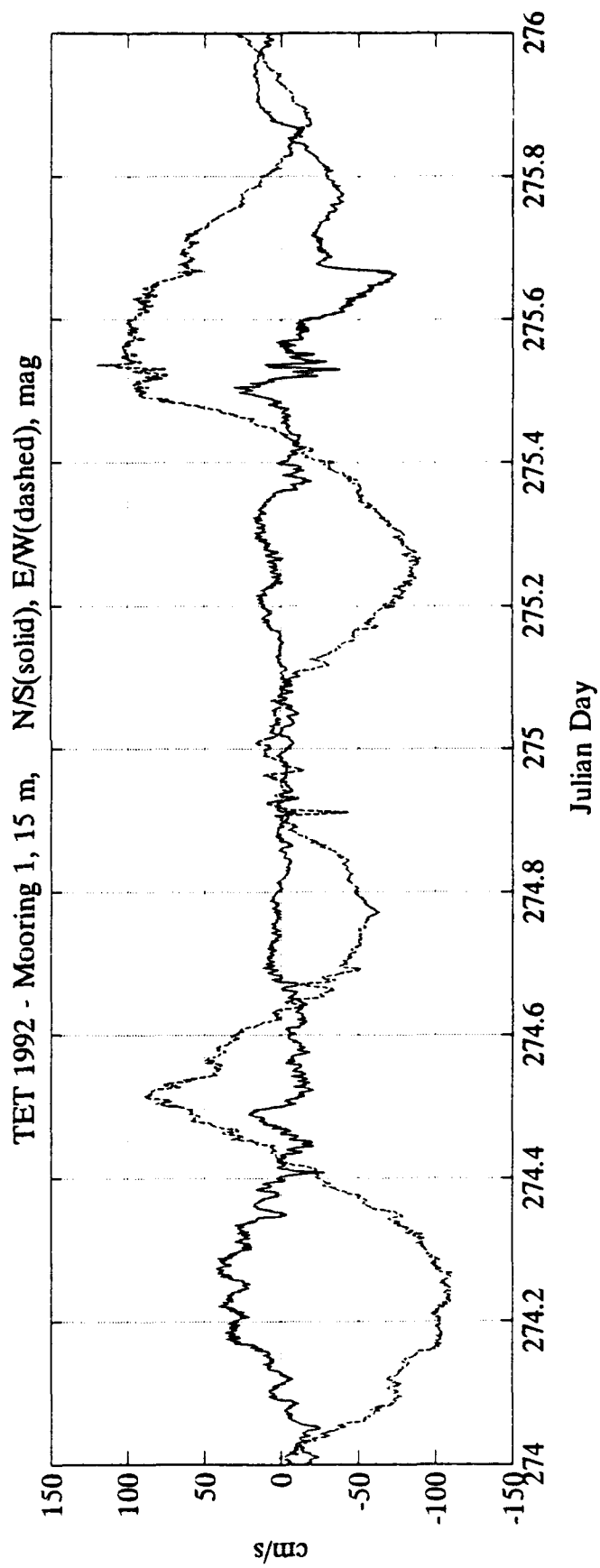
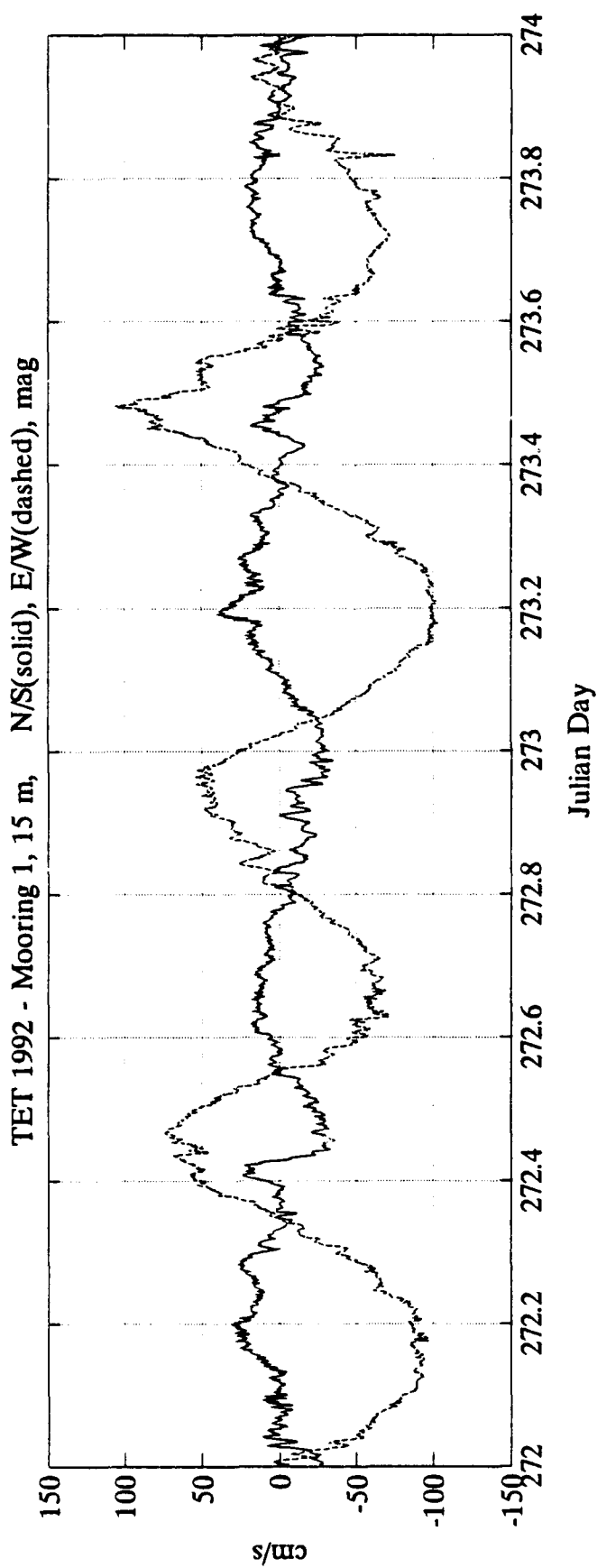


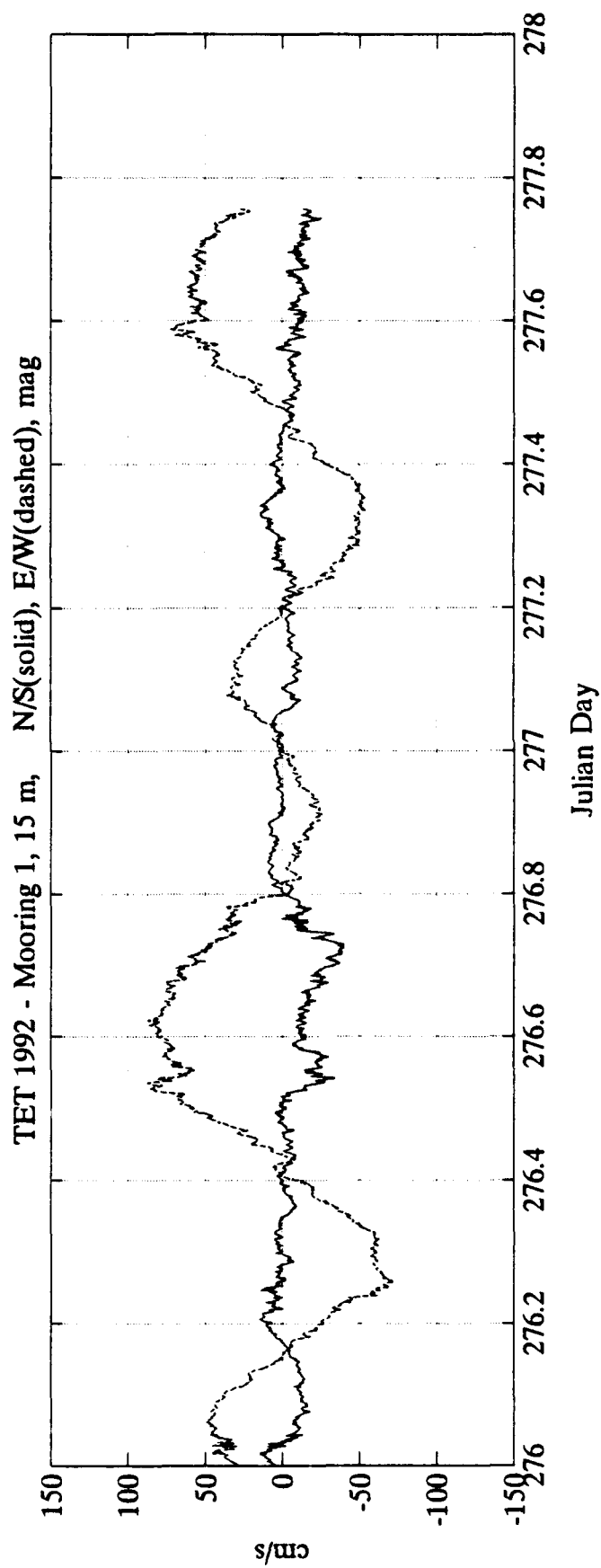
TET 1992 - Mooring 1, 15 m, N/S(solid), E/W(dashed), mag



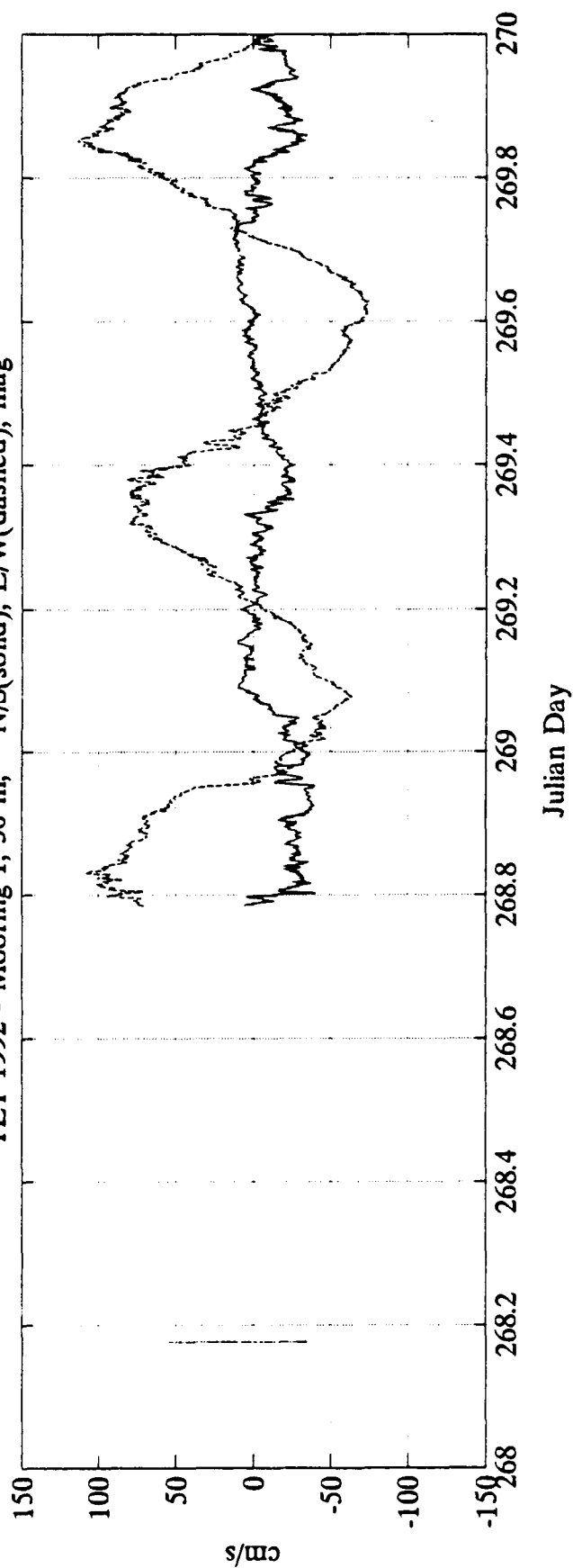
TET 1992 - Mooring 1, 15 m, N/S(solid), E/W(dashed), mag



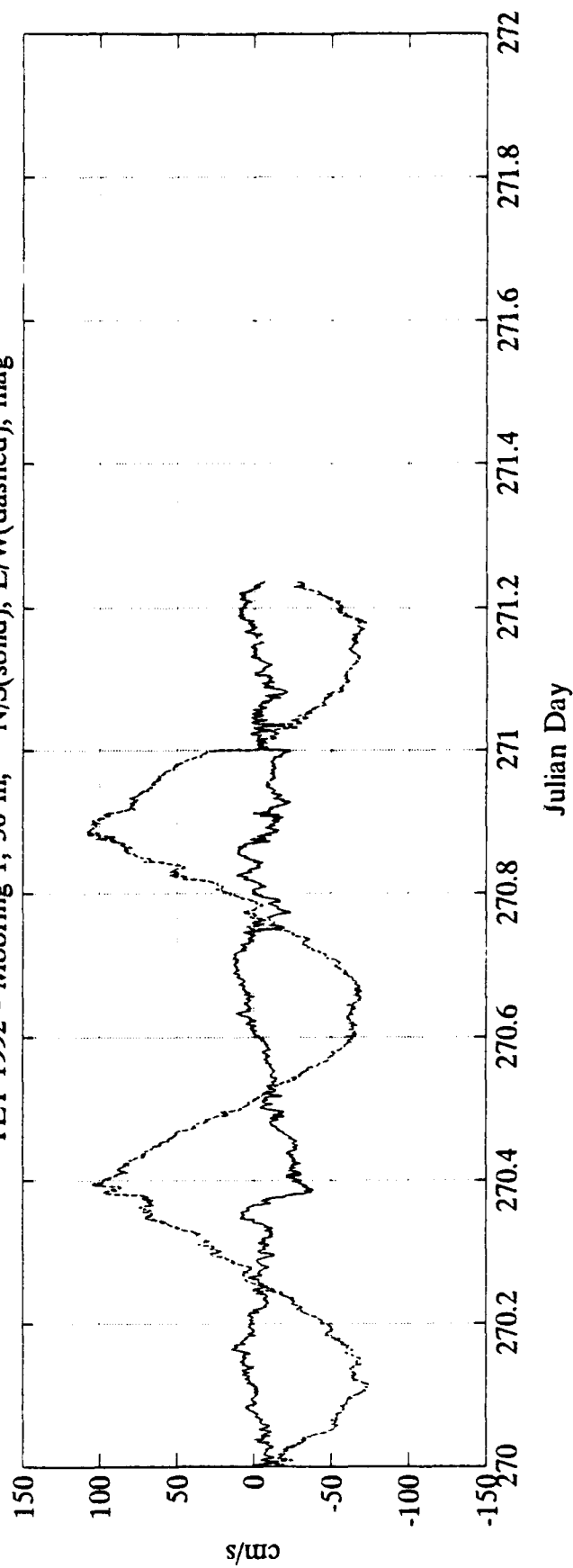


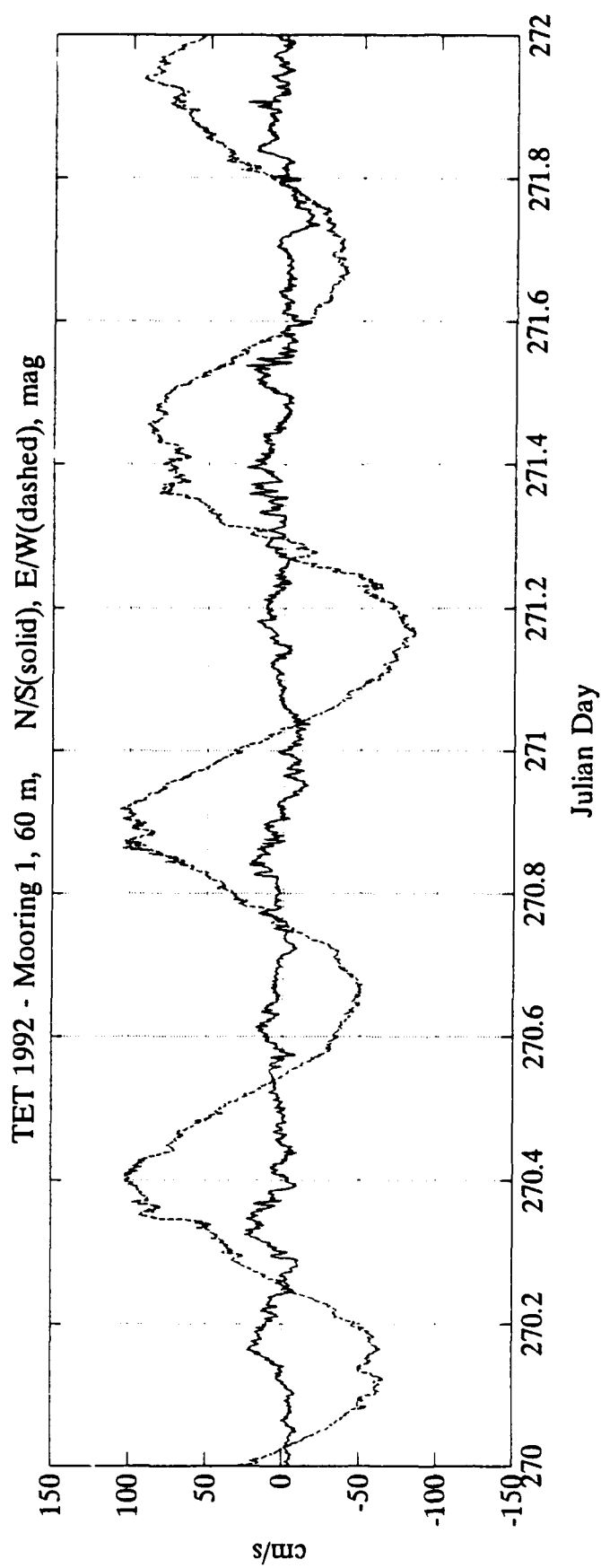
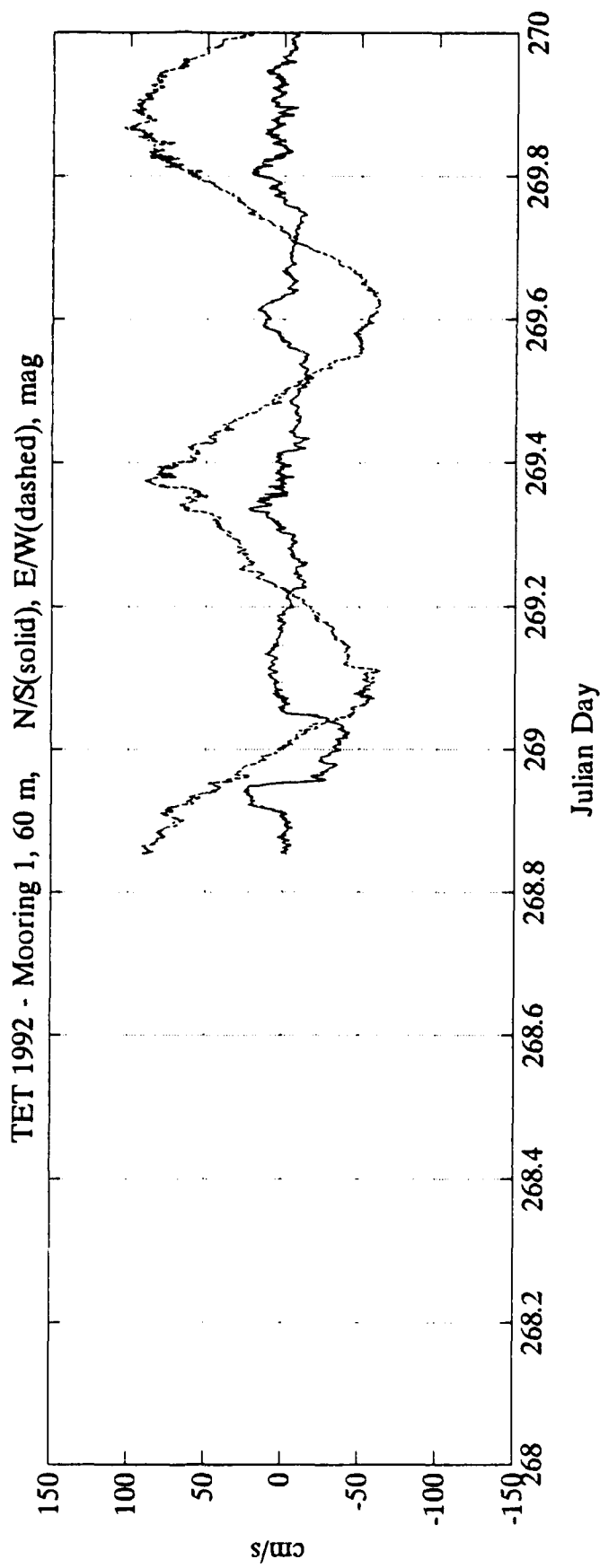


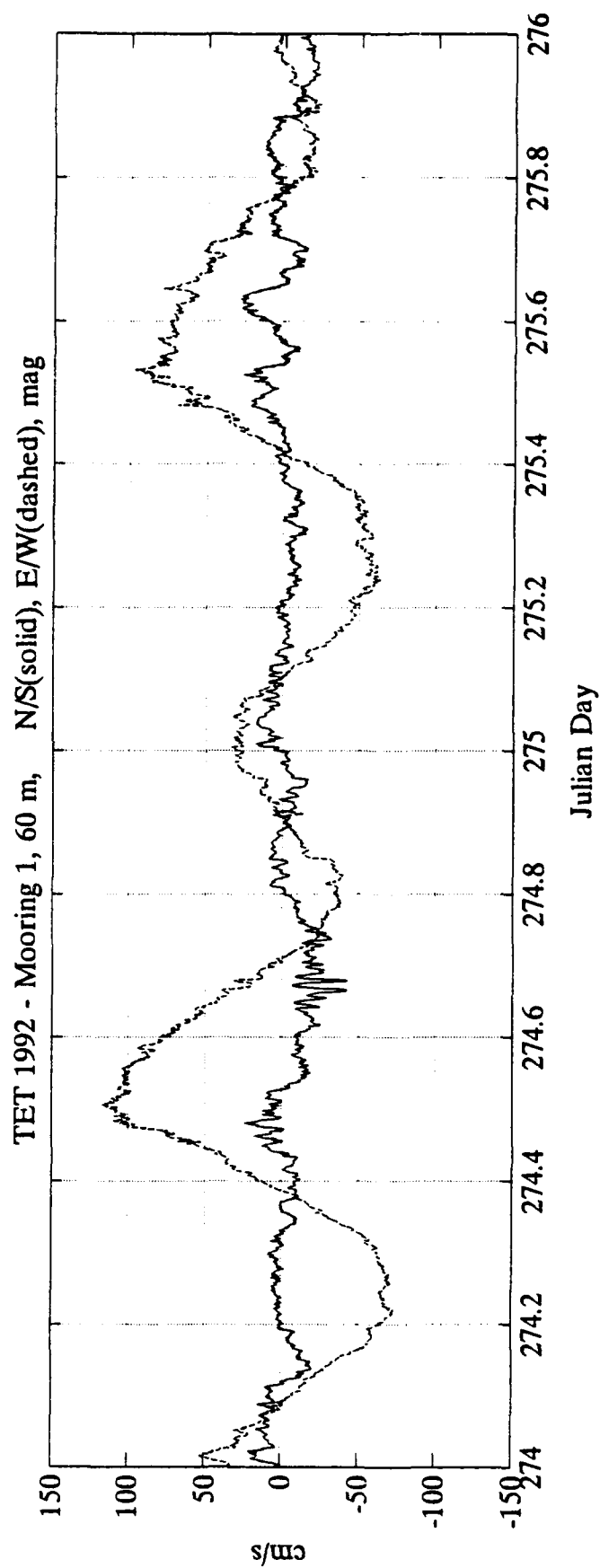
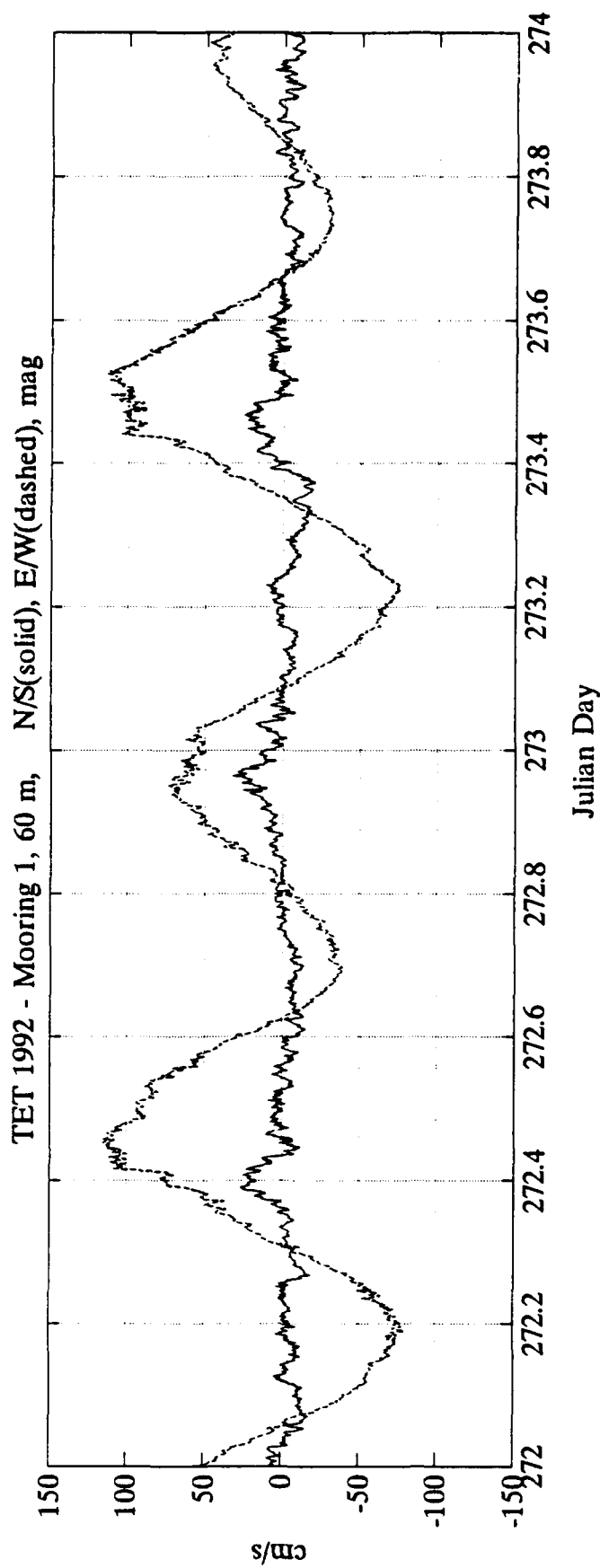
TET 1992 - Mooring 1, 30 m, N/S(solid), E/W(dashed), mag

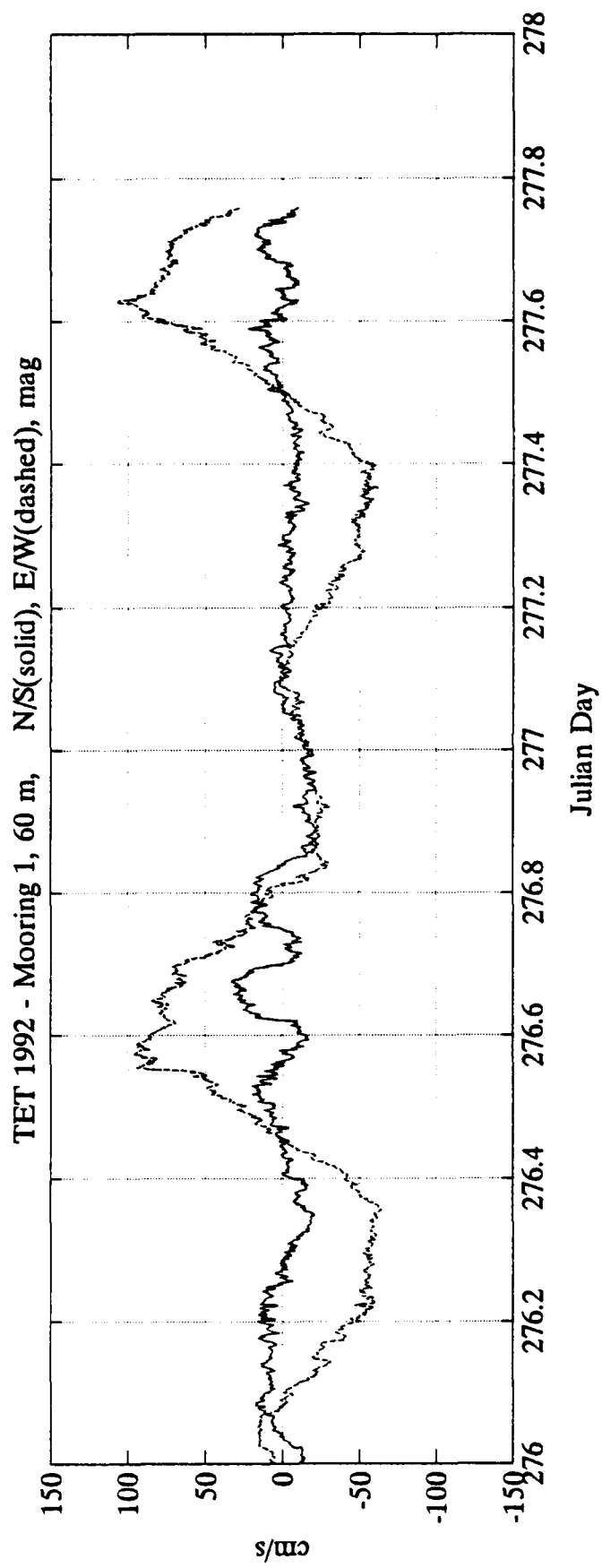


TET 1992 - Mooring 1, 30 m, N/S(solid), E/W(dashed), mag

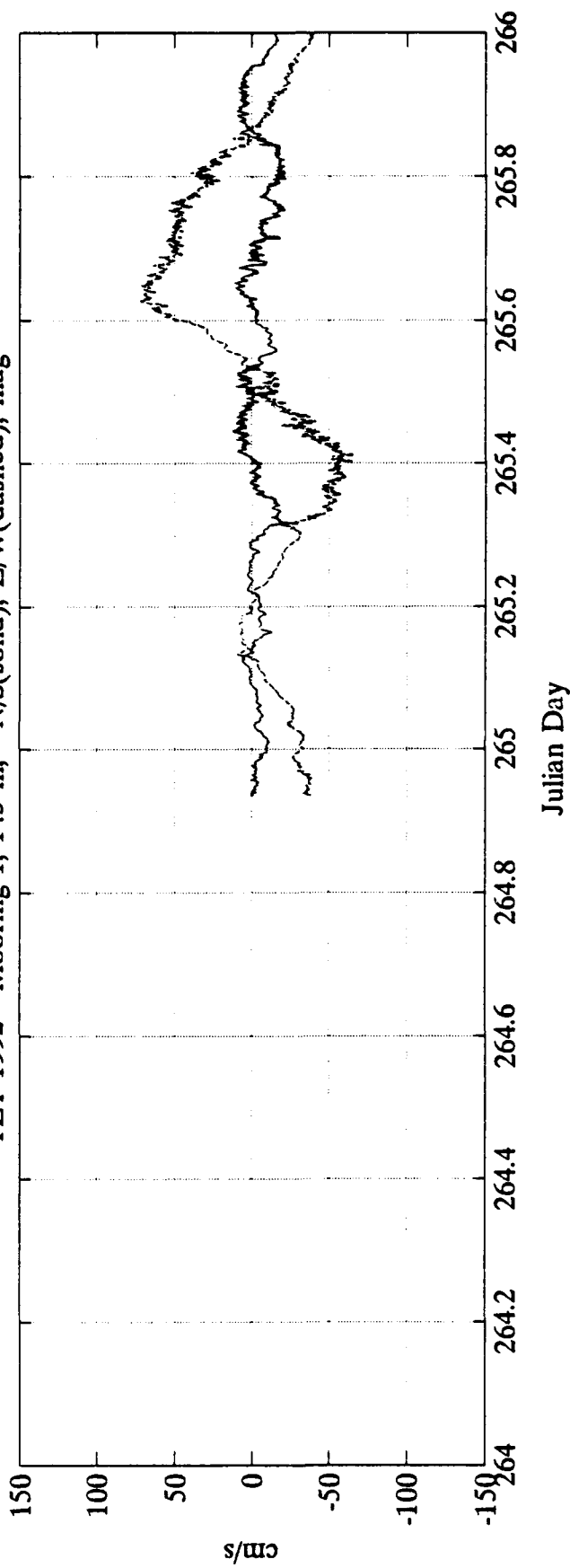




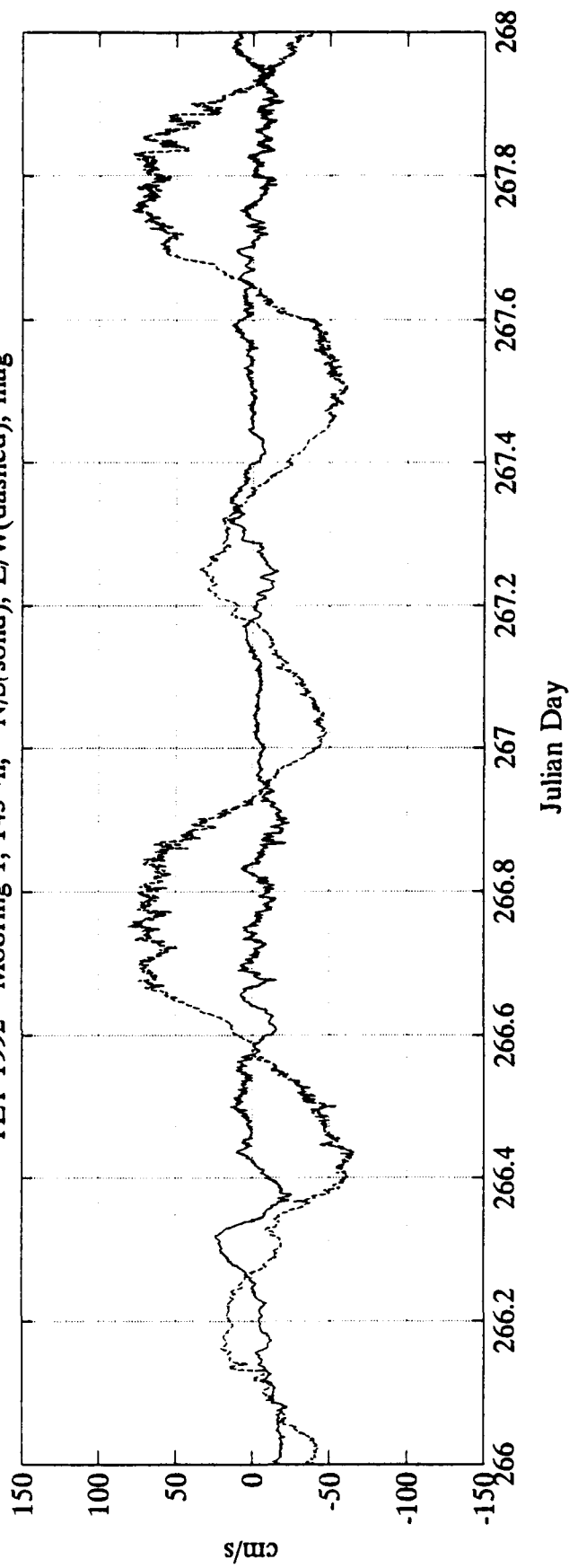


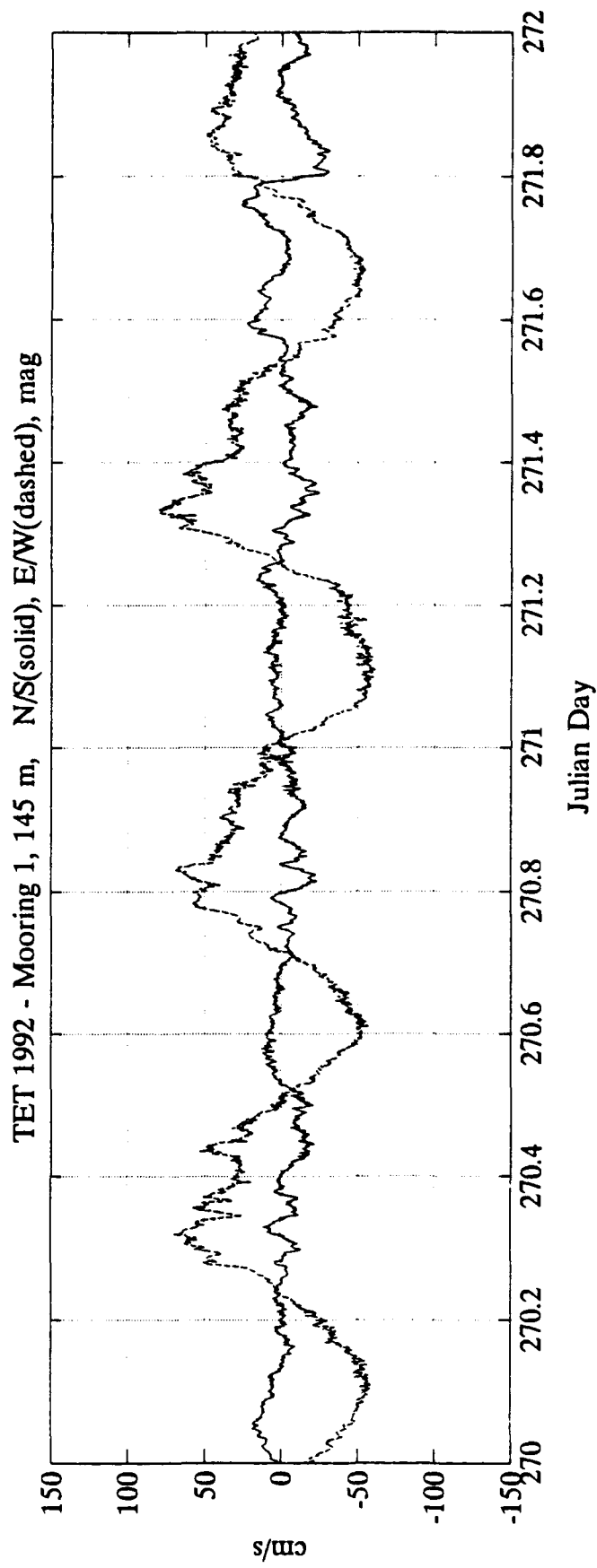
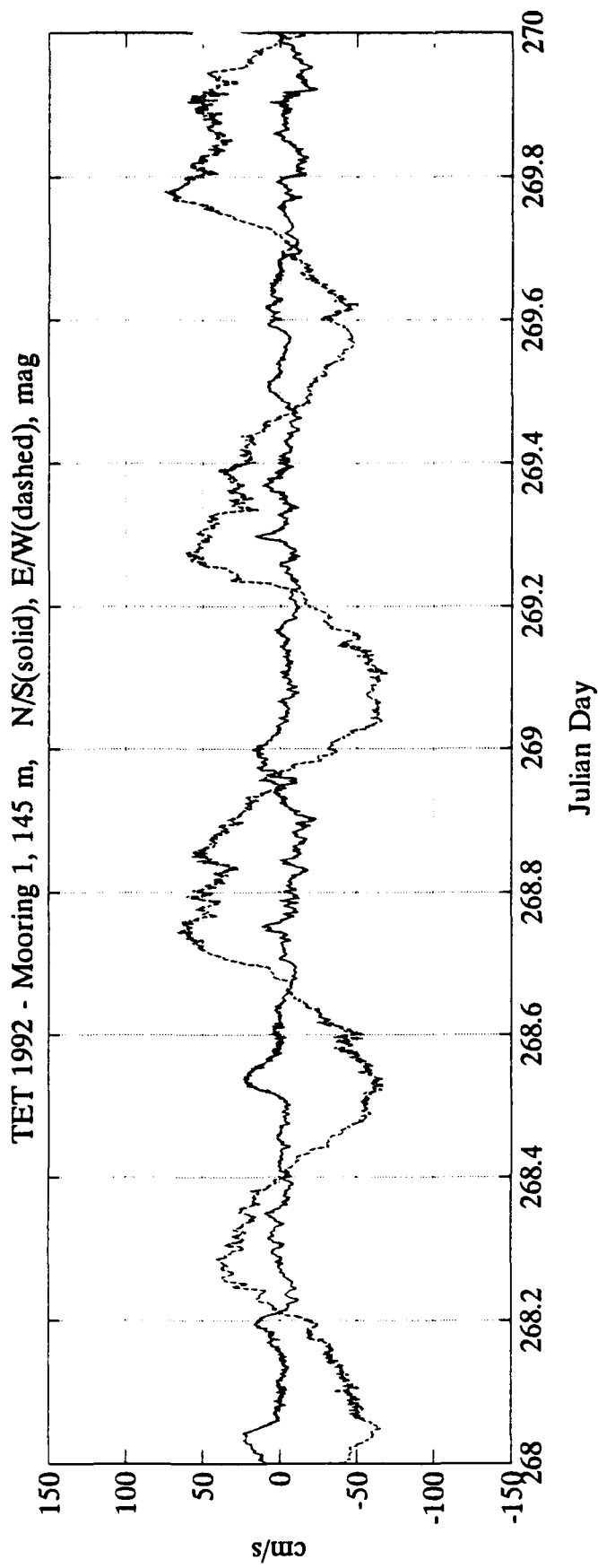


TET 1992 - Mooring 1, 145 m, N/S(solid), E/W(dashed), mag

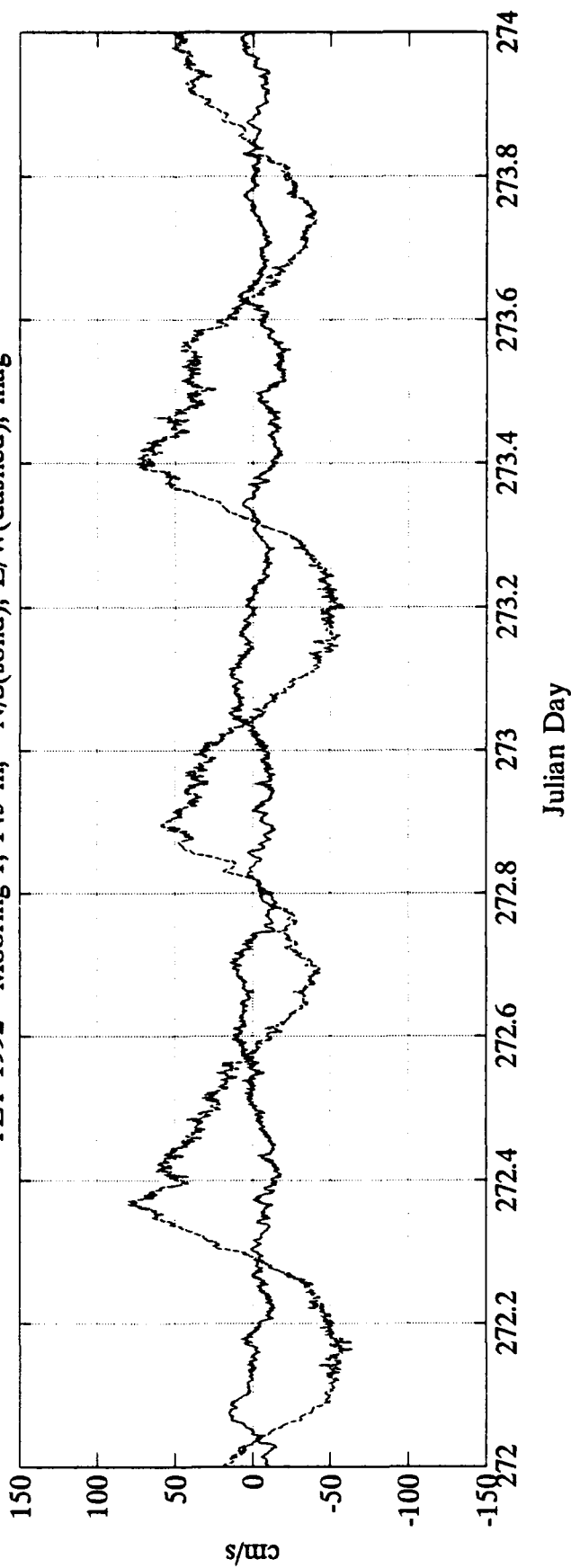


TET 1992 - Mooring 1, 145 m, N/S(solid), E/W(dashed), mag

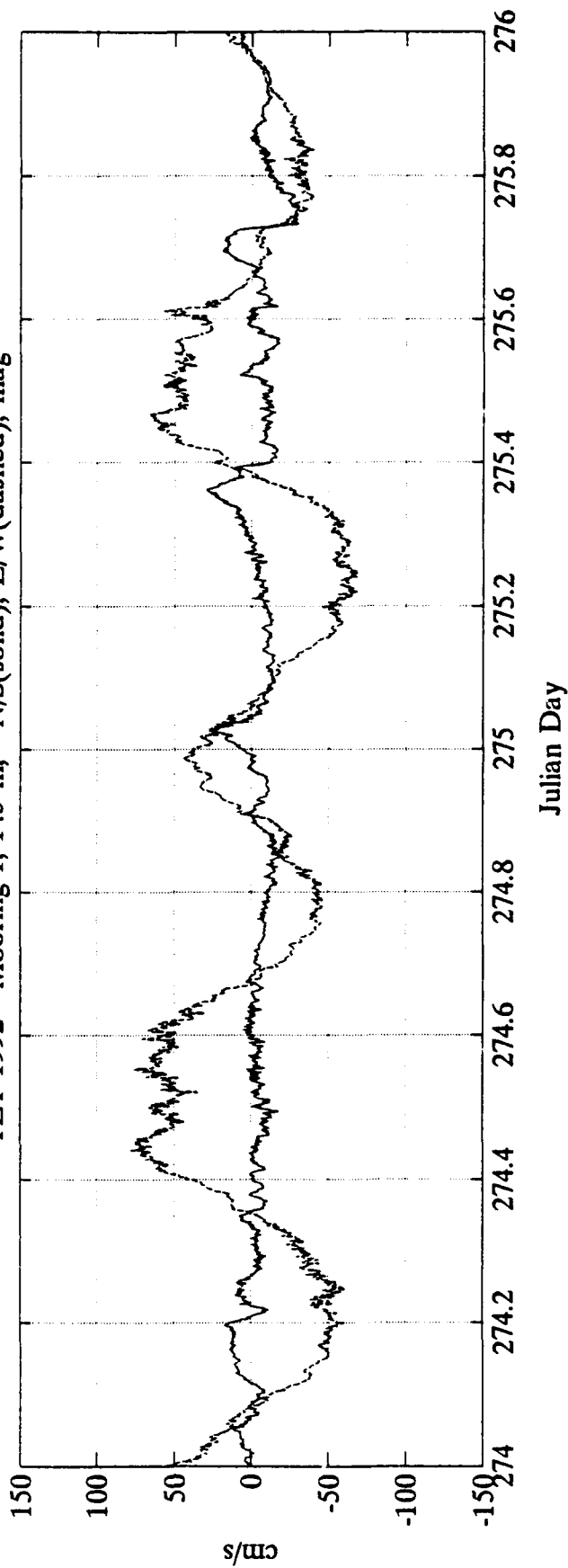




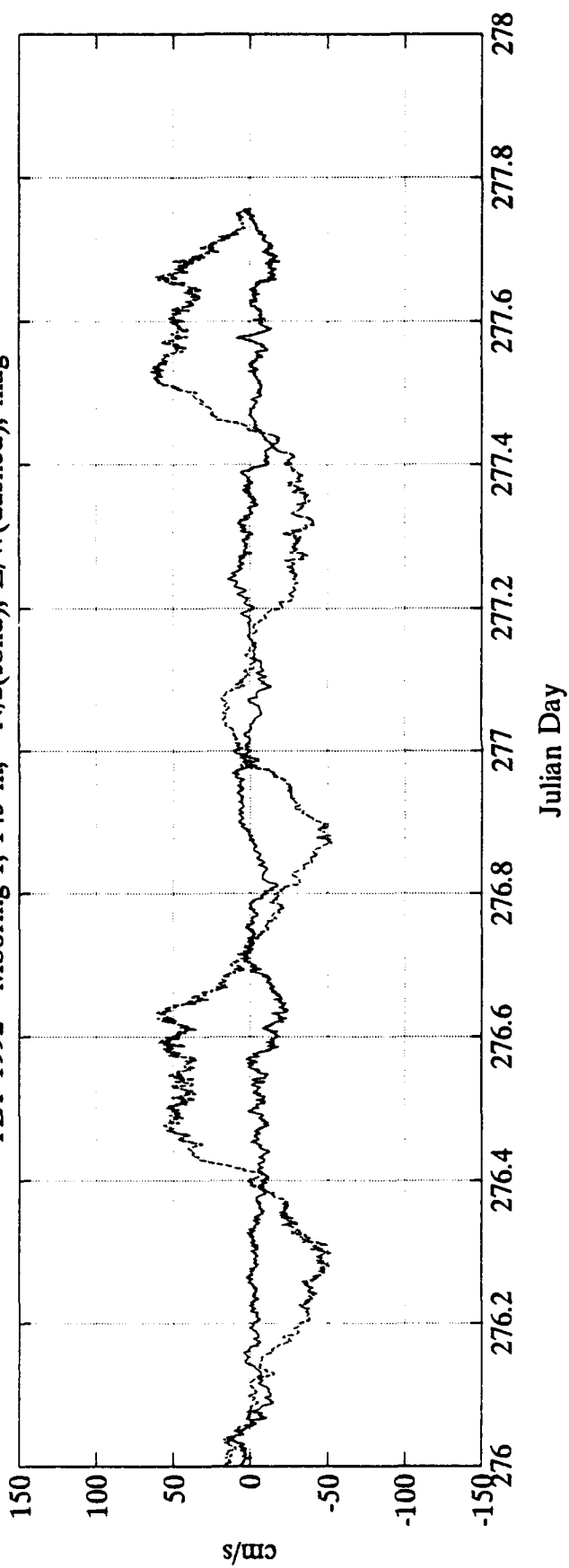
TET 1992 - Mooring 1, 145 m, N/S(solid), E/W(dashed), mag



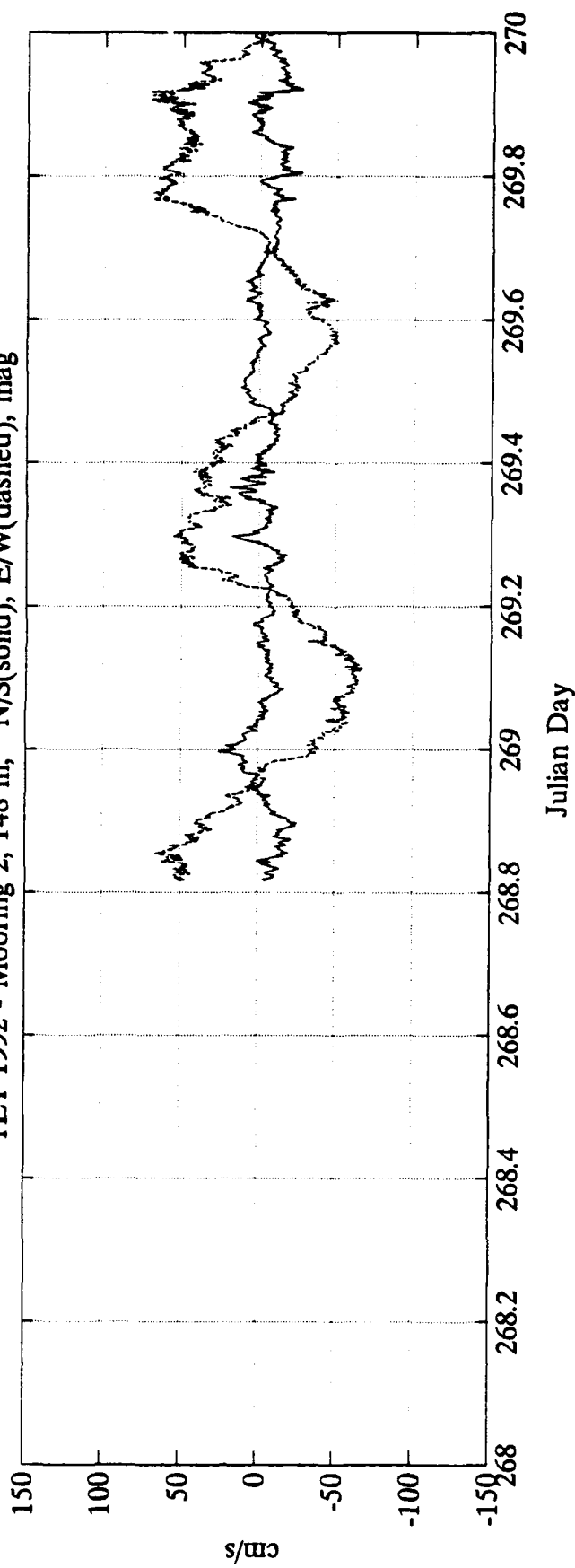
TET 1992 - Mooring 1, 145 m, N/S(solid), E/W(dashed), mag



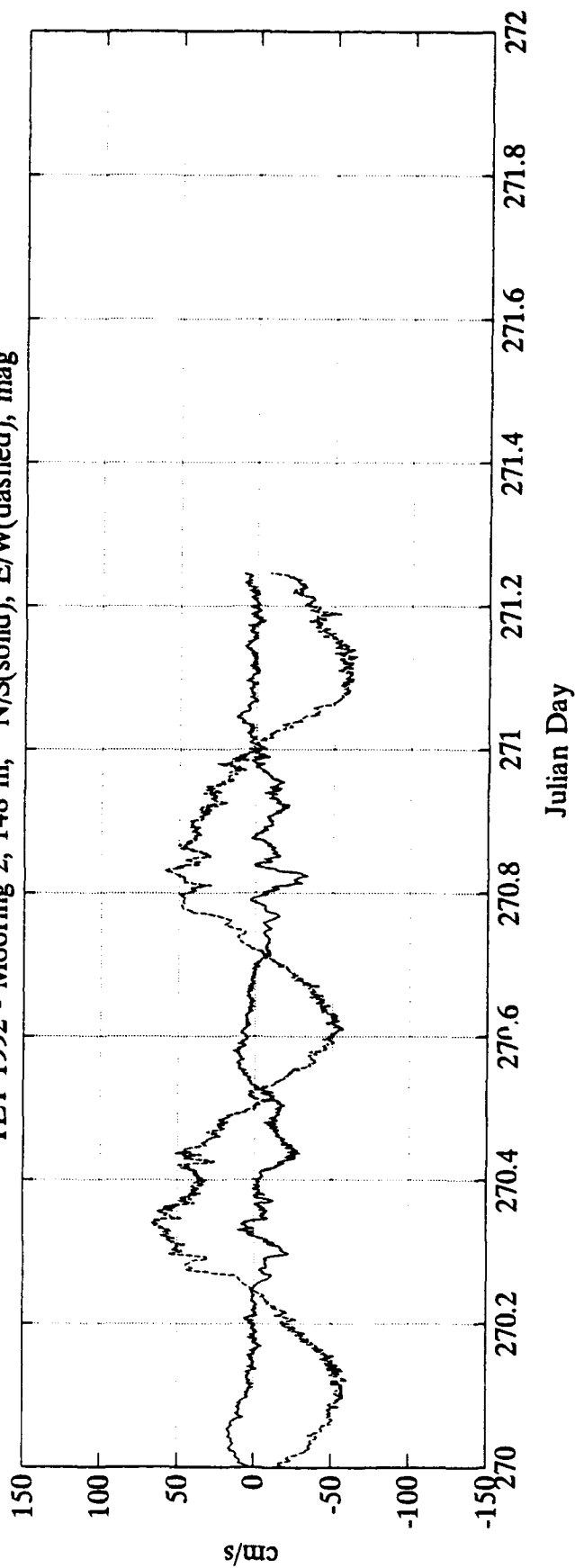
TET 1992 - Mooring 1, 145 m, N/S(solid), E/W(dashed), mag



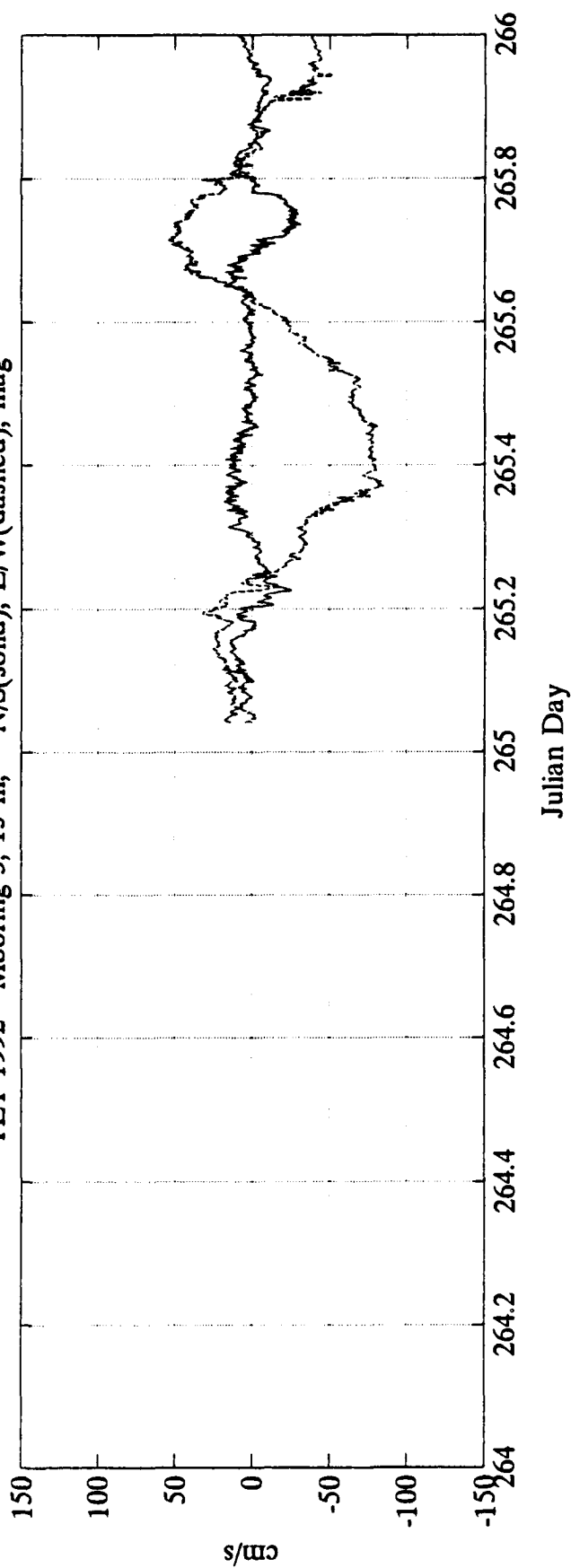
TET 1992 - Mooring 2, 148 m, N/S(solid), E/W(dashed), mag



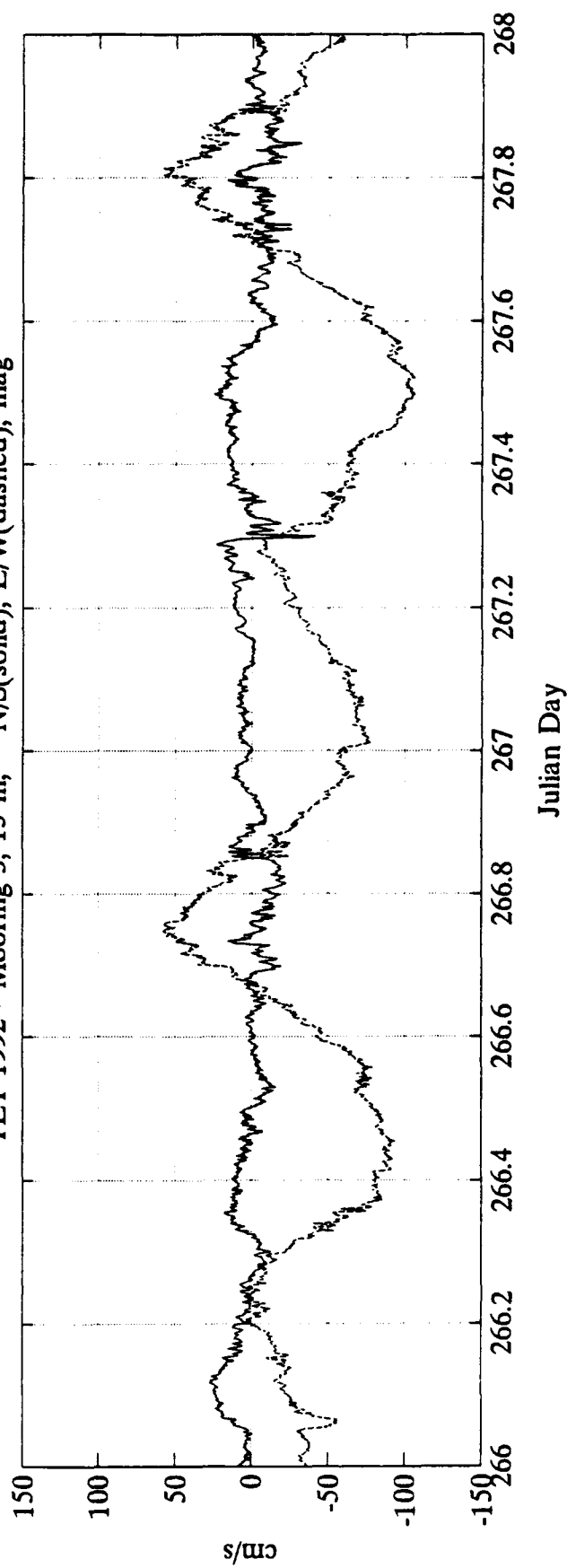
TET 1992 - Mooring 2, 148 m, N/S(solid), E/W(dashed), mag



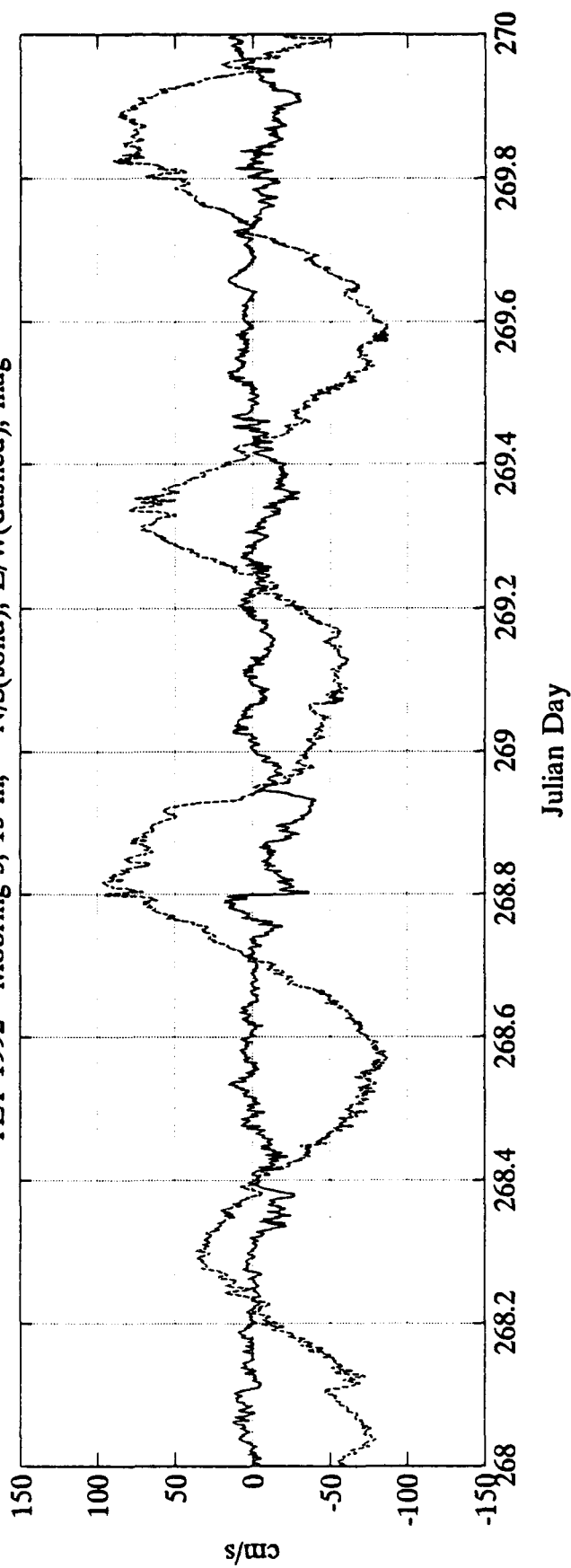
TET 1992 - Mooring 3, 15 m, N/S(solid), E/W(dashed), mag



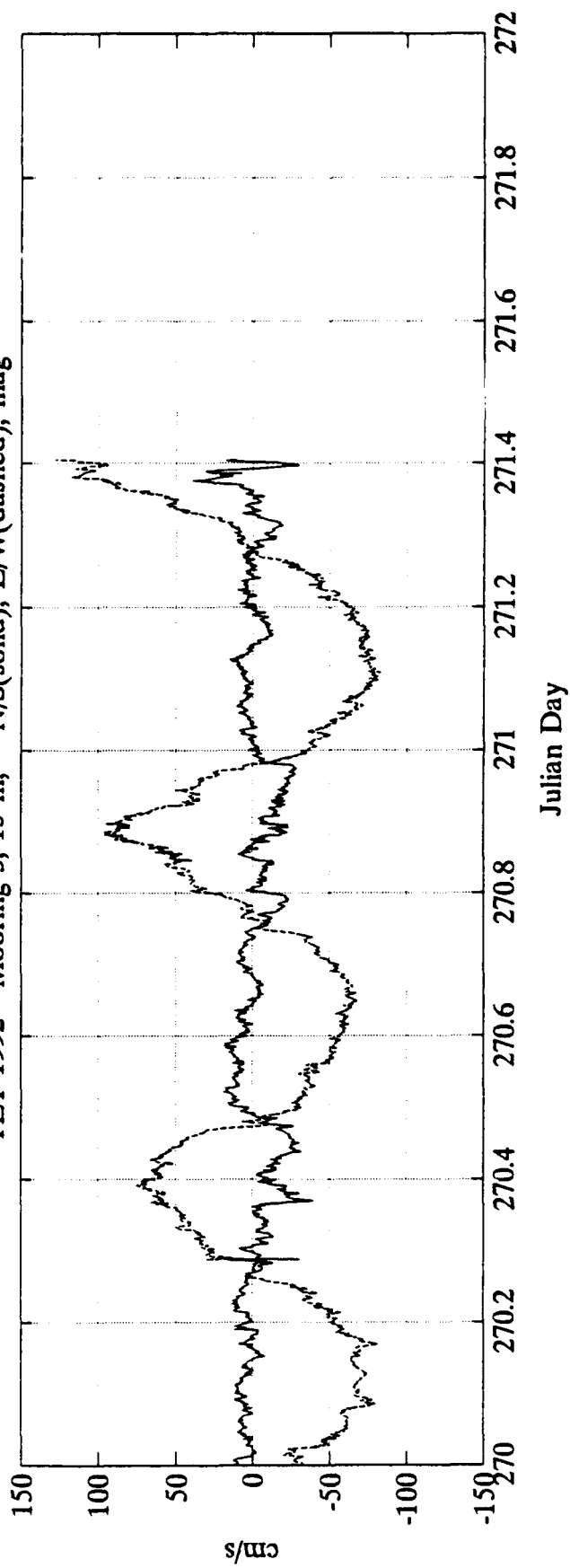
TET 1992 - Mooring 3, 15 m, N/S(solid), E/W(dashed), mag

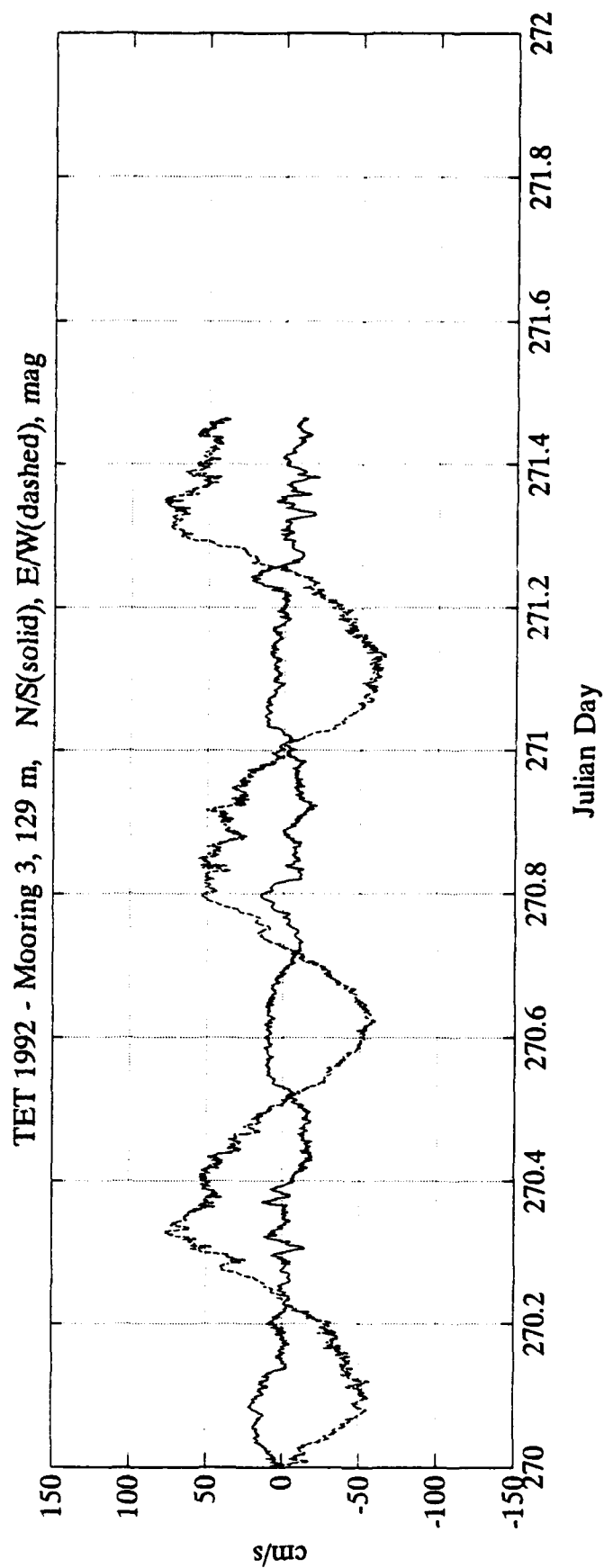
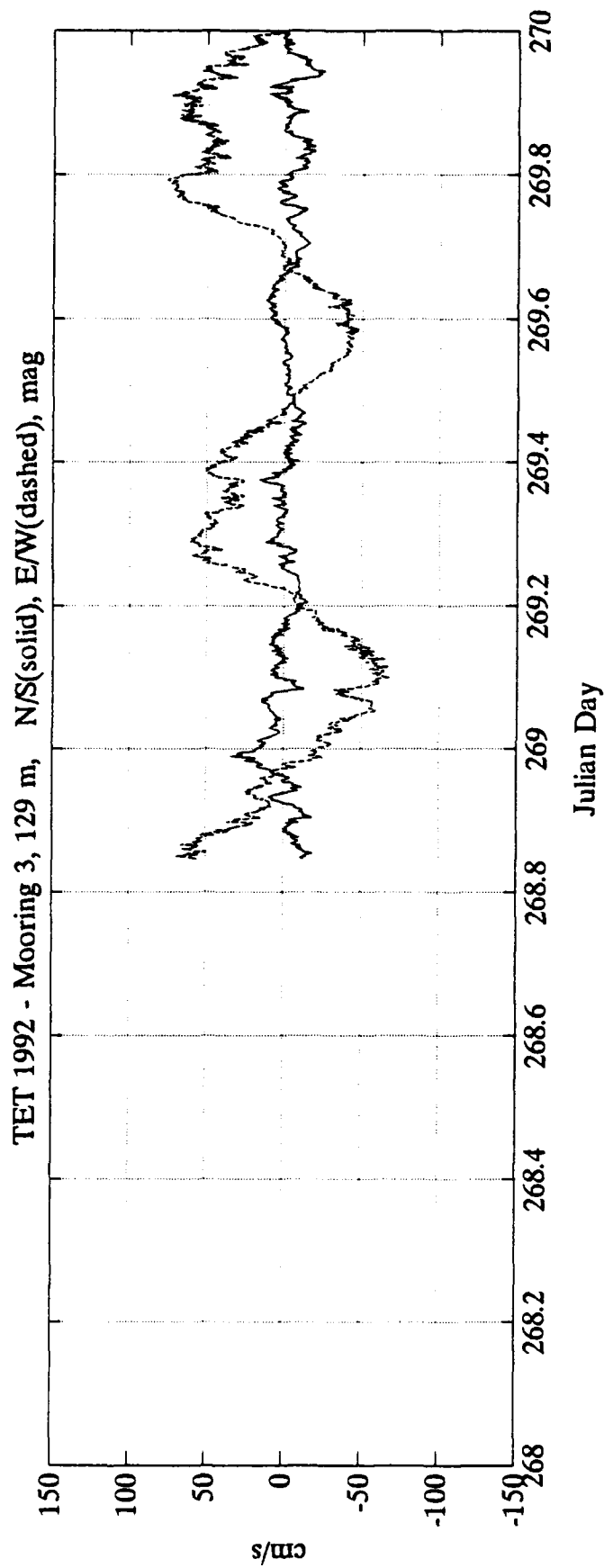


TET 1992 - Mooring 3, 15 m, N/S(solid), E/W(dashed), mag

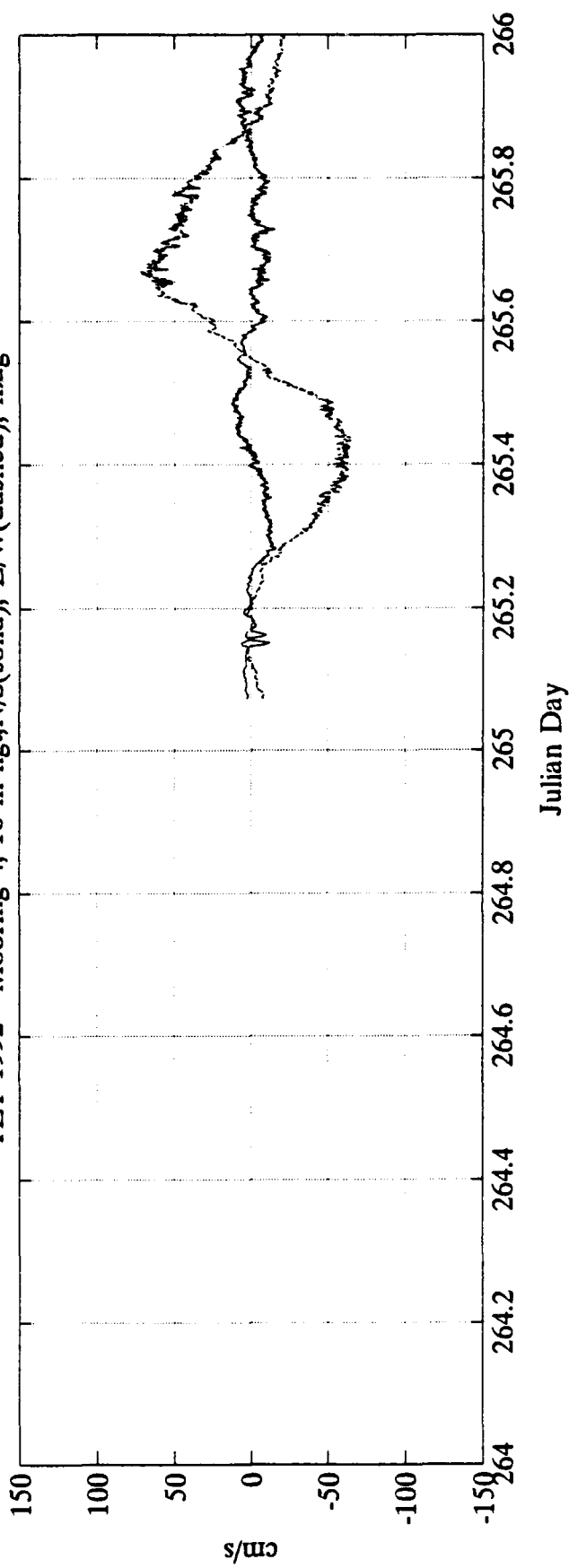


TET 1992 - Mooring 3, 15 m, N/S(solid), E/W(dashed), mag

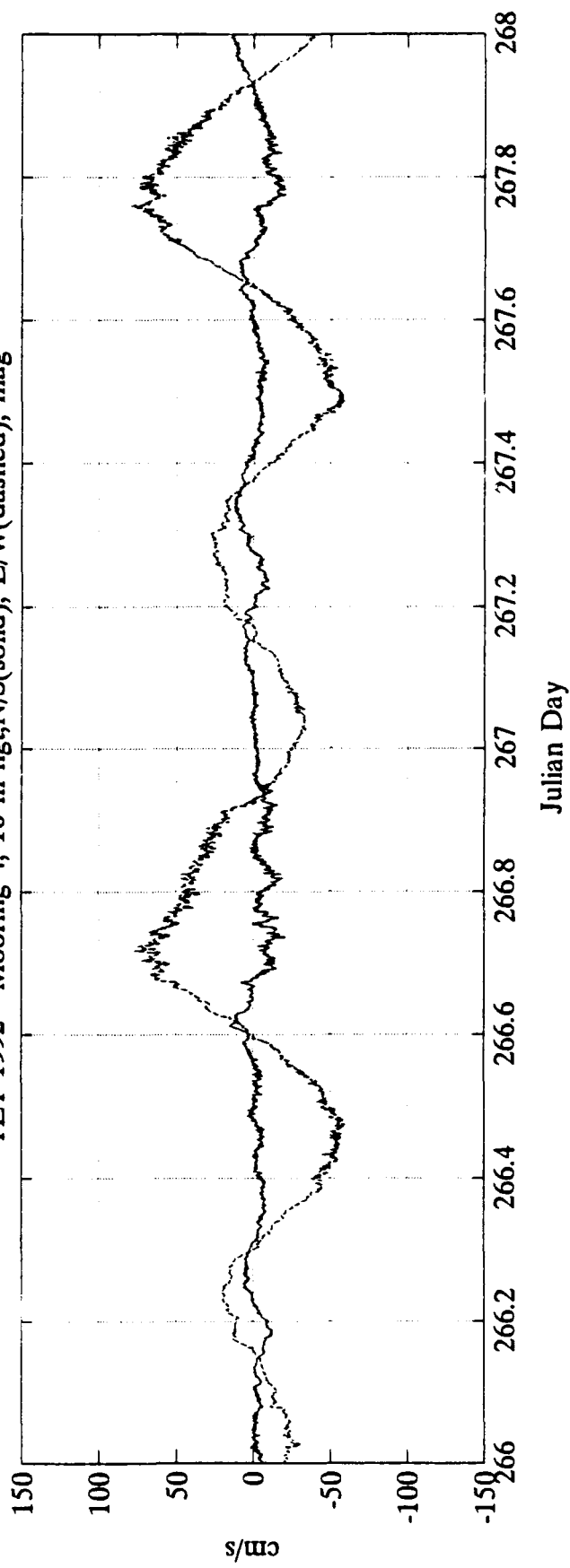




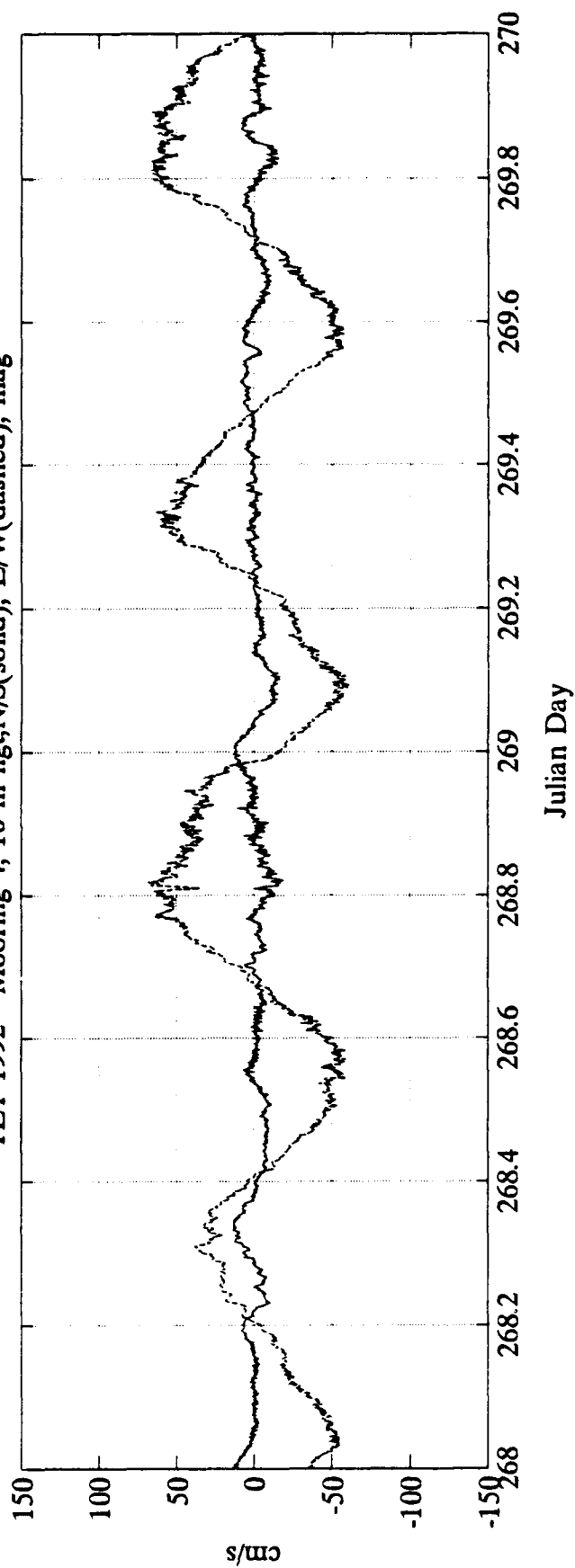
TET 1992 - Mooring 4, 10 m hgt, N/S(solid), E/W(dashed), mag



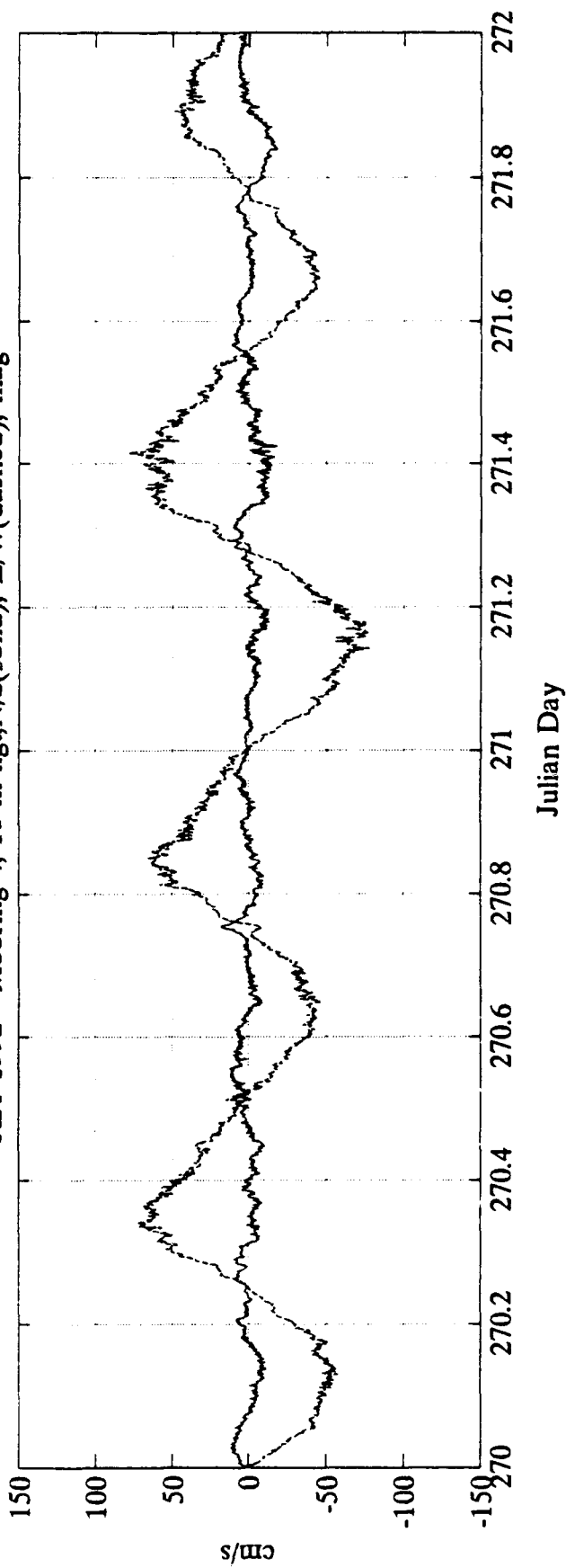
TET 1992 - Mooring 4, 10 m hgt, N/S(solid), E/W(dashed), mag



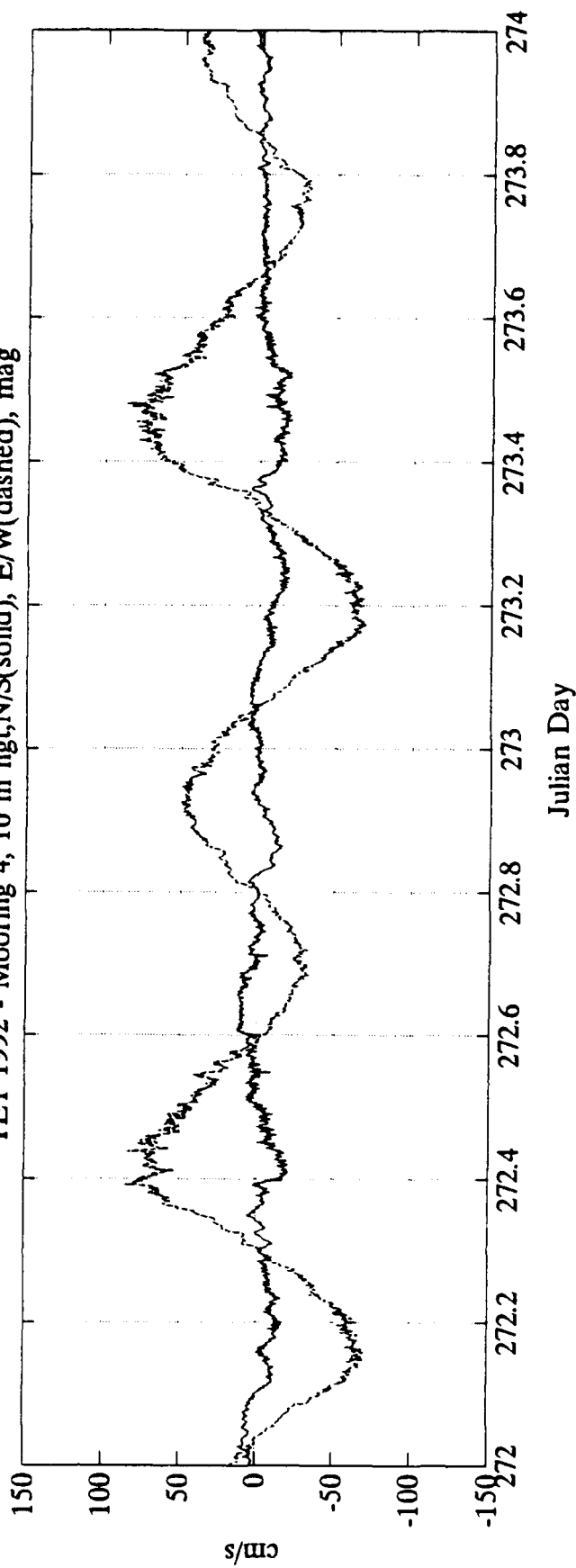
TET 1992 - Mooring 4, 10 m hgt, N/S(solid), E/W(dashed), mag



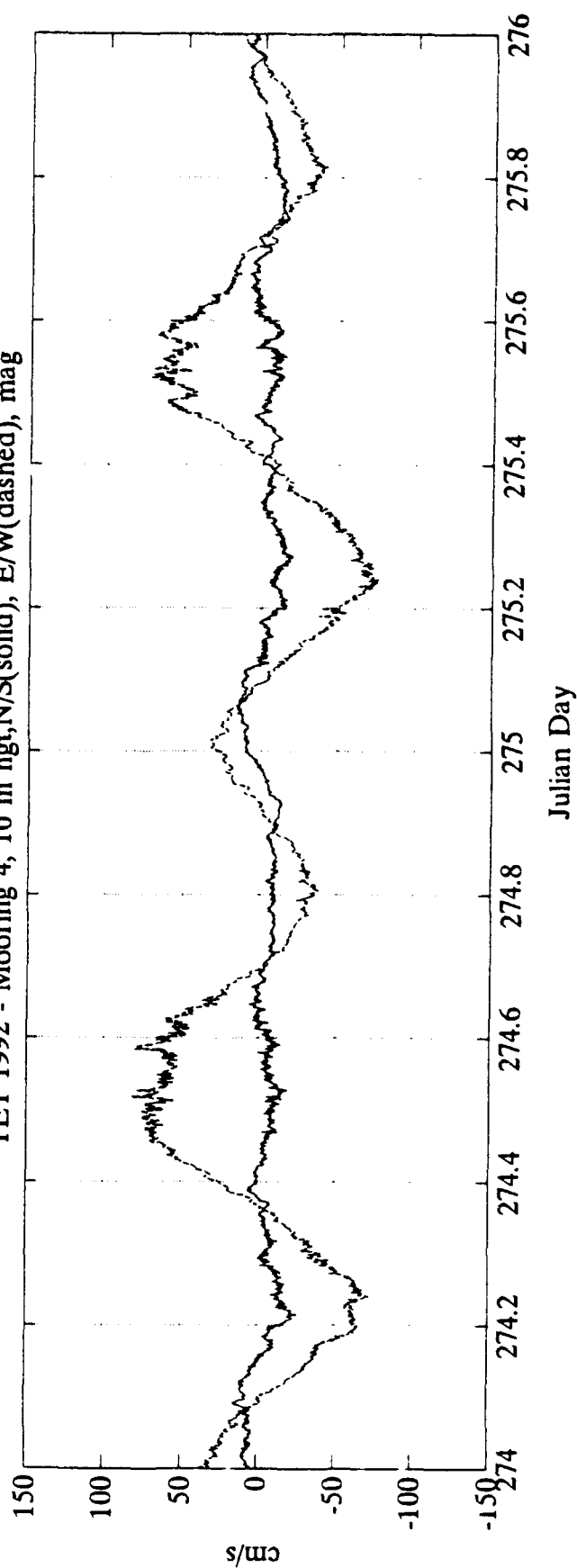
TET 1992 - Mooring 4, 10 m hgt, N/S(solid), E/W(dashed), mag

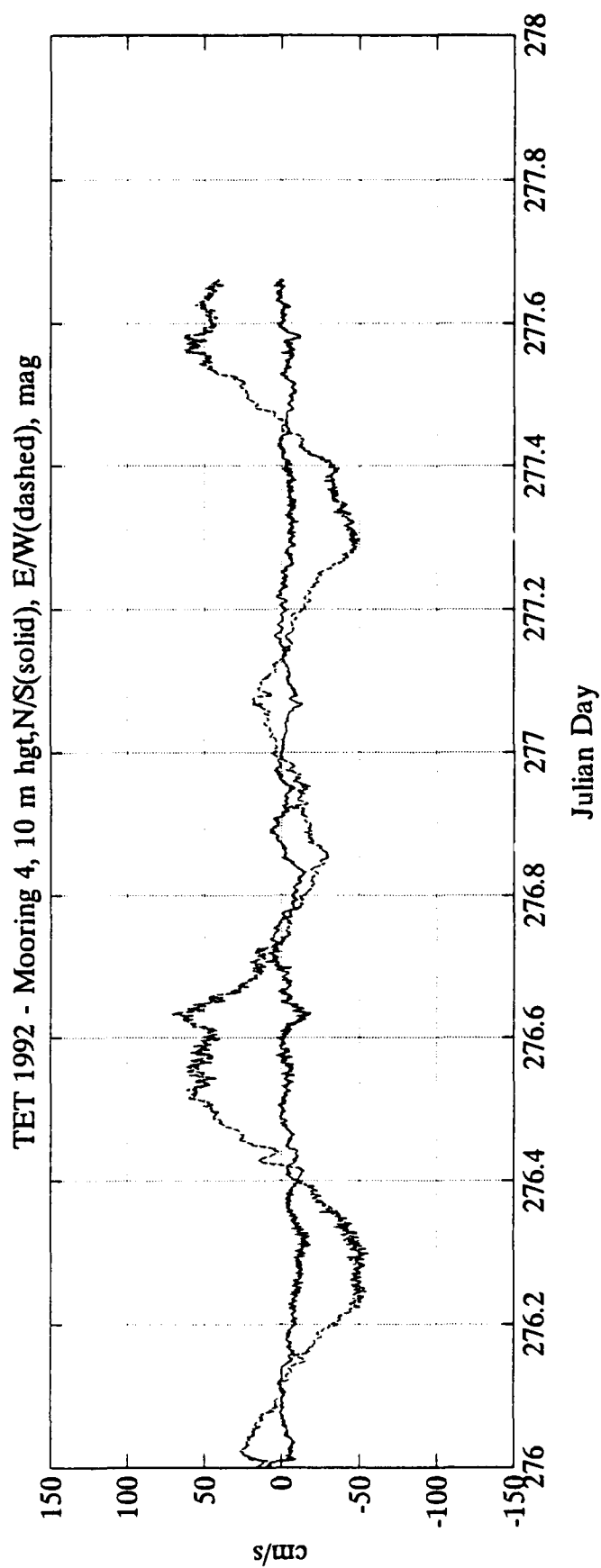


TET 1992 - Mooring 4, 10 m hgt, N/S(solid), E/W(dashed), mag

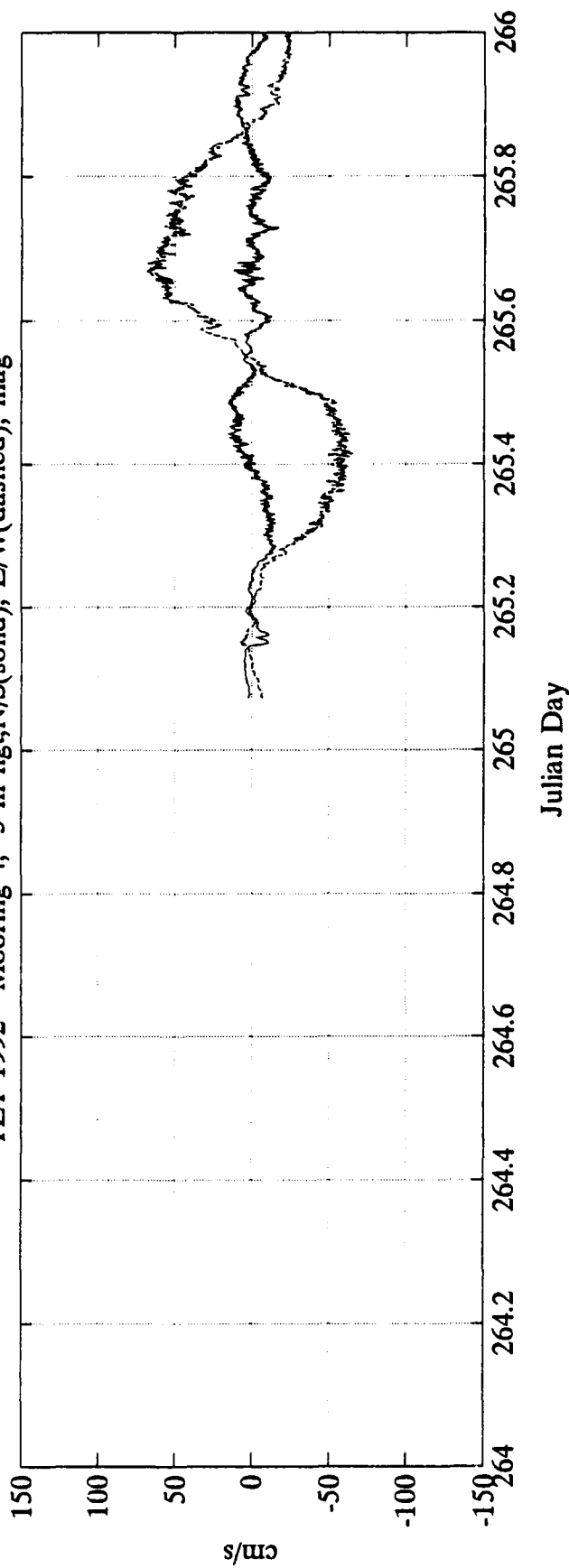


TET 1992 - Mooring 4, 10 m hgt, N/S(solid), E/W(dashed), mag

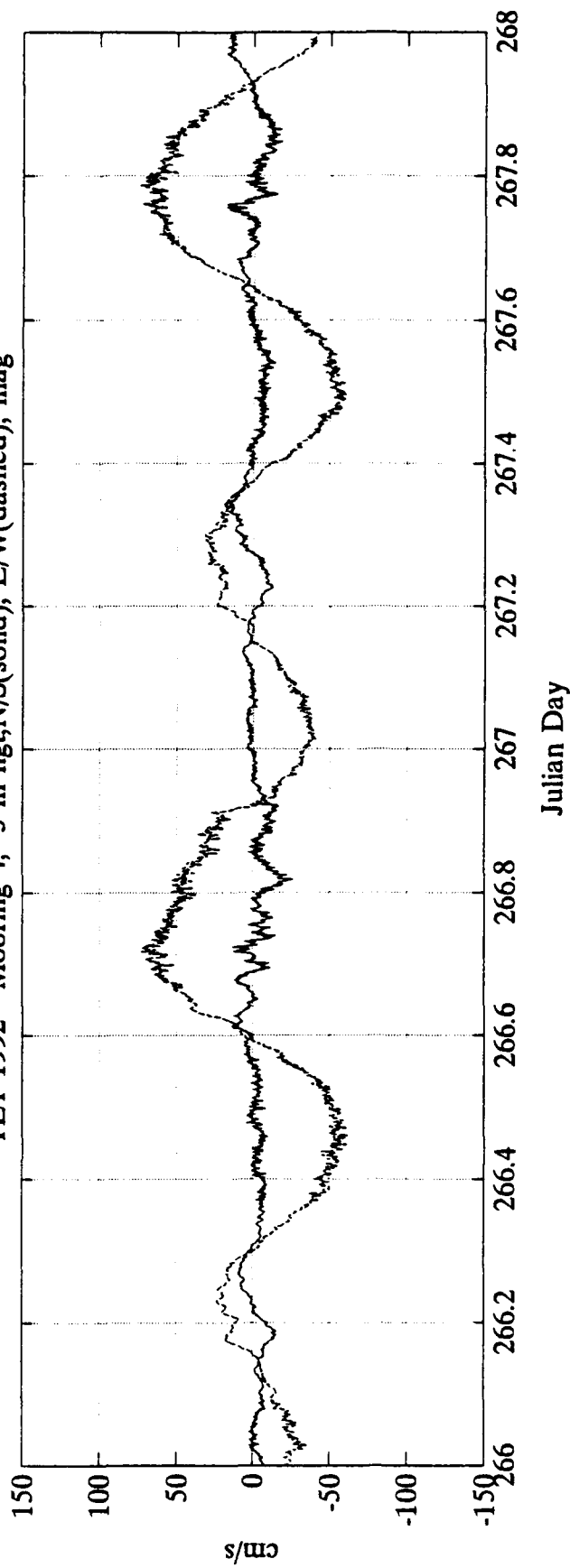




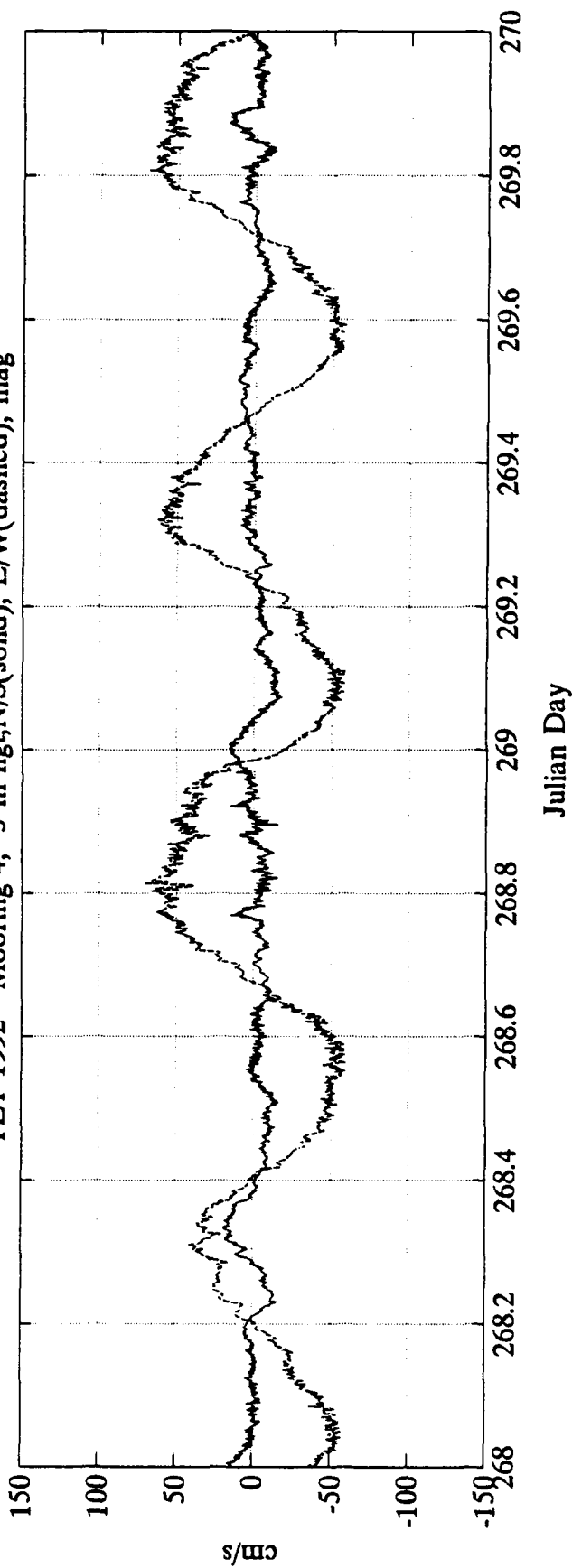
TET 1992 - Mooring 4, 5 m hgt, N/S(solid), E/W(dashed), mag



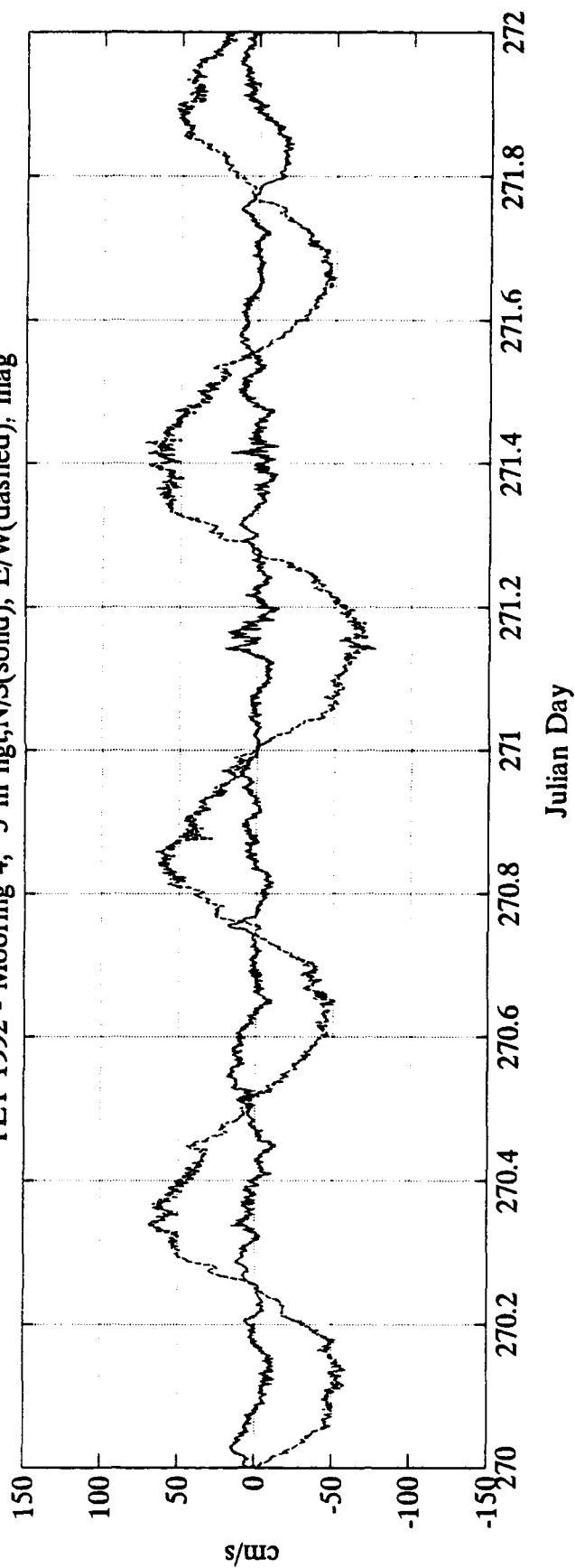
TET 1992 - Mooring 4, 5 m hgt, N/S(solid), E/W(dashed), mag



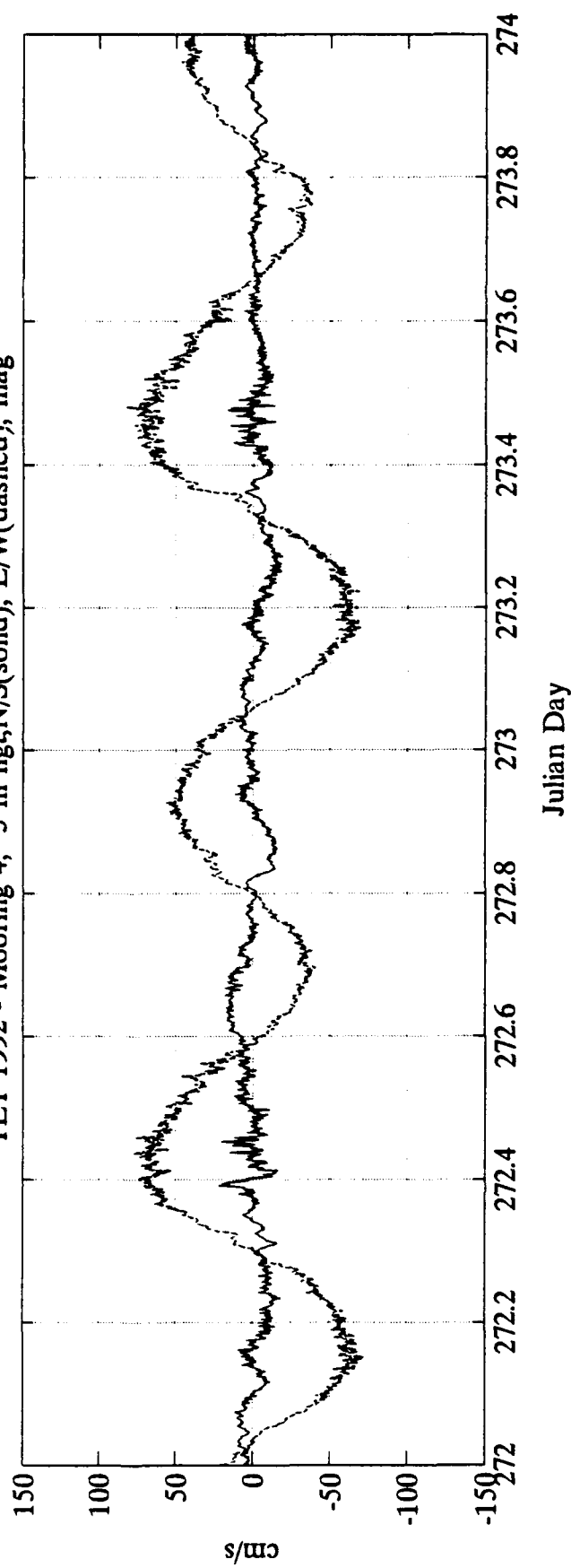
TET 1992 - Mooring 4, 5 m hgt,N/S(solid), E/W(dashed), mag



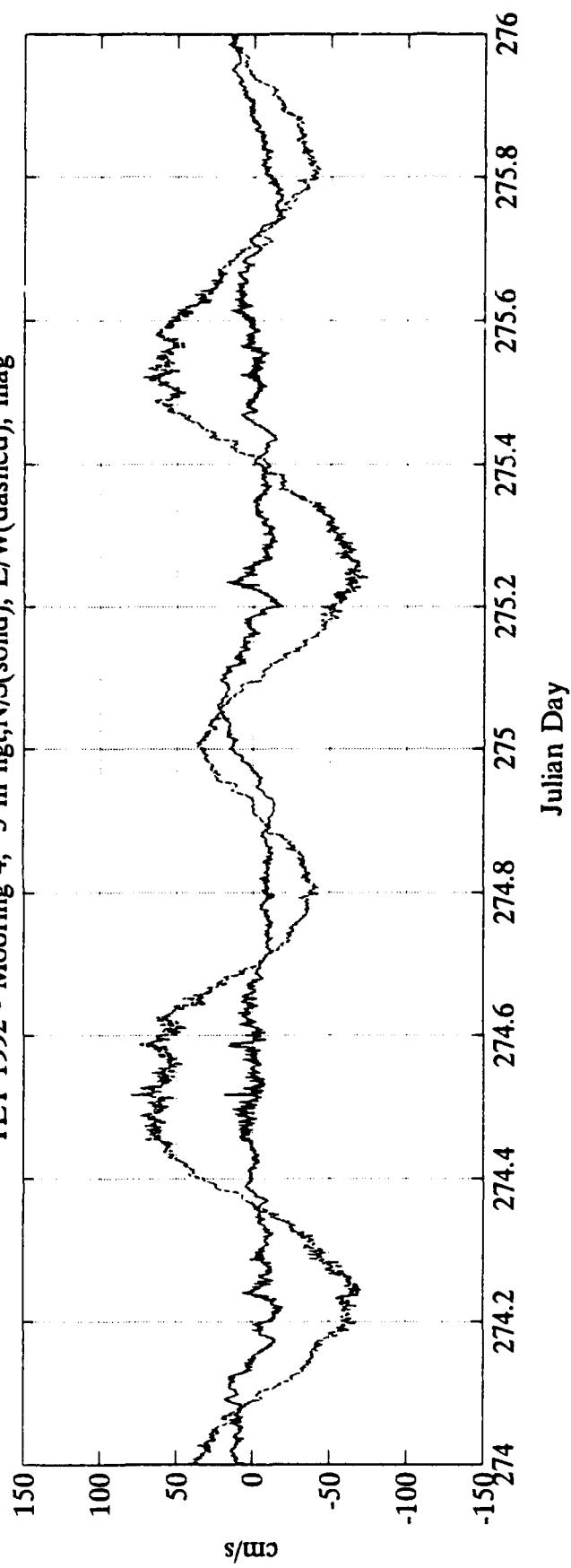
TET 1992 - Mooring 4, 5 m hgt,N/S(solid), E/W(dashed), mag



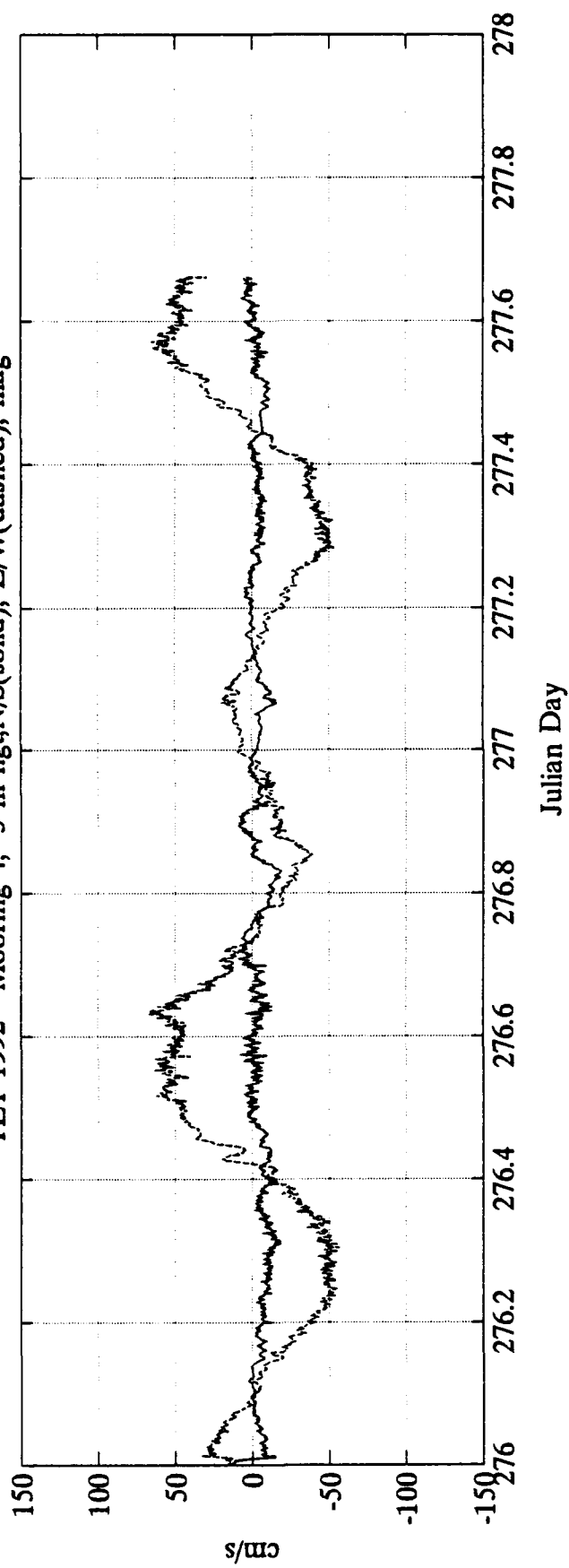
TET 1992 - Mooring 4, 5 m hgt, N/S(solid), E/W(dashed), mag



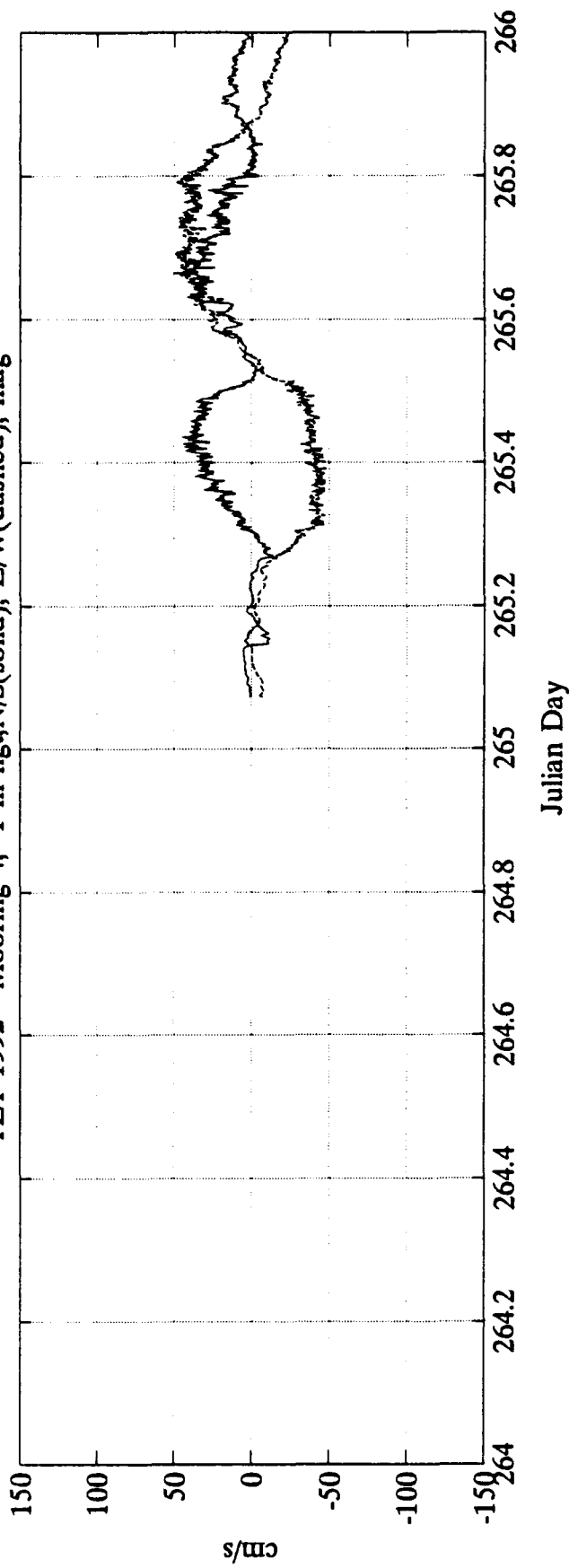
TET 1992 - Mooring 4, 5 m hgt, N/S(solid), E/W(dashed), mag



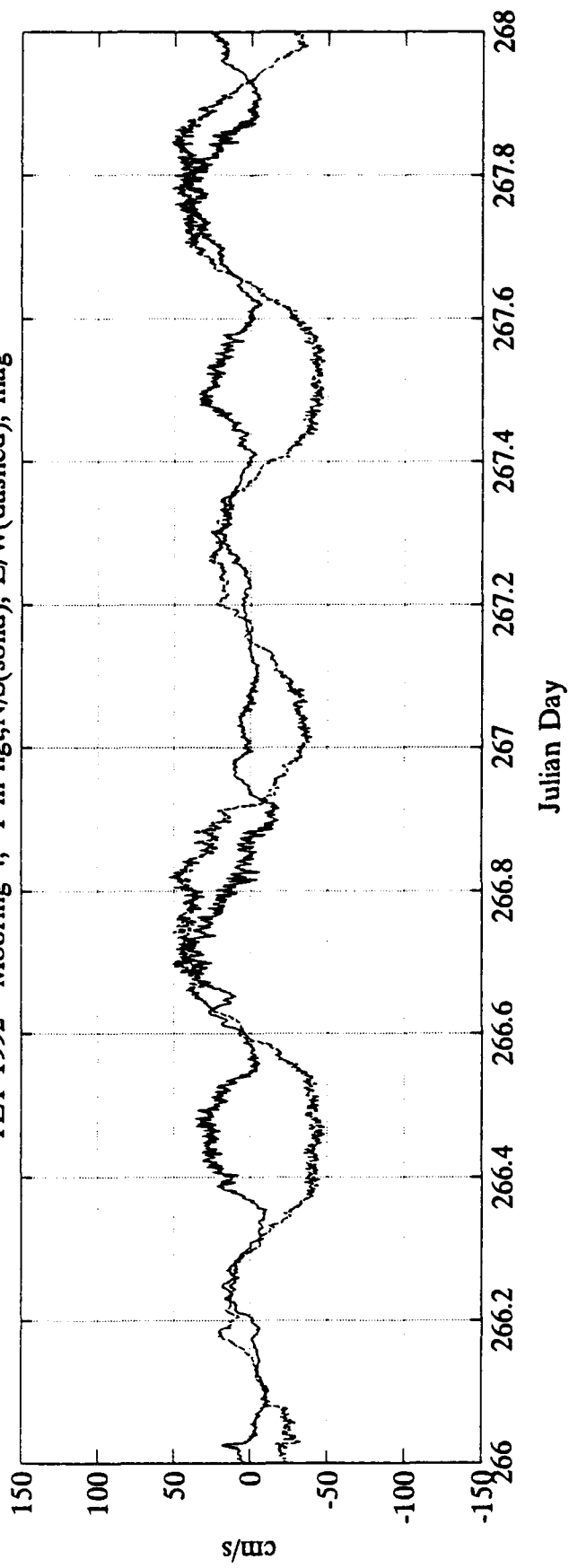
TET 1992 - Mooring 4, 5 m hgt,N/S(solid), E/W(dashed), mag

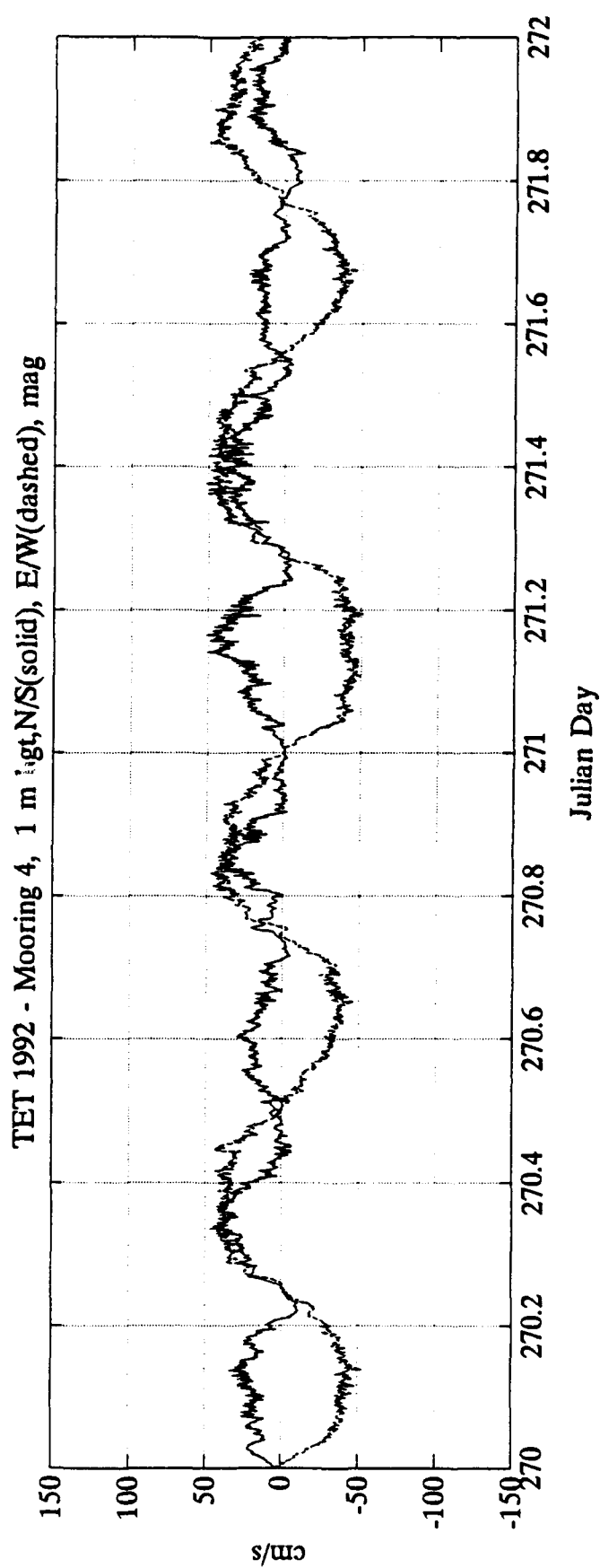
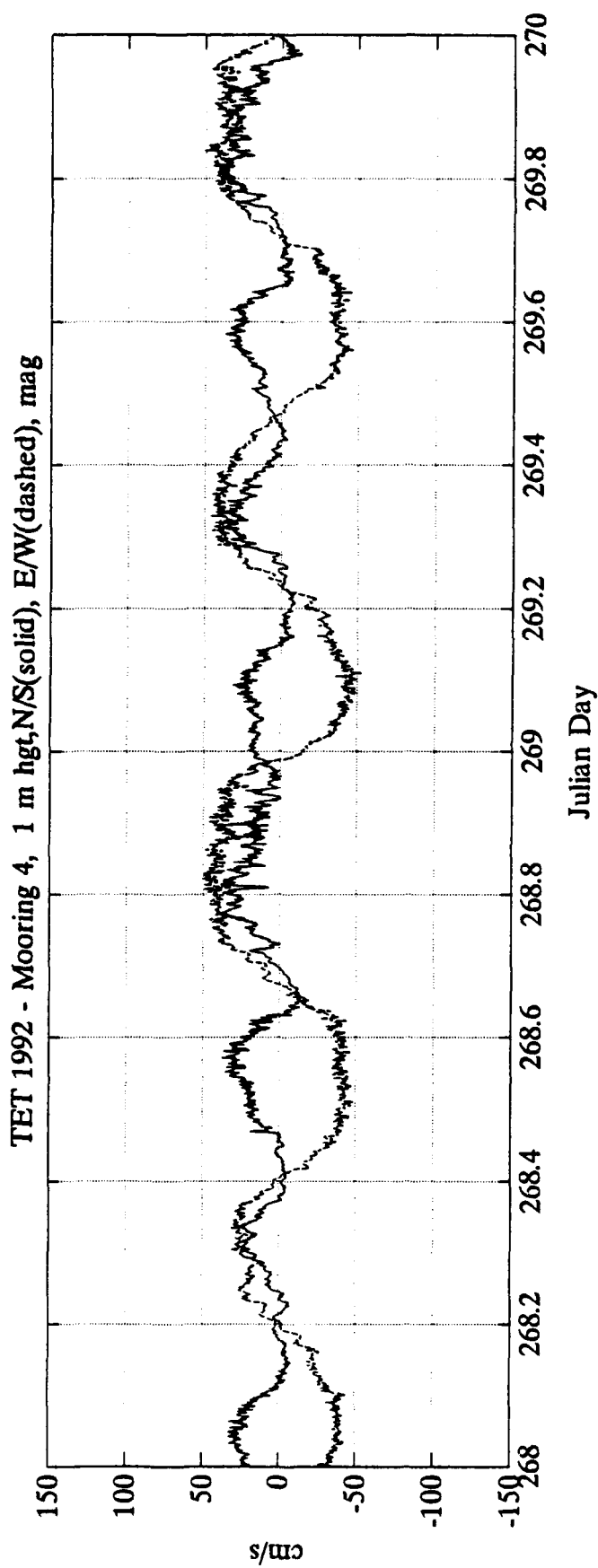


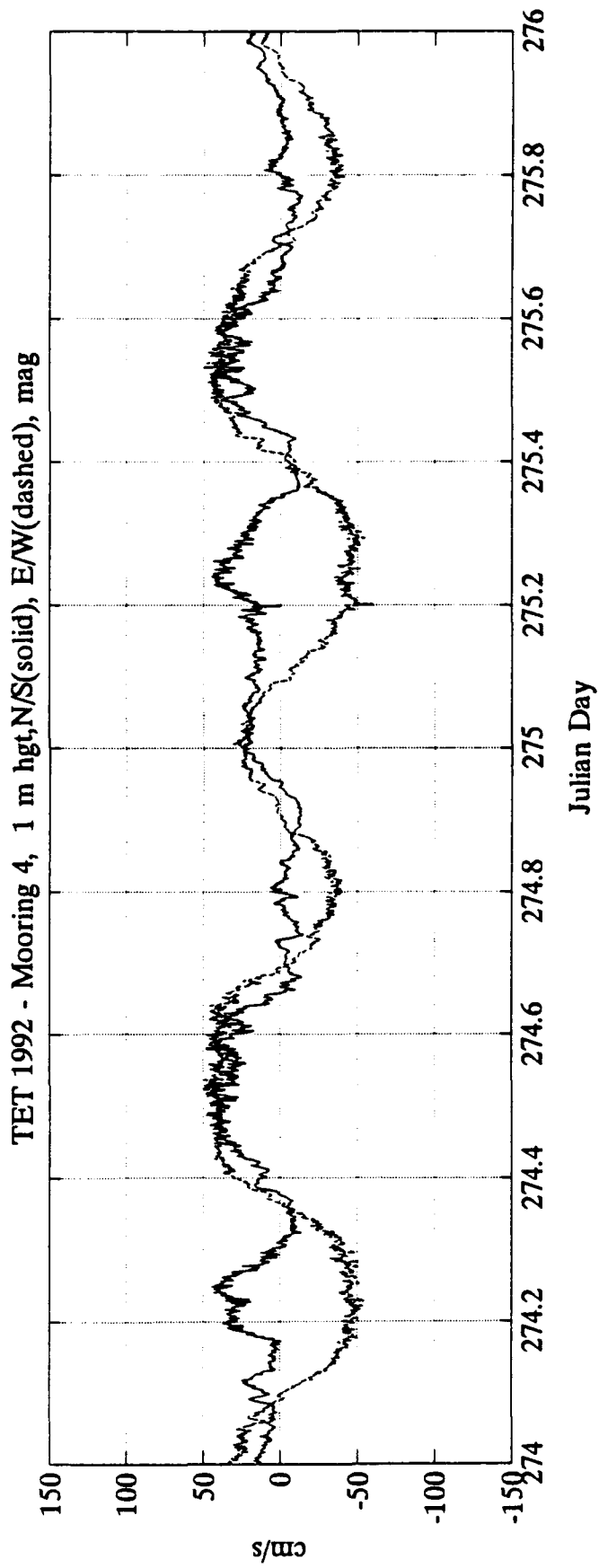
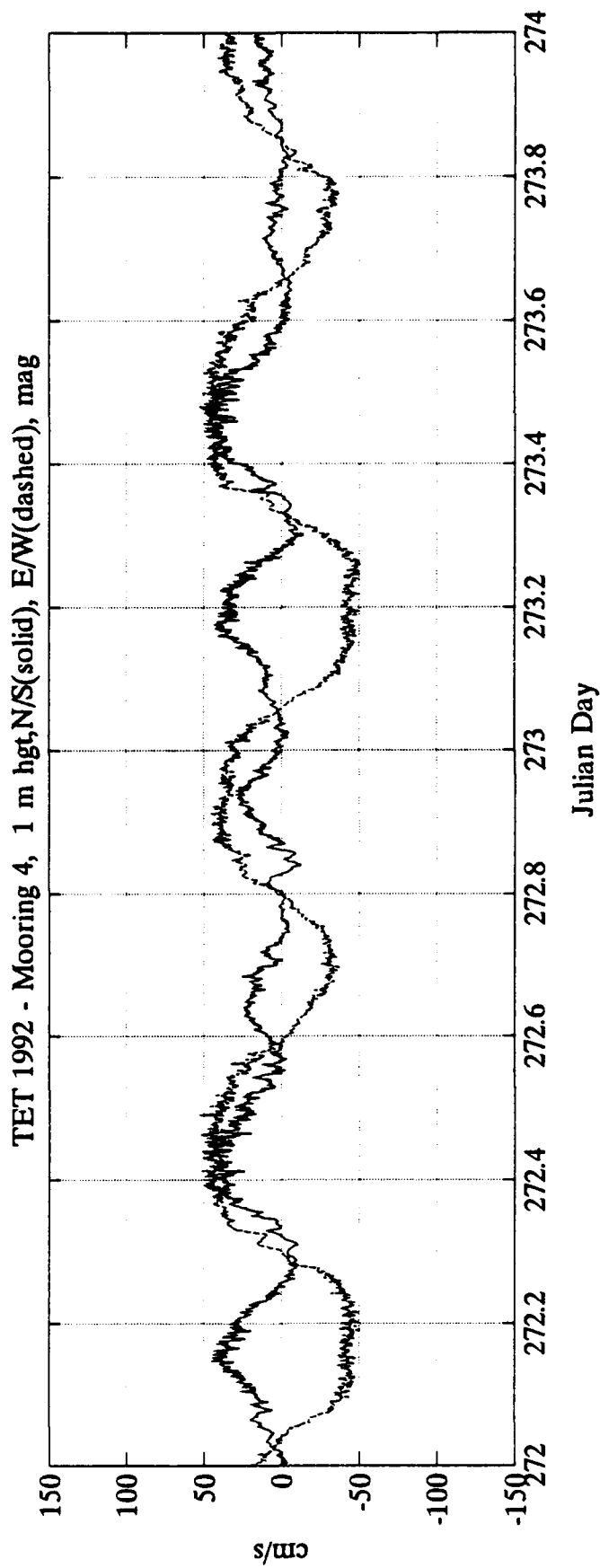
TET 1992 - Mooring 4, 1 m hgt,N/S(solid), E/W(dashed), mag

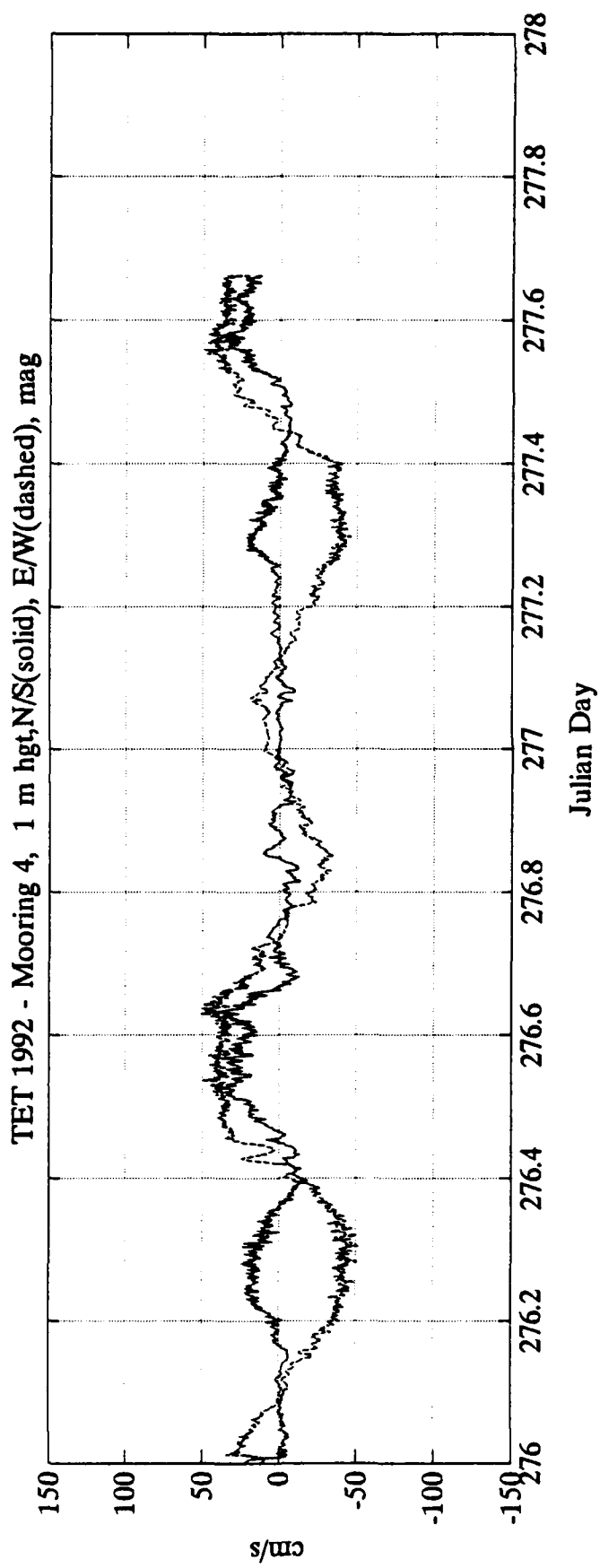


TET 1992 - Mooring 4, 1 m hgt,N/S(solid), E/W(dashed), mag









APPENDIX B

Time Series of Temperature Isotherms and Current Velocity at 15 m, Mooring 1

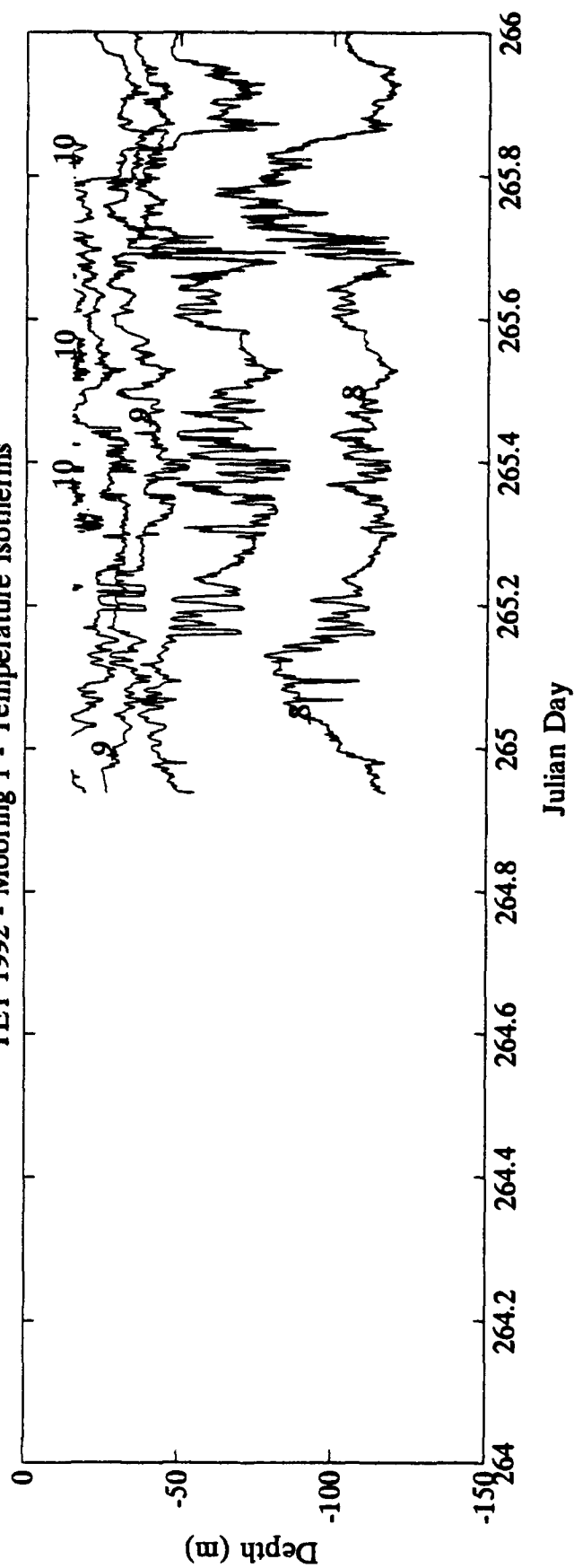
Time series plots of Temperature Isotherms throughout the water column and two day alongshore (E/W) and across shore (N/S) current velocity time series plots are shown at 15 meters for mooring 1. Alongshore currents are shown with a dashed line and across shore currents are shown with a solid line. Directions are in magnetic North. There are 2 two day windows plotted on each page.

LIST OF FIGURES

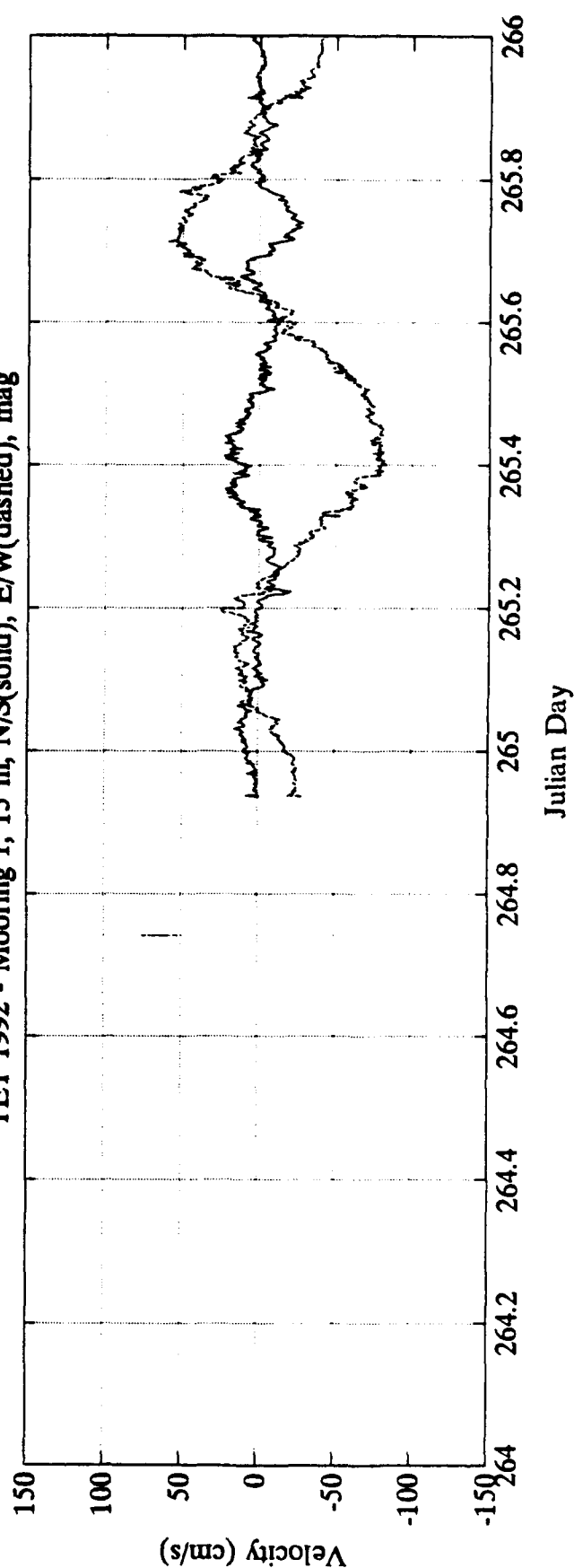
APPENDIX B

Mooring 1 Temperature Isotherms and Current Velocity at 15 m, JD 264 - 266	B-3
Mooring 1 Temperature Isotherms and Current Velocity at 15 m, JD 266 - 268	B-4
Mooring 1 Temperature Isotherms and Current Velocity at 15 m, JD 268 - 270	B-5
Mooring 1 Temperature Isotherms and Current Velocity at 15 m, JD 270 - 272	B-6
Mooring 1 Temperature Isotherms and Current Velocity at 15 m, JD 272 - 274	B-7
Mooring 1 Temperature Isotherms and Current Velocity at 15 m, JD 274 - 276	B-8
Mooring 1 Temperature Isotherms and Current Velocity at 15 m, JD 276 - 278	B-9

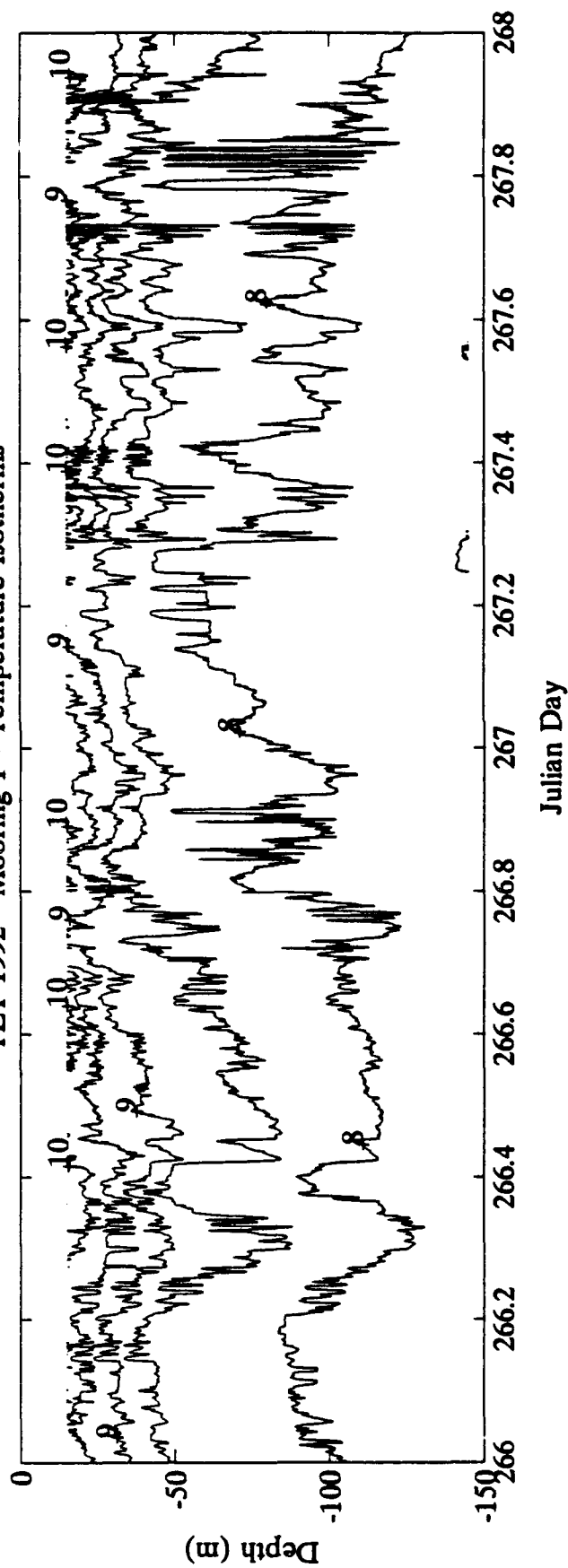
TET 1992 - Mooring 1 - Temperature Isotherms



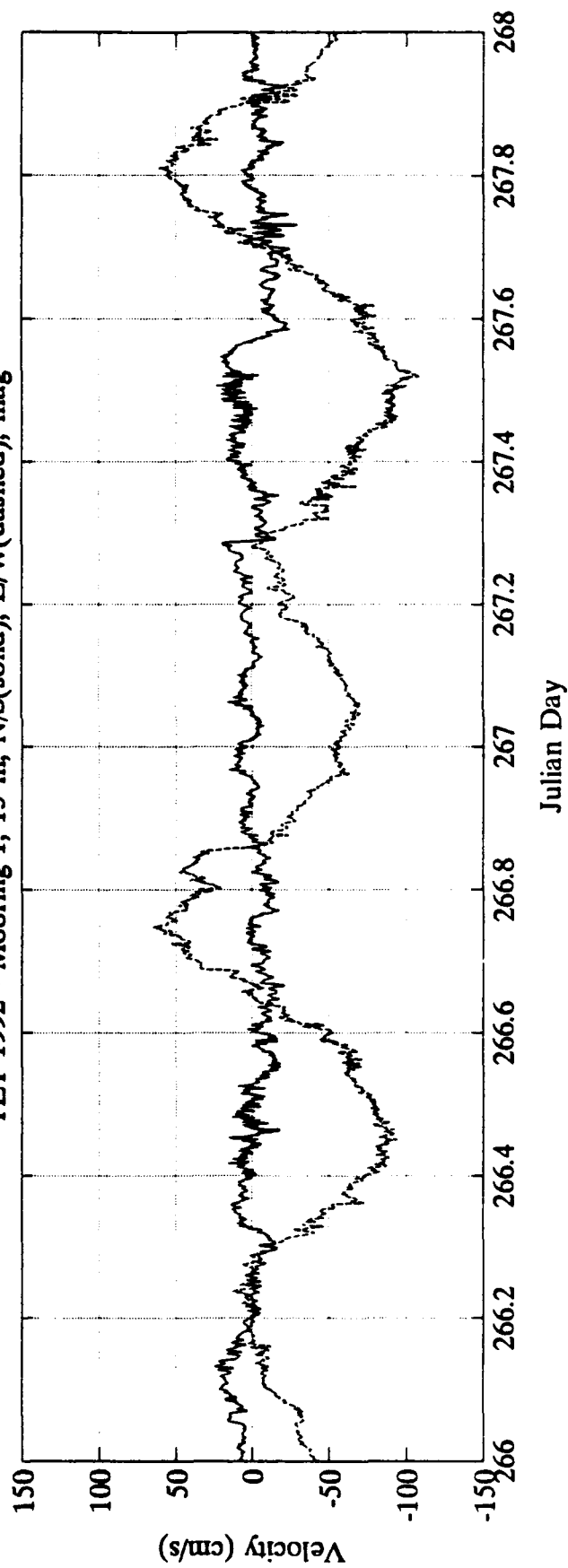
TET 1992 - Mooring 1, 15 m, N/S(solid), E/W(dashed), mag



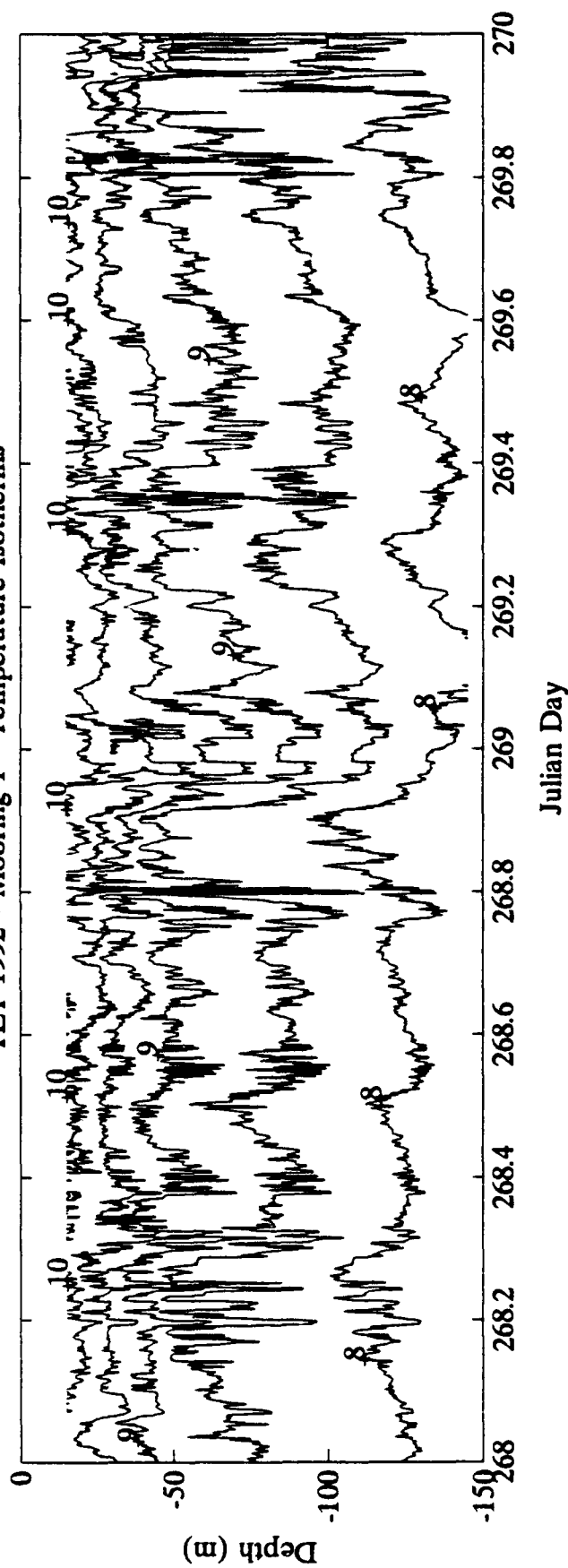
TET 1992 - Mooring 1 - Temperature Isotherms



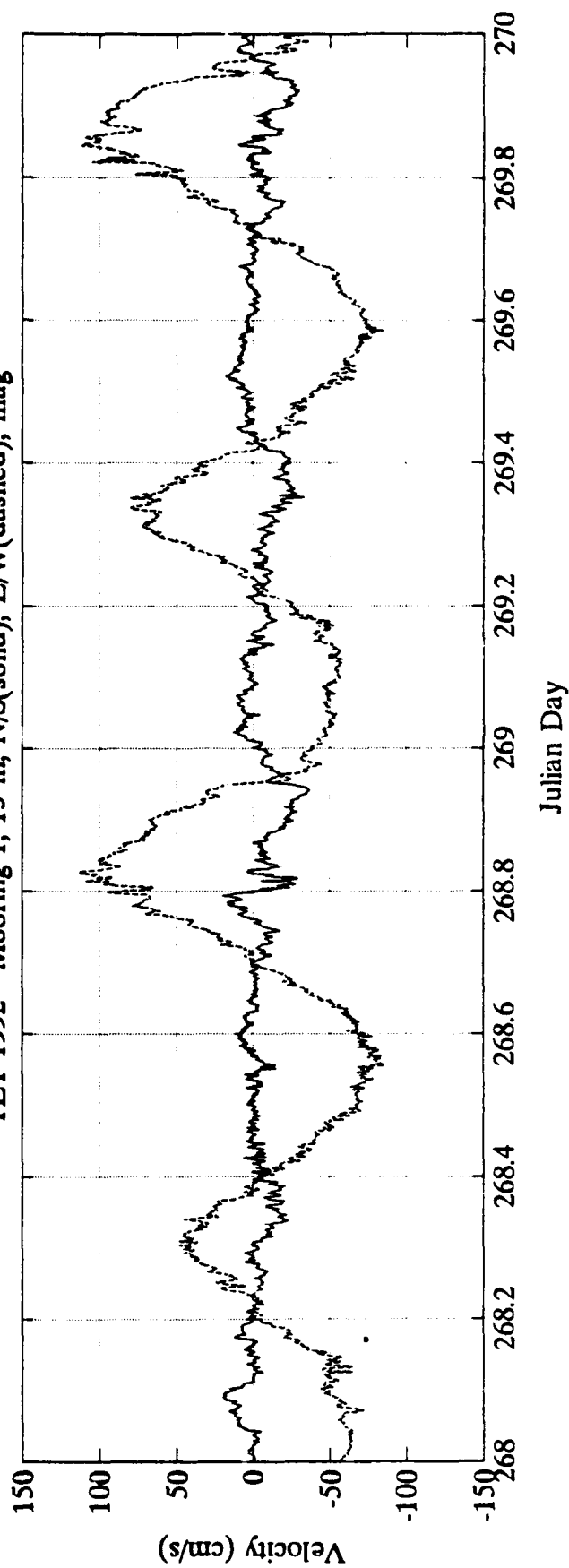
TET 1992 - Mooring 1, 15 m, N/S(solid), E/W(dashed), mag



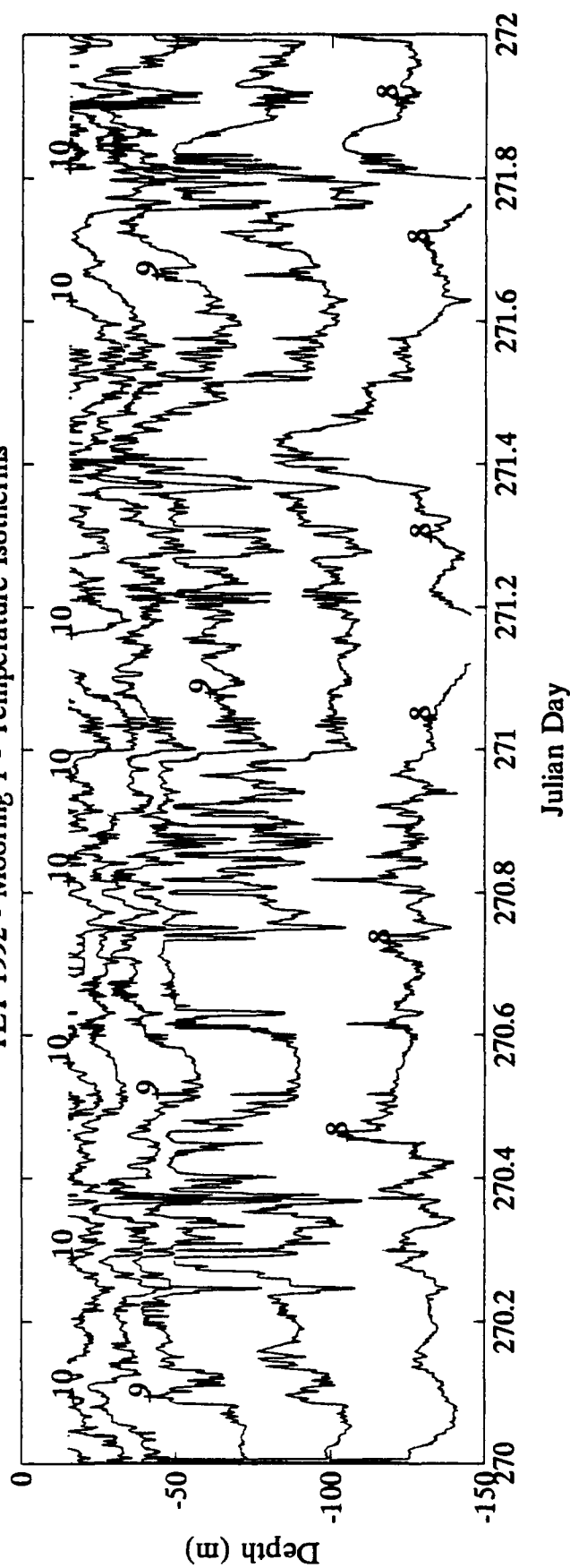
TET 1992 - Mooring 1 - Temperature Isotherms



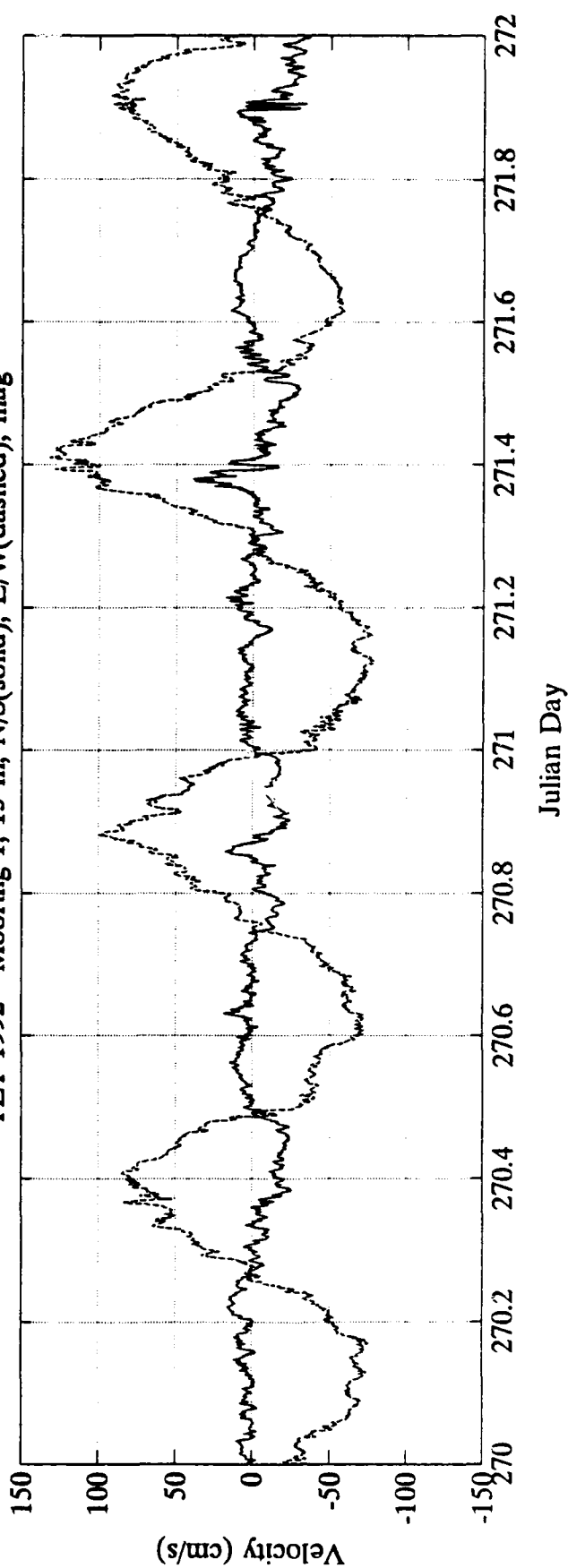
TET 1992 - Mooring 1, 15 m, N/S(solid), E/W(dashed), mag



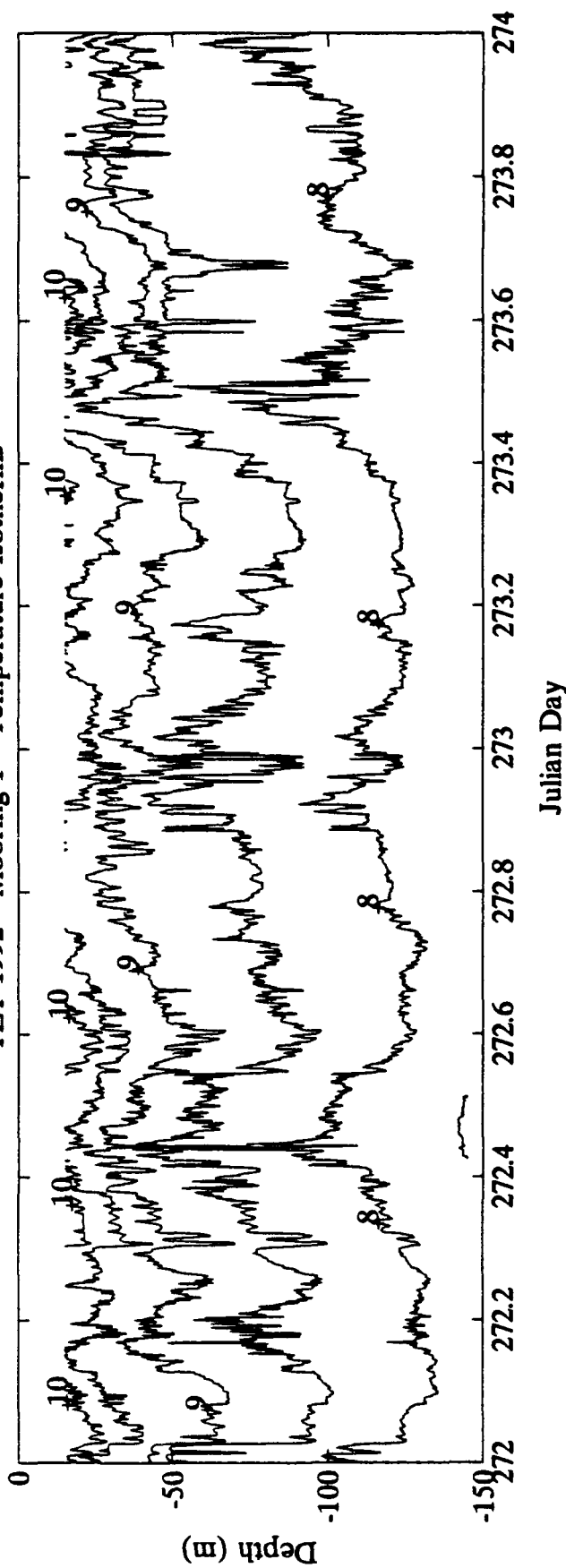
TET 1992 - Mooring 1 - Temperature Isotherms



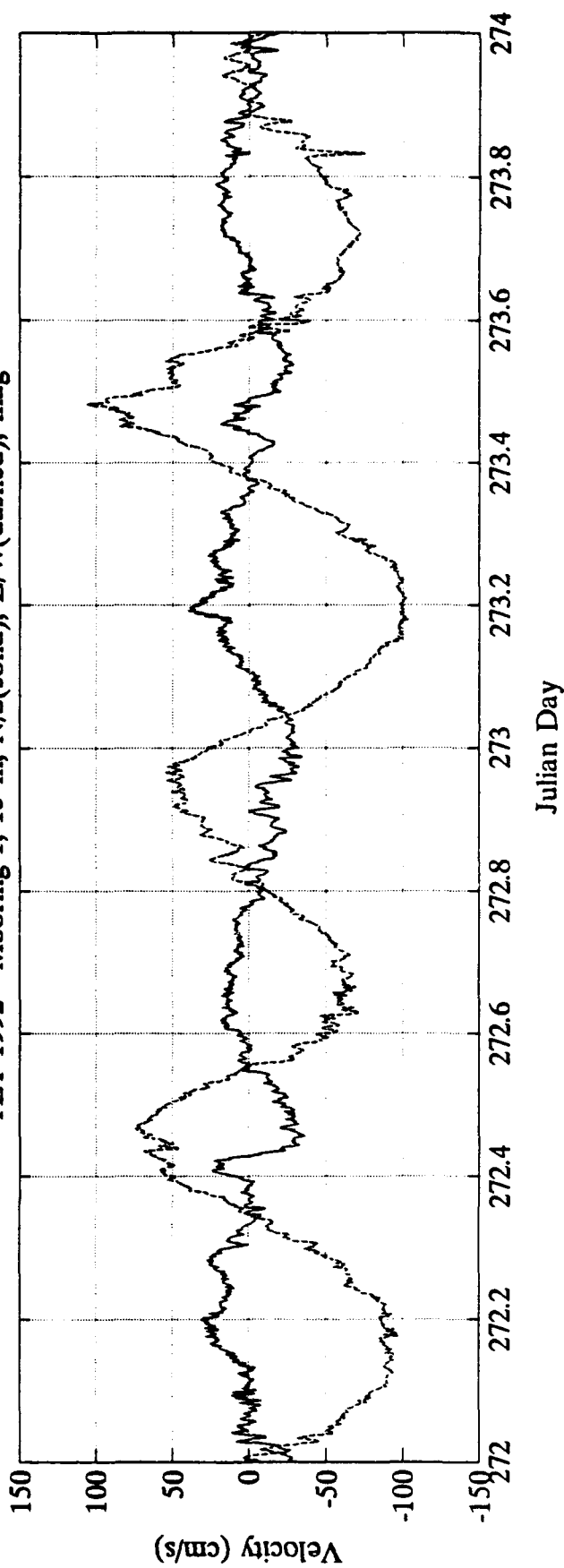
TET 1992 - Mooring 1, 15 m, N/S(solid), E/W(dashed), mag



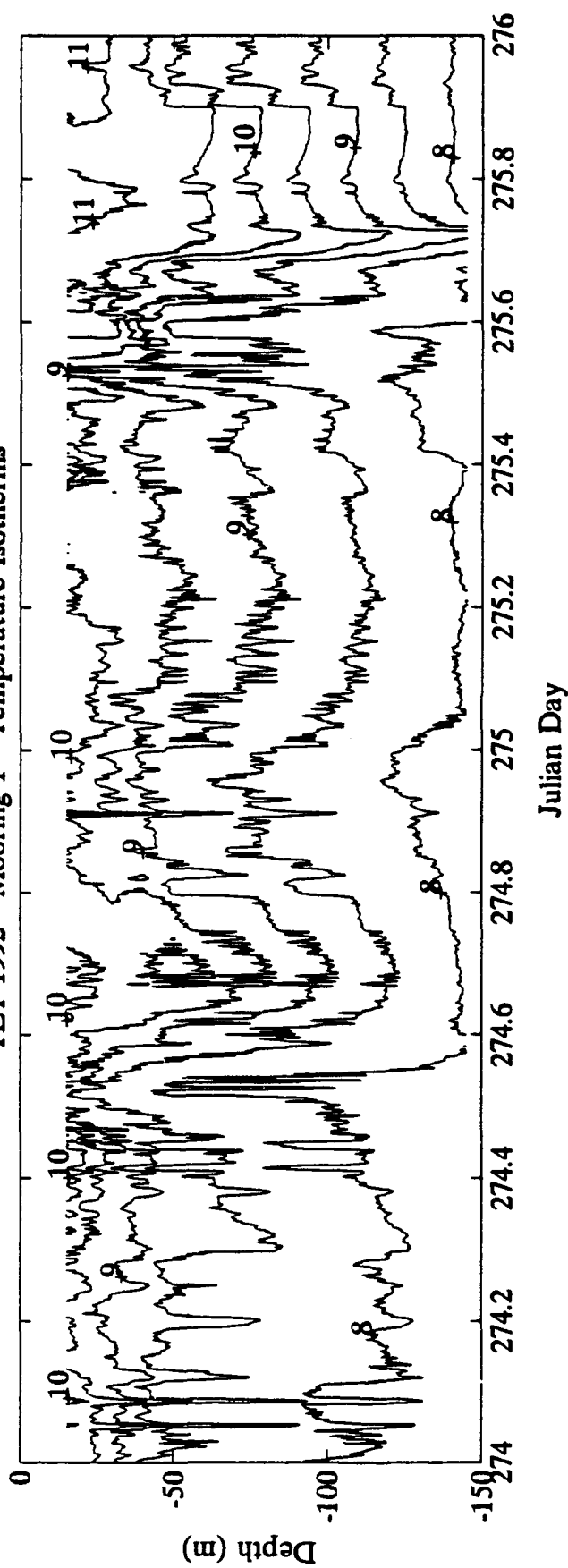
TET 1992 - Mooring 1 - Temperature Isotherms



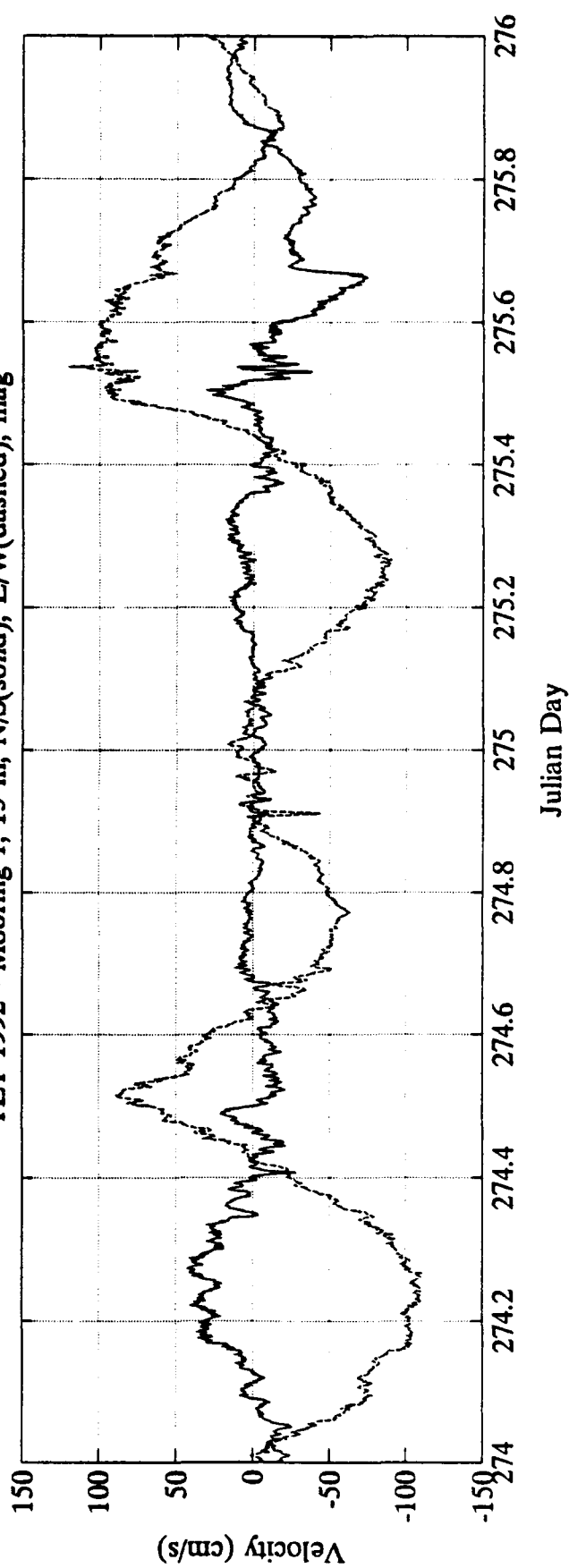
TET 1992 - Mooring 1, 15 m, N/S(solid), E/W(dashed), mag



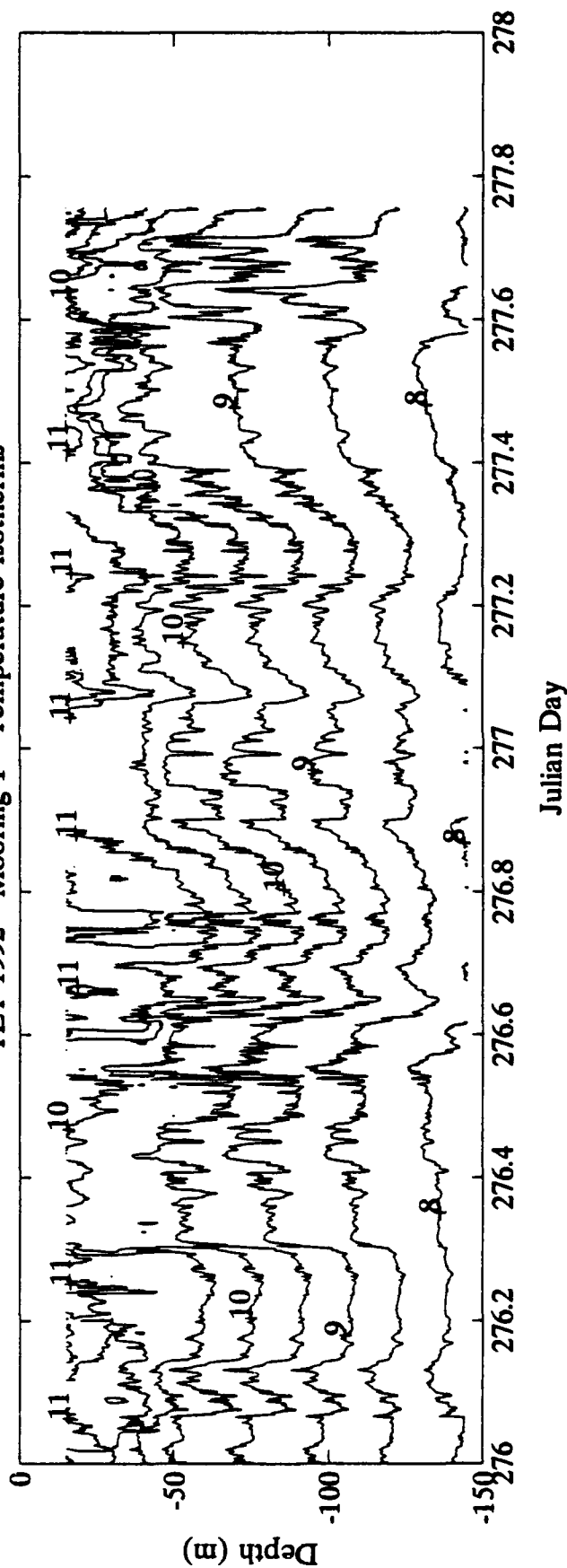
TET 1992 - Mooring 1 - Temperature Isotherms



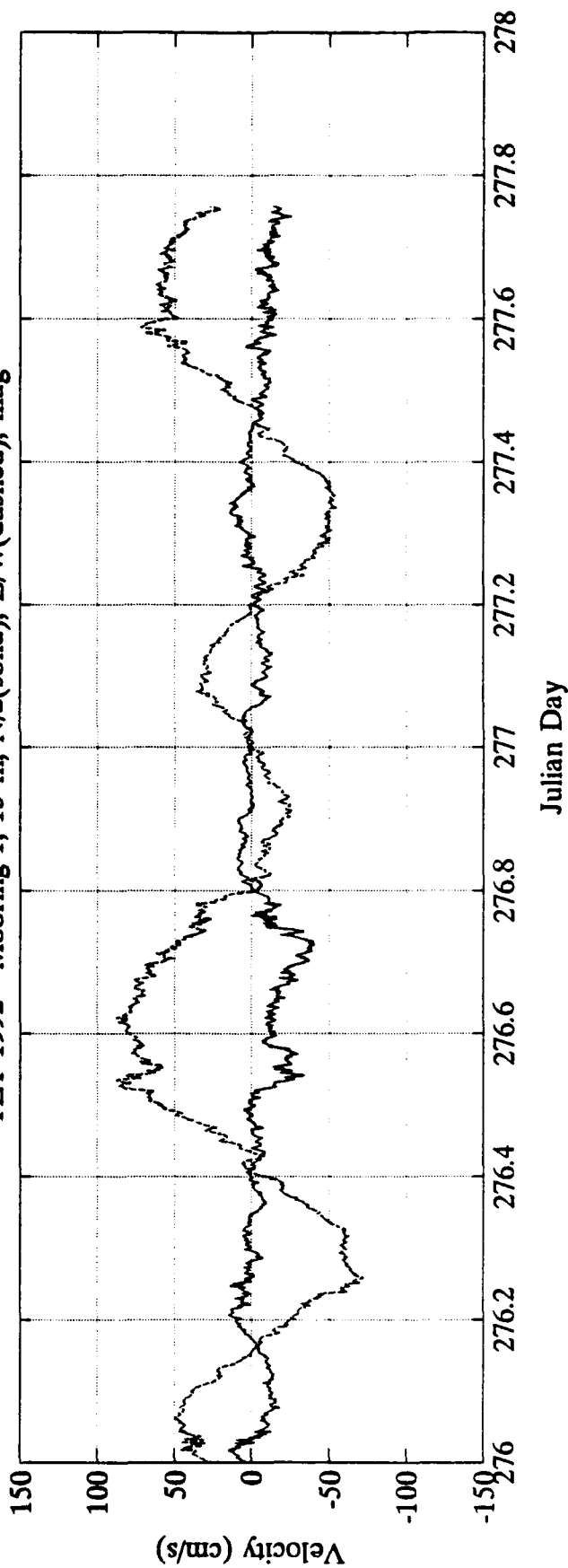
TET 1992 - Mooring 1, 15 m, N/S(solid), E/W(dashed), mag



TET 1992 - Mooring 1 - Temperature Isotherms



TET 1992 - Mooring 1, 15 m, N/S(solid), E/W(dashed), mag



APPENDIX C

ADCP Drift Tracks

ADCP Drift Tracks are shown for each drift that was taken. The beginning of each drift is shown by an "S" near the starting position. Current Meter Mooring locations are shown with a "+" for reference.

LIST OF FIGURES

APPENDIX C

ADCP Drift Track, Drift #1, 21 September 1992	C-5
ADCP Drift Track, Drift #2, 21 September 1992	C-6
ADCP Drift Track, Drift #1, 24 September 1992	C-7
ADCP Drift Track, Drift #2, 24 September 1992	C-8
ADCP Drift Track, Drift #3, 24 September 1992	C-9
ADCP Drift Track, Drift #4, 24 September 1992	C-10
ADCP Drift Track, Drift #5, 24 September 1992	C-11
ADCP Drift Track, Drift #1, 28 September 1992	C-12
ADCP Drift Track, Drift #2, 28 September 1992	C-13
ADCP Drift Track, Drift #3, 28 September 1992	C-14
ADCP Drift Track, Drift #1, 29 September 1992	C-15
ADCP Drift Track, Drift #2, 29 September 1992	C-16
ADCP Drift Track, Drift #3, 29 September 1992	C-17
ADCP Drift Track, Drift #4, 29 September 1992	C-18
ADCP Drift Track, Drift #5, 29 September 1992	C-19
ADCP Drift Track, Drift #1, 30 September 1992	C-20
ADCP Drift Track, Drift #2, 30 September 1992	C-21
ADCP Drift Track, Drift #3, 30 September 1992	C-22
ADCP Drift Track, Drift #4, 30 September 1992	C-23
ADCP Drift Track, Drift #5, 30 September 1992	C-24

LIST OF TABLES

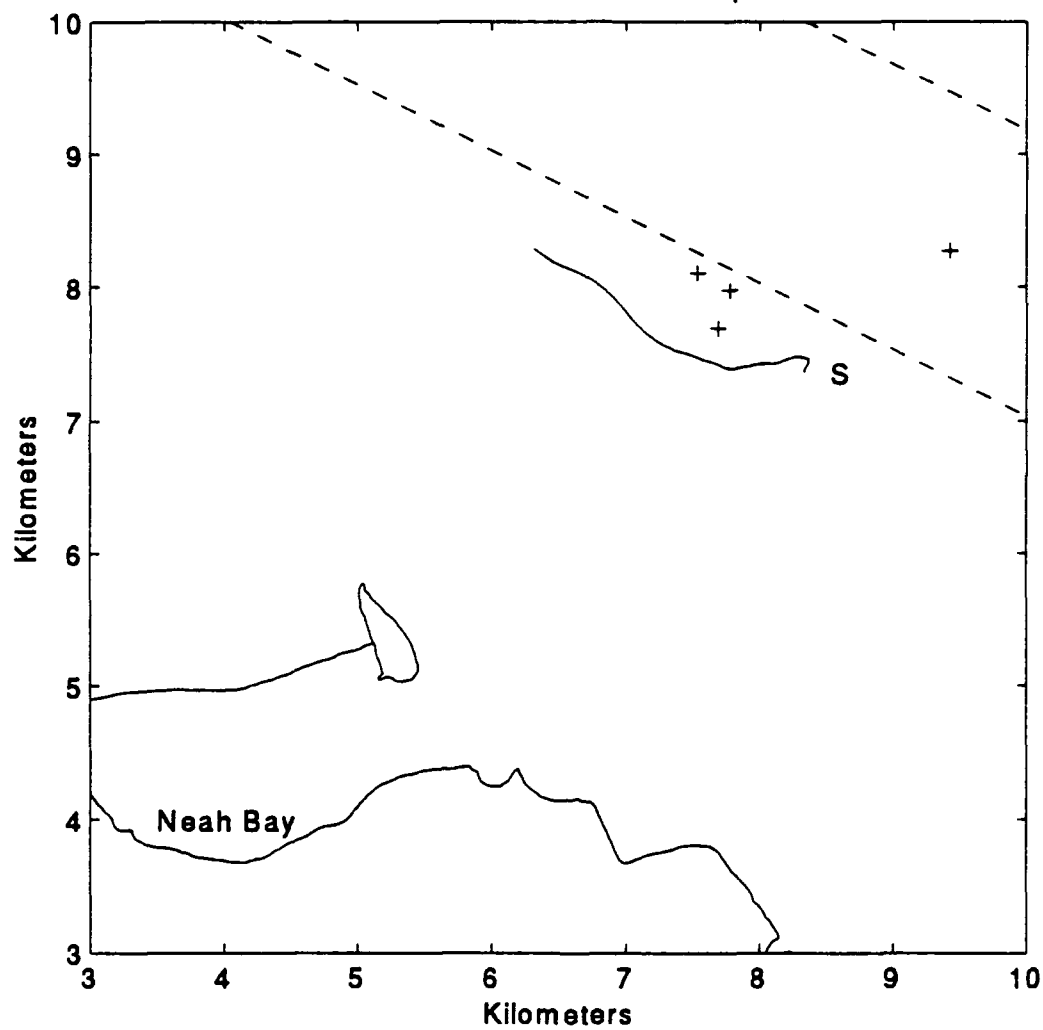
APPENDIX C

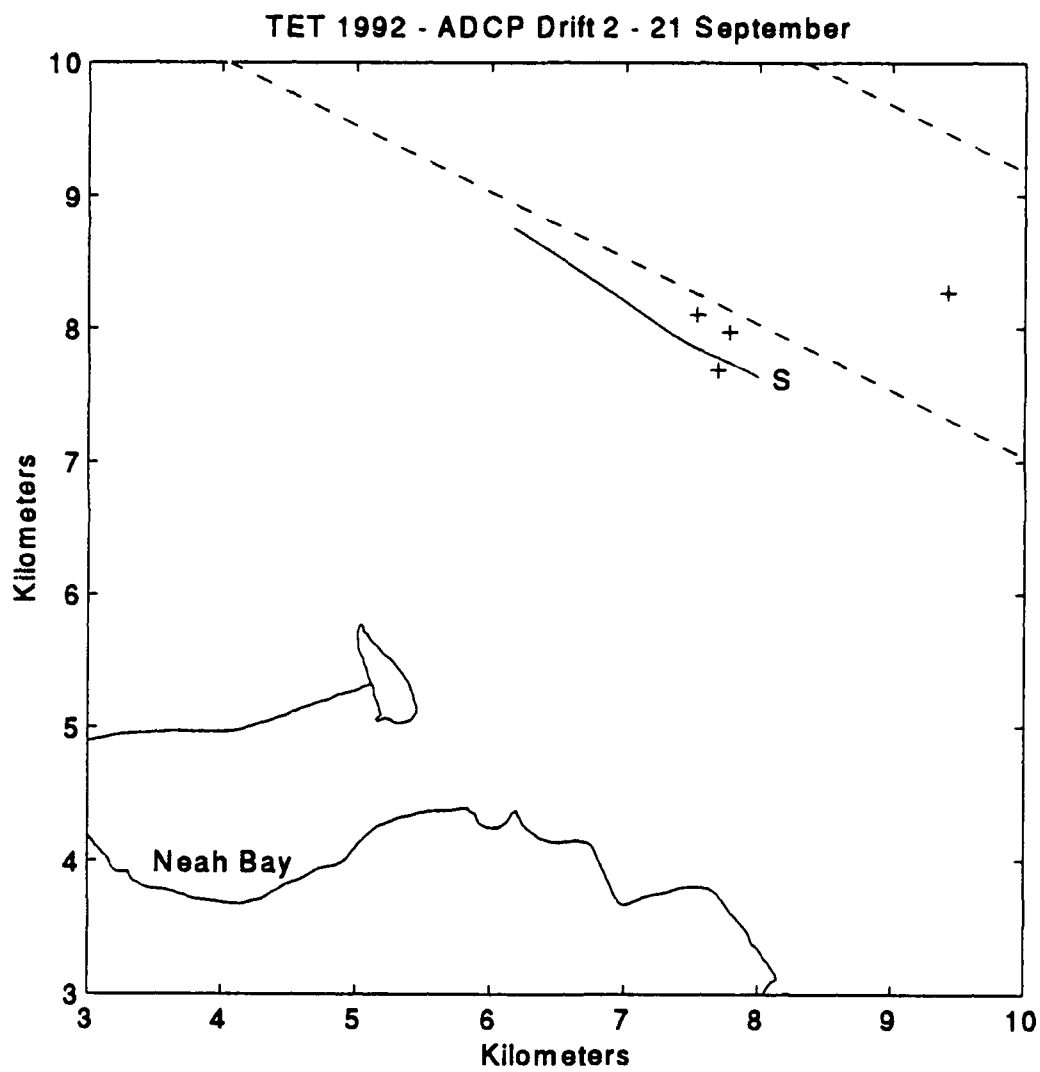
ADCP Drift Times and Duration C-4

Table C-1 ADCP Drift Times

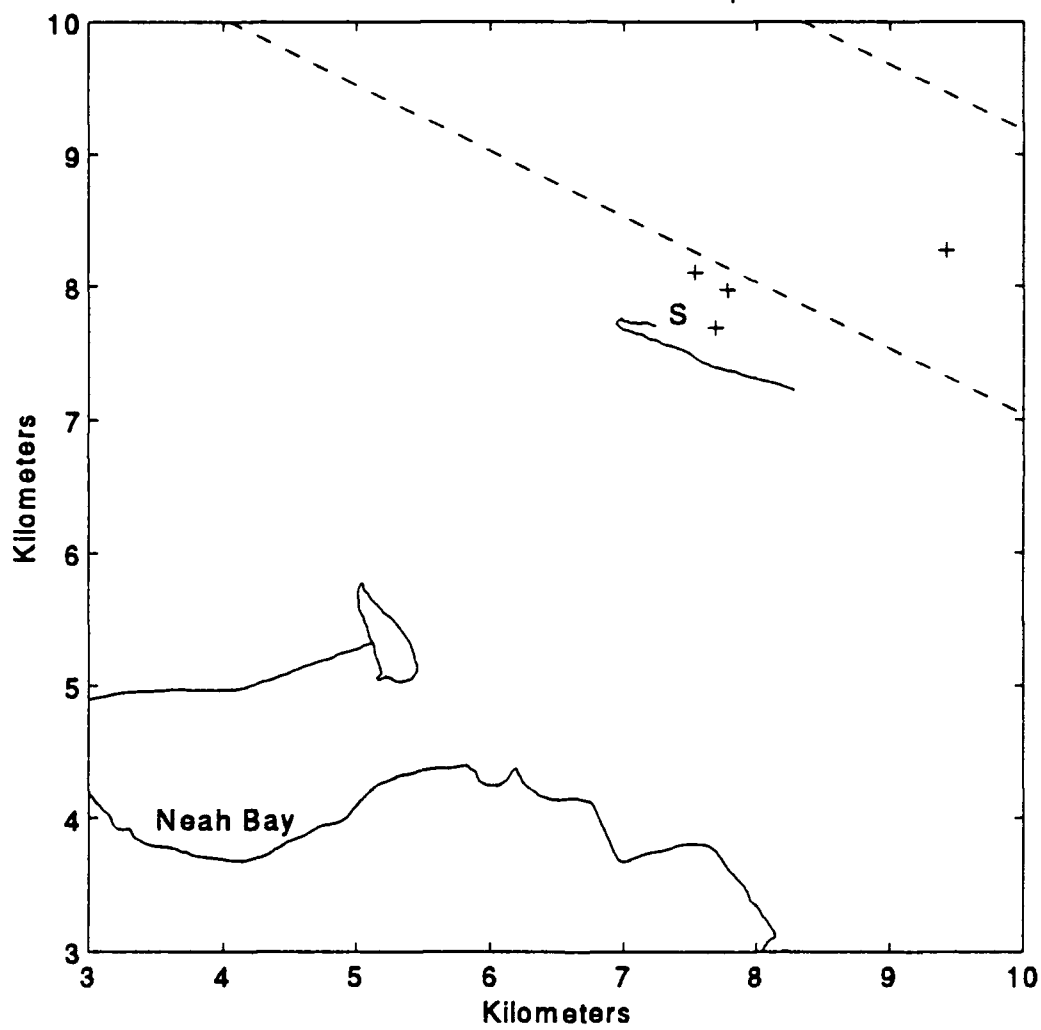
Julian Day	Date	Drift	Start	Stop	Duration
			hh:mm		
265	09/21/92	1	19:56	22:23	02:27
		2	22:48	23:35	00:46
268	09/24/92	1	16:02	18:11	02:09
		2	18:36	19:28	00:51
		3	19:59	20:53	00:53
		4	21:33	22:44	01:10
		5	23:07	23:15	00:07
272	09/28/92	1	17:00	18:16	01:15
		2	18:46	20:03	01:17
		3	23:03	00:04	01:01
273	09/29/92	1	15:33	16:40	01:06
		2	17:36	18:22	00:46
		3	18:54	20:10	01:16
		4	20:37	22:13	01:36
		5	22:37	00:13	01:36
274	09/30/92	1	15:57	17:16	01:19
		2	17:57	18:18	00:20
		3	18:33	18:54	00:20
		4	19:01	21:19	02:18
		5	21:34	00:00	02:26

TET 1992 - ADCP Drift 1 - 21 September

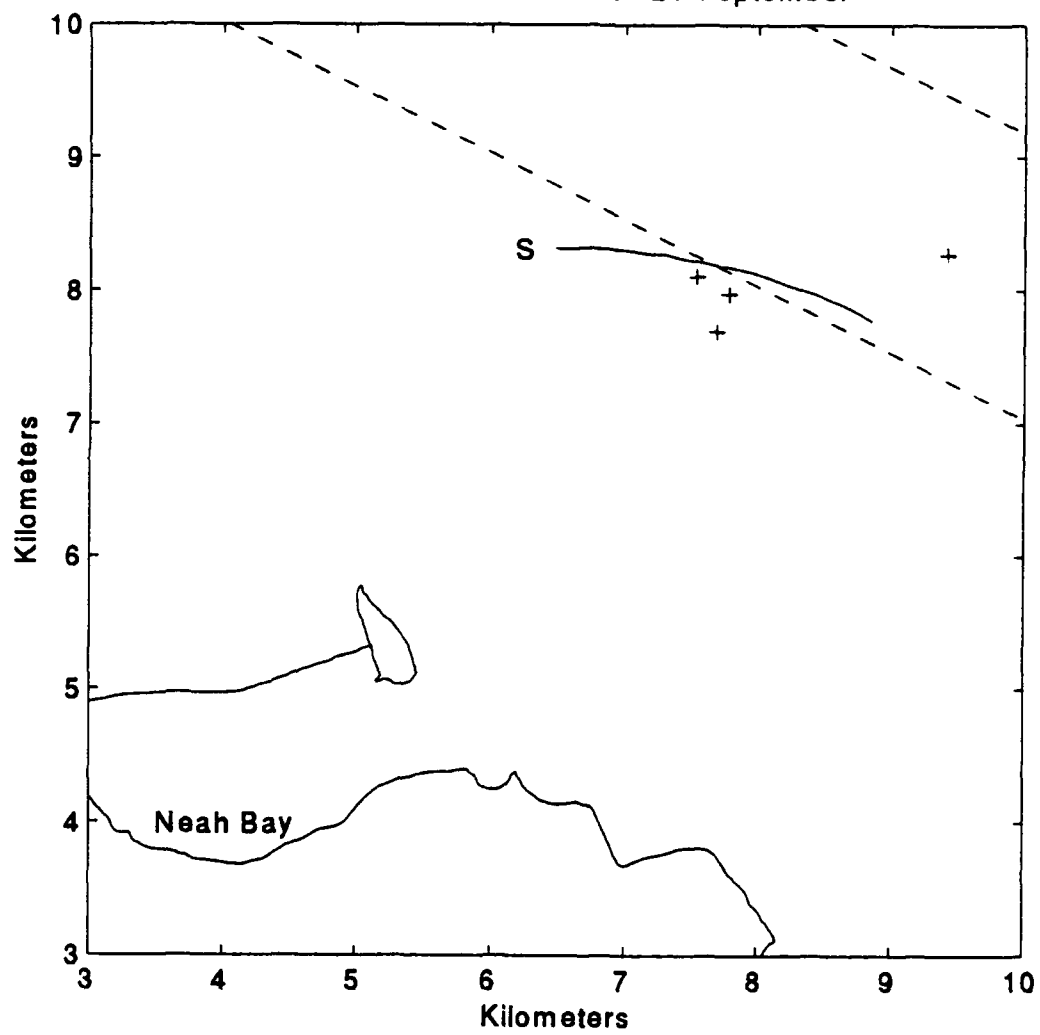




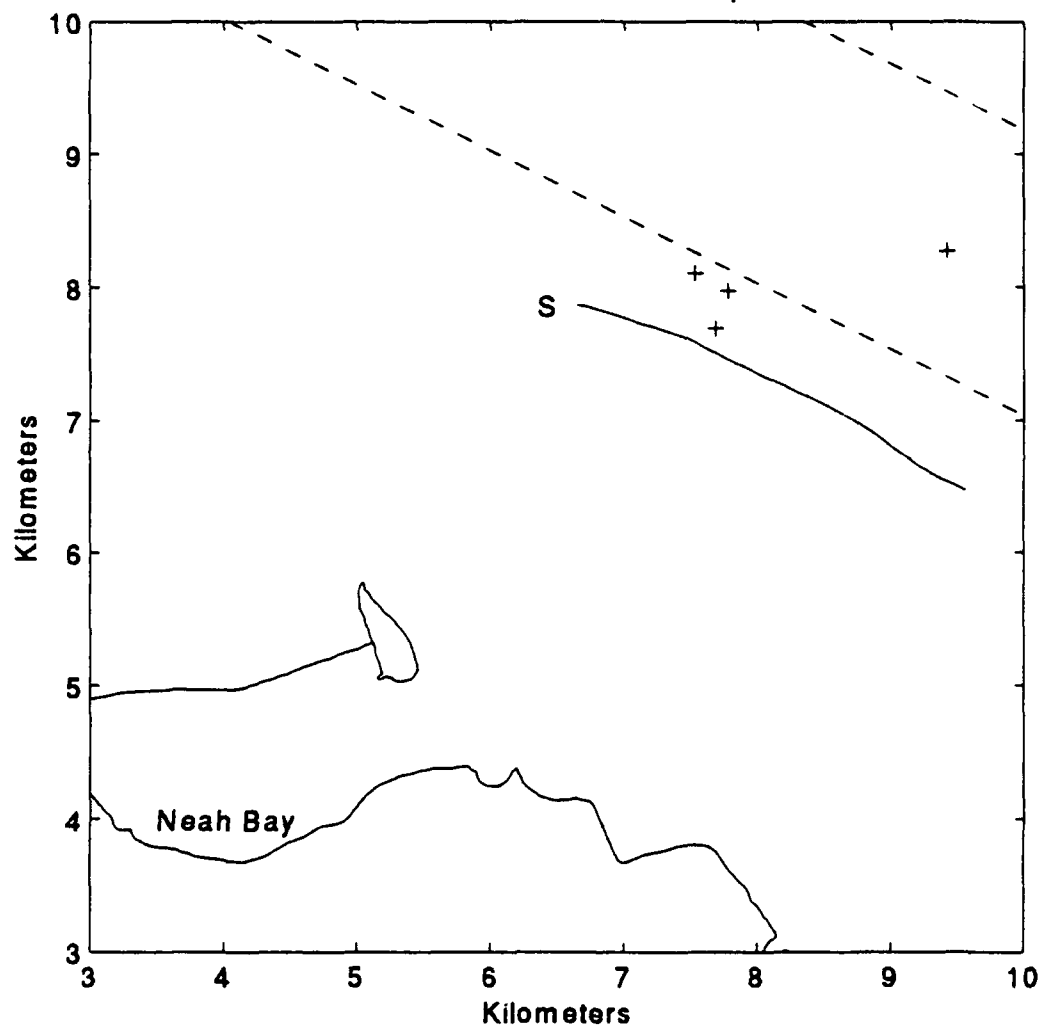
TET 1992 - ADCP Drift 1 - 24 September



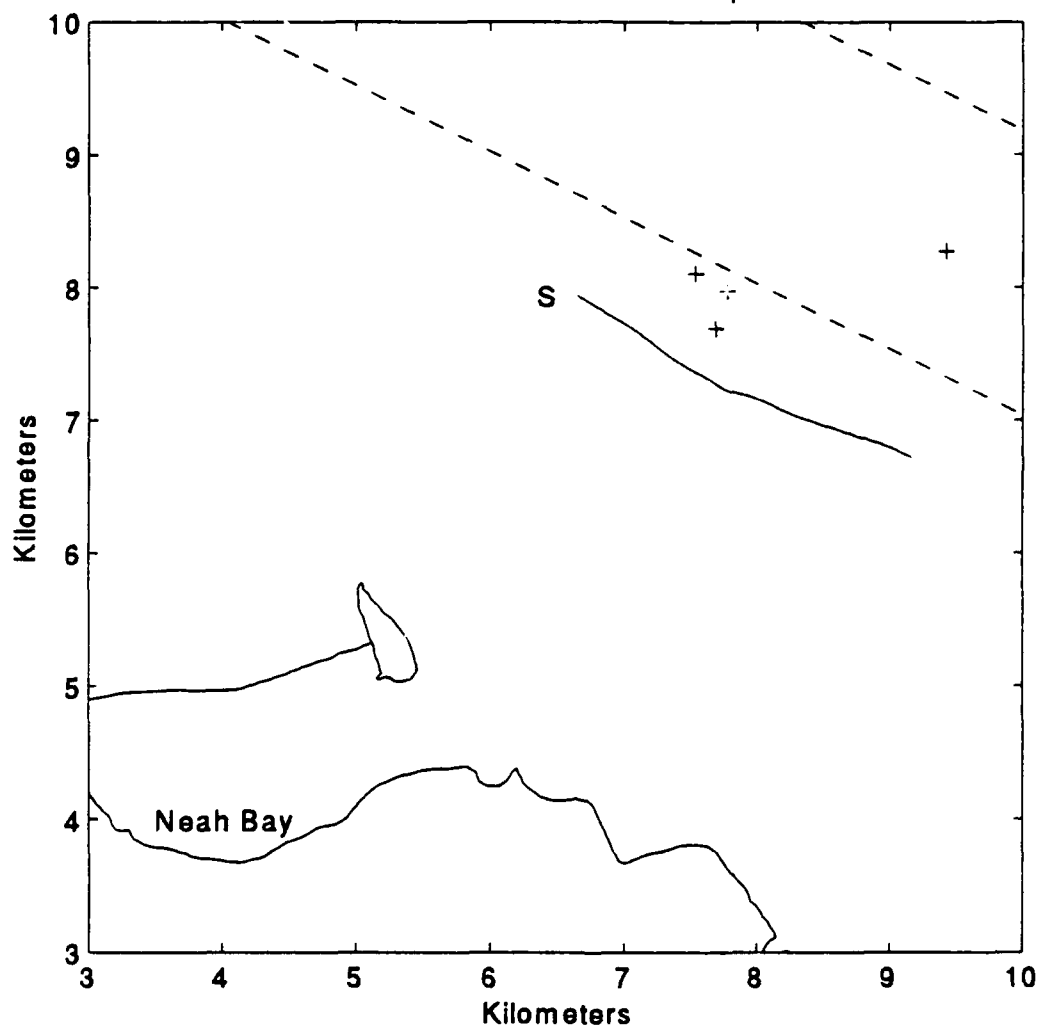
TET 1992 - ADCP Drift 2 - 24 September



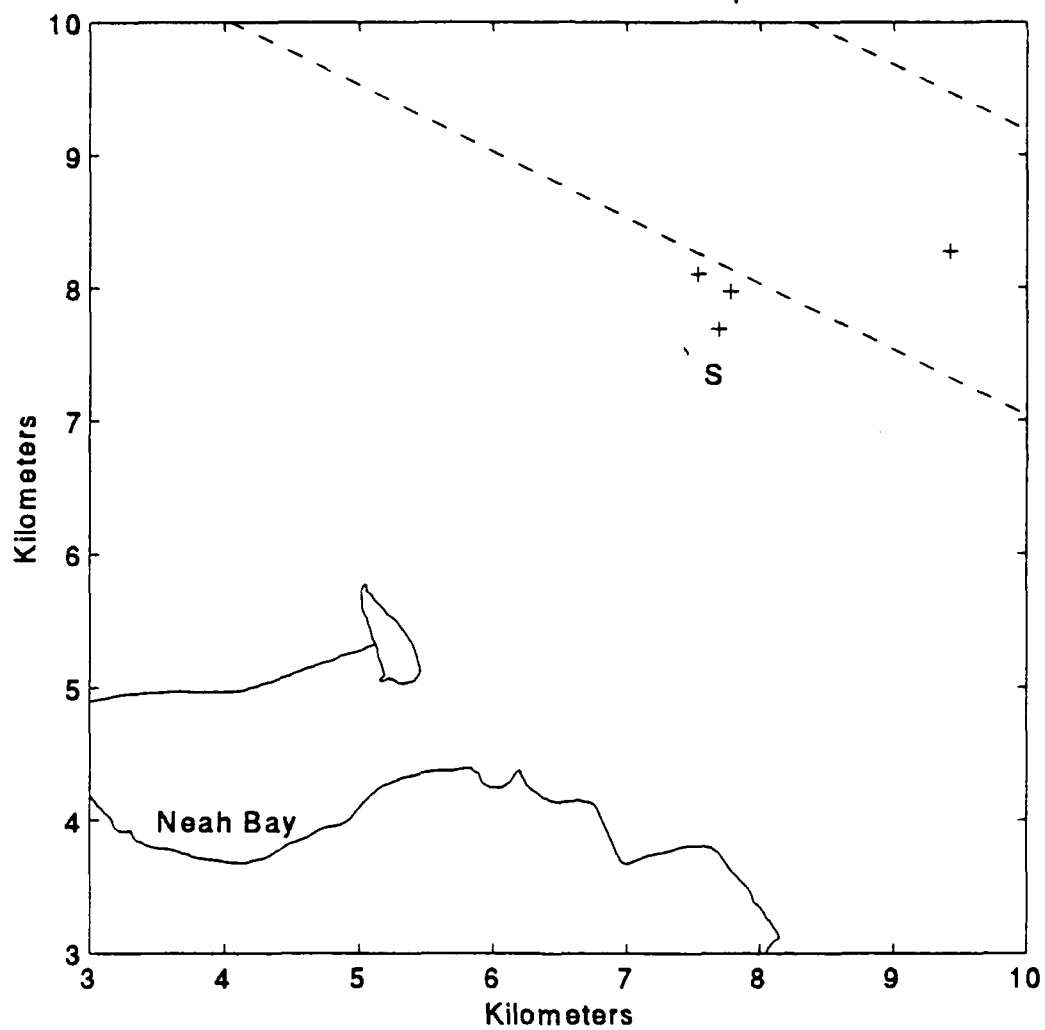
TET 1992 - ADCP Drift 3 - 24 September

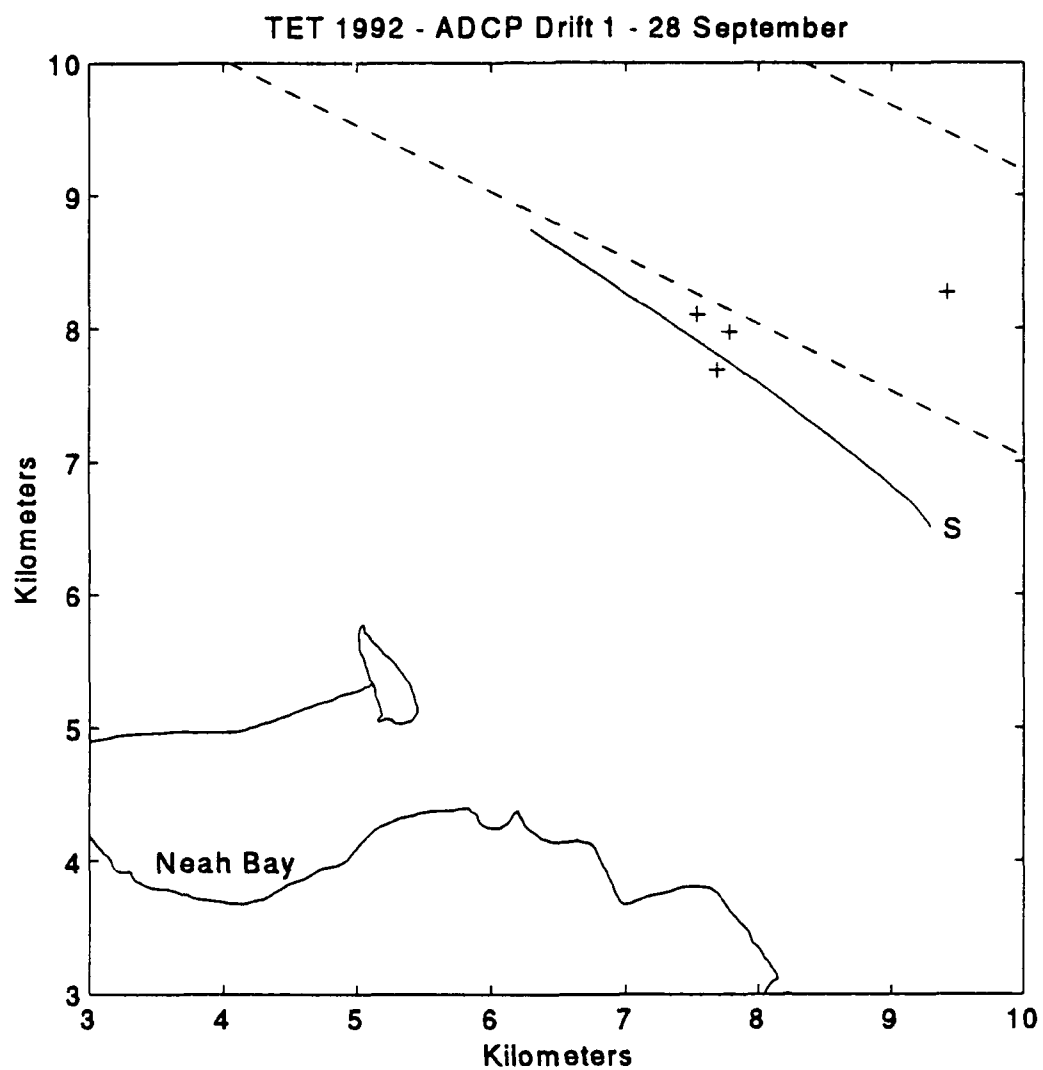


TET 1992 - ADCP Drift 4 - 24 September

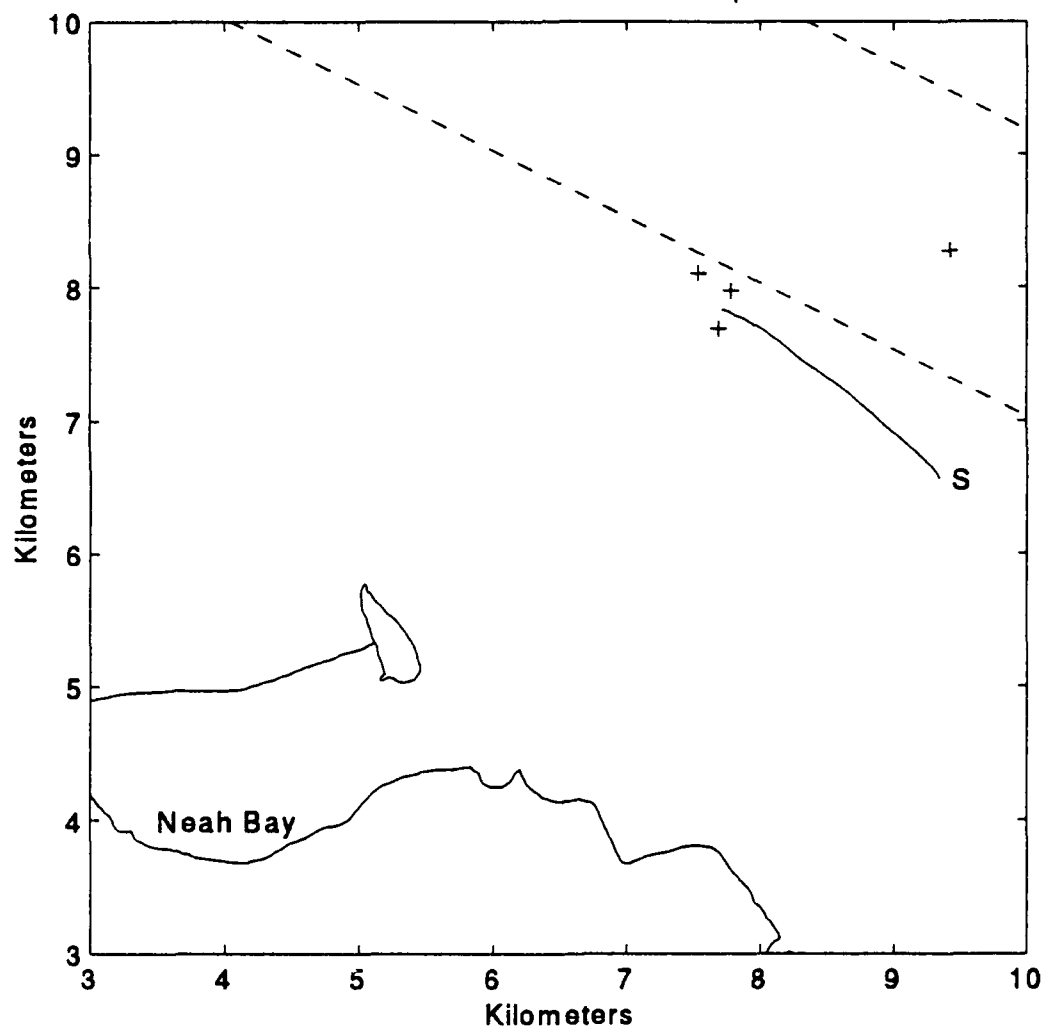


TET 1992 - ADCP Drift 5 - 24 September

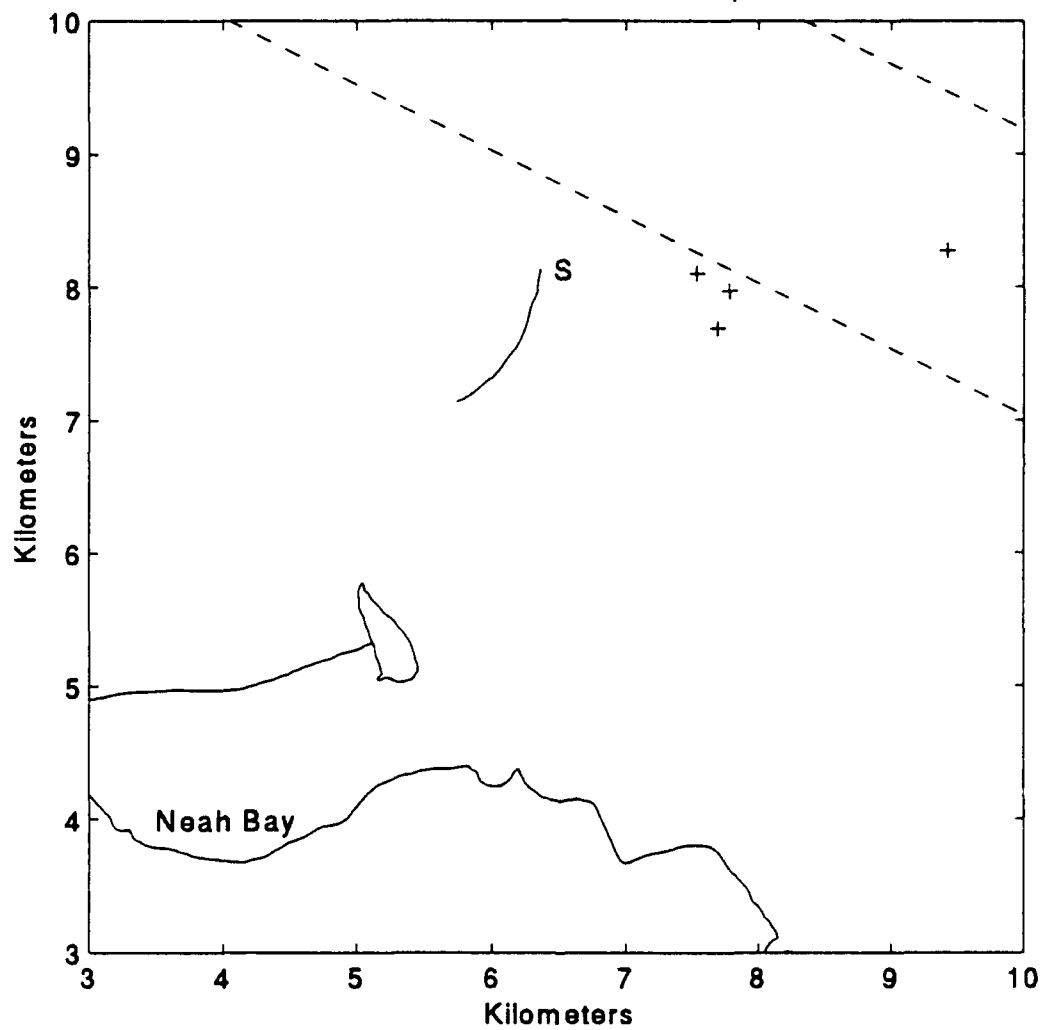


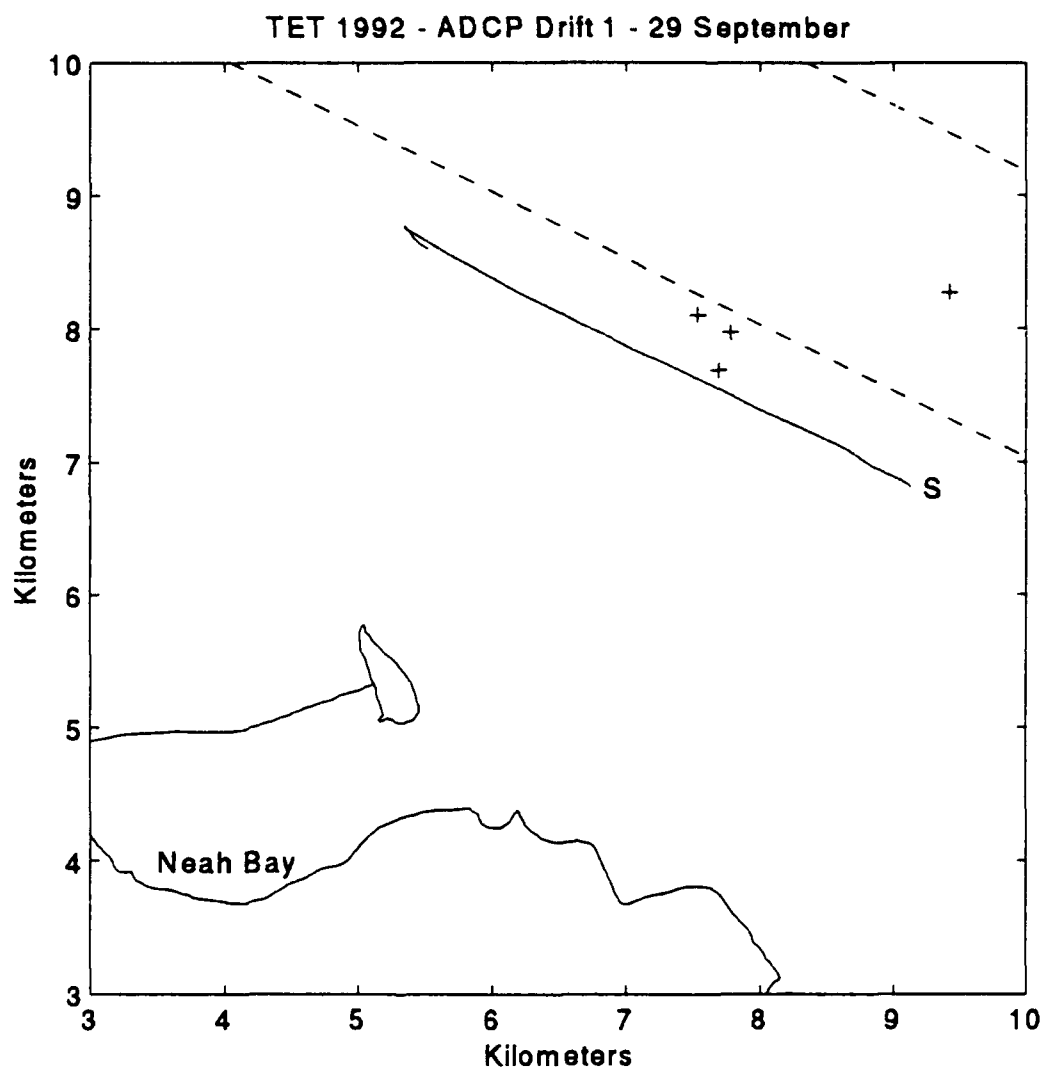


TET 1992 - ADCP Drift 2 - 28 September

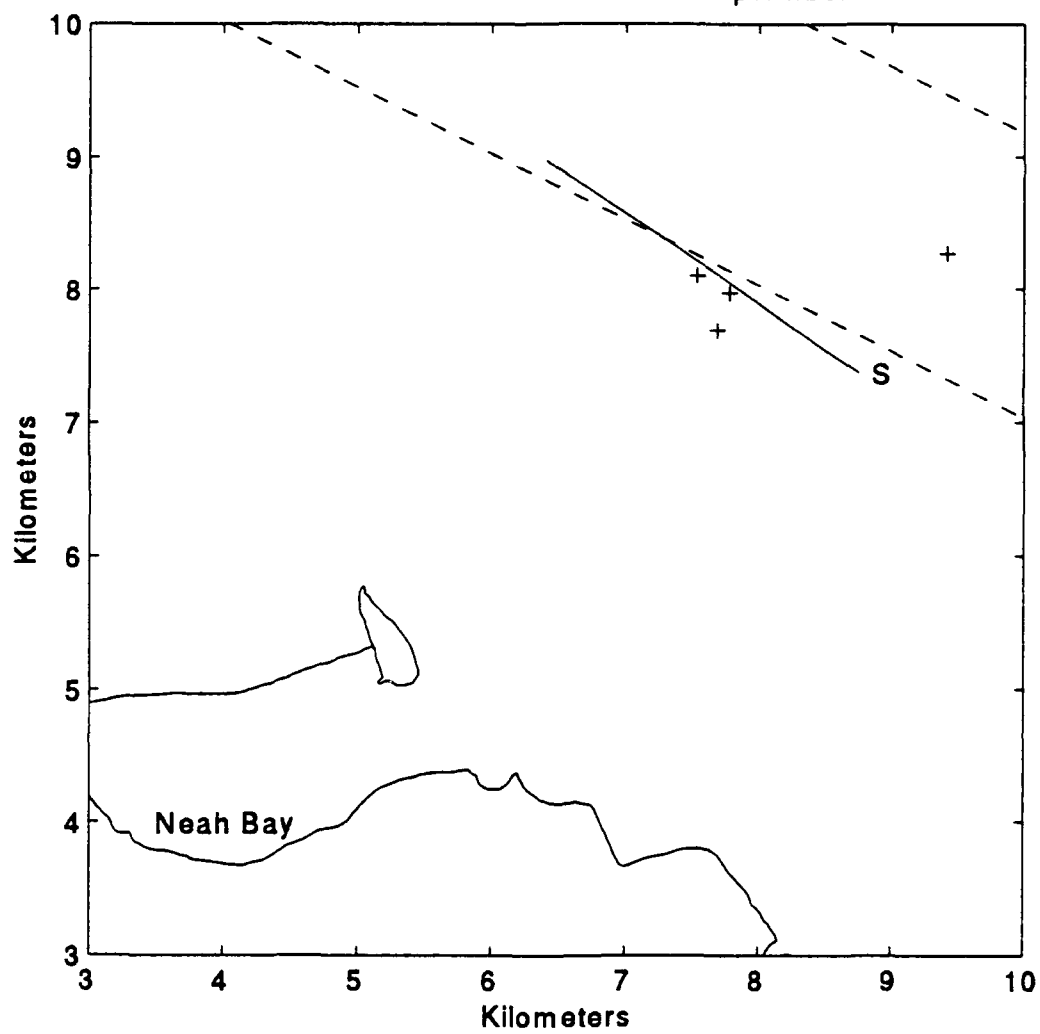


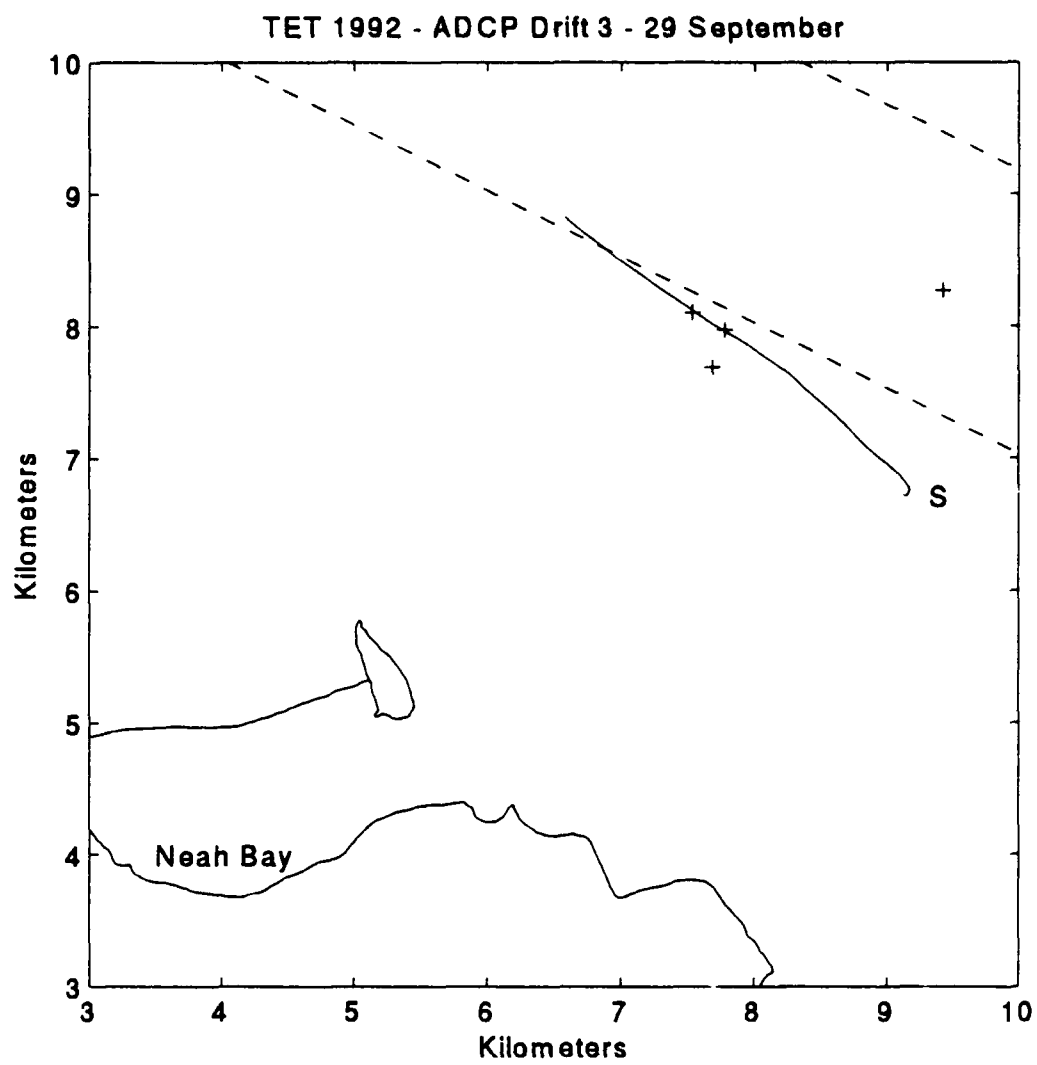
TET 1992 - ADCP Drift 3 - 28 September



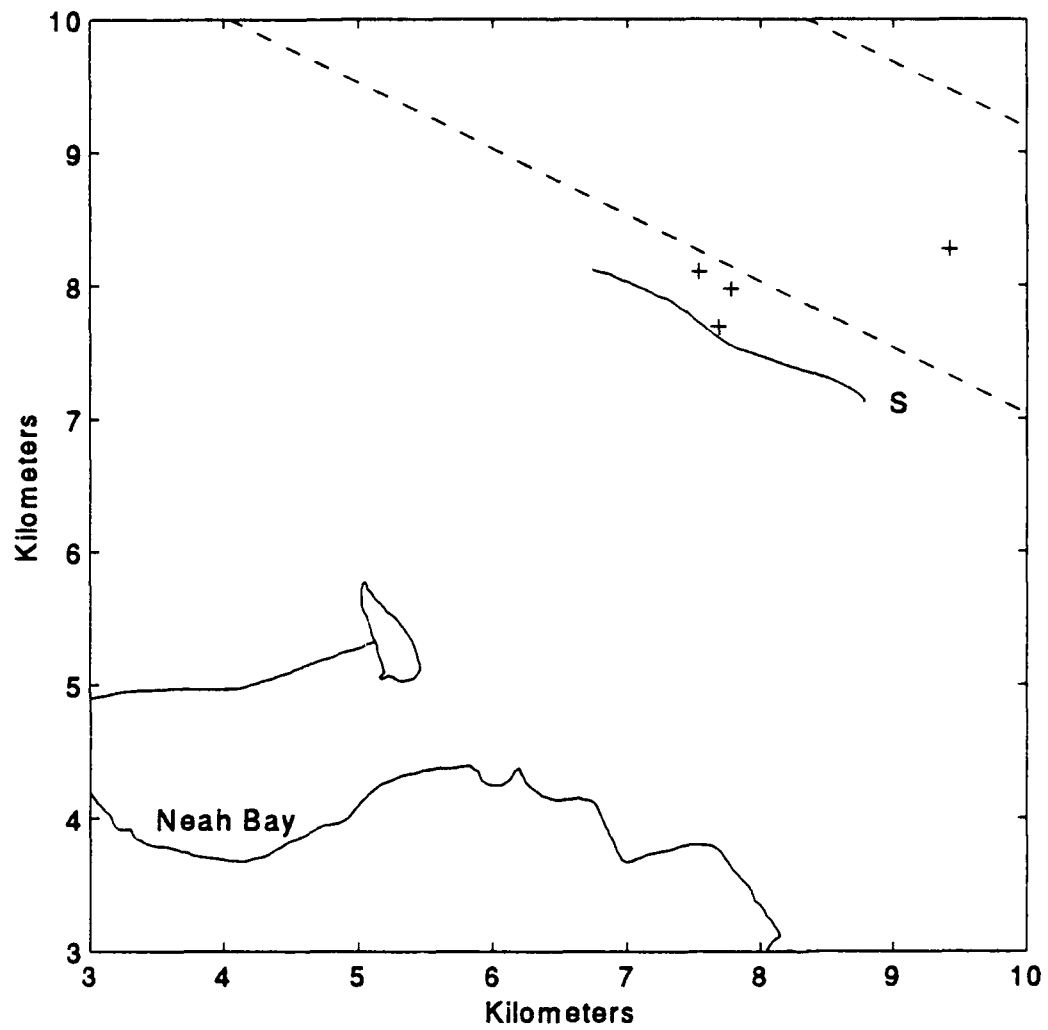


TET 1992 - ADCP Drift 2 - 29 September

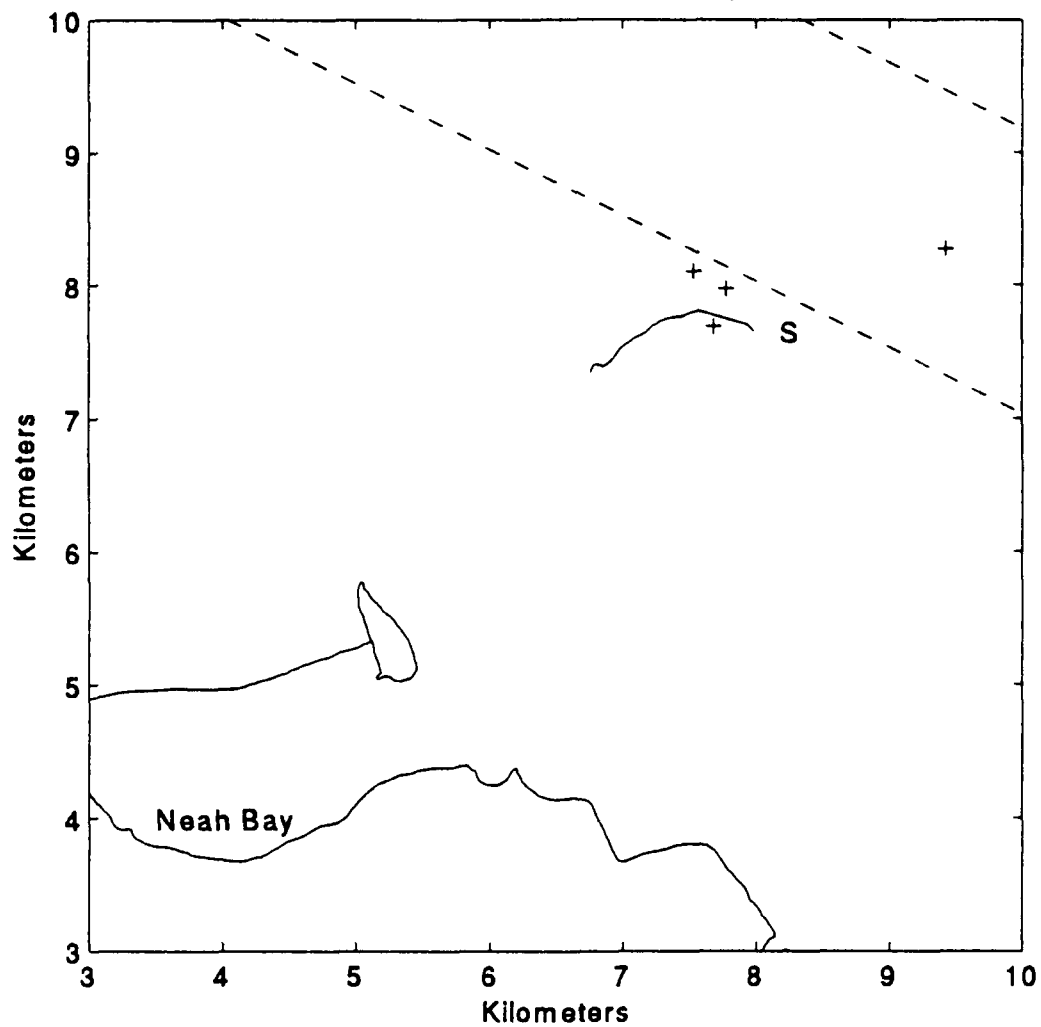


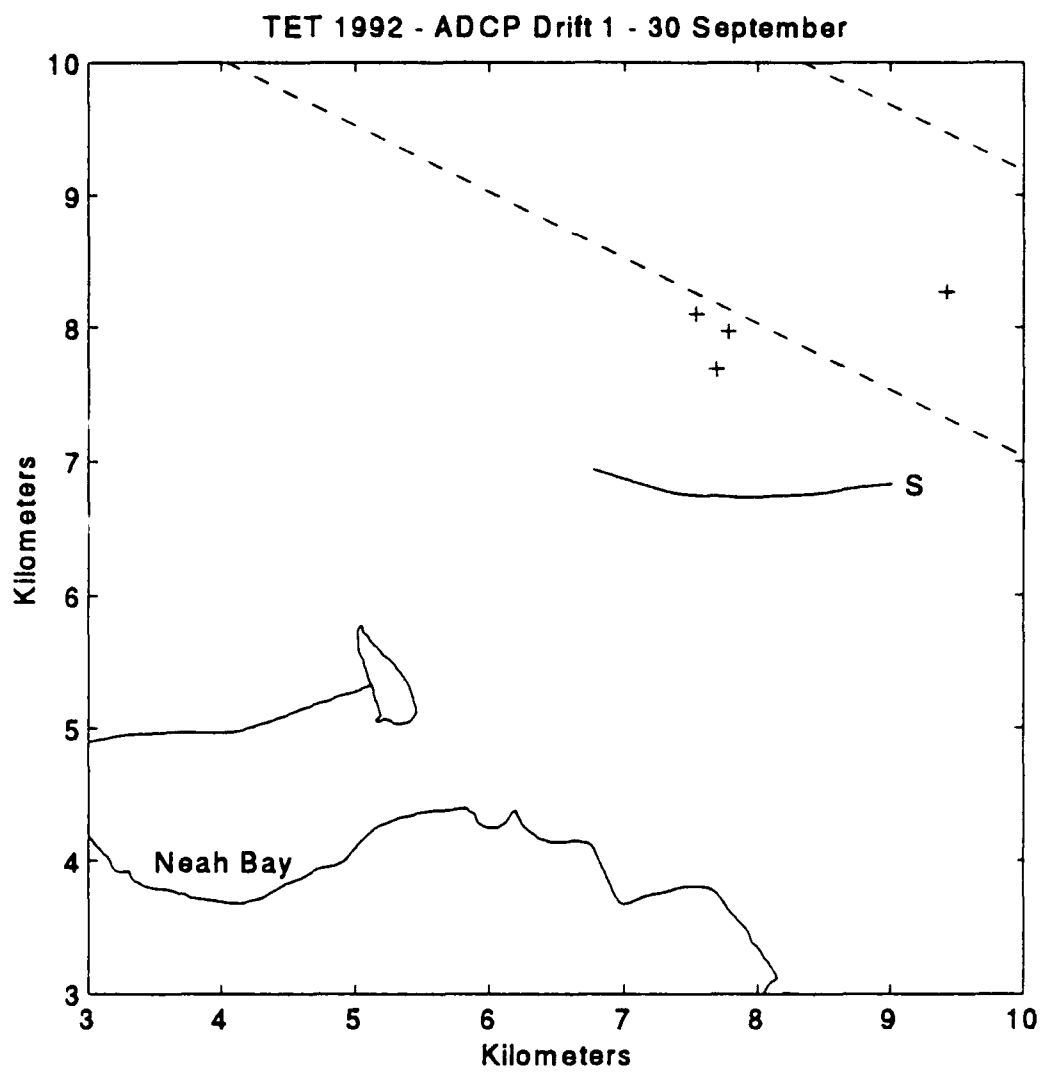


TET 1992 - ADCP Drift 4 - 29 September

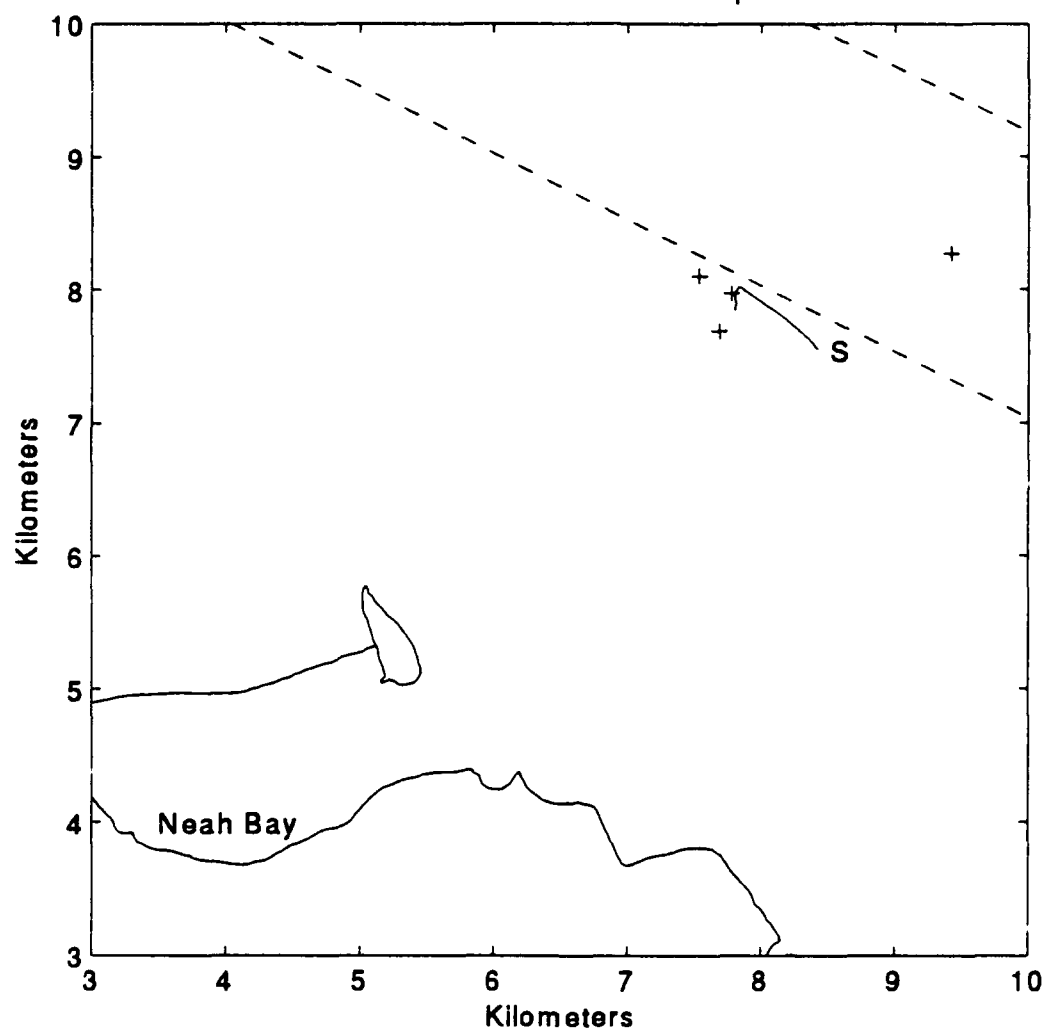


TET 1992 - ADCP Drift 5 - 29 September

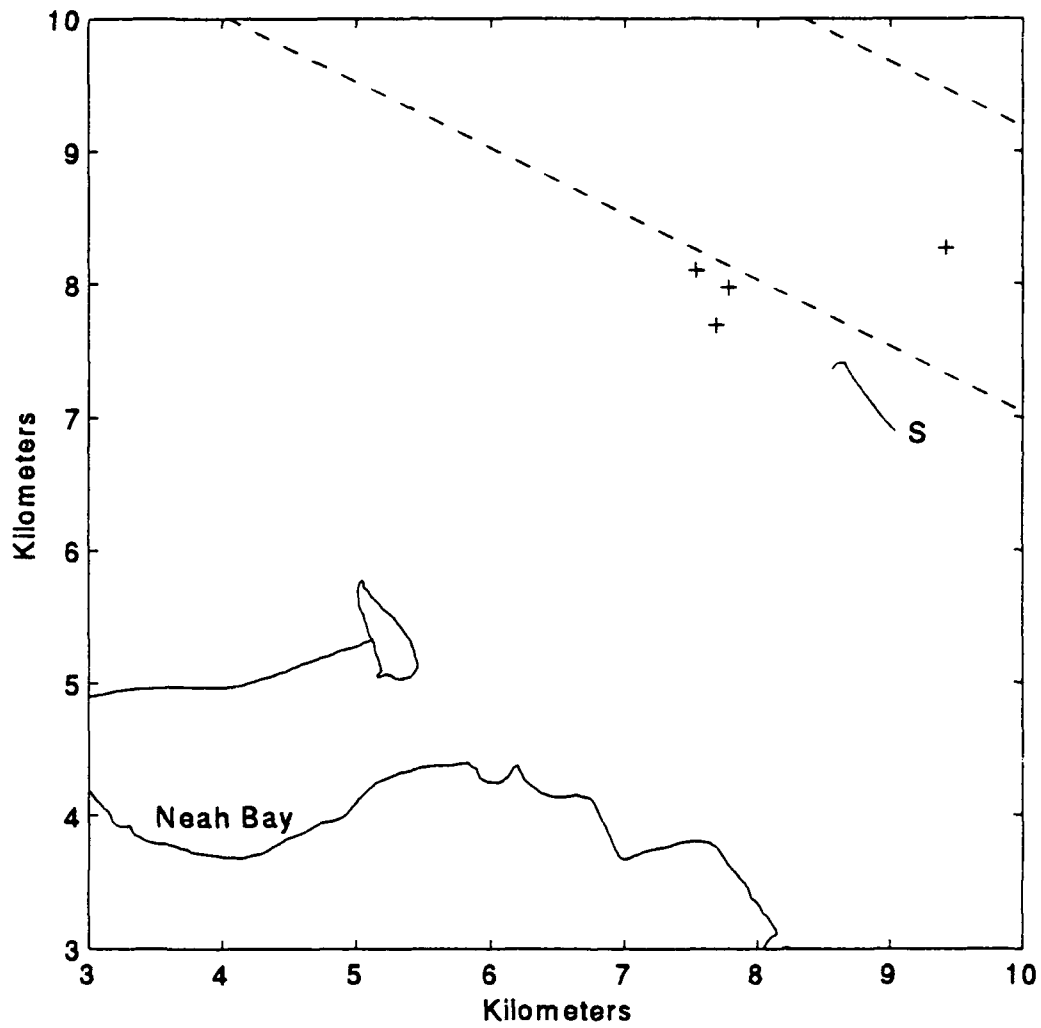




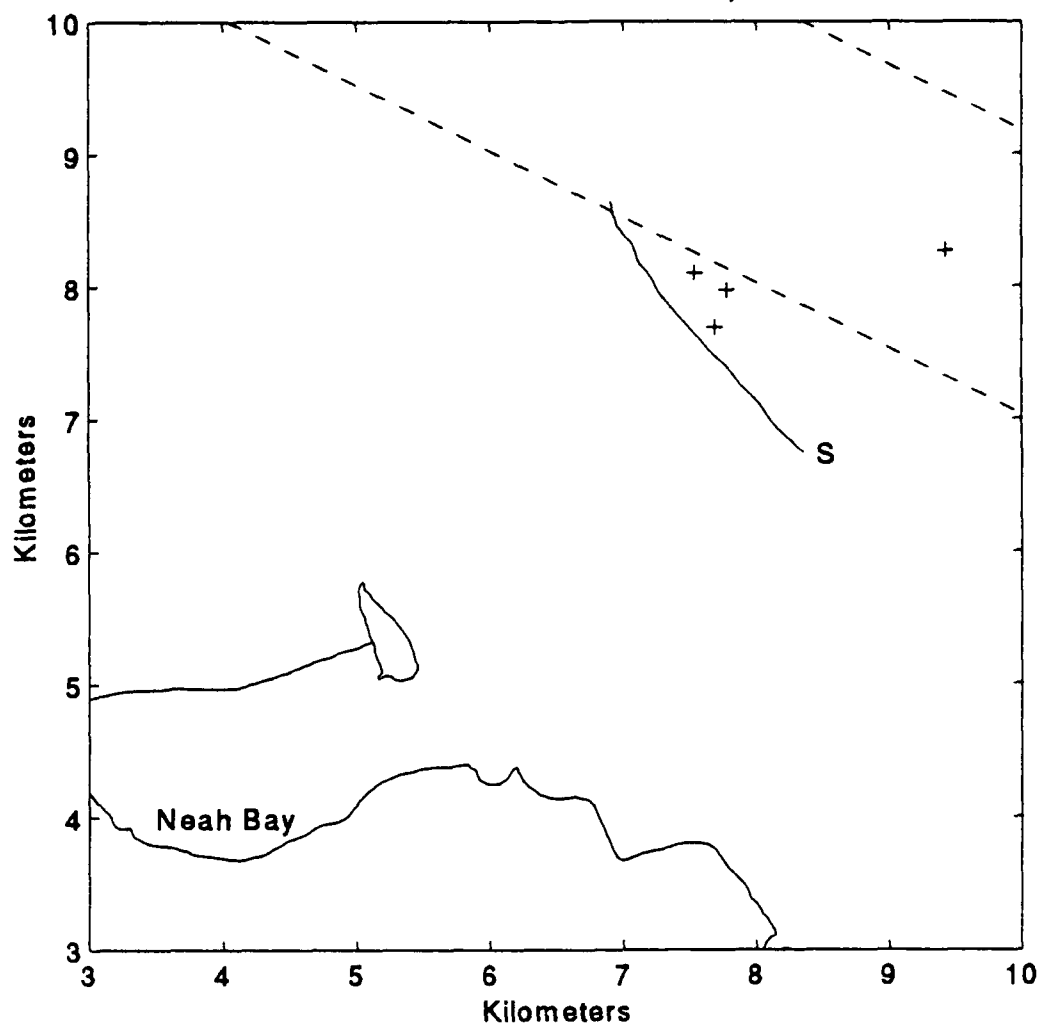
TET 1992 - ADCP Drift 2 - 30 September



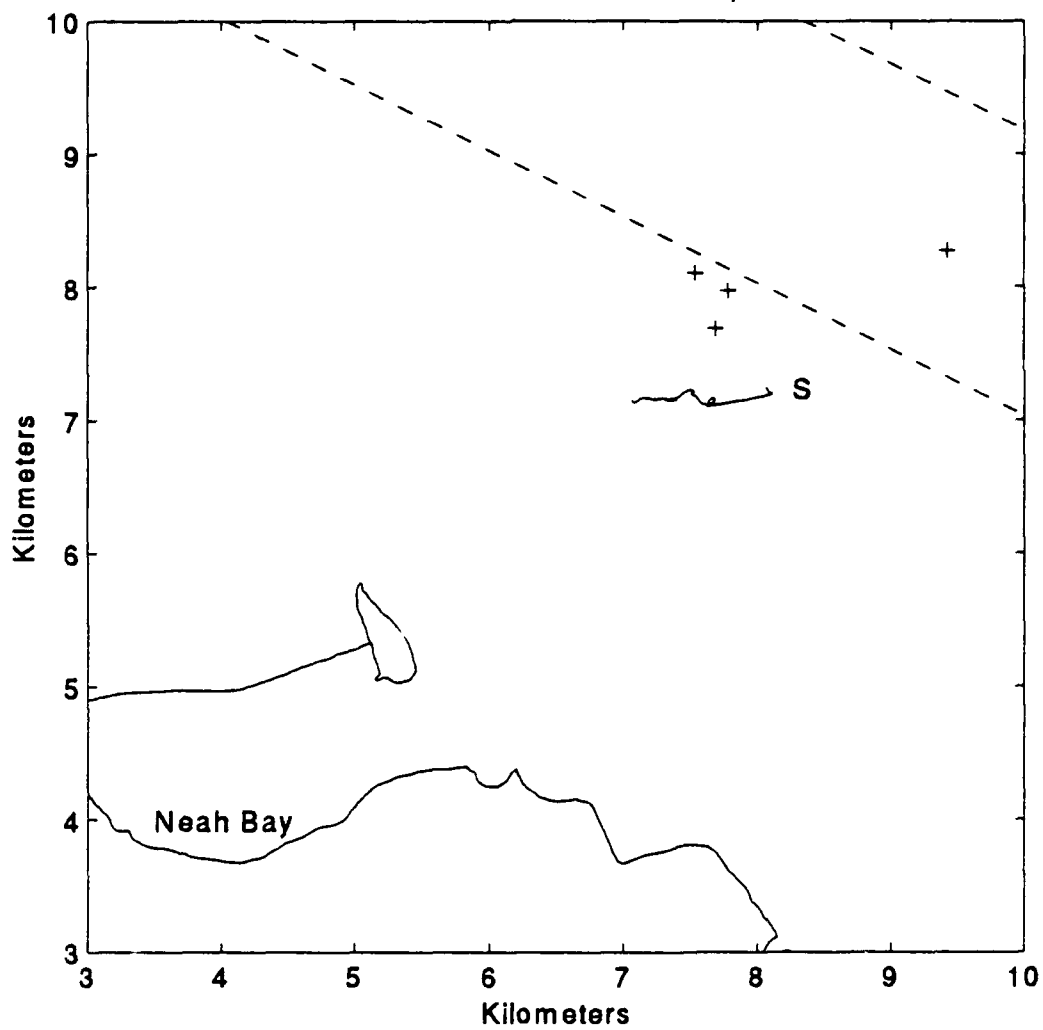
TET 1992 - ADCP Drift 3 - 30 September



TET 1992 - ADCP Drift 4 - 30 September



TET 1992 - ADCP Drift 5 - 30 September



APPENDIX D

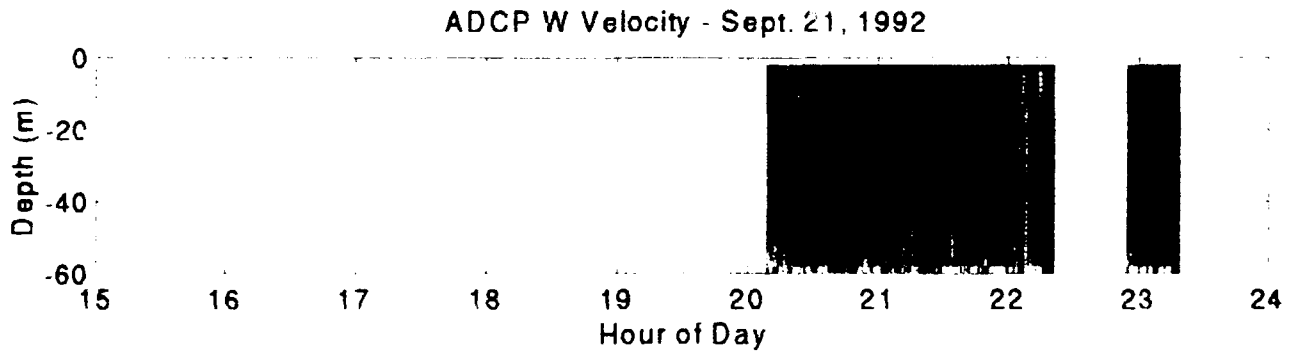
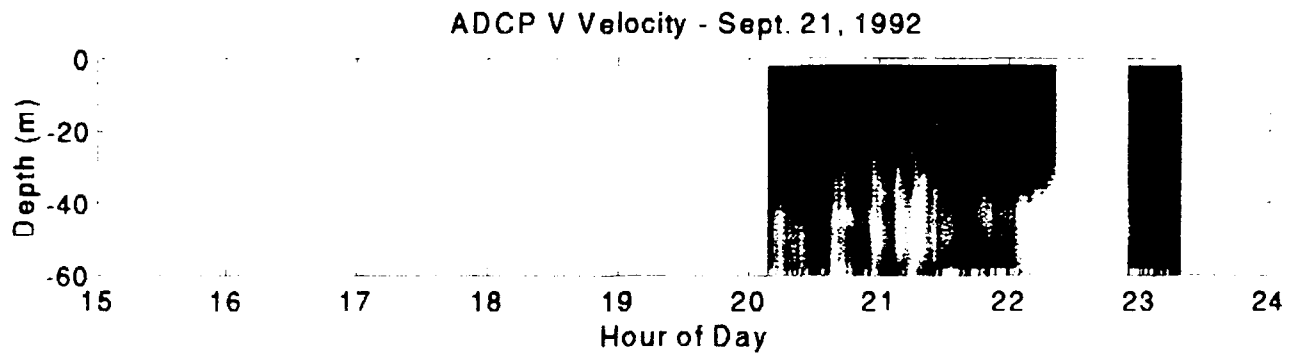
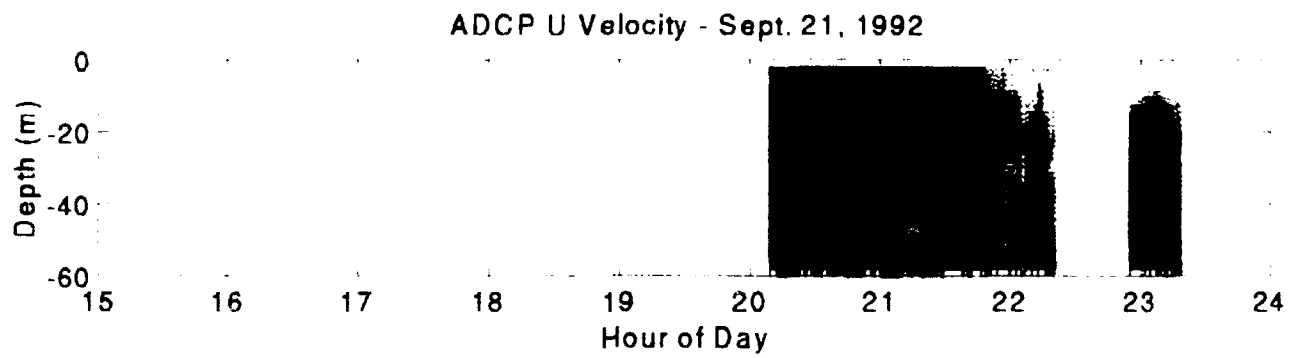
Alongshore, Across-Shore and Vertical Current Time Series from ADCP Drifts

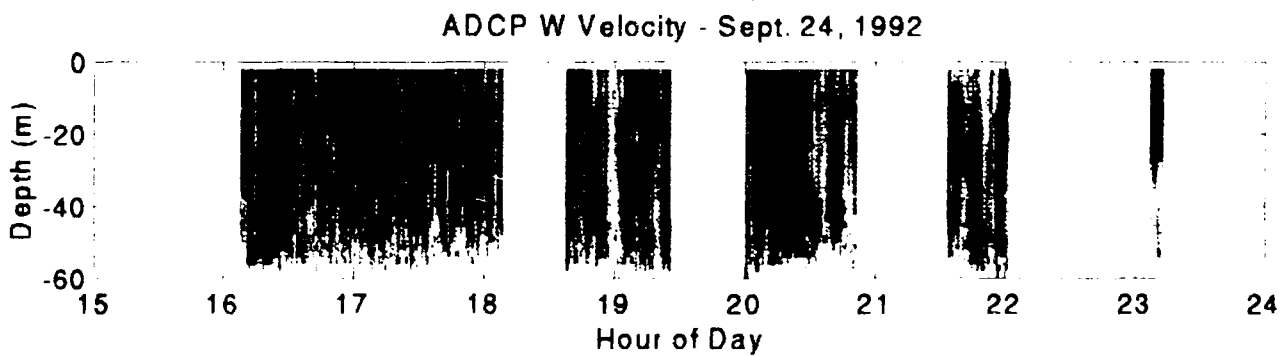
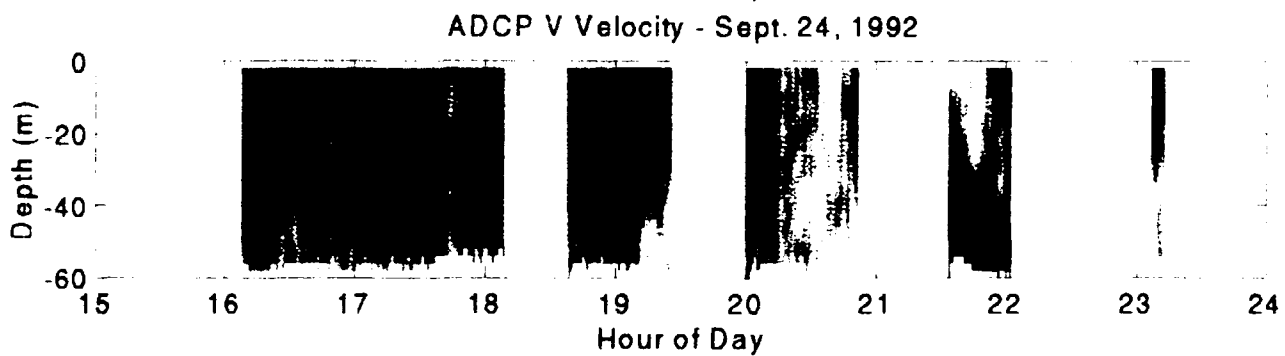
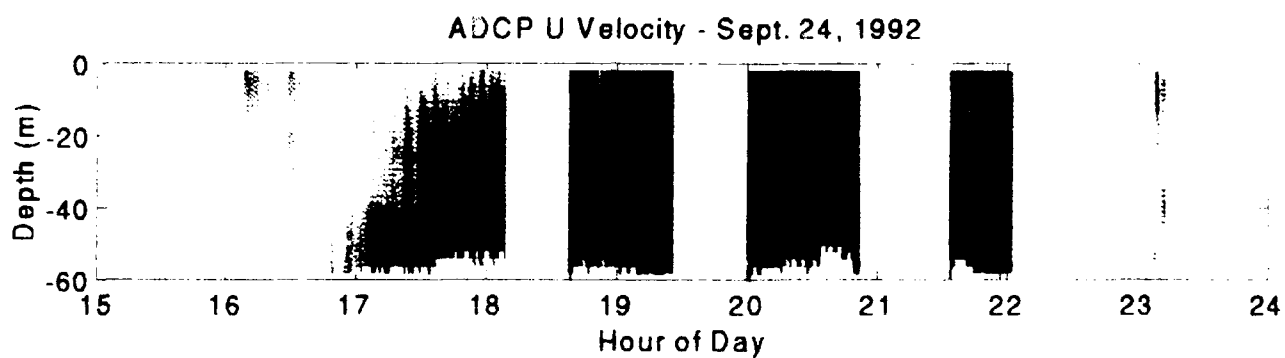
Colormap for velocity scale for U and V components is included at end of Appendix for each day's drifts. Velocity scale for vertical velocity, W, was -10 to 10 cm/s for same range of colors for all plots.

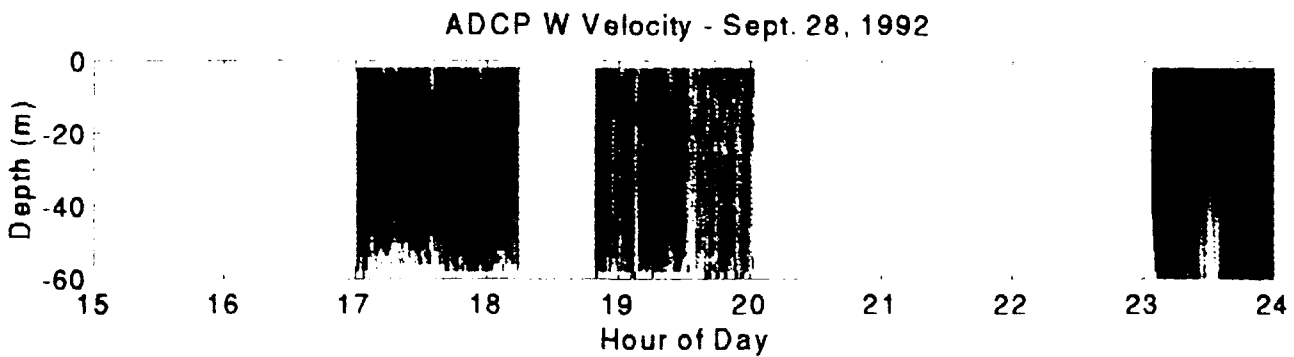
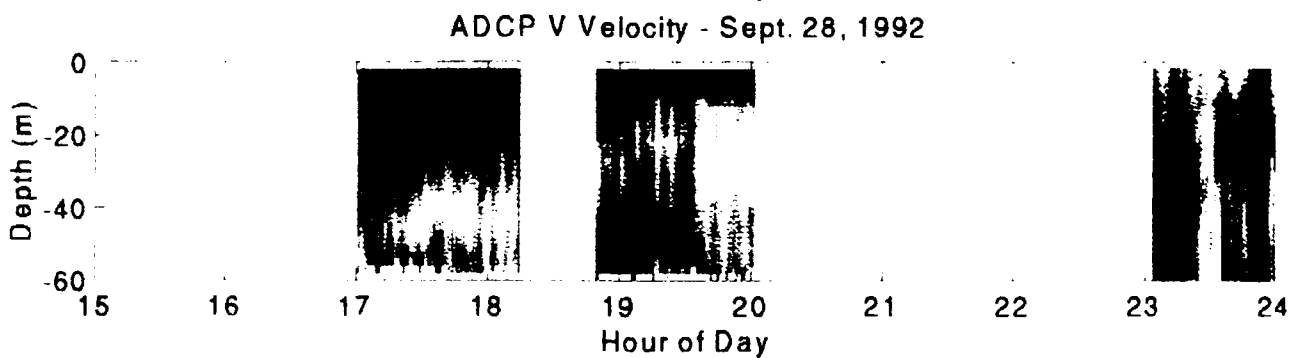
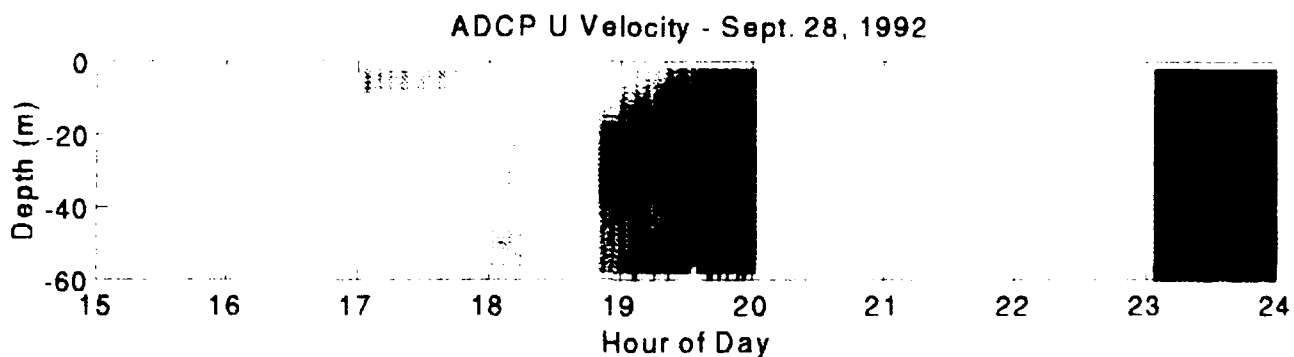
LIST OF FIGURES

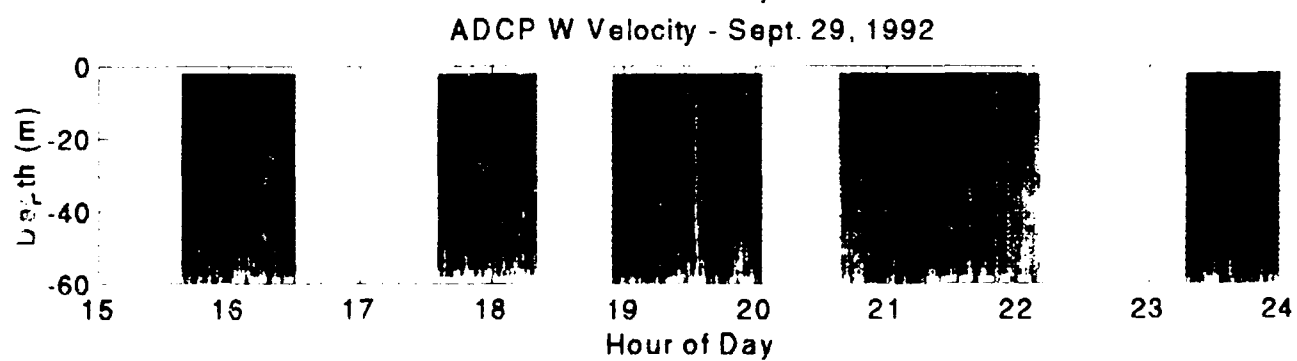
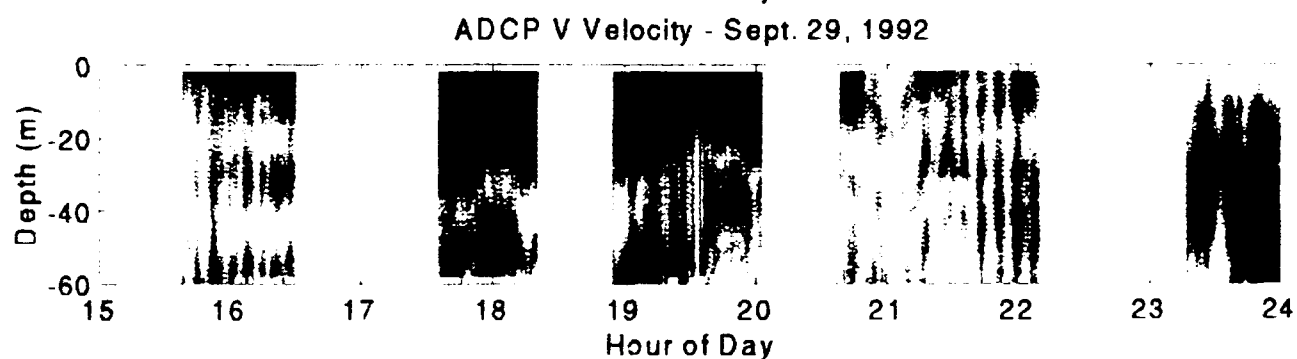
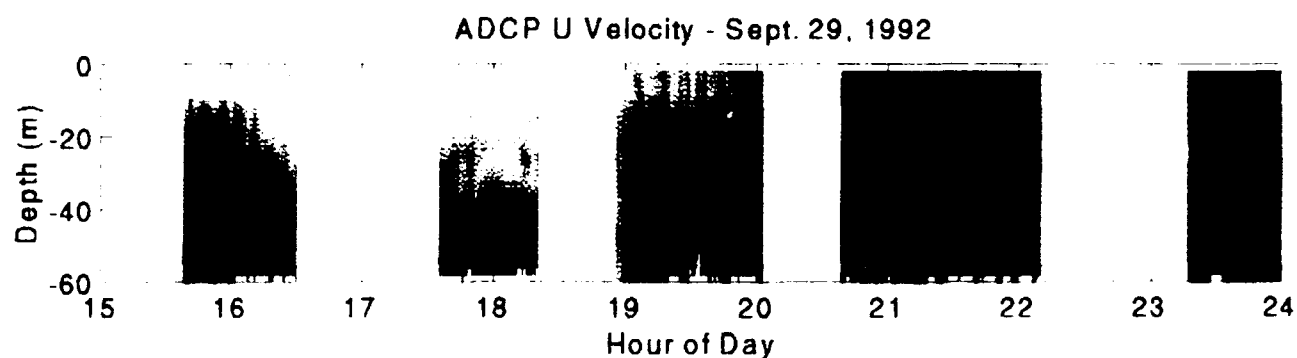
APPENDIX D

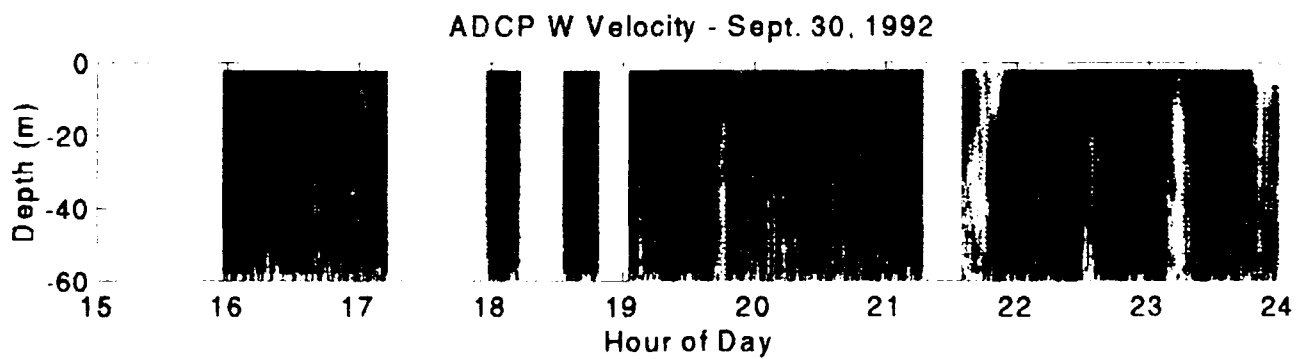
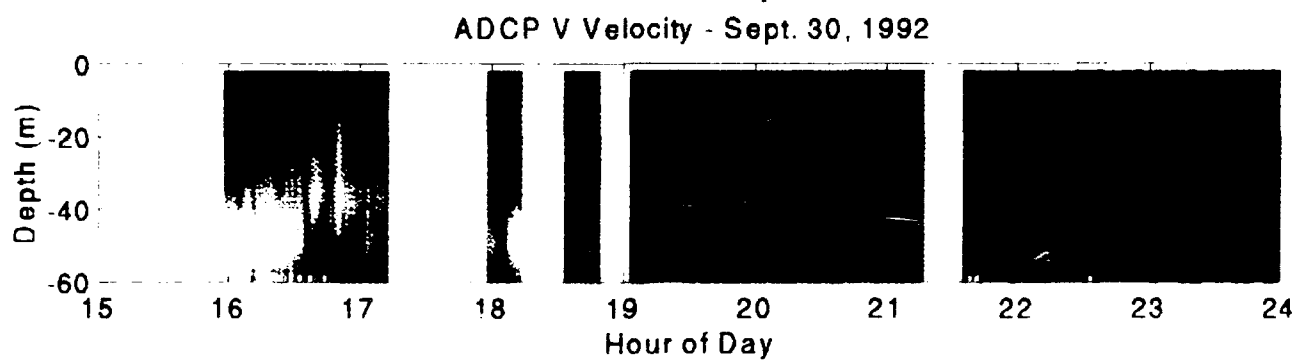
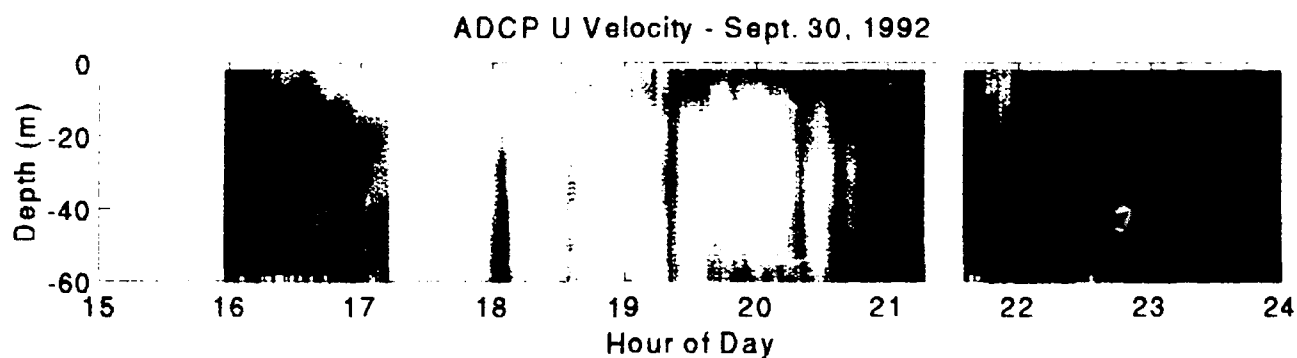
ADCP Current Velocity, 15:00 - 24:00, 21 September 1992	D-3
ADCP Current Velocity, 15:00 - 24:00, 24 September 1992	D-4
ADCP Current Velocity, 15:00 - 24:00, 28 September 1992	D-5
ADCP Current Velocity, 15:00 - 24:00, 29 September 1992	D-6
ADCP Current Velocity, 15:00 - 24:00, 30 September 1992	D-7

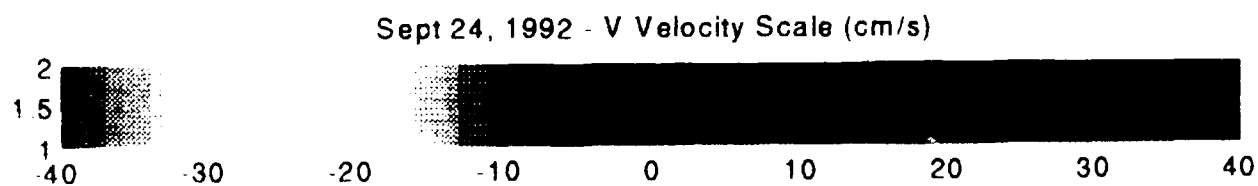
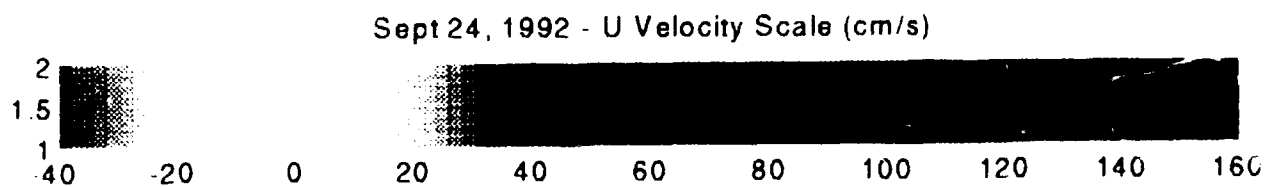
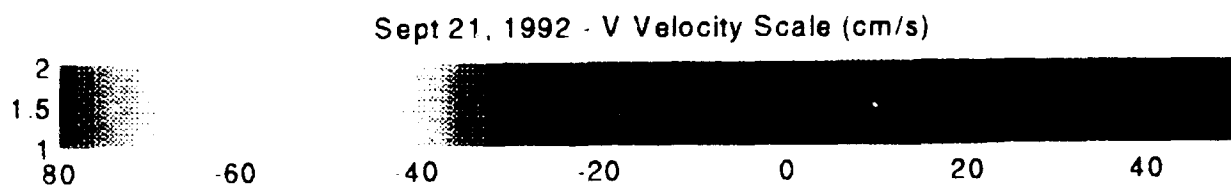
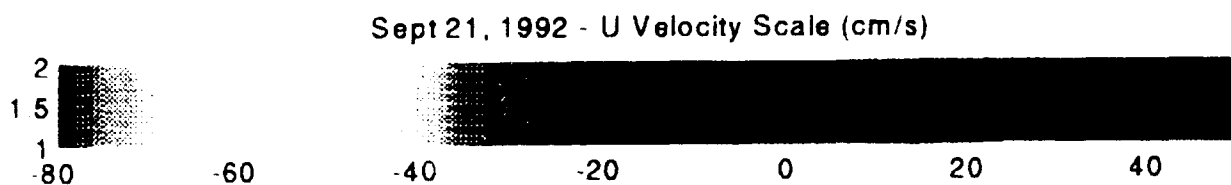




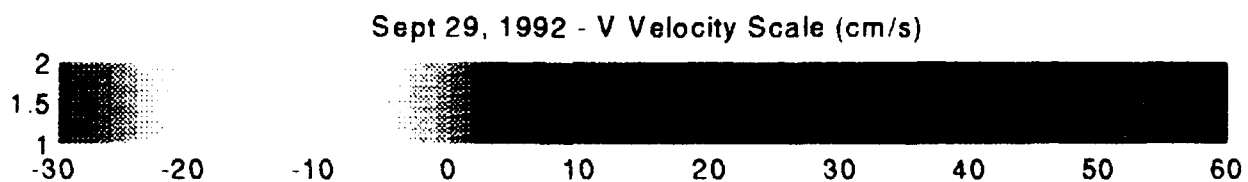
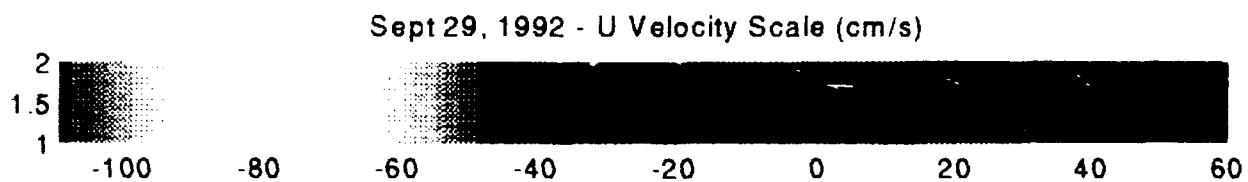
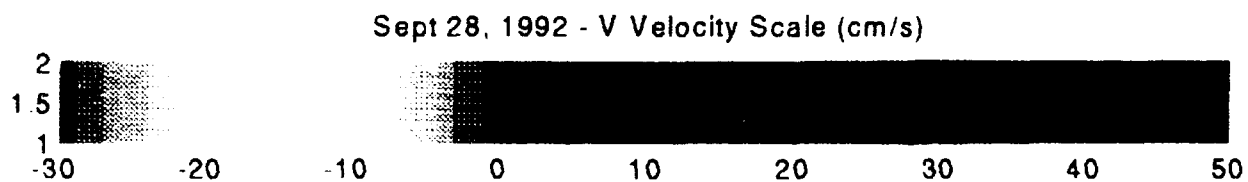
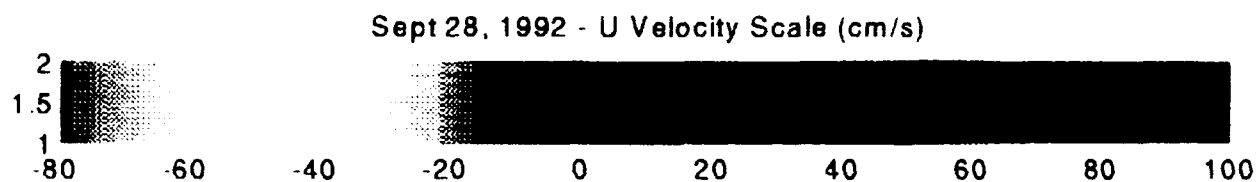




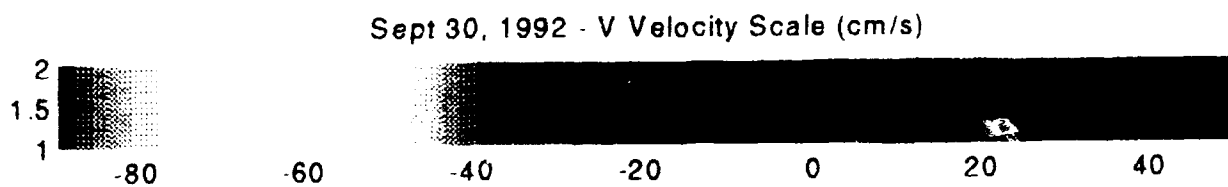
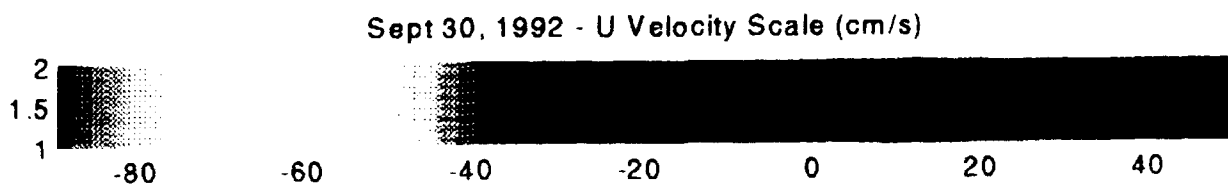




Velocity Scale Color Map



Velocity Scale Color Map



Velocity Scale Color Map

APPENDIX E

CTD Station Locations

Each CTD cast is plotted with an "X" representing the Transect casts and a "." representing the Time Series casts. Since the Time Series casts are clustered in the same area only a "TS" is printed for the cast name. The Current Meter Moorings are shown with a "+" for reference. The following table lists each cast with Date (PDT), Time(UTC), Latitude, and Longitude.

LIST OF FIGURES

APPENDIX E

CTD Station Locations	E-4
---------------------------------	-----

LIST OF TABLES

APPENDIX E

CTD Station Date, Time, & Positions E-5

TET 1992 - CTD Stations

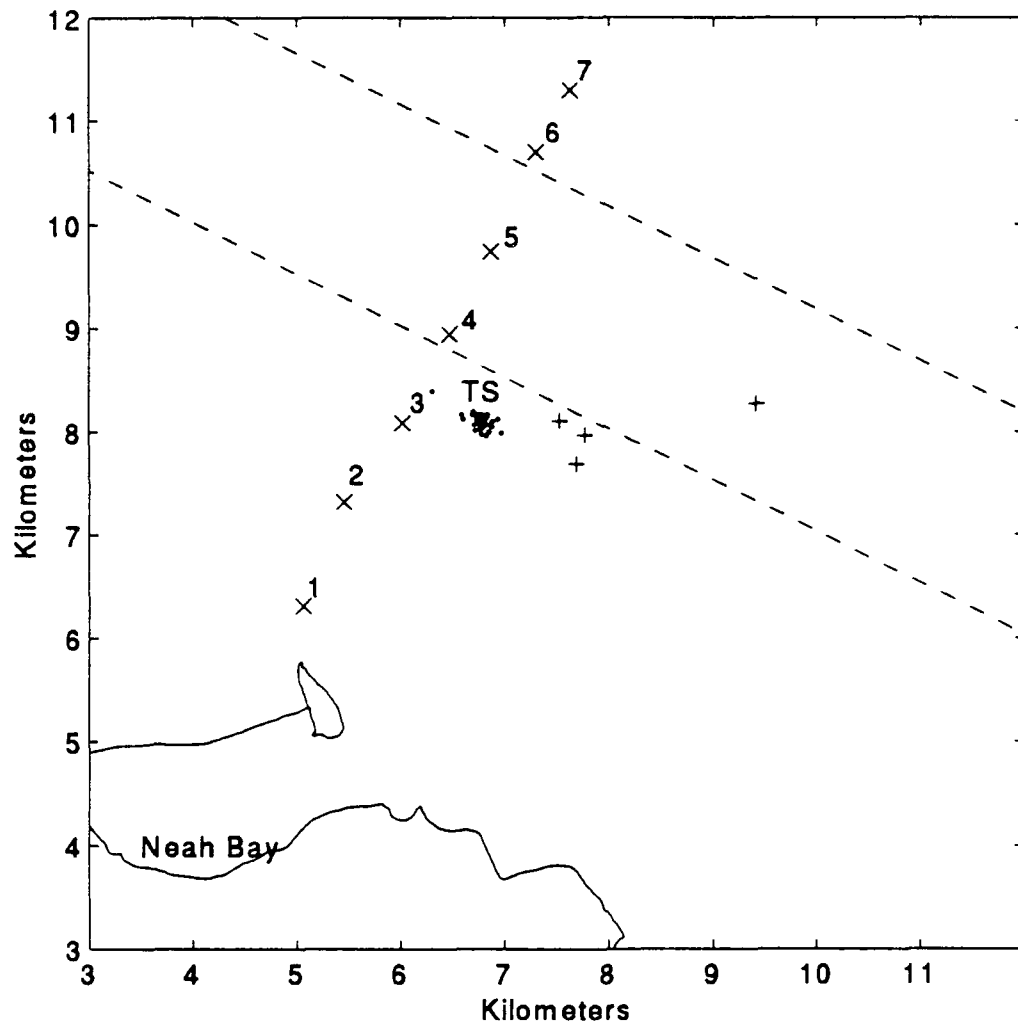


Table E-1 CTD Cast Times and Locations

Date	JD	Station	Time	Depth (m)	Latitude (N)			Longitude (W)		
					D	M	S	D	M	S
09/22/92	266	1	16:12	48	48	23	24.41	124	35	53.20
09/22/92	266	2	16:34	89	48	23	57.09	124	35	34.22
09/22/92	266	3	17:02	120	48	24	22.04	124	35	6.45
09/22/92	266	4	17:24	180	48	24	49.62	124	34	44.48
09/22/92	266	5	17:52	200	48	25	15.47	124	34	25.08
09/22/92	266	6*	18:25	235	48	25	46.60	124	34	4.29
09/22/92	266	7	18:58	243	48	26	5.91	124	33	48.39
09/23/92	267	TS1	15:28	143	48	24	32.05	124	34	52.25
09/23/92	267	TS2	15:58	135	48	24	23.71	124	34	26.66
09/23/92	267	TS3*	16:29	134	48	24	22.97	124	34	29.08
09/23/92	267	TS4*	17:00	130	48	24	18.54	124	34	19.77
09/23/92	267	TS5	17:29	132	48	24	22.96	124	34	28.93
09/23/92	267	TS6	17:58	135	48	24	24.47	124	34	26.50
09/23/92	267	TS7	18:31	132	48	24	22.36	124	34	28.22
09/23/92	267	TS8	19:01	132	48	24	23.19	124	34	28.06
09/23/92	267	TS9	19:29	130	48	24	22.11	124	34	29.34
09/23/92	267	TS10	20:00	130	48	24	21.31	124	34	26.99
09/23/92	267	TS11	20:30	132	48	24	24.62	124	34	31.25
09/23/92	267	TS12	21:01	132	48	24	24.52	124	34	32.77
09/23/92	267	TS13	21:30	123	48	24	18.28	124	34	29.23
09/23/92	267	TS14*	22:00	132	48	24	23.90	124	34	31.21
09/23/92	267	TS15	22:30	123	48	24	18.20	124	34	29.10
09/23/92	267	TS16	23:02	130	48	24	21.29	124	34	30.01
09/23/92	267	TS17	23:31	124	48	24	19.04	124	34	25.61
09/23/92	268	TS18	00:00	122	48	24	17.83	124	34	27.15

Table E-1 CTD Cast Times and Locations

Date	JD	Station	Time	Depth (m)	Latitude (N)			Longitude (W)		
					D	M	S	D	M	S
09/25/92	269	1	15:01	48	48	23	26.41	124	35	55.39
09/25/92	269	2	15:24	87	48	23	57.59	124	35	32.87
09/25/92	269	3	15:48	122	48	24	26.95	124	35	9.12
09/25/92	269	4	16:08	172	48	24	47.68	124	33	44.68
09/25/92	269	5	16:44	210	48	25	15.86	124	34	24.10
09/25/92	269	6	17:12	235	48	25	45.43	124	34	1.69
09/25/92	269	7	17:40	242	48	26	5.40	124	33	48.79
09/25/92	269	TS1	18:34	130	48	24	21.31	124	34	29.80
09/25/92	269	TS2	19:04	132	48	24	22.45	124	34	24.15
09/25/92	269	TS3	19:29	134	48	24	23.44	124	34	27.56
09/25/92	269	TS4	20:00	130	48	24	20.70	124	34	24.70
09/25/92	269	TS5	20:29	130	48	24	21.58	124	34	29.27
09/25/92	269	TS6	20:59	128	48	24	21.32	124	34	32.36
09/25/92	269	TS7	21:30	135	48	24	25.65	124	34	33.40
09/25/92	269	TS8	22:01	135	48	24	22.37	124	34	21.88
09/25/92	269	TS9	22:30	133	48	24	24.18	124	34	28.29
09/25/92	269	TS10	23:00	132	48	24	22.84	124	34	27.86
09/25/92	269	TS11	23:29	132	48	24	24.39	124	34	33.58
09/25/92	269	TS12	23:59	128	48	24	21.90	124	34	30.81

Table E-1 CTD Cast Times and Locations

Date	JD	Station	Time	Depth (m)	Latitude (N)			Longitude (W)		
					D	M	S	D	M	S
10/01/92	275	1	15:37	52	48	23	27.5	124	35	51.9
10/01/92	275	2	15:56	87	48	23	57.4	124	35	30.9
10/01/92	275	3	16:13	122	48	24	23.9	124	35	3.4
10/01/92	275	4	16:31	175	48	24	44.5	124	34	42.4
10/01/92	275	5	17:04	210	48	25	14.2	124	34	19.8
10/01/92	275	6	17:36	234	48	25	46.6	124	34	3.4
10/01/92	275	7	18:10	240	48	26	6.2	124	33	53.6
10/01/92	275	TS1	18:56	125	48	24	19.5	124	34	32.3
10/01/92	275	TS2	19:31	130	48	24	21.98	124	34	30.07
10/01/92	275	TS3	19:58	130	48	24	20.64	124	34	28.55
10/01/92	275	TS4	20:29	130	48	24	23.35	124	34	28.66
10/01/92	275	TS5	21:00	130	48	24	23.14	124	34	29.21
10/01/92	275	TS6	21:30	132	48	24	23.85	124	34	29.40
10/01/92	275	TS7	22:00	130	48	24	22.94	124	34	31.39
10/01/92	275	TS8	22:30	134	48	24	23.70	124	34	30.40
10/01/92	275	TS9	22:58	130	48	24	23.70	124	34	28.46
10/01/92	275	TS10	23:30	130	48	24	21.59	124	34	29.96
10/01/92	276	TS11	00:00	130	48	24	22.41	124	34	28.10

Table E-1 CTD Cast Times and Locations

Date	JD	Station	Time	Depth (m)	Latitude (N)			Longitude (W)		
					D	M	S	D	M	S
10/02/92	276	1	16:19	48	48	23	23.10	124	35	43.80
10/02/92	276	2	16:32	88	48	23	59.53	124	35	33.26
10/02/92	276	3	16:51	122	48	24	24.66	124	35	6.34
10/02/92	276	4	17:12	176	48	24	48.95	124	34	42.24
10/02/92	276	5	17:39	209	48	25	15.53	124	34	22.91
10/02/92	276	6	18:06	235	48	25	48.19	124	34	5.68
10/02/92	276	7	18:32	240	48	26	5.25	124	33	51.94
10/02/92	276	TS1	19:13	132	48	24	21.18	124	34	25.06
10/02/92	276	TS2	19:45	130	48	24	21.04	124	34	29.58
10/02/92	276	TS3	20:15	132	48	24	24.34	124	34	29.11
10/02/92	276	TS4	20:43	131	48	24	22.97	124	34	37.86
10/02/92	276	TS5	21:14	132	48	24	22.78	124	34	31.5
10/02/92	276	TS6*	21:44	138	48	24	24.39	124	34	38.51
10/02/92	276	TS7*	22:15	132	48	24	22.90	124	34	31.5
10/02/92	276	TS8*	22:45	130	48	24	19.73	124	34	29.7
10/02/92	276	TS9*	23:16	133	48	24	23.59	124	34	28.54
10/02/92	276	TS10*	23:44	130	48	24	23.79	124	34	27.2
10/02/92	277	TS11*	00:15	133	48	24	22.74	124	34	28.58
10/02/92	277	TS12*	00:45		48	24	23.42	124	34	29.94

* = Bad or no data

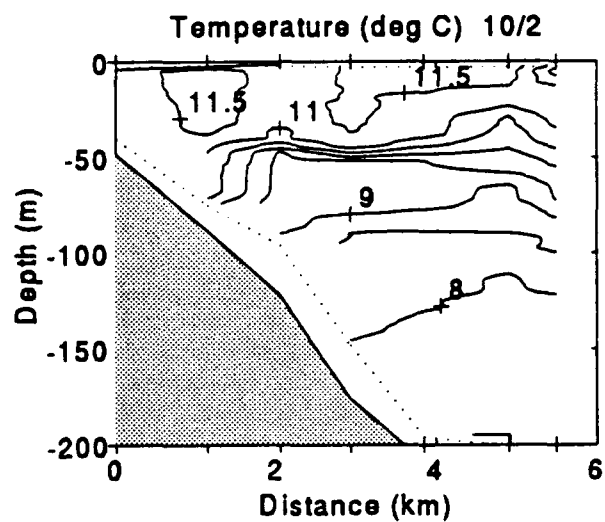
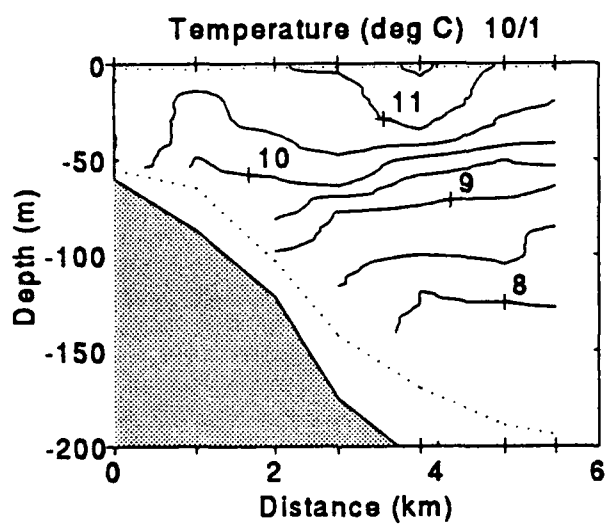
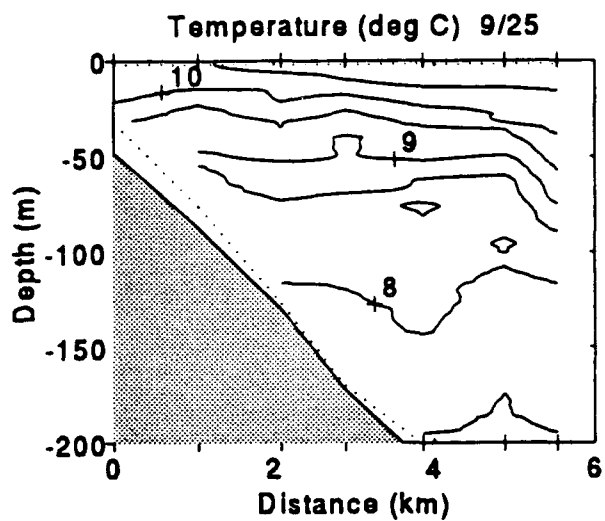
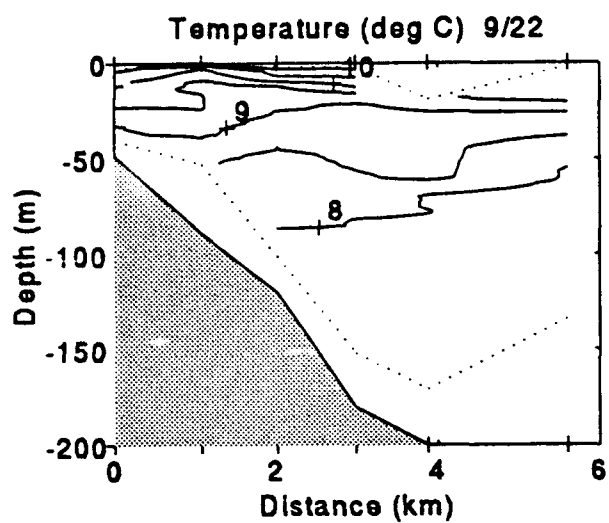
APPENDIX F

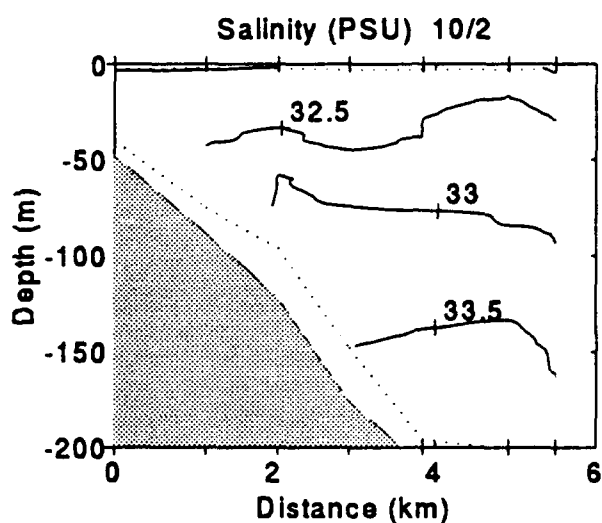
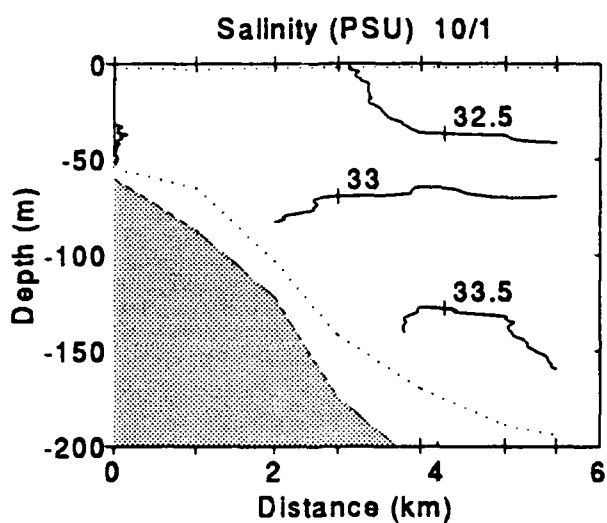
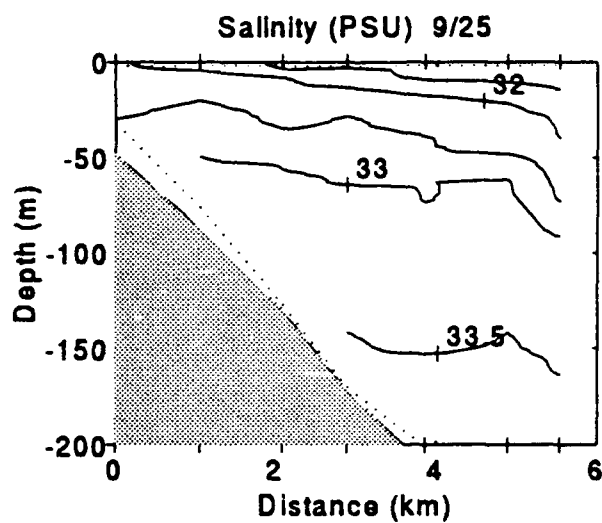
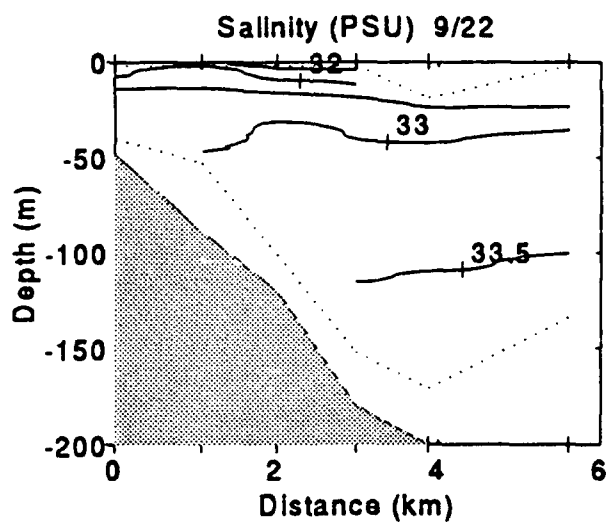
CTD Transects: Temperature, Salinity, Density, and B-V Frequency

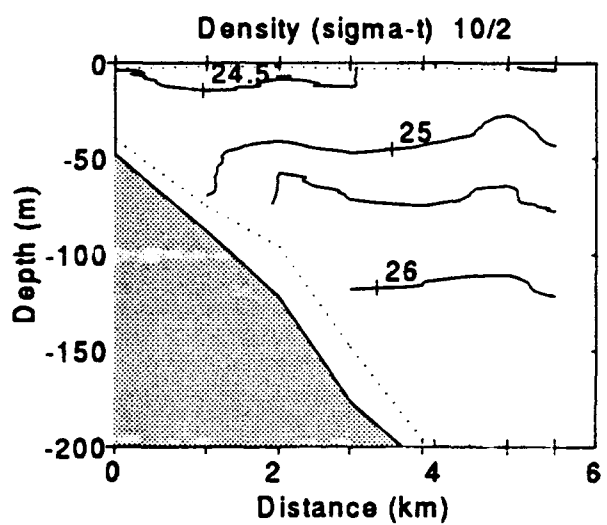
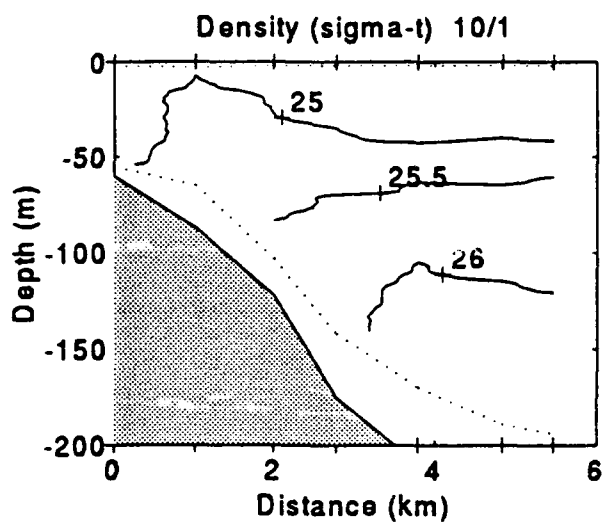
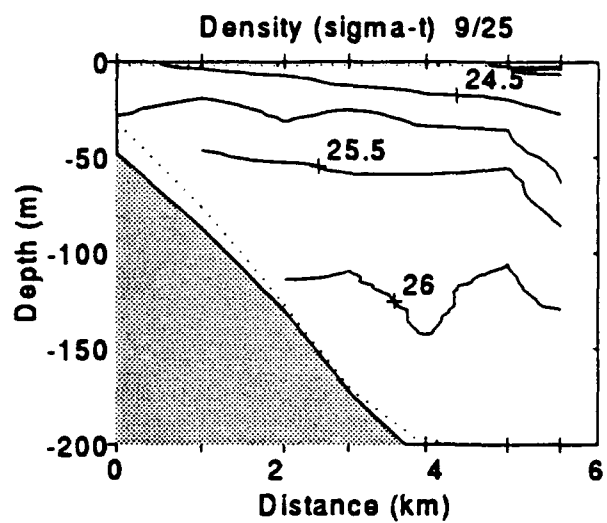
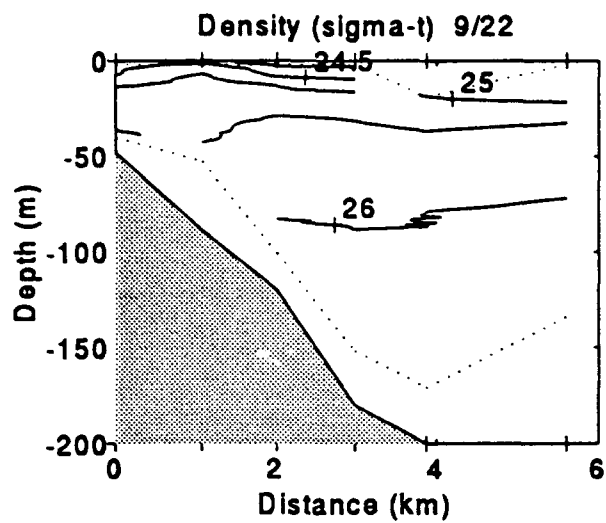
LIST OF FIGURES

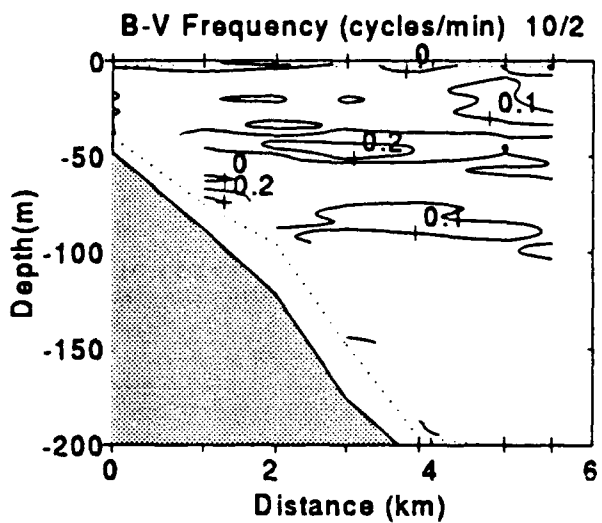
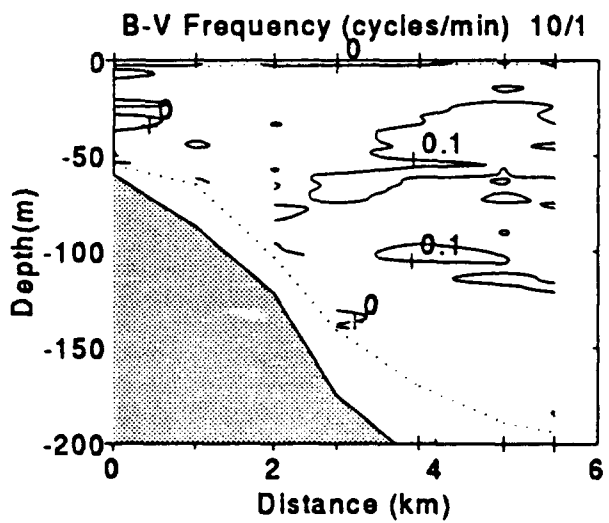
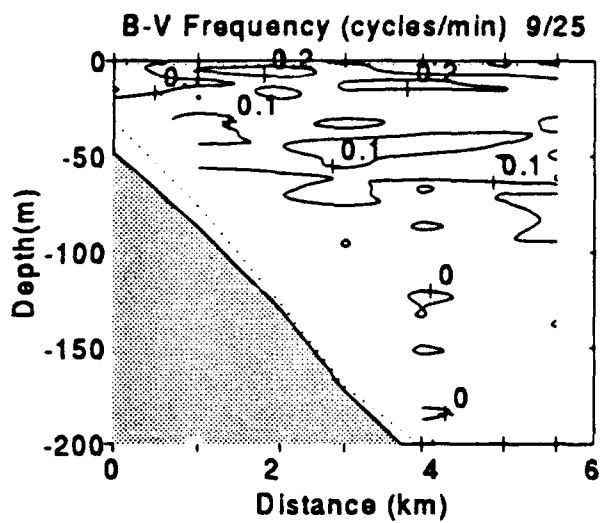
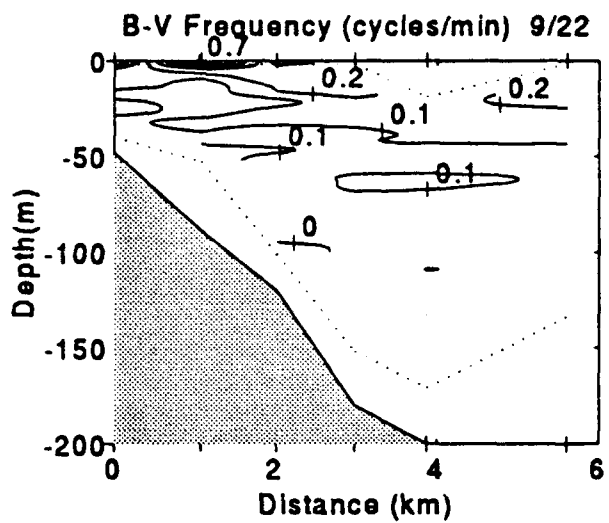
APPENDIX F

CTD Transects, Temperature, 22 September - 2 October	F-3
CTD Transects, Salinity, 22 September - 2 October	F-4
CTD Transects, Density, 22 September - 2 October	F-5
CTD Transects, Brunt-Väisälä Frequency, 22 September - 2 October	F-6









APPENDIX G

CTD Station Time Series: Temperature, Salinity, Density, and B-V Frequency

LIST OF FIGURES

APPENDIX G

CTD Time Series, Temperature, 23 September - 2 October	G-3
CTD Time Series, Salinity, 23 September - 2 October	G-4
CTD Time Series, Density, 23 September - 2 October	G-5
CTD Time Series, Brunt-Väisälä Frequency, 23 September - 2 October	G-6

